Tests of Electroweak Symmetry Breaking at e^+e^- Colliders:

Technicolor Searches with OPAL and Higgs Simulations for ILC

Dissertation
zur Erlangung des Doktorgrades
des Fachbereichs Physik
der Universität Hamburg

vorgelegt von
Niels Meyer
aus Hamburg

Hamburg
Dezember 2004

Gutachter der Dissertation	:	Univ. Prof. Dr. R.-D. Heuer Univ. Prof. Dr. P. Schleper
Gutachter der Disputation	:	Univ. Prof. Dr. R.-D. Heuer Univ. Prof. Dr. B. Naroska
Datum der Disputation	:	14.01.2005
Vorsitzender des Prüfungsausschusses	:	Univ. Prof. Dr. G. Heinzelmann
Vorsitzender des Promotionsausschusses	:	Univ. Prof. Dr. R. Wiesendanger
Dekan des Fachbereichs	:	Univ. Prof. Dr. G. Huber

Abstract

This thesis describes three analyses on issues connected to electroweak symmetry breaking. A search for Technicolor signatures in e^+e^- collisions at $\sqrt{s} = 189 - 209\,\mathrm{GeV}$ recorded with the OPAL detector in the years 1998 to 2000 is presented. No evidence for a signal in data is observed. The results are interpreted in the framework of the Technicolor Straw-man Model (TCSM) to derive exclusion limits in the parameter space spanned by the mass of technipions $\pi_T^{\pm}$ and technivector states ρ_T^0/ω_T^0. An absolute lower limit $m_{\pi_T} > 87\,\mathrm{GeV}$ is obtained independent on m_{ρ_T/ω_T} at the 95 % confidence level for a model with 9 technifermion doublets.

Further, two simulations on Standard Model Higgs bosons at the future International Linear Collider ILC are performed. It is shown, that the total decay width of the Higgs boson can be measured from the reconstructed lineshape with an uncertainty of 23 − 34 % for $m_H = 200 - 320\,\mathrm{GeV}$. The width is extracted from a model-independent fit, from which also the Higgs mass and the event rate are obtained. In addition, the analysis allows to determine the branching ratios of the Higgs to W- and Z-bosons under the assumption, that these are the only decay modes.

The last analysis investigates effects of beam-beam background at the ILC on the analysis of Higgs production in WW-fusion. Collisions of beamstrahlung photons can cause hadronic events $\gamma\gamma \to$ hadrons, which have significant probability to overlap with events from e^+e^- collisions. If the detector can not tag (time-stamp) single bunch-crossings, hadronic two-photon events are accumulated over more than one bunch crossing. The impact of this pile-up effect on the reconstruction of events from Higgs signal is studied in different scenarios for the detector time-stamping capability assuming the two technology proposals for the ILC, the superconducting TESLA and the normal-conducting NLC/GLC. Significant degradation of the separation of Higgs signal events from $e^+e^- \to b\bar{b}\,\nu\bar{\nu}$ background is found for the normal-conducting technology. In this case, detector time-stamping capabilities of better than 10 ns are needed.

Zusammenfassung

Diese Arbeit beschreibt drei Analysen, die Fragen im Zusammenhang mit der elektroschwachen Symmetriebrechung untersuchen. In Daten von e^+e^- Kollisionen mit $\sqrt{s} = 189-209\,\mathrm{GeV}$, die zwischen 1998 und 2000 mit dem OPAL Detektor aufgezeichnet wurden, wird nach Signaturen von Technicolor gesucht. Es wird keine Evidenz für ein Signal beobachtet. Um Grenzen auf die Masse von Technipionen $\pi_T^{\pm}$ und Technicolor Vektorzuständen ρ_T^0/ω_T^0 zu ermitteln, werden die Ergebnisse im Rahmen des Technicolor Straw-man Modells (TCSM) interpretiert. Für ein Modell mit neun Technifermion-Dubletts wird mit einem Vertrauensniveau von 95 % eine absolute untere Grenze von $m_{\pi_T} > 87\,\mathrm{GeV}$ gefunden.

Desweiteren werden zwei Messungen zu dem Higgsboson des Standardmodells am zukünftigen International Linear Collider ILC simuliert. Es wird gezeigt, dass die totale Zerfallsbreite für Higgsbosonen mit $m_H = 200 - 320\,\mathrm{GeV}$ mit einer Genauigkeit von $23 - 34\,\%$ in der Verteilung der rekonstruierten Higgsmasse gemessen werden kann. Die Breite wird dabei mit einer modellunabhängigen Anpassung ermittelt, von der auch die Higgsmasse und die Ereignisrate bestimmt werden können. Darüber hinaus liefert die Analyse Ergebnisse für die Zerfallsraten des Higgsbosons in W- und Z-Bosonpaare, wenn man annimmt, dass keine weiteren Zerfallskanäle existieren.

Die letzte Analyse untersucht den Einfluß von Strahlinduziertem Untergrund am ILC auf die Analyse der Produktion von Higgsbosonen durch WW-Fusion. Kollisionen von Photonen aus der sogenannten "Beamstrahlung" können über den Prozess $\gamma\gamma \to$ Hadronen zu hadronischen Endzuständen führen, die mit großer Wahrscheinlichkeit gleichzeitig zu den e^+e^- Wechselwirkungen auftreten. Wenn der Detektor nicht in der Lage ist, Ereignisse einzelnen Kollisionen von Teilchenpaketen zuzuordenen, wird der hadronische Strahluntergrund zudem aus mehrere Paketkollisionen zusammen aufgezeichnet. Der Einfluß dieser Akkumulation auf die Rekonstruktion von Higgsbosonen wird unter mehreren Annahmen für die Beschleunigertechnologie (TESLA oder NLC/GLC) und Höhe der Untergrundakkumulation untersucht. Im Falle der NLC/GLC Technologie wird eine erhebliche Verschlechterung der Trennung von Higgssignal und $e^+e^- \to b\bar{b}\nu\bar{\nu}$ Untergrund beobachtet, was in diesem Fall einen Detektor nötig macht, der den Zeitpunkt eines Ereignisses mit besser als 10 ns bestimmen kann.

Contents

Chapter 1

Introduction

Today, elementary particles and their interactions are successfully described by the Standard Model. The matter particles are introduced as fermions, i.e. particles with spin one-half, which interact by exchanging bosonic particles with integer spin. Different bosons appear for the three different observed interactions: Photons mediate the electromagnetic interaction, which describes a large spectrum of phenomena like electricity, magnetism, and light. The weak interaction, which describes nuclear processes like e.g. radioactive decays of atomic nuclei or the processes that fuel the sun, is mediated by the $W^{\pm}$- and the Z^0-boson. Gluons mediate the strong interaction, which e.g. binds quarks inside protons and neutrons.

A crucial ingredient to the Standard Model is the concept of local gauge invariance. In fact, the existence of exchange bosons is postulated by the requirement, that the fundamental equations of the theory (so-called Lagrange densities) are invariant under local gauge transformation w.r.t. a certain symmetry group. Local gauge invariance can only be accomplished for massless fermions and bosons. However, all fermions and the W- and Z-bosons are found to be massive. This implies, that the part of the Standard Model gauge group describing the W- and Z-boson must be broken. In the Standard Model, this "electroweak symmetry breaking" is described by the Higgs mechanism, which predicts another new particle, the Higgs boson. This particle has not been observed directly. The best exclusion limit comes from the Large Electron Positron collider LEP. The Higgs boson is the only missing piece in the experimental confirmation of the Standard Model.

The non-observation of the Higgs boson arising from the Higgs mechanism in the Standard Model justifies the search for particles from alternative approaches to explain electroweak symmetry breaking. Some of these theories for physics beyond the Standard Model are minimal invasive in the sense that they alter the Higgs sector, but leave the rest of the Standard Model unchanged, which for instance applies to general two Higgs doublet models. A fundamentally different approach introduces new strong interactions and new fermions with respective charges to explain electroweak symmetry breaking dynamically rather than through an elementary Higgs field. Technicolor is such a model. While a specific implementation of dynamical electroweak symmetry breaking which satisfies all constraints from precision electroweak measurements has not yet been formulated, the 'low energy' phenomenology of such models is rather clear.

Both approaches predict the presence of at least one new particle. Thus, the search for these particles is the first step on an experimental roadmap to explore electroweak symmetry breaking. In case no signatures of new physics are found, the results however can be used to constrain the respective theory. For instance, no evidence for the Standard Model Higgs has been observed so far. However, physicists have a well motivated idea about the mass range, where this particle is expected, if it exists at all. Of course, the discovery of a new particle is a more pointing hint than the exclusion of one model after another. The Large Hadron Collider LHC will be best suited for searches of new phenomena, and it is expected that particles from a rich spectrum of theories could be discovered there.

Once a new particle is found, two further questions arise: Is it responsible for the masses of the SM fermions and bosons, and: What is the underlying theory, e.g. have we found the Standard Model Higgs boson or something else? The latter question arises from the fact, that particles from different theories might be very similar in their properties. Both of these questions need very precise measurements of the properties of the newly-found particle, e.g. its production cross-sections and decay rates. For these measurements, e^+e^- colliders are much better suited than hadron colliders, since they provide a much cleaner experimental environment with well defined initial conditions and low backgrounds.

The International Linear Collider ILC is a project currently under development for an e^+e^- linear collider, which is planned to complement the discovery potential of LHC with the potential of high precision measurements. Recently, the technology for the ILC has been chosen from two concurring technologies.

This thesis includes three analyses connected to both of these general steps. A search for Technicolor is presented in data recorded with the OPAL experiment at LEP. The second analysis investigates the potential of the ILC for determining the Higgs width, i.e. the uncertainty for a simulated measurement of this parameter. The method developed also allows for the determination of the Higgs mass, the event rate from one specific production process and of the branching ratios to pairs of W- and Z-bosons. The last analysis was initiated by the evaluations of the design proposals in course of the technology decision for the ILC and studies the impact of hadronic background from beam-beam interactions on the analysis of Higgs production in WW-fusion for both proposed ILC technologies.

Chapter 2

Theory and Experimental Status

The physics of fundamental particles and their interactions is described by the Standard Model (SM). It provides a coherent description of three of the four forces observed in Nature (see Tab. 2.1), as well as of all elementary particles. Only gravity is not incorporated as quantum theory, and so far Standard Model and General Relativity could not be combined to give a coherent description. The effect of gravity on particle physics is negligible compared to the other interactions. Only at energies of the Planck scale $\Lambda_{\mathrm{Pl}} \sim 10^{19}\,\mathrm{GeV}$, gravity will be as strong as the other interactions. Therefore, it will not be considered further.

Interaction	Mediated by	Coupling constant		Charge
Strong	Gluon g	$\alpha_s = g_s^2/4\pi$	≈ 0.12	color
Weak	$\mathrm{W}^{\pm}$, Z^0	$g^2/4\pi$	≈ 0.03	(weak) isospin
Electromagnetic	Photon γ	$\alpha = e^2/4\pi$	$\approx 8 \times 10^{-3}$	electric charge
Gravity	Graviton (?) G	G_N	$\approx 6.71 \times 10^{-39}\,\mathrm{GeV}^{-2}$	(E, p) tensor

Table 2.1: *The fundamental interactions and the particles, by which they are mediated, their coupling strengths at energies of order*)(100 GeV) *and the charge they couple to. Gravity is by far the weakest interaction and not included in the Standard Model.*

The Standard Model is based on three pillars:

- **Matter particles**
  The fundamental particles of the Standard Model are fermions, which are classified as leptons and quarks according to their interactions. Six leptons and six quarks are known, which can be grouped into three (expect for their mass) identical families:

$$\text{Leptons} \quad \begin{pmatrix} \nu_{\mathrm{e}} \\ \mathrm{e} \end{pmatrix}, \quad \begin{pmatrix} \nu_{\mu} \\ \mu \end{pmatrix}, \quad \begin{pmatrix} \nu_{\tau} \\ \tau \end{pmatrix}$$

$$\text{Quarks} \quad \begin{pmatrix} \mathrm{u} \\ \mathrm{d} \end{pmatrix}, \quad \begin{pmatrix} \mathrm{c} \\ \mathrm{s} \end{pmatrix}, \quad \begin{pmatrix} \mathrm{t} \\ \mathrm{b} \end{pmatrix}$$

  The propagation of the fermions and their anti-particles is described by Dirac's equation.

- **Local gauge invariance**
  By demanding local gauge invariance of the free particles' Lagrangian, gauge fields have to be introduced. Interactions between the fermion fields then are described by exchange of gauge field quanta. The strong interaction is described by Quantum Chromo

Dynamics (QCD), and the gauge field quanta are eight massless gluons g. Weak and electromagnetic interactions are described by the electroweak theory. The gauge fields of this group mix to yield the fields of $W^{\pm}$- and Z-boson (which mediate the weak interaction) and the photon γ. Photon exchange alone can also be described by Quantum Electro Dynamics (QED).

- **Electroweak symmetry breaking**
  Local gauge invariance under the SM gauge groups can only be achieved for massless fermions and massless gauge bosons. This contradicts experimental observations, which show that all particles but gluons and photons are massive. This implies, that the electroweak gauge symmetry is broken down to the gauge symmetry of QED, while the QCD gauge symmetry remains intact. The Higgs mechanism [1] is an elegant way to explain apparent gauge boson and fermion masses in a gauge invariant formulation. The minimal theory as incorporated in the Standard Model predicts one additional scalar particle, the Higgs boson.

The Standard Model is one of the best tested physical theories, and there is no experimental evidence from particle physics experiments that contradict its predictions. However, strong arguments exist against the validity of the theory up to the Planck scale. In the following section, the Standard Model is outlined. The phenomenology and current experimental status of the SM Higgs sector is described, and possible extensions of the minimal Higgs sector are introduced. The chapter is completed with a general introduction of Technicolor and a more detailed description of an effective low-energy Technicolor model.

2.1 The Standard Model

Electroweak Theory

The electromagnetic and weak interactions are described together by the electroweak theory as formulated by Glashow, Salam and Weinberg [2]. The theory is based on the gauge group $SU(2)_I \times U(1)_Y$ with charges (weak) isospin I and (weak) hypercharge Y.

The weak interaction is found to violate parity [3], i.e. inversion of the three directions. This can be described by grouping left handed[1] particles to isospin doublets with $I = 1/2$ and right handed particles to isospin singlets $I = 0$.

The hypercharge Y combines the third component of the isospin and the electric charge. It is defined as $Y = 2(Q - I_3)$ and thus yields the same value for the both components of an isospin doublet. The isospin multiplets for the lightest leptons are

$$\begin{array}{ll} L = & \begin{pmatrix} \nu_L \\ e_L \end{pmatrix} \\ R = & e_R \end{array} \qquad I_3 = \begin{cases} 1/2 \\ -1/2 \\ 0 \end{cases} \qquad Q = \begin{cases} 0 \\ -1 \\ -1 \end{cases} \qquad Y = \begin{cases} -1 \\ -1 \\ -2 \end{cases} .$$

The isospin $SU(2)_I$ rotation transforms

$$L \to L' = \exp\left(ig\alpha^i \frac{\sigma_i}{2}\right) L \qquad \text{and} \qquad R \to R' = R, \tag{2.2}$$

[1] Fermions have two helicity states, named left and right handed, defined as

$$\psi_L = \frac{1-\gamma^5}{2}\psi \qquad \text{and} \qquad \psi_R = \frac{1+\gamma^5}{2}\psi, \tag{2.1}$$

where ψ is the fermion field and $\gamma^5 = i\gamma^0\gamma^1\gamma^2\gamma^3$ the product of all four γ-matrices.

where g is a coupling constant, σ_i, $i = 1...3$ are the Pauli matrices as a representation of $SU(2)$, and α^i are three functions of space-time. In analog, the $U(1)$ hypercharge transformation has the form

$$L \rightarrow L' = \exp\left(ig'\beta\frac{Y}{2}\right) L \qquad \text{and} \qquad R \rightarrow R' = \exp\left(ig'\beta\frac{Y}{2}\right) R. \tag{2.3}$$

Here, g' is another coupling constant and β another space-time dependent function. The Lagrangian of the free fields

$$\mathcal{L} = i\left(\bar{L}\gamma^\mu\partial_\mu L + \bar{R}\gamma^\mu\partial_\mu R\right) \tag{2.4}$$

is not invariant under either $SU(2)$ or $U(1)$ transformation. This is achieved by two further steps. First, the covariant derivative ∂_μ has to be extended by terms containing gauge fields:

$$\partial_\mu \rightarrow D_\mu = i\left(\partial_\mu + igI\sigma_i \mathrm{W}^i_\mu + ig'\frac{Y}{2}\mathrm{B}_\mu\right). \tag{2.5}$$

The second step is to require that the gauge fields transform according to

$$\mathrm{W}^i_\mu \rightarrow \mathrm{W}^{i\,\prime}_\mu = \mathrm{W}^i_\mu - \frac{1}{g}\partial_\mu\alpha^i - \epsilon^{ijk}\alpha_j\mathrm{W}_{k\mu} \qquad \text{and} \tag{2.6}$$

$$\mathrm{B}_\mu \rightarrow \mathrm{B}'_\mu = \mathrm{B}_\mu - \frac{1}{g'}\partial_\mu\beta. \tag{2.7}$$

The electroweak Lagrangian now reads

$$\mathcal{L}_{EW} = -\frac{1}{4}F^i_{\mu\nu}F^{i\mu\nu} - \frac{1}{4}f_{\mu\nu}f^{\mu\nu} + i\left(\bar{L}\gamma^\mu D_\mu L + \bar{R}\gamma^\mu D_\mu R\right), \tag{2.8}$$

where the field strength tensors are defined as

$$F^i_{\mu\nu} = \partial_\mu\mathrm{W}_\nu - \partial_\nu\mathrm{W}_\mu - g\epsilon^{ijk}\mathrm{W}_{j\mu}\mathrm{W}_{k\nu} \qquad \text{and} \tag{2.9}$$

$$f_{\mu\nu} = \partial_\mu\mathrm{B}_\nu - \partial_\nu\mathrm{B}_\mu. \tag{2.10}$$

Compared to Eq. 2.4, additional terms arise from the requirement of gauge invariance. New vector fields W^i_μ and B_μ are introduced, all of which couple to fermions. While the W^i_μ fields couple only to left handed fermions, the B_μ also has right handed couplings. Due to the non-abelian structure of the $SU(2)$ gauge group, self coupling terms among the W^i_μ fields appear. This can be seen from the last term of the field strength tensor $F^i_{\mu\nu}$ in Eq. 2.9, which is missing in the abelian tensor $f_{\mu\nu}$ of Eq. 2.10.

The field combinations

$$\mathrm{W}^\pm_\mu = \frac{1}{\sqrt{2}}\left(\mathrm{W}^1_\mu \pm i\mathrm{W}^2_\mu\right) \tag{2.11}$$

describe the transition between left handed electron and neutrino, and thus have the expected characteristics of the $\mathrm{W}^\pm$ bosons. On the contrary, the assignment

$$\mathrm{W}^3_\mu \rightarrow \mathrm{Z}^0_\mu \qquad \text{and} \qquad \mathrm{B}_\mu = \mathrm{A}_\mu \tag{2.12}$$

contradicts experimental findings. The B_μ field couples to neutrinos, which is not observed for the photon field A_μ. The fields of Z-boson and photon have to be mixtures of the W^3_μ and B_μ fields:

$$\begin{pmatrix} \mathrm{Z}_\mu \\ \mathrm{A}_\mu \end{pmatrix} = \begin{pmatrix} \cos\theta_W & -\sin\theta_W \\ \sin\theta_W & \cos\theta_W \end{pmatrix} \begin{pmatrix} \mathrm{W}^3_\mu \\ \mathrm{B}_\mu \end{pmatrix}. \tag{2.13}$$

The value of $\cos\theta_W$ is fixed by the requirement of vanishing neutrino-photon coupling, i.e. that the couplings of W^3_μ and B_μ to neutrinos cancel each other. This is achieved for

$$\cos\theta_W = \frac{g}{\sqrt{g^2+g'^2}}. \tag{2.14}$$

The W-bosons of Eq. 2.12 only couple to fermions of one isospin doublet. Concerning leptons, this correctly describes the experimental findings of lepton flavor conservation[2]. Treating quarks the same way would lead to stable bound states with second and third generation quarks, like Kaons, which clearly contradicts observations. The puzzle is solved by mixing of the $I_3 = -1/2$ quark mass eigenstates d_L, s_L and b_L to the weak eigenstates d'_L, s'_L and b'_L by the unitary Cabbibo-Kabayashi-Maskawa matrix V_{CKM}

$$\begin{pmatrix} d' \\ s' \\ b' \end{pmatrix}_L = V_{CKM} \begin{pmatrix} d \\ s \\ b \end{pmatrix}_L = \begin{pmatrix} V_{ud} & V_{us} & V_{ub} \\ V_{cd} & V_{cs} & V_{bb} \\ V_{td} & V_{ts} & V_{tb} \end{pmatrix} \begin{pmatrix} d \\ s \\ b \end{pmatrix}_L . \tag{2.15}$$

The off-diagonal elements of the CKM matrix are small, which suppresses couplings between quarks of different families.

It is of special interest that flavors of either leptons or quarks are only changed via $W^\pm$ exchange. Indeed, no strong flavor changing neutral currents (FCNC) which e.g. would arise from tree-level $c \to u$ transitions are observed experimentally. Also, no transition between quarks and leptons arises, which leads e.g. to a stable proton.

The $W^\pm$ and Z bosons are found to be massive, which is not compatible with local gauge invariance. On the other hand, the photon is massless, and thus can be regarded as the gauge quantum of Quantum Electro Dynamics (QED). QED describes the electromagnetic interaction with the gauge group $U(1)_Q$, where Q indicates that the gauge field couples to electric charge, thus has the coupling constant e. Both models describe the electron-photon vertex, and equivalence of the coupling strengths yields the mutual dependence of the coupling constants:

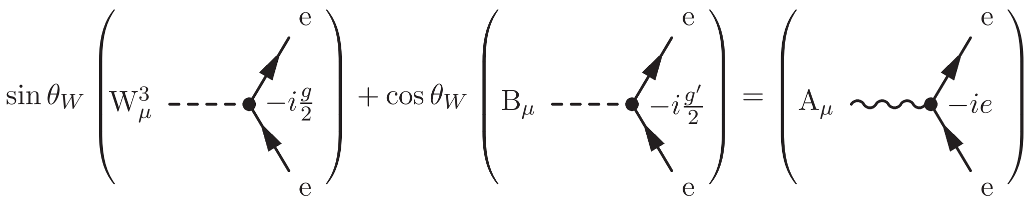

$$\Longrightarrow \quad e = g\sin\theta_W = g'\cos\theta_W = \frac{gg'}{\sqrt{g^2+g'^2}}. \tag{2.16}$$

To explain the masses of the weak gauge bosons, the gauge group $SU(2)_I \times U(1)_Y$ of electroweak theory must be broken down to the still conserved $U(1)_Q$ of QED. Spontaneous symmetry breaking and its implementation into the Standard Model is introduced in Sec. 2.2.

Quantum Chromo Dynamics

The theory of strong interaction is called Quantum Chromo Dynamics (QCD). It is based on the gauge group $SU(3)_C$, where the index C refers to the color degree of freedom. Leptons

[2]Recent experiments [4, 5, 6, 7] indicate neutrino mixing, which violates lepton flavor. As a consequence, a neutrino mixing matrix in analog to the CKM matrix has to be introduced.

do not carry color charge, while quarks appear in three color states, usually denoted as red, green and blue. The free quark Lagrangian thus can be written as

$$\mathcal{L}_\mathrm{q} = i\bar{\Psi}\gamma^\mu\partial_\mu\Psi \qquad \text{with} \qquad \Psi = \begin{pmatrix} \mathrm{q}_\mathrm{red} \\ \mathrm{q}_\mathrm{green} \\ \mathrm{q}_\mathrm{blue} \end{pmatrix}. \tag{2.17}$$

In analog to electroweak theory, gauge fields are introduced by requiring gauge invariance of the free quark Lagrangian under $SU(3)$ color rotation

$$\Psi \rightarrow \Psi' = \exp\left(i\frac{g_s}{2}\lambda_i\xi^i\right)\Psi. \tag{2.18}$$

Here, λ_i are eight generators of the $SU(3)$ group, ξ^i are eight space-time dependent functions, and g_s is the strong coupling constant.

$SU(N)$ invariance requires N^2-1 gauge fields. The gauge quanta are called gluons, because they act like a strong 'glue' between quarks. The gluons are massless, and $SU(3)_C$ is thus an unbroken symmetry. The fields transform in analog to Eq. 2.6, which means that gluon self-interaction arises from the non-abelian nature of the gauge group.

Effective Coupling Constants

In lowest order, QED scattering processes are described by single photon exchange. In higher orders, the photon breaks up to form virtual fermion loops, as depicted in Fig. 2.1 a). The integral over the fermion momentum diverges, and so the contribution of the whole diagram would be infinite. However, finite results can be obtained by renormalization. Gauge invariant theories can generally be renormalized [8], while interactions with dimensional coupling constants like the Fermi-theory of weak interaction are always non-renormalizable.

Renormalization causes the coupling constant $\alpha = e^2/4\pi$ to be dependent on the momentum transfer Q^2 of the photon according to

$$\alpha \rightarrow \alpha\left(Q^2\right) = \frac{\alpha_0}{1 - \frac{\alpha_0}{3\pi}\log\left(\frac{Q^2}{Q_0^2}\right)}, \tag{2.19}$$

where Q_0 is a small energy of the order of the masses of the fermions in the loop (dominated by electrons), and $\alpha_0 \approx 1/137$ is the fine structure constant. For very large Q^2, $\alpha(Q^2)$ is logarithmically divergent.

The evolution of α is completely dominated by electron loops. Contributions from other leptons are suppressed due to their larger mass, while quarks only have fractional electric charge and thus weaker coupling to photons.

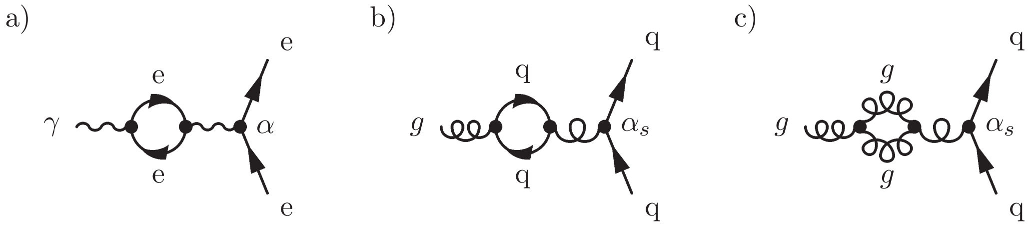

Figure 2.1: *Loop corrections to photon and gluon propagator. The fermion/quark loops in the first two diagrams get polarized and thus enhance the vertex charge α/α_s. In contrast, the gluons in the loop of the third diagram shield the vertex charge.*

In QCD, the most simple process is single gluon exchange, and higher order contributions to the gluon propagator arise from virtual quark loops (Fig. 2.1 b) in analogy to the electron loops in QED. But, due to the gluon self-interaction, additional corrections with virtual gluon loops arise (Fig. 2.1 c). These yield opposite contribution to the coupling evolution, which reads

$$\alpha_s \to \alpha_s \left(Q^2\right) = \frac{12\pi}{(33 - 2N_f) \log\left(\frac{Q^2}{\Lambda^2_{QCD}}\right)}. \tag{2.20}$$

N_f is the number of quark flavors contributing in the quark loops, and Λ_{QCD} is a characteristic energy scale, which is determined to be

$$\Lambda_{QCD} \approx 200 - 300\,\mathrm{MeV}. \tag{2.21}$$

from measurements of $\alpha_s \approx 0.12$ at $Q^2 \approx 100\,\mathrm{GeV}$. For very high $Q^2 \gg \Lambda_{QCD}$, α_s approaches zero. This effect is referred to as asymptotic freedom. For decreasing momentum transfer, α_s becomes stronger and reaches unity at distances $r = 1/Q \approx 1\,\mathrm{fm}$. Quarks are constrained to distances less than r, they form color neutral hadrons. This effect is named confinement.

It is interesting to note, that the progress of evolution of α_s is a function of the number of quark flavors, and that additional quark flavors would slow down the decrease of the coupling with increasing Q^2. On the contrary, additional color degrees of freedom would speed up the coupling evolution.

Chiral Symmetry Breaking

Although QCD and electroweak theory are completely independent, QCD includes a mechanism which gives effective masses to the weak gauge bosons. The mechanism is based on interactions between the weak gauge bosons and quark condensates and thus is often referred to as dynamical symmetry breaking. In this section, the mechanism will be introduced and it will be shown that the effect is not sufficient to explain the observed masses of W- and Z-bosons.

The strong isospin describes rotations in the u − d flavor space, and QCD is invariant under $U(2)$ isospin rotations. The invariance holds separately for left and right handed quarks, since QCD also does not distinguish the quarks' chirality. The theory is said to have

$$U_L(2) \times U_R(2) = SU_V(2) \times SU_A(2) \times U_V(1) \times U_A(1) \tag{2.22}$$

chiral symmetry. The subscripts refer to left (L) and right (R) handed or vector ($V = R + L$) and axial-vector ($A = R - L$) symmetry transformations respectively.

The $SU_V(2) \times U_V(1)$ symmetry describes $SU(2)$ flavor invariance and baryon number conservation, both very well established by experiments. On the contrary, no experimental evidences for $SU_A(2)$ or $U_A(1)$ invariance have been found. For instance, no chiral partner of the proton (which has spin-parity of $\frac{1}{2}^+$) with about the same mass and spin-parity of $\frac{1}{2}^-$ exists.

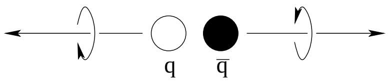

Figure 2.2: *A fermion and its anti-fermion are referred to as chiral pair if they have opposite momentum and spin orientation.*

Breaking of $SU_A(2) \times U_A(1)$ symmetry can be accomplished by the assumption, that the vacuum is filled with quark-antiquark condensates. The quarks in these condensates have to be chiral pairs as in Fig. 2.2, e.g. have opposite momentum and spin, to ensure that the vacuum has no net momentum or angular momentum. The invariance under $U_L(2) \times U_R(2)$ breaks down to invariance under $U_L(2) = U_R(2)$ transformations. By this, the quark condensates yield non-vanishing expectation values

$$\langle 0\,|\bar{\mathrm{q}}\mathrm{q}|\,0\rangle = \langle 0\,|\bar{\mathrm{q}}_L\mathrm{q}_R + \bar{\mathrm{q}}_R\mathrm{q}_L|\,0\rangle \neq 0. \tag{2.23}$$

Goldstone's theorem [9] states, that one massless spinless boson arises for each broken generator of a symmetry group. These so-called Goldstone bosons play a crucial role in giving mass to the weak gauge bosons. Massive vector bosons have three states of polarization, while massless bosons only have two. The Goldstone bosons are needed to provide the additional degree of freedom.

From chiral symmetry breaking, four massless Goldstone bosons are expected. Three of them can be identified with the pions $\pi^{\pm}, \pi^0$, while the fourth mixes with additional states arising from strange quarks (which are completely omitted during this discussion) to form the η^0. Due to the small masses of the u- and d-quarks, chiral symmetry is only approximate, and the Goldstone bosons are only approximately massless.

The presence of quark condensates with non-zero expectation value modifies the W-boson propagator by couplings to the Goldstone pions

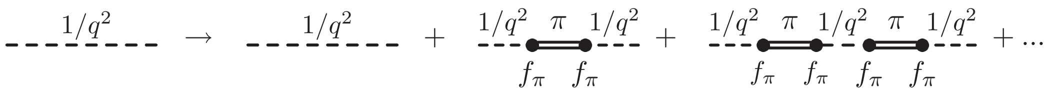

leading to a mass of the W-boson of

$$m_{\mathrm{W}} = \frac{g f_\pi}{2}. \tag{2.24}$$

The parameter f_π is called the pion decay constant. It parameterizes the coupling between charged pions and W-bosons, and also determines the pion decay (Fig. 2.3). It is measured from the pion decay width [10] with a value of

$$f_\pi = 93\,\mathrm{MeV} \qquad \Longrightarrow \qquad m_{\mathrm{W}} \approx 30\,\mathrm{MeV}. \tag{2.25}$$

This value is more than three orders of magnitude too small compared to the measured W-mass [11] of

$$m_{\mathrm{W}} = 80.425 \pm 0.038\,\mathrm{GeV}. \tag{2.26}$$

A new QCD like interaction with $F_\pi = v = 246\,\mathrm{GeV}$ would however yield the correct W-mass without introduction of a fundamental scalar. This is one of the motivations for Technicolor, which will be introduced in Sec. 2.6.

Spontaneous symmetry breaking

Another approach to explain the observed gauge boson masses is spontaneous symmetry breaking. This mechanism is embedded into the Standard Model and does not depend on postulation of additional interactions.

A gauge theory is said to be spontaneously broken if its Lagrangian is gauge invariant, but the ground state is not. In case of the Standard Model, this means that the vacuum is

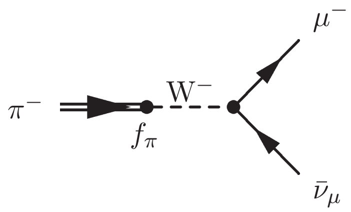

Figure 2.3: *The pion decay is determined by the effective coupling f_π between pion and* W-*boson. Therefore, f_π is called pion decay constant.*

not invariant under $SU(3)_C \times SU(2)_I \times U(1)_Y$ transformations, but only under $U(1)_Q$ and $SU(3)_C$ transformations.

The Higgs mechanism [1] describes spontaneous symmetry breaking by scalar fields with non-vanishing vacuum expectation value. These scalar fields might either be fundamental or composite. The SM explains gauge boson and fermion masses by the minimal fundamental field configuration, which is an isospin doublet of complex scalar fields.

A complex doublet of scalar fields has four degrees of freedom. Symmetry breaking is accomplished in only one of these dimension, and one Goldstone boson arises. This can be identified with a new particle, the Higgs boson. The remaining three degrees of freedom are absorbed by the longitudinal polarization states of the W- and Z-bosons, which arise for massive particles only.

The Higgs mechanism and the phenomenology of the Higgs boson is introduced in the next section. Results on Higgs boson searches at recent colliders are presented, and prospects at future colliders are outlined. Also, extensions of the minimal Higgs sector will be discussed briefly.

2.2 The Higgs Mechanism and its Implementation in the Standard Model

In the Standard Model, a scalar isospin doublet

$$\Phi = \begin{pmatrix} \Phi^+ \\ \Phi^0 \end{pmatrix} \tag{2.27}$$

of complex scalar fields is introduced *ad hoc* into the theory. The Lagrangian of the Higgs field has the form

$$\mathcal{L}_{\mathrm{H}} = \left(D_\mu \Phi\right)^\dagger \left(D^\mu \Phi\right) - V\left(\Phi\right) \tag{2.28}$$

with the covariant derivative D_μ from Eq. 2.5. The potential

$$V\left(\Phi\right) = -\mu^2 \Phi^\dagger \Phi + \lambda^2 \left(\Phi^\dagger \Phi\right)^2 \qquad \text{with} \qquad \lambda,\, \mu \in \mathbb{R}^+. \tag{2.29}$$

is constructed to have a non vanishing expectation value

$$\langle \Phi \rangle = \frac{v}{\sqrt{2}} = \frac{\mu}{\sqrt{2}\lambda}. \tag{2.30}$$

The field Φ is color neutral to preserve $SU(3)_C$ symmetry and the expectation value of the charged field $\langle \Phi^+ \rangle$ has to be zero to avoid breaking of $U(1)_Q$ symmetry. The potential is shown in Fig. 2.4 as a function of the two field components of Φ^0. The rotation angle in the complex Φ^0 plane can be chosen freely to yield $\left\langle \mathrm{Im}\Phi^0 \right\rangle = 0$ and $\left\langle \mathrm{Re}\Phi^0 \right\rangle = v/\sqrt{2}$. This choice

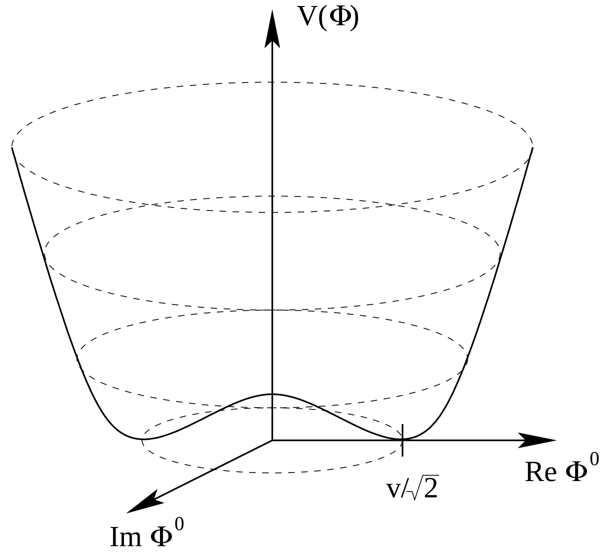

Figure 2.4: *The Higgs potential in the complex plane of the neutral component of the Higgs doublet. All minima of the rotational symmetric potential are equivalent. Fixing the gauge to one specific states spontaneously breaks the symmetry.*

corresponds to choosing one specific gauge functional α_i in the $SU(2)_I$ transformation (2.2) and spontaneously breaks the gauge invariance of the ground state.

Small excitations of the vacuum state

$$\Phi = \frac{1}{\sqrt{2}} \begin{pmatrix} 0 \\ v+\eta \end{pmatrix} \tag{2.31}$$

modify the Lagrangian 2.28 to give

$$\mathcal{L}_\mathrm{H} = \frac{1}{2}\left(\partial_\mu \eta\right)\left(\partial^\mu \eta\right) - \frac{1}{2}(\sqrt{2}v\lambda)^2\eta^2 + \frac{1}{2}\left(\frac{g(v+\eta)}{2}\right)^2 \left(\left|\mathrm{W}_\mu^+\right|^2 + \left|\mathrm{W}_\mu^-\right|^2 + \frac{|\mathrm{Z}_\mu|^2}{\cos\theta_W}\right). \tag{2.32}$$

The Lagrangian now includes a new field η. The quanta of the η field are called Higgs bosons, and its mass is determined by the Higgs self-coupling parameter λ, for which follows from the second term of (2.32)

$$m_\mathrm{H} = \sqrt{2}\lambda v. \tag{2.33}$$

The last part of the Lagrangian describes couplings between the weak gauge boson fields and the Higgs field, with vertices of the type

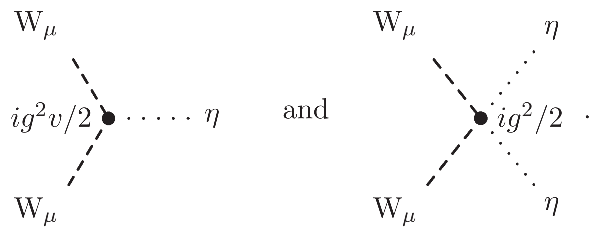

(2.34)

In addition, there are couplings of the form $(vg/2)^2\,|\mathrm{W}_\mu|^2$, which modify the boson propagators

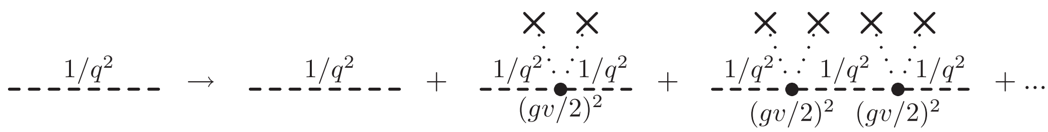

(2.35)

The helicity state of the initial boson changes by factors of ± 2 at each vertex. Only massive particles have a time-evolution and thus can change their helicity. Indeed, the W-propagator can be re-written as

$$\frac{1}{q^2} \to \frac{1}{q^2} + \frac{1}{q^2}\left(\frac{gv}{2}\right)^2 \frac{1}{q^2} + \frac{1}{q^2}\left(\frac{gv}{2}\right)^2 \frac{1}{q^2}\left(\frac{gv}{2}\right)^2 \frac{1}{q^2} + \ldots = \frac{1}{q^2 + (gv/2)^2} = \frac{1}{q^2 + m_{\mathrm{W}}^2}, \tag{2.36}$$

so the gauge boson fields aquire an effective mass

$$m_{\mathrm{W}} = \frac{gv}{2} \qquad \text{and} \qquad m_{\mathrm{Z}} = \frac{gv}{2\cos\theta_W}. \tag{2.37}$$

It is remarkable, that the weak mixing angle θ_W, which is fixed to eliminate couplings between neutrinos and photons, also prevents the photon to obtain mass.

In Equ. 2.31, only excitations of $\mathrm{Re}\,\Phi^0$ are considered. Excitations of the other three components of Φ give rise to three massless Goldstone bosons. The degrees of freedom of these fields are absorbed by the longitudinal states of polarization of the now massive $\mathrm{W}^{\pm}$ and Z fields.

Fermions can aquire mass by the same mechanism. Yukawa terms

$$\mathcal{L}_{\mathrm{Yukawa}} = -g_{\mathrm{f}}\left[\bar{R}_{\mathrm{f}}\left(\Phi^{\dagger} L_{\mathrm{f}}\right) + \left(\bar{L}_{\mathrm{f}}\Phi\right) R_{\mathrm{f}}\right] \tag{2.38}$$

have to be introduced to the Lagrangian for each fermion f. L_{f} and R_{f} are the left and right handed fermion fields, and g_{f} is a constant for each fermion type, which is not predicted by the theory. With the scalar field Φ from (2.31), coupling terms between fermion and Higgs fields arise, as well as couplings between fermion fields and vacuum. The latter modify the fermion propagator

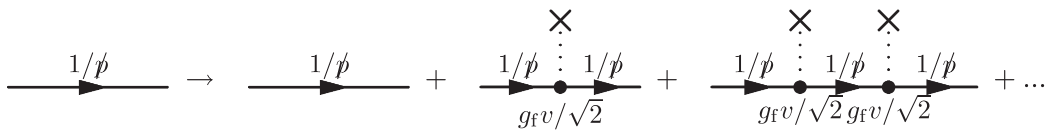

$$\frac{1}{\not{p}} \longrightarrow \frac{1}{\not{p}} + \frac{1}{\not{p}}\frac{g_{\mathrm{f}}v}{\sqrt{2}}\frac{1}{\not{p}} + \frac{1}{\not{p}}\frac{g_{\mathrm{f}}v}{\sqrt{2}}\frac{1}{\not{p}}\frac{g_{\mathrm{f}}v}{\sqrt{2}}\frac{1}{\not{p}} + \ldots = \frac{1}{\not{p} + g_{\mathrm{f}}v/\sqrt{2}} = \frac{1}{\not{p} + m_{\mathrm{f}}} \tag{2.39}$$

and the fermions aquire effective masses

$$m_{\mathrm{f}} = g_{\mathrm{f}}\frac{v}{\sqrt{2}}. \tag{2.40}$$

The Higgs mechanism with one fundamental scalar isospin doublet is a very elegant way to introduce masses for gauge bosons and for fermions while keeping the theory renormalizable, i.e. the gauge principle intact. The phenomenology of the Higgs boson depends on the fermion masses and the self-coupling parameter λ, which determines the Higgs mass. All of these parameters are not predicted by the Standard Model, however the fermion masses are determined experimentally. More details on the SM Higgs boson phenomenology are summarized in Sec. 2.2.1.

2.2.1 Standard Model Higgs Phenomenology

As outlined in Sec. 2.2, the phenomenology of the SM Higgs sector is fully determined by the Higgs mass, which is the only free parameter. The Higgs boson couples to massive fermions f and weak gauge bosons V = W, Z with coupling strengths

$$g_{\mathrm{Hff}} = \frac{\sqrt{2}}{v} m_{\mathrm{f}} \qquad \text{and} \qquad g_{\mathrm{HVV}} = \frac{2\sqrt{2}}{v} m_{\mathrm{V}}^2. \tag{2.41}$$

There are no tree-level couplings between Higgs bosons and gluons or photons, since these particles are massless. However, effective couplings occur at the one loop level (Fig. 2.5), where all colored/charged massive particles contribute. Since the Higgs couples proportional to the masses of the particles in the loop, the effective Higgs-gluon and Higgs-photon couplings are very sensitive to new, heavy particles beyond the particle spectrum predicted by the Standard Model.

Figure 2.5: *Effective vertices for a) Higgs-gluon and b) Higgs-photon couplings. All massive particles, which have color (electric) charge contribute to the Higgs-gluon (Higgs-photon) coupling. The major contributions arise from* t, b *(*W, t*).*

SM Higgs production

In e^+e^- collisions, Higgs bosons can be produced predominantly in association with a Z-boson or in weak boson fusion (Fig. 2.6). Boson fusion involving Z bosons is suppressed by a factor $\approx 1/10$ with respect to W bosons. Another possible process is Yukawa production, where the Higgs is radiated off a heavy quark. The cross-section is much lower than for the processes discussed so far, but top Yukawa production at very high energies is interesting to study the top-Higgs coupling.

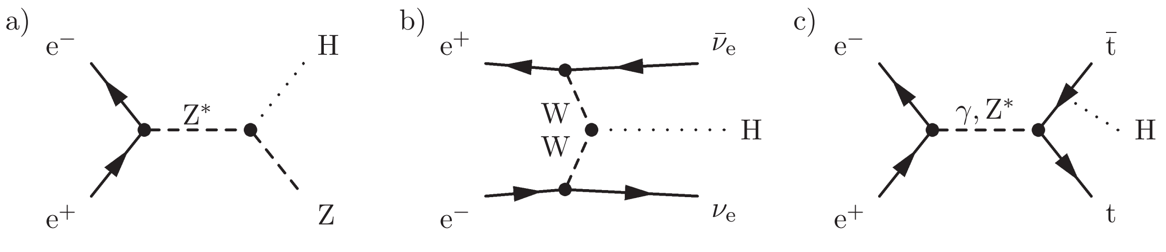

Figure 2.6: *Major Higgs production processes Higgsstrahlung a) and weak boson fusion b). Top-Yukawa production c) is of interest at very high collision energies.*

Unlike the Z-boson, Higgs bosons cannot be produced as a s-channel resonance in e^+e^- collisions due to the tiny electron-Higgs coupling. This implies, that the dependence of production cross-sections on the collision energy $\sqrt{s}$ is rather moderate. The cross-section of

Higgsstrahlung is

$$\sigma_{\mathrm{HZ}} = \frac{g^2_{\mathrm{HZZ}}}{4\pi} \frac{G_F\left(v_{\mathrm{e}}^2 + a_{\mathrm{e}}^2\right)}{96\sqrt{2}\mathrm{s}} \beta_{\mathrm{HZ}} \frac{\beta^2_{\mathrm{HZ}} + 12 m^2_{\mathrm{Z}}/\mathrm{s}}{\left(1 - m^2_{\mathrm{Z}}/\mathrm{s}\right)^2}, \tag{2.42}$$

where $\beta_{\mathrm{HZ}} = \left[1 - (m_{\mathrm{H}} + m_{\mathrm{Z}})^2/\mathrm{s}\right]\left[1 - (m_{\mathrm{H}} - m_{\mathrm{Z}})^2/\mathrm{s}\right]$. The vector and axial couplings between electron and Z-boson are $v_{\mathrm{e}} = -1 + 4\sin^2\theta_W$ and $a_{\mathrm{e}} = -1$. The cross-section shows a $1/\mathrm{s}$ energy dependence with the center-of-mass energy $\sqrt{\mathrm{s}}$ and dominates at low energies.

The cross-section for WW-fusion rises with $\log \mathrm{s}$, and the process dominates at high center-of-mass energies. In the high energy limit the cross-section is given by

$$\sigma_{\mathrm{H}\nu_{\mathrm{e}}\bar{\nu}_{\mathrm{e}}} \longrightarrow \frac{g^2_{\mathrm{HWW}}}{4\pi} \frac{G_F^2}{8\pi^2}\left[\left(1 + \frac{m^2_{\mathrm{H}}}{\mathrm{s}}\right)\log\frac{\mathrm{s}}{m^2_{\mathrm{H}}} - 2\left(1 - \frac{m^2_{\mathrm{H}}}{\mathrm{s}}\right)\right]. \tag{2.43}$$

Both cross-sections are shown in Fig. 2.7 as a function of $\sqrt{\mathrm{s}}$.

a) b)

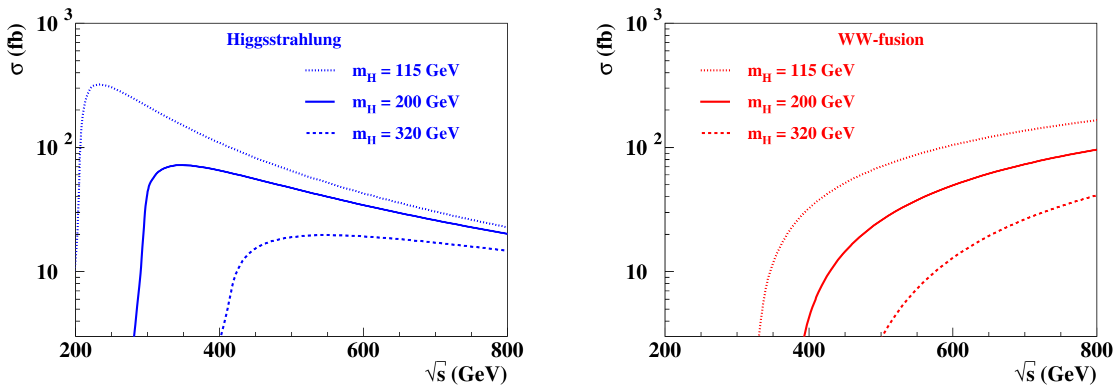

Figure 2.7: *Standard Model prediction for Higgs boson production cross-sections. Above threshold, the cross-sections show* $1/\mathrm{s}$ *and* $\log \mathrm{s}$ *behavior for Higgsstrahlung and* WW*-fusion respectively. Top-quark Yukawa production is not shown and has cross-sections of only few* fb *depending on* $\sqrt{\mathrm{s}}$ *(Calculated with* `HZHA` *[12]).*

SM Higgs decay

The different couplings to gauge bosons and fermions are also reflected in the predicted decay spectrum of the Higgs boson. For small masses, decays to gauge bosons are kinematically forbidden, and a rich spectrum of fermionic decays should be observable, as is depicted in Fig. 2.8 a). The partial decay width to fermions is given by

$$\Gamma_{\mathrm{f\bar{f}}} = \frac{g^2_{\mathrm{Hff}}(m_{\mathrm{H}})}{4\pi} \frac{N_C}{2} m_{\mathrm{H}} \left(1 - \frac{4m^2_{\mathrm{f}}}{m^2_{\mathrm{H}}}\right)^{3/2}, \tag{2.44}$$

where $N_C = 1\,(3)$ for leptons (quarks) is the number of color states of the respective fermions. For $m_{\mathrm{H}} \lesssim 140\,\mathrm{GeV}$, the most dominant decay is to pairs of b-quarks, with a branching ratio in excess of 80 %. Decays to pairs of τ-leptons and c-quarks occur at the level of few percent, and are of the same order than decays to gluon pairs. The latter is mediated by a quark loop, with major contribution of t- and b-quarks. The effective coupling as shown in Fig. 2.5 is

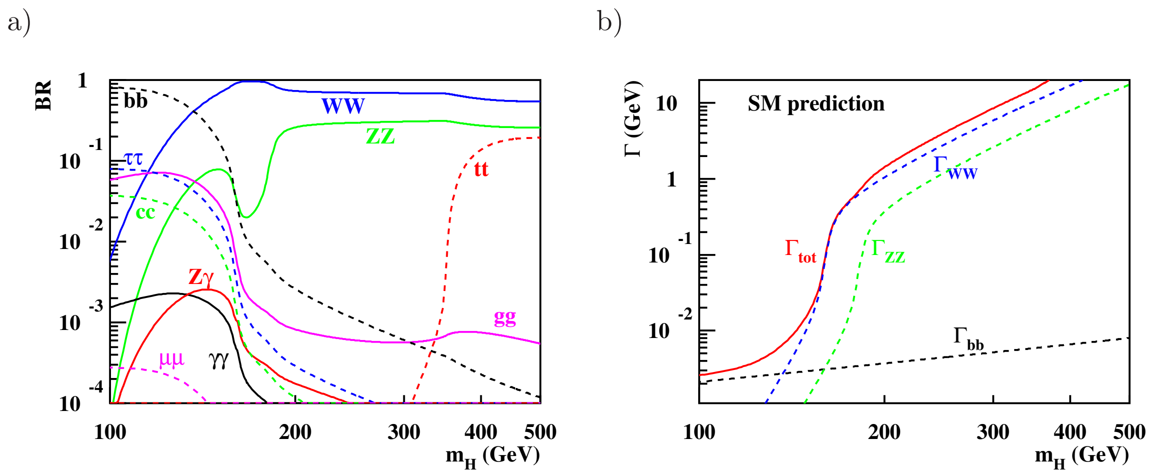

Figure 2.8: *Standard Model prediction for the Higgs boson branching ratios a) and the most important partial decay widths including the total width b). (Calculated with* `HDECAY` *[13])*

relatively large, since the gluon-quark coupling in the loop are strong, and the Higgs-quark coupling is enhanced due to the large quark masses.

The decays to photon pairs or to one photon and one Z-boson are induced by loops as well. Here, the main contribution comes from W-bosons and t-quarks. The effective coupling is small, due to the electroweak couplings inside the loop.

If in contrast the Higgs is heavier than twice the mass of the W-boson, Higgs decays are completely dominated by gauge boson decays. The partial width is given by

$$\Gamma_{\mathrm{VV}} = \frac{g_{\mathrm{VV}}^2}{4\pi}\frac{3\delta_{\mathrm{V}}}{8m_{\mathrm{H}}}\left(1-\frac{m_{\mathrm{H}}^2}{3m_{\mathrm{V}}^2}+\frac{m_{\mathrm{H}}^4}{12m_{\mathrm{V}}^4}\right)\left(1-\frac{4m_{\mathrm{V}}^2}{m_{\mathrm{H}}^2}\right)^{1/2}, \tag{2.45}$$

where $\delta = 2\,(1)$ for $\mathrm{V} = \mathrm{W}\,(\mathrm{Z})$. The partial width for decays to gauge bosons is much larger than that for decays to fermions. This results in almost exclusive $\mathrm{H} \to \mathrm{WW}$ and $\mathrm{H} \to \mathrm{ZZ}$ decays and a rapid growth in the total decay width above threshold, as shown in Fig. 2.8 b).

This aspect is of special implication for measurements of the Higgs width. The achievable detector mass resolution of hadronic systems[3] is of order 1 GeV even for very ambitious detector designs. Only if the Higgs decay width is of the same order, it can be determined directly from the measured mass distribution. In the Standard Model, this translates into a Higgs mass of at least 200 GeV. For lower masses, the total Higgs decay width can only be probed via measurements of the Higgs couplings [14].

Theoretical SM Higgs Mass Constraints

The scattering amplitudes of these states, e.g. in the process $\mathrm{W}_L^-\mathrm{W}_L^+ \to \mathrm{W}_L^-\mathrm{W}_L^+$ increases with the logarithm of the center-of-mass energy. At $\sqrt{s} \sim 1.2\,\mathrm{TeV}$, this process violates unitarity, if only the diagrams a) to c) of Fig. 2.9 are taken into account.

This divergent behavior however cancels, if an additional scalar particle is present, which couples proportional to the W-boson mass. It happens that the SM Higgs boson matches these requirements, and indeed do the diagrams d) and e) of Fig. 2.9 yield opposite contributions to the scattering amplitude. The contributions depend on the Higgs mass, and are only large

[3] Note that this is the mass resolution for one single event. The Higgs mass itself can be determined with much higher precision.

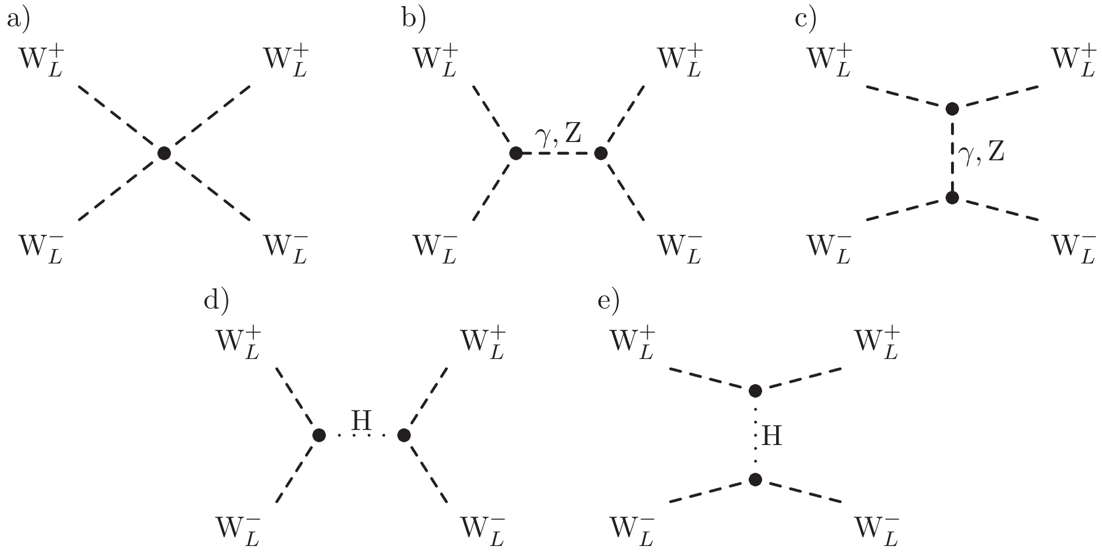

Figure 2.9: *Tree level diagrams of elastic scattering of longitudinal* W-*bosons. The amplitude diverges if only diagrams a)-c) are considered and violates unitarity from* $\sqrt{s} \approx 1.2\,\text{GeV}$ *on. Additional exchange of a scalar particle with coupling strength proportional to the* W-*mass can cancels the divergencies. The SM Higgs matches this requirement if it is not too heavy.*

enough to preserve unitarity, if the Higgs is lighter than about 870 GeV [15]. This is the most general mass constraint on the SM Higgs under the requirement, that the SM is valid without additional particles up to energy scales beyond the TeV range.

The allowed Higgs mass range can be lowered further. If the Standard Model should be valid up to an energy scale Λ, the momenta of particles appearing in higher order loop corrections have to be integrated up to this scale. Such loops appear for example as corrections to the Higgs self-coupling. Fig. 2.10 shows the tree level diagram and higher order corrections with t-quark or Higgs boson loops. The tree-level diagram gives increasing contribution to the effective self-coupling as the Higgs mass rises. The same is true for the second diagram with the Higgs loop. On the contrary, the last diagram with a virtual t-quark loop gives opposite contributions due to the different spin statistics of the particles inside the loop.

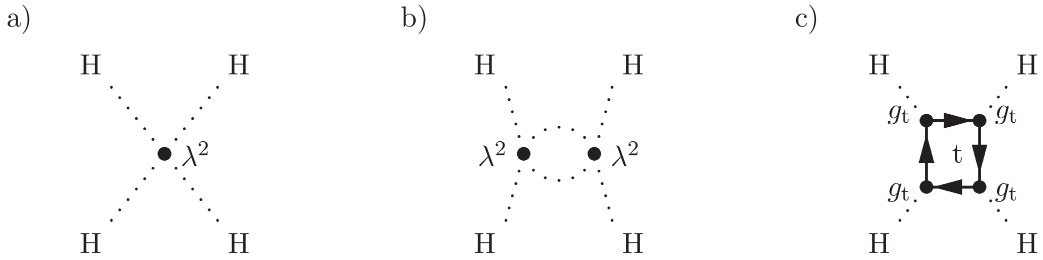

Figure 2.10: *Loop corrections to the Higgs self-coupling. The first two diagrams dominate at large Higgs masses and give upper theoretical bounds on the Higgs mass. For very light Higgs bosons, the third diagram dominates and places a lower theoretical bound on the Higgs mass.*

For small Higgs masses, the diagram with the t-quark loop dominates. If the Higgs mass is too small, the effective self-coupling would eventually be negative, and the Higgs potential would have no minimum. If in contrast the Higgs mass is very large, the Higgs self-coupling becomes very strong and eventually violates unitarity.

Both effects depend on Λ. The allowed range for the Higgs mass as a function of Λ is shown in Fig. 2.11 [16]. If the Standard Model is valid up to the Planck scale $\Lambda_{\mathrm{Pl}} \approx 10^{19}$ GeV, the Higgs boson mass has to lie in a small mass window around 160 GeV.

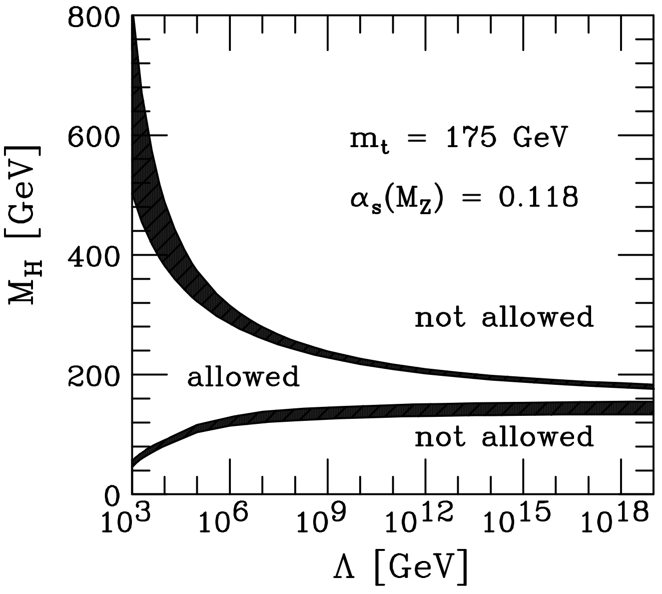

Figure 2.11: *Bounds on the Higgs mass from vacuum stability (lower band) and unitarity (upper band) as a function of the cut-off scale Λ. Only a narrow window around $m_{\mathrm{H}} \sim 160$ GeV is allowed, if the SM is valid up to the Planck scale. (From [16])*

2.3 Experimental Situation and Prospects

The SM Higgs boson so far has not been observed. At LEP, bounds on its mass are derived from direct searches [17] and from indirect fits to SM precision observables [18], which are sensitive to loop corrections involving Higgs bosons.

Most sensitive for direct searches at LEP is the Higgsstrahlung process, which has a cross-section maximum at $\sqrt{s} \approx 1.1 \times (m_{\mathrm{H}} + m_{\mathrm{Z}})$. For smaller center-of-mass energies, the cross-section has a sharp cut-off. The most important Higgs decay is $\mathrm{H} \to \mathrm{b\bar{b}}$, which makes up about 86 % of all decays for Higgs masses around the highest possible Higgs masses of $m_{\mathrm{H}} \sim 115$ GeV. The second-most important Higgs decay channel is to τ-leptons with about 7 %.

At LEP, four search channels are explored (numbers are estimates for $m_{\mathrm{H}} = 115$ GeV):

- The four jet channel $\mathrm{HZ} \to \mathrm{b\bar{b}\,q\bar{q}}$ is the most common final states and makes up about 60 % of all Higgsstrahlung events;
- The lepton channel $\mathrm{HZ} \to \mathrm{b\bar{b}}\,\ell^+\ell^-$ with $\ell = \mathrm{e}, \mu$ is the cleanest channel, but makes up less than 6 % of all Higgsstrahlung events;
- The τ-channel has two contributions: $\mathrm{HZ} \to \mathrm{b\bar{b}}\,\tau^+\tau^-$ and $\mathrm{HZ} \to \tau^+\tau^-\,\mathrm{q\bar{q}}$, since τ-leptons can appear both in H- and Z-decays. Together, they make up about 8 % of all Higgsstrahlung events;
- The missing energy channel $\mathrm{HZ} \to \mathrm{b\bar{b}}\,\nu\bar{\nu}$ covers another 16 % of the Higgsstrahlung events.

During the last month of running at LEP in autumn 2000, some candidate events were recorded by the four LEP experiments, which are compatible with a mass of $m_\mathrm{H} = 115\,\mathrm{GeV}$. The combined significance of all channels and all four experiments is less than three sigma in the end. However, a lower exclusion limit of $m_\mathrm{H} > 114.4\,\mathrm{GeV}$ is placed at the 95 % confidence level [17].

Besides on-shell production, the Higgs affects SM precision observables. The most significant modification arises from Higgs loops in the Z-boson propagator, see Fig. 2.12 a). Similar loops with top-quarks (Fig. 2.12 b) allowed the prediction of the top-quark mass before the direct discovery at TEVATRON. The loop corrections from top-quarks depend quadratical on the top-mass, while the corrections from Higgs bosons only scale with the logarithm of the Higgs mass.

a) b)

Figure 2.12: *Corrections to the Z-boson propagator from loops with a) Higgs bosons and b) top-quarks. The dependence on the Higgs mass is only logarithmic, while the dependence on the top-mass is quadratic.*

The χ^2 variation of a fit to sensitive SM precision observables of the Higgs mass is shown in Fig. 2.13. The solid curve corresponds to a fit of all high energy measurements, and the band shows the theoretical uncertainty from the higher order calculations. The most recent scenario is represented by the thick dotted line, which is based on the latest world average for $m_\mathrm{t} = 178 \pm 4.3\,\mathrm{GeV}$ [19] and includes also the most precise low-energy measurements.

The best fit result [18] is achieved for $m_\mathrm{H} = 117\,\mathrm{GeV}$, which is close above the current exclusion. An upper limit with 95 % confidence level corresponding to a $\Delta\chi^2 \approx 4$ is placed at $m_\mathrm{H} < 252\,\mathrm{GeV}$.

At the moment, TEVATRON is the only running collider which in principle could discover the Higgs. However, the integrated luminosity will most likely only be sufficient to confirm the exclusion limits by LEP. More realistic is the discovery at the LHC. Studies show that the SM Higgs can be discovered with 5σ significance within the whole mass range from the LEP exclusion up to the TeV scale [20].

In Fig. 2.14 the search channels are shown, together with the corresponding significances with $\int\mathcal{L} = 30\,\mathrm{fb}^{-1}$. At very low masses, the main search channel arises from Yukawa production, where the Higgs is radiated of a top-quark from $pp \to \mathrm{t\bar{t}} + X$. The cross-section of this process decreases with increasing Higgs mass. For heavier Higgs masses, the Higgs is reconstructed from gluon fusion $gg \to \mathrm{H}$. Due to the large hadronic background at LHC, it is difficult to reconstruct $\mathrm{H} \to \mathrm{b\bar{b}}$ decays without constraints from associate production with other particles. The most sensitive decay therefore is $\mathrm{H} \to \mathrm{ZZ}^* \to 4\ell$, which is very rare. These decays are suppressed for small Higgs masses. Reconstruction of $\mathrm{H} \to \gamma\gamma$ and selection of events from Higgs production in vector boson fusion are necessary to achieve enough sensitivity for discovery in the mass window $m_\mathrm{H} = 100 - 130\,\mathrm{GeV}$.

After discovery of the Higgs boson, the next step would be the precise measurement of its properties. This is necessary to test whether the SM Higgs has been found, or a new particle of some more general theory. Some possible scenarios of extended Higgs sectors and alternative models of electroweak symmetry breaking will be discussed in the next section.

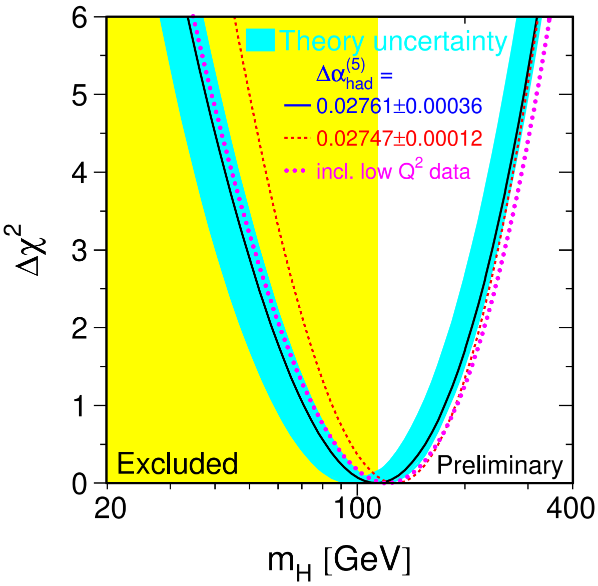

Figure 2.13: *Experimental Higgs mass limits. The yellow area indicates the direct exclusion limit from non-observation. The solid curve with the band indicate the variation in χ^2 of a fit to all relevant high energy precision data. The thick dotted line indicates the results of a similar fit which also considers the most precise low energy data. (From [18])*

While LHC is best suited to discover the Higgs, a precise determination of all its parameters is only possible at a future e^+e^- linear collider, the ILC. This concept will be introduced in more detail in Sec. 3.3. The physics objectives of both projects are complementary, and great benefits are expected from mutual influence.

2.4 Higgs Sector Beyond the Standard Model

The Higgs sector discussed in the last section does not necessarily need to be minimal as is assumed in the Standard Model. Arbitrary compositions of Higgs singlets and multiplets are imaginable, with some general restrictions. At least one Higgs doublet seems necessary for two reasons: Singlets with non vanishing vacuum expectation value would yield a massive photon, and fermion masses cannot be generated by triplets or higher multiplet representations [21].

Also, an extended Higgs sector is restricted by the relation of the masses from W- and Z-bosons and the weak mixing angle θ_W, which is measured to be [11]:

$$\rho := \frac{m_{\mathrm{W}}^2}{m_{\mathrm{Z}}^2 \cos^2\theta_W} = 0.9998^{+0.0008}_{-0.0005}. \tag{2.46}$$

The minimal Higgs sector yields $\rho = 1$ at tree-level, which is also obtained from models containing only Higgs singlets and doublets [22]. For models involving higher multiplet representations, an unnatural tuning of the vacuum expectation values is needed, unless the isospin I and hypercharge Y of each multiplet satisfy [23]:

$$(2I+1)^2 - 3\,Y^2 = 1. \tag{2.47}$$

Besides the ρ-parameter, structural constraints arise from the observed strong suppression of flavor changing neutral currents (FCNC) [11], e.g. direct couplings between u- and c-quark.

A natural suppression can be achieved for example in models with exclusively Higgs doublets, if all fermions of one charge couple to the same doublet [24].

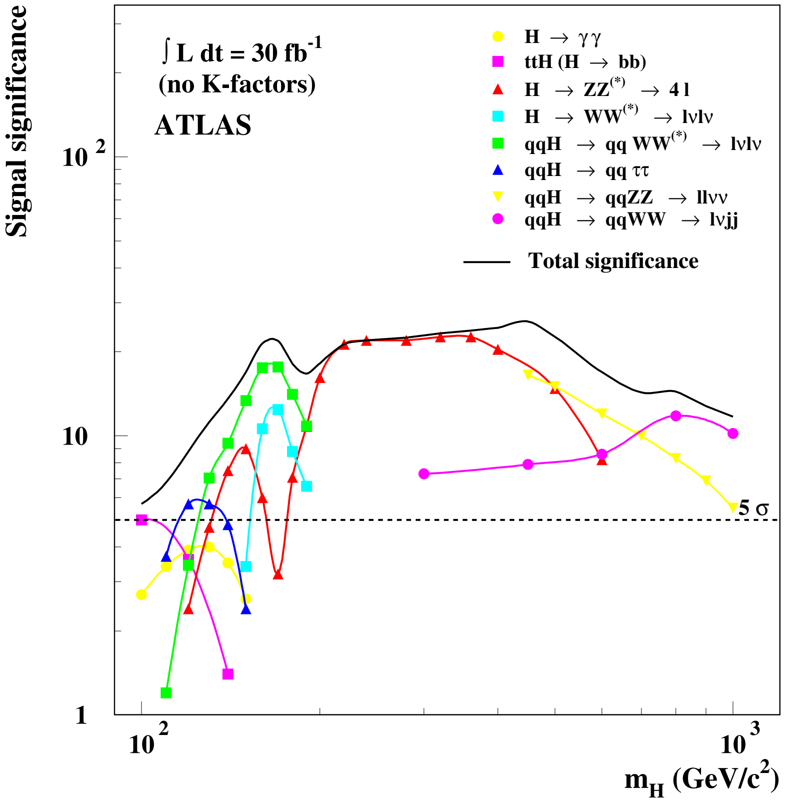

Figure 2.14: *Higgs discovery potential at* LHC. *Shown is the significance of the discovery channels for* $\int\mathcal{L} = 30\,\mathrm{fb}^{-1}$. *For masses* $m_{\mathrm{H}} = 100 - 130\,\mathrm{GeV}$, *the Higgs can only be discovered by combination of all channels. (From [20])*

In the following, some straight forward extensions of the minimal Higgs sector will be introduced. The selection is meant as a short overview of concepts and neither complete nor extensive. Much more details can be found e.g. in [25].

Two Higgs doublets

Two Higgs doublets are the minimal Higgs sector in supersymmetric theories such as the Minimal Supersymmetric extension of the Standard Model (MSSM) [26], but arise also in general Two Higgs Doublet Models (2HDM) [27]. The prior extend the SM particle spectrum by one fermionic (bosonic) partner for each SM boson (fermion) and thus introduces symmetry between matter (fermions) and force carriers (bosons). In the latter, only the Higgs sector is extended by one additional complex doublet.

From two complex Higgs doublets, five particle states arise: Two neutral CP even (h^0, H^0), one CP odd (A^0) and a pair of charged ($H^{\pm}$) Higgs bosons. In CP violating scenarios, the three neutral mass eigenstates are mixtures of the CP eigenstates. An important parameter of the Higgs sector is the ratio $\tan\beta$ between the vacuum expectation values v_1 and v_2 of the two Higgs doublets, defined as

$$\tan\beta = \frac{v_1}{v_2}. \tag{2.48}$$

The lightest CP-even Higgs boson h^0 can have properties very much similar to those predicted for the SM Higgs boson H. However, this is not necessarily the case. For example, in some scenarios the decay to b-quarks is suppressed, on which the searches for the SM Higgs boson at LEP are mainly based upon.

One Higgs doublet plus singlets

As discussed above, Higgs singlets should have no vacuum expectation values to retain the photon massless. The particles of the Standard Model thus only 'feel' the presence of the Higgs doublet field, and the Higgs boson arising from the doublet has the same couplings as the SM Higgs boson. However, one exception arises from the coupling ω between the doublet Higgs and the singlet states $\vec{\varphi}$. This coupling does not necessarily depend on the $\vec{\varphi}$ mass, which might result in a very large partial width of $\mathrm{H} \to \varphi\varphi$ decays. In these stealthy Higgs models, the Higgs boson decays invisible and might have a very large total decay width [28].

Models with Higgs triplets

Higgs triplets can arise for example from left-handed Higgs triplet models (LHTM) [29] or from left-right symmetric models (LRM) [30]. In these models, several Higgs bosons are predicted, which partly have double electric charge. These doubly charged Higgs bosons can only couple to pairs of like-charged leptons or W-bosons and thus have a clear final state signature.

One Higgs doublet plus extra dimensions

Also extensions of the Standard Model not directly connected to electroweak symmetry breaking can change the phenomenology of the Higgs sector. An example is the Randall-Sundrum model [31], which proposes one extra compactified space dimension. The Higgs sector is retained with one complex doublet.

From the compactified extra dimension, a tower of spinless excitations is predicted, called radions r. These can mix with the Higgs state h, which originates from the Higgs doublet. Depending on the mixing angle ξ, the couplings of the mixed mass eigenstates to Standard Model particles can be different from the SM Higgs. Especially, the dominant SM Higgs decay $\mathrm{H} \to \mathrm{b\bar{b}}$ can be suppressed, which has substantial impact on the Higgs searches at LEP [32].

2.5 Grand unification, Fine-Tuning and Hierarchy

Not only the SM Higgs sector is a complete mystery, the theory also faces some fundamental difficulties. Two of them will be discussed in some more detail here: The fine-tuning problem and the hierarchy problem. Both arise because of the large spread between the energy scale of electroweak symmetry breaking, which is of order $\mathcal{O}(100\,\mathrm{GeV})$ and the scale of Grand Unified Theories (GUT).

Chiral anomalies of triangular loops in electroweak interaction give raise to non-renormalizable divergencies. These anomalies cancel, if the fundamental relation

$$N_C\,(Q_\mathrm{u} + Q_\mathrm{d}) = -Q_\mathrm{e} \tag{2.49}$$

holds, where N_C is the number of color degrees of freedom, and Q_i is the electric charge of particle i. In the Standard Model, this relation is satisfied, but there is no reason why. This implies, that there is also lepton-quark invariance at some point, which would be realized by unification of all three Standard Model interactions at some high energy scale $\Lambda_{GUT} \sim 10^{16}$ GeV. The fact, that this Grand Unification scale is larger compared to the scale of electroweak symmetry breaking of order 10^2 GeV is mysterious and referred to as the hierarchy problem.

If the Standard Model is valid up to an energy scale Λ, all integrals in loop calculations have to be calculated up to this energy scale. Fig. 2.15 shows loop corrections to the Higgs propagator, which yield quadratic divergent correction to the Higgs mass of

$$\Delta m_{\mathrm{H}}^2 \propto \int^{\Lambda} \frac{d^4k}{(2\pi)^4} \frac{1}{k^2} \approx \Lambda^2, \tag{2.50}$$

where k is the momentum of the particles inside the loop. Similar corrections of fermion propagators only diverge logarithmically, and the correction to the fermion masses stays of order of the mass itself. As a consequence, the natural mass scale of the SM Higgs boson is of order of the cut-off scale, and parameter fine-tuning with a relative precision of Λ/m_{H} is necessary to explain smaller Higgs masses. If the Standard Model was valid up to the scale of Grand Unification, corrections $\Lambda_{GUT}/m_{\mathrm{H}} \sim 10^{13}$ are necessary to explain Higgs masses below a TeV. This so-called fine-tuning problem is closely related to the hierarchy problem.

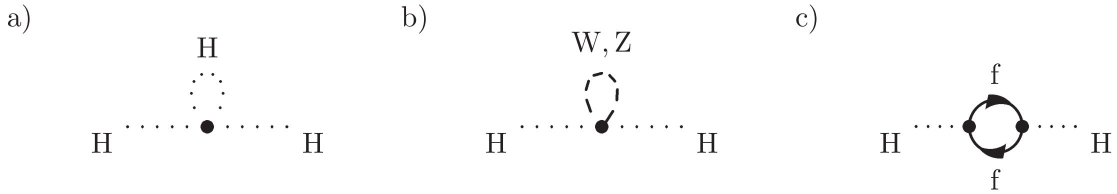

Figure 2.15: *Loops within the Higgs propagator cause corrections to the Higgs mass with quadratic divergent behavior.*

In supersymmetric theories like the MSSM already mentioned, the fine-tuning problem does not arise. Besides the SM particles, also the supersymmetric partners contribute to loop corrections. Due to the different spin statistics, the quadratic divergencies cancel pairwise, and the corrections to the Higgs mass evolve only logarithmically with the cut-off scale. However, the large spread between the scales of electroweak symmetry breaking and grand unification remains.

2.6 Technicolor

The Standard Model has been severely tested experimentally during the last 20 years, and so far no measurement in particle physics is in clear disagreement with the theoretical predictions. One could state, that no question is answered incorrectly by the Standard Model. Anyhow, there are questions not answered at all, which might be a hint that the Standard Model is a 'low energy' approximation of a more fundamental theory. Taking into account the great experimental successes of the Standard Model it is fair to say that this approximation is very good, however.

One of these alternative models is Technicolor. It explains electroweak symmetry breaking by dynamics at a higher energy scale. In Technicolor theories, the hierarchy problem is circumvented by several new energy scales, which fill up the energy range between the scale of electroweak symmetry breaking and the GUT scale. The fine-tuning problem does not arise, because at every new energy scale loop corrections are stabilized by additional interactions connected to the new scales.

A general overview of the concepts of Technicolor theories is presented in this section. An effective Technicolor model with predictive phenomenology is introduced in Sec. 2.7.

2.6.1 Electroweak symmetry breaking and Technicolor

Technicolor [33, 34] (TC) is meant to provide a description of dynamical breaking of electroweak symmetry. One motivation was the premise, that every fundamental energy scale should have a dynamical origin. The general structure of Technicolor is adopted from QCD, which also includes reproduction of fundamental QCD features like confinement and asymptotic freedom.

In the simplest Technicolor models, new massless technifermions F are introduced, which interact via Technicolor interactions described by the gauge group $SU(N_{\mathrm{TC}})$. To avoid anomalies, the technifermions are assumed to transform like SM fermions under the Standard Model gauge group, i.e. for left-handed doublets and right-handed singlets of the weak isospin

$$F = \begin{pmatrix} U^i \\ D^i \end{pmatrix}_L \;,\; U^i_R \;,\; D^i_R \tag{2.51}$$

where $i = 1, ..., N_{\mathrm{TC}}$ is an index over the Technicolor degrees of freedom.

Electroweak symmetry is broken by the formation of technifermion condensates, which breaks $U(2)_L \times U(2)_R$ chiral symmetry. Four Goldstone bosons arise, which are named technipions $\Pi^\pm$, Π^0, $\Pi^{0\prime}$ in analogy to QCD. The coupling between these technipions and the weak gauge bosons is parameterized by a coupling F_{TC} in analog to f_π in QCD. The W-boson acquires mass

$$m_{\mathrm{W}} = \frac{g}{2} F_{\mathrm{TC}}. \tag{2.52}$$

The assignment $F_{\mathrm{TC}} = v = 246\,\mathrm{GeV}$ leads to the correct W-mass. The Z-mass and the massless photon are described also correctly in analog to Equ. 2.37.

The energy scale Λ_{TC} of Technicolor interaction can be estimated by naïve scaling from QCD via

$$\frac{f_\pi}{\Lambda_C} \approx \frac{F_{\mathrm{TC}}}{\Lambda_{\mathrm{TC}}} \qquad \Longrightarrow \qquad \Lambda_{\mathrm{TC}} \approx 500\,\mathrm{GeV}. \tag{2.53}$$

2.6.2 Fermion masses and Extended Technicolor

Fermion masses cannot be incorporated in the simplest Technicolor models. Replacing the vacuum expectation value v by condensates $F\bar{F}$ of technifermions would lead to four-point coupling structures in the diagrams shown in Eq. 2.35:

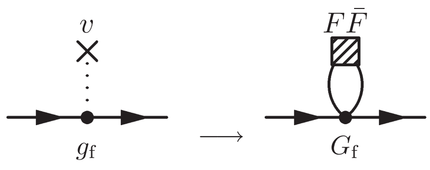

(2.54)

The coupling constant G_{f} in this case has dimensions mass^{-2}, like the Fermi constant G_F. Such theories are not renormalizable.

Therefore, new so-called Extended Technicolor (ETC) interactions are introduced, which couple SM fermions to technifermions. ETC is described by a more complex gauge group, in which the TC $SU(N_{\mathrm{TC}})$ and the Standard Model gauge groups are embedded. In general, ETC gauge fields can be scalar or vector fields. To avoid the general problems of scalar fields, usually only vector fields are considered, which lead to spin-1 gauge bosons. The coupling of

SM fermions f and technifermions F by exchange of an ETC gauge boson V_{ETC} is depicted in Fig. 2.16 together with the corrections to the SM fermion propagator leading to effective masses. The effective low energy coupling G_{f} is then given by

$$G_f \propto \frac{g^2_{V\mathrm{f}F}}{m_V^2} \qquad \Longrightarrow \qquad m_{\mathrm{f}} \propto \frac{g^2_{V\mathrm{f}F}}{m_V^2} \left\langle 0 \left| F\bar{F} \right| 0 \right\rangle \approx \frac{g^2_{V\mathrm{f}F}}{m_V^2} \, \mathcal{O}\left(\Lambda^3_{\mathrm{TC}}\right) \tag{2.55}$$

with a fermion and technifermion dependent coupling constant $g_{V\mathrm{f}F}$ and the mass of the ETC vector boson m_V. ETC interactions also describe the decays of technifermions to SM fermions. Since these kind of couplings are assumed to give mass to SM fermions, technifermions are expected to decay to the heaviest particles possible.

Figure 2.16: *a) Extended Technicolor couples SM fermions and technifermions via exchange of an ETC vector boson V_{ETC}. b) Renormalizable couplings to technifermion condensates arise, which lead to masses of SM fermions.*

In the most straight forward models, technifermions reflect the color and charge structure of SM fermions. Therefore, the family of technifermions from Equ. 2.51 is extended to contain quark- and lepton-like particles:

$$Q = \begin{pmatrix} U^{a,i} \\ D^{a,i} \end{pmatrix}_L \, , \; U_R^{a,i} \, , \; D_R^{a,i} \qquad\qquad L = \begin{pmatrix} E^{i} \\ N^{i} \end{pmatrix}_L \, , \; E_R^{i} \, , \; N_R^{i}. \tag{2.56}$$

$i = 1, .., N_{\mathrm{TC}}$ is an index over Technicolor degrees of freedom and $a = 1, 2, 3$ an index over QCD colors. Right handed neutrino-like states N_R^i are allowed and can obtain mass.

If the ETC gauge group is spontaneously broken down to the Technicolor group in steps at different energy scales (i.e. it is 'tumbling' down), different masses of the ETC gauge bosons can be realized. This again could explain the mass hierarchy between the SM fermion families.

Breaking of the ETC gauge group is assumed to be initiated again by condensates of technifermions. However, the formation of condensates in this case is due ETC interactions and happens at much higher energy scales

$$\Lambda_{\mathrm{ETC}} \approx 100 - 500\,\mathrm{TeV}. \tag{2.57}$$

2.6.3 Effective models

Technicolor and Extended Technicolor as described above is challenged by experimental constraints. ETC interaction should also incorporate quark mixing, e.g. should contain couplings between same-charged quarks of different families. To avoid large flavor changing neutral currents, the ETC energy scale has to be very high.

This again suppresses the contributions to SM fermion masses, as can be seen from Equ. 2.55. In this case, naïve scaling of QCD would yield too small fermion masses. Possible enhancement can be achieved by very slow or 'walking' (instead of running) evolution [35, 36, 37, 38, 39] of the TC coupling constant α_{TC} between the energy scales Λ_{TC} and Λ_{ETC}. This can be obtained by introducing many doublets of technifermions, implying that the Technicolor scale and the lightest technicolor-neutral bound states of technifermions may be much lighter than 1 TeV and could be observed at present colliders [40, 41, 42].

General models of Technicolor and Extended Technicolor are not very predictive, i.e. reliable calculations of modifications to electroweak precision observables is not possible. Since the fundamental energy scales Λ_{TC} and Λ_{ETC} are too high to be explored directly, an effective low-energy model of Technicolor phenomenology has been developed. This Technicolor Straw-man Model [41, 43] (TCSM) will be introduced in the next section.

2.7 Phenomenology of the Technicolor Straw-man Model

The Technicolor Straw-man Model [41, 43] (TCSM) is meant to provide reasonable predictions of the low-energy phenomenology of walking ETC with a limited number of free parameters. It is assumed, that the lightest technifermion doublet

$$\begin{pmatrix} U_{\mathrm{TC}} \\ D_{\mathrm{TC}} \end{pmatrix}$$

alone determines the particle spectrum and the phenomenology.

The bound states of U_{TC} and D_{TC} are scalar and vector mesons. They form triplets and singlets with respect to the TC isospin, i.e. rotations in the $U_{\mathrm{TC}} - D_{\mathrm{TC}}$ flavor space.

	Scalar (spin 0)	Vector (spin 1)
Iso-triplets	$\Pi_{\mathrm{T}}^{\pm,0}$	$\rho_{\mathrm{T}}^{\pm,0}$
Iso-singlets	$\Pi_{\mathrm{T}}^{0\prime}$	ω_{T}^{0}

The scalar states are not mass-eigenstates. Moreover, they arise from mixing of the longitudinal gauge bosons W_L, which are the true Goldstone modes of electroweak symmetry breaking, and new Technicolor mass eigenstates π_{T} (called technipions) via

$$\left|\Pi_{\mathrm{T}}^{\pm}\right\rangle = \sin\chi\left|\mathrm{W}_{\mathrm{L}}^{\pm}\right\rangle + \cos\chi\left|\pi_{\mathrm{T}}^{\pm}\right\rangle \tag{2.58}$$

$$\left|\Pi_{\mathrm{T}}^{0}\right\rangle = \sin\chi\left|\mathrm{Z}_{\mathrm{L}}\right\rangle + \cos\chi\left|\pi_{\mathrm{T}}^{0}\right\rangle . \tag{2.59}$$

The mixing angle χ is a free parameter of the model. In a similar way, the $\Pi_{\mathrm{T}}^{0\prime}$ mixes with a new mass eigenstate $\pi_{\mathrm{T}}^{0\,\prime}$ and further TC states from heavier technifermion doublets with the mixing angle χ'. Note, that no longitudinal photon appears to retain the photon massless. As proposed in [41], $\chi' = \chi$ is assumed.

The scalar and vector states are assumed to be mass degenerate separately, as is naturally the case for TC isospin conservation. Besides the mass parameters $m_{\pi_{\mathrm{T}}}$ and $m_{\rho_{\mathrm{T}}}$, the TCSM is determined by the following free parameters:

1. The number of Technicolor degrees of freedom N_{TC}. This parameter influences the strength $\alpha_\rho = 2.91\,(3/N_{\mathrm{TC}})$ of Technicolor interaction, which is derived from naïve scaling of QCD. Since technifermion condensates arise from all doublets, all doublets contribute the weak gauge boson masses. Therefore, the technipion constant F_{TC} from Equ. 2.52 is $F_{\mathrm{TC}} = 246\,\mathrm{GeV}/\sqrt{N_D}$.

2. The mixing angle χ between technipions and weak Goldstone modes as already discussed. Usually, the mixing angle is related to the number of technifermion doublets N_D by $\sin^2\chi = 1/N_D$. To achieve a slow or 'walking' evolution of the Technicolor coupling, a large number of technifermion doublets is required.

3. Two mass parameters m_A and m_V, which influence the coupling between technifermions and transversely polarized SM gauge bosons. The axial and vector mass parameters should be $m_A \approx m_V \approx \mathcal{O}(100\,\text{GeV})$.

4. The sum of the charges of the technifermions in one doublet $Q = Q_U + Q_D$. This parameter influences the coupling of technifermions to (transversally polarized) gauge bosons. To avoid anomalies, the charge difference must be $Q_U - Q_D = 1$ as for all SM fermions.

A default set of values for the parameters as proposed in [41] is listed in Tab. 2.2. Unless mentioned otherwise, these values are assumed in the following discussion of TCSM cross-sections and decay ratios.

m_{π_T}	m_{ρ_T}	N_{TC}	$\sin\chi$ (N_D)	m_A	m_V	Q
80 GeV	250 GeV	4	$\frac{1}{3}$ (9)	200 GeV	200 GeV	5/3

Table 2.2: *The parameters of the TCSM. Values listed are proposed and motivated in [41].*

Production and decay

At LEP, the neutral vector states ρ_T^0 and ω_T^0 can be produced in the s-channel via propagator mixing with the Z-boson. Feynman diagrams of this process are shown in Fig. 2.17.

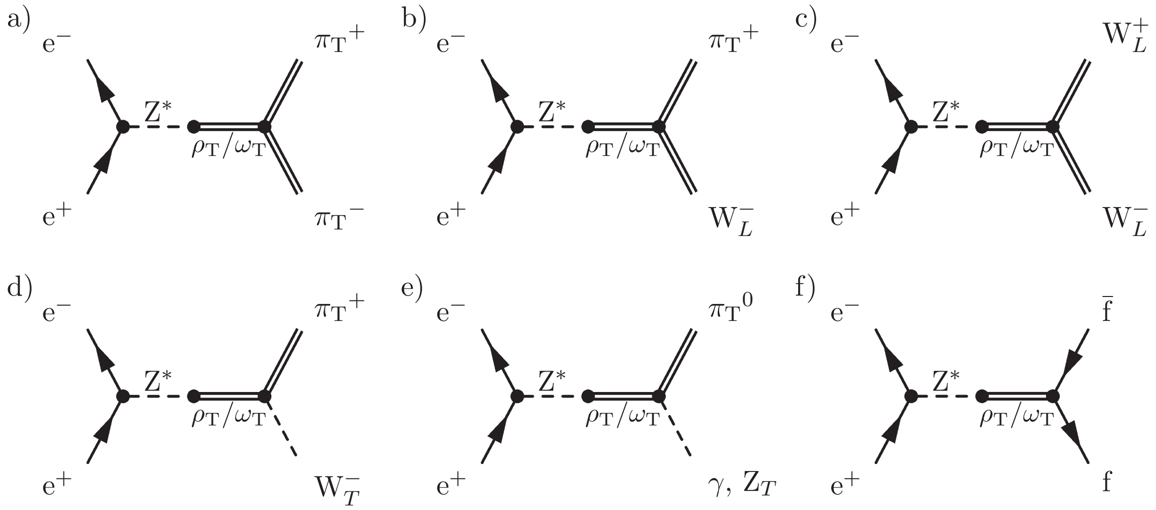

Figure 2.17: *Technivector states ρ_T^0 and ω_T^0 are produced in the s-channel by propagator mixing with the Z-boson. These states decay via TC interaction a)-c), via weak interaction d)-e) or to pairs of SM fermions f). TC induced decays are dominant in most of the TCSM parameter space.*

The ρ_T dominantly decays via Technicolor interaction. The general decay is

$$\rho_T^0 \to \Pi_T^+ \Pi_T^- \qquad \text{with} \qquad \Gamma \propto \alpha_\rho, \tag{2.60}$$

where Γ denotes the partial decay width. This leads to following decay channels (see also

Fig. 2.17 a-c) and partial decay width proportionalities:

$$\begin{aligned}
\rho_{\mathrm{T}}^{0} \rightarrow \quad & \pi_{\mathrm{T}}^{+}\pi_{\mathrm{T}}^{-} && \Gamma \propto \alpha_{\rho}\, \cos^{4}\chi && (2.61)\\
& \pi_{\mathrm{T}}^{\pm}\mathrm{W}_{\mathrm{L}}^{\mp} && \Gamma \propto \alpha_{\rho}\, \sin^{2}\chi\, \cos^{2}\chi && (2.62)\\
& \mathrm{W}_{\mathrm{L}}^{+}\mathrm{W}_{\mathrm{L}}^{-} && \Gamma \propto \alpha_{\rho}\, \sin^{4}\chi. && (2.63)
\end{aligned}$$

Note, that in decays through Technicolor interaction only longitudinal states W_L arise. Transverse polarized gauge bosons W_T, Z_T and γ arise from decays through weak interaction (Fig. 2.17 d-e). These decay modes scale with the fine-structure constant α and show additional dependence on the mass parameters m_{A}, m_{V} and on the charge sum Q:

$$\begin{aligned}
\rho_{\mathrm{T}}^{0} \rightarrow \quad & \pi_{\mathrm{T}}^{\pm}\mathrm{W}_{\mathrm{T}}^{\mp} && \Gamma \propto \alpha\, \cos^{2}\chi / m_{\mathrm{A}}^{2} && (2.64)\\
& \pi_{\mathrm{T}}^{0}\mathrm{Z}_{\mathrm{T}}^{0} && \Gamma \propto \alpha\, \cos^{2}\chi\, (Q/m_{\mathrm{V}})^{2} && (2.65)\\
& \pi_{\mathrm{T}}^{0}\gamma && \Gamma \propto \alpha\, \cos^{2}\chi\, (Q/m_{\mathrm{V}})^{2}. && (2.66)
\end{aligned}$$

The weak decay modes are suppressed with respect to decays through Technicolor mainly due to the ratio $\alpha/\alpha_{\rho} \ll 1$. However, if $\rho_{\mathrm{T}} \rightarrow \pi_{\mathrm{T}}^{+}\pi_{\mathrm{T}}^{-}$ is kinematically forbidden and other Technicolor induced decays are suppressed by small values of $\sin\chi$, the weak decays can become dominant.

In addition to the decay modes discussed already, the ρ_{T}^{0} can also decay to pairs of SM fermions (Fig. 2.17 f). Here, the ρ_{T} resonates back to a SM gauge boson, which subsequently decays to a pair of fermions. The partial width is suppressed by a small coupling

$$\rho_{\mathrm{T}}^{0} \rightarrow \mathrm{f}\bar{\mathrm{f}} \qquad \Gamma \propto \alpha^{2}/\alpha_{\rho}. \tag{2.67}$$

If TC isospin is approximately conserved, the techniomega is expected to decay dominantly to three TC pion eigenstates

$$\omega_{\mathrm{T}}^{0} \rightarrow \Pi_{\mathrm{T}}\, \Pi_{\mathrm{T}}\, \Pi_{\mathrm{T}}. \tag{2.68}$$

However, for large areas of the TCSM parameter space this decay is kinematically forbidden. Technicolor induced decays of the ω_{T}^{0} thus are only possible in the isospin violating decays to two TC pion eigenstates, which result in the same channels as for the ρ_{T}^{0}. Also the partial decay widths show the same parameter dependence. However, the absolute values are smaller by

$$\Gamma\left(\omega_{\mathrm{T}}^{0} \rightarrow \Pi_{\mathrm{T}}^{+}\Pi_{\mathrm{T}}^{-}\right) = \left|\epsilon_{\rho\omega}\right|^{2}\, \Gamma\left(\rho_{\mathrm{T}}^{0} \rightarrow \Pi_{\mathrm{T}}^{+}\Pi_{\mathrm{T}}^{-}\right), \tag{2.69}$$

where $|\epsilon_{\rho\omega}|$ is the $\rho_{\mathrm{T}}^{0} - \omega_{\mathrm{T}}^{0}$ mixing amplitude, which is assumed to be $\approx 5\,\%$ as in QCD.

Also the ω_{T}^{0} can decay via weak interaction. However, the dependence of the respective partial widths is different from the analog ρ_{T}^{0} decays:

$$\begin{aligned}
\omega_{\mathrm{T}}^{0} \rightarrow \quad & \pi_{\mathrm{T}}^{\pm}\mathrm{W}_{\mathrm{T}}^{\mp} && \Gamma \propto \alpha\, \cos^{2}\chi / m_{\mathrm{V}}^{2} && (2.70)\\
& \pi_{\mathrm{T}}^{0}\mathrm{Z}_{\mathrm{T}}^{0} && \Gamma \propto \alpha\, \cos^{2}\chi / m_{\mathrm{V}}^{2} && (2.71)\\
& \pi_{\mathrm{T}}^{0}\gamma && \Gamma \propto \alpha\, \cos^{2}\chi / m_{\mathrm{V}}^{2} && (2.72)\\
& \mathrm{f}\bar{\mathrm{f}} && \Gamma \propto \alpha^{2}\, Q/\alpha_{\rho}. && (2.73)
\end{aligned}$$

In addition to the appearance in vector resonance decays, TC pion eigenstates can be pair-produced via a direct electroweak coupling to an s-channel Z-boson. The resulting channels are

$$\mathrm{e}^{+}\mathrm{e}^{-} \rightarrow \mathrm{Z} \rightarrow \pi_{\mathrm{T}}^{+}\pi_{\mathrm{T}}^{-},\ \ \pi_{\mathrm{T}}^{\pm}\mathrm{W}_{\mathrm{L}}^{\mp},\ \ \mathrm{W}_{\mathrm{L}}^{+}\mathrm{W}_{\mathrm{L}}^{-}. \tag{2.74}$$

Only longitudinal states W_{L} arise from this process.

Technipions decay to pairs of SM fermions induced by Extended Technicolor interactions. Since ETC is meant to give mass to the SM fermions, the decay rates are proportional to the masses of the involved fermions

$$\Gamma\left(\pi_{\mathrm{T}}^{0} \to \mathrm{f\bar{f}}\right) \propto m_{\mathrm{f}}^{2} \qquad \text{and} \qquad \Gamma\left(\pi_{\mathrm{T}}^{\pm} \to \mathrm{f\bar{f}'}\right) \propto (m_{\mathrm{f}} + m_{\mathrm{f'}})^{2}\,. \tag{2.75}$$

At LEP center-of-mass energies, only technipions with $m_{\pi_{\mathrm{T}}} \lesssim 125\,\mathrm{GeV}$ can be produced, which cannot decay to top-quarks. Decays therefore are dominated by b-quarks with branching ratios BR

$$\pi_{\mathrm{T}}^{0} \to \mathrm{b\bar{b}} \qquad \mathrm{BR} \approx 85\,\% \tag{2.76}$$

$$\pi_{\mathrm{T}}^{-} \to \mathrm{b\bar{c}} \qquad \mathrm{BR} \approx 56\,\% \tag{2.77}$$

$$\mathrm{b\bar{u}} \qquad \mathrm{BR} \approx 36\,\%. \tag{2.78}$$

Cross-sections and parameter dependencies

The technirho and techniomega states are produced in the s-channel. The cross-section thus follows a resonance distribution as depicted in Fig. 2.18. Mixing between ρ_{T}^{0} and ω_{T}^{0} appears for approximate TC isospin conservation, i.e. mass degeneracy $m_{\rho_{\mathrm{T}}^{0}} \approx m_{\omega_{\mathrm{T}}^{0}}$. In this case, mixing effects are predicted at the cross-section resonance. The impact on the result of experimental searches for Technicolor however is small, since the effect from mixing on the cross-section is marginal for $\sqrt{\mathrm{s}} < m_{\rho_{\mathrm{T}}^{0}/\omega_{\mathrm{T}}^{0}}$. In the following, $m_{\rho_{\mathrm{T}}^{0}} = m_{\omega_{\mathrm{T}}^{0}} =: m_{\rho_{\mathrm{T}}/\omega_{\mathrm{T}}}$ is assumed.

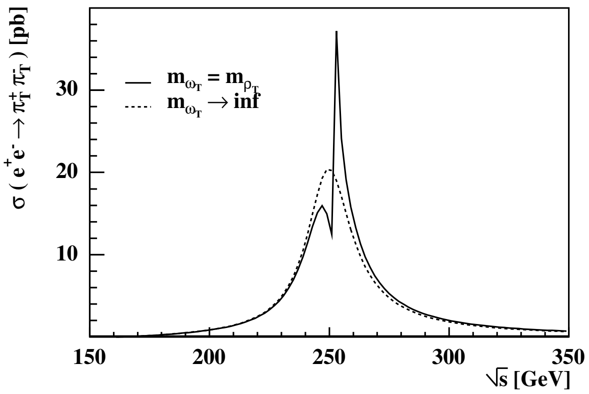

Figure 2.18: *The cross-section of* $\mathrm{e^{+}e^{-}} \to \pi_{\mathrm{T}}^{+}\pi_{\mathrm{T}}^{-}$ *is resonant for* $\sqrt{\mathrm{s}} \sim m_{\rho_{\mathrm{T}}^{0}}$ ($= 250\,\mathrm{GeV}$ *in the plot).* $\rho_{\mathrm{T}}^{0} - \omega_{\mathrm{T}}^{0}$ *mixing affects the cross-section if* $m_{\omega_{\mathrm{T}}^{0}} \approx m_{\rho_{\mathrm{T}}^{0}}$. *Effects for* $\sqrt{\mathrm{s}} < m_{\rho_{\mathrm{T}}^{0}}$ *however are small. Other model parameters are assumed as listed in Tab. 2.2.*

As outlined above, Technicolor induced decays of ρ_{T}^{0} and ω_{T}^{0} are dominant. Among these, the final state with two longitudinally polarized W-bosons is very difficult to access experimentally, since it is indistinguishable from Standard Model $\mathrm{e^{+}e^{-}} \to \mathrm{WW}$ production. Weak experimental limits on the corresponding cross-section of $\mathrm{e^{+}e^{-}} \to \rho_{\mathrm{T}}^{0}/\omega_{\mathrm{T}}^{0} \to \mathrm{W_{L}^{+}W_{L}^{-}}$ thus can only be derived from re-interpretation of SM cross-section measurements [44]. Much more promising for direct searches are the channels $\rho \to \pi_{\mathrm{T}}^{+}\pi_{\mathrm{T}}^{-}$ and $\pi_{\mathrm{T}}^{\pm}\mathrm{W_{L}^{\mp}}$. The $\pi_{\mathrm{T}}^{\pm}\mathrm{W}^{\mp}$ final state also has contributions from the weak decay $\rho_{\mathrm{T}}^{0}/\omega_{\mathrm{T}}^{0} \to \pi_{\mathrm{T}}^{\pm}\mathrm{W_{T}^{\mp}}$, which depend on the values of the vector mass parameter m_{V} and are small for $m_{\mathrm{V}} = 200\,\mathrm{GeV}$ as shown in Fig. 2.19.

The cross-sections of $\mathrm{e^{+}e^{-}} \to \pi_{\mathrm{T}}^{+}\pi_{\mathrm{T}}^{-}$, $\pi_{\mathrm{T}}^{\pm}\mathrm{W_{L}^{\mp}}$, $\pi_{\mathrm{T}}^{\pm}\mathrm{W_{T}^{\mp}}$ are shown in Fig. 2.20 a) as a function of the $\rho_{\mathrm{T}}/\omega_{\mathrm{T}}$ mass. They show thresholds at $m_{\rho_{\mathrm{T}}/\omega_{\mathrm{T}}} = 2\,m_{\pi_{\mathrm{T}}}$ or $= m_{\pi_{\mathrm{T}}} + m_{\mathrm{W}}$,

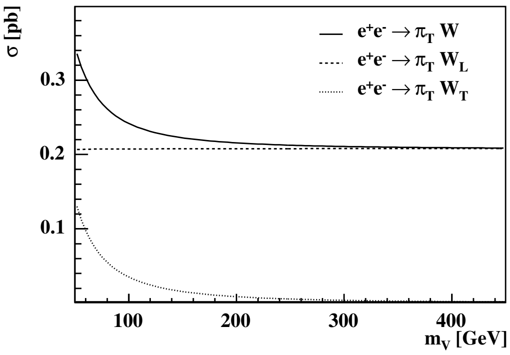

Figure 2.19: *The mass parameters* m_{A} *and* m_{V} *only affect the cross-sections involving weak* $\rho_{\mathrm{T}}/\omega_{\mathrm{T}}$ *decays such as* $\mathrm{e^+e^-} \to \pi_{\mathrm{T}}^{\pm}\mathrm{W}_{\mathrm{T}}^{\mp}$. *Processes with TC induced decays like* $\mathrm{e^+e^-} \to \pi_{\mathrm{T}}^{\pm}\mathrm{W}_{\mathrm{L}}^{\mp}$ *show no dependence on* m_{A} *and* m_{V}. $m_{\mathrm{A}} = m_{\mathrm{V}}$ *is assumed, which does not affect the picture. Other model parameters are assumed as listed in Tab. 2.2.*

i.e. the kinematic limit of the respective final states . The cross-sections exhibit the expected resonance at $m_{\rho_{\mathrm{T}}/\omega_{\mathrm{T}}} = \sqrt{\mathrm{s}}$. Also, the finite cross-section for $\mathrm{e^+e^-} \to \pi_{\mathrm{T}}^{+}\pi_{\mathrm{T}}^{-}$ and $\to \pi_{\mathrm{T}}^{\pm}\mathrm{W}_{\mathrm{L}}^{\mp}$ in the limit of $m_{\rho_{\mathrm{T}}/\omega_{\mathrm{T}}} \to \infty$ is visible, where the cross-section for the weak process $\mathrm{e^+e^-} \to \pi_{\mathrm{T}}^{\pm}\mathrm{W}_{\mathrm{T}}^{\mp}$ vanishes.

a) b)

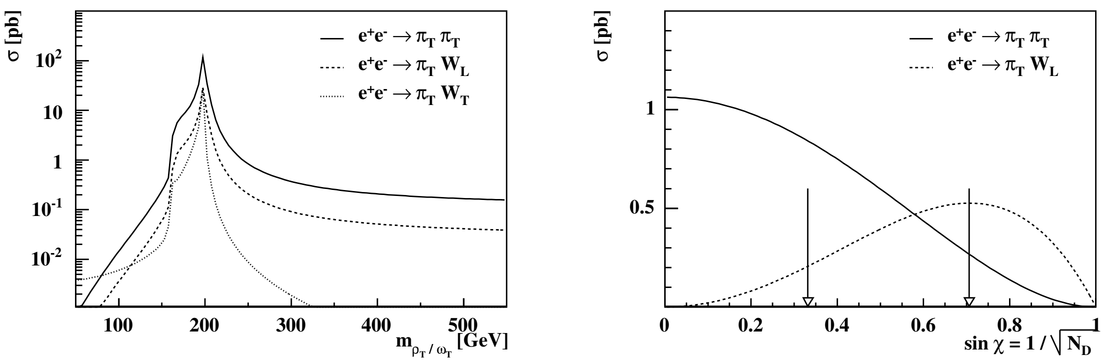

Figure 2.20: *Cross-section dependencies on a)* $m_{\rho_{\mathrm{T}}/\omega_{\mathrm{T}}}$ *and b)* $\sin\chi$. *Cross-sections for* $\mathrm{e^+e^-} \to \pi_{\mathrm{T}}^{+}\pi_{\mathrm{T}}^{-}$, $\pi_{\mathrm{T}}^{\pm}\mathrm{W}_{\mathrm{L}}^{\mp}$ *are non-vanishing in the limit of* $m_{\rho_{\mathrm{T}}/\omega_{\mathrm{T}}} \to \infty$ *due processes without s-channel* $\rho_{\mathrm{T}}^{0}/\omega_{\mathrm{T}}^{0}$ *states. The ratio of these two cross-sections depends on* $\sin\chi = 1/\sqrt{N_D}$. *Arrows in b) indicate the preferred model point at* $N_D = 9$ *and the disfavored scenario with* $N_D = 2$. *Other model parameters are assumed as listed in Tab. 2.2.*

The cross-section ratio of $\mathrm{e^+e^-} \to \pi_{\mathrm{T}}^{+}\pi_{\mathrm{T}}^{-}$ and $\mathrm{e^+e^-} \to \pi_{\mathrm{T}}^{\pm}\mathrm{W}_{\mathrm{L}}^{\mp}$ is almost independent of $m_{\rho_{\mathrm{T}}/\omega_{\mathrm{T}}}$, but sensitive to the number of technifermion doublets N_D, which determines the mixing angle χ. The cross-section dependencies on $\sin\chi$ are depicted in Fig. 2.20 b). As outlined above, N_D is preferably large. Arrows in the plot indicate the preferred model point $N_D = 9$, $\sin\chi = 1/3$ and a disfavored scenario with $N_D = 2$, $\sin\chi = 1/\sqrt{2}$.

For $\sin\chi = 1/3$, the cross-sections are shown in Fig. 2.21 as a function of the technipion mass in the limit of $m_{\rho_{\mathrm{T}}/\omega_{\mathrm{T}}} \to \infty$. Also $m_{\pi_{\mathrm{T}}}$ affects the relative cross-section ratio for $\mathrm{e^+e^-} \to \pi_{\mathrm{T}}^{+}\pi_{\mathrm{T}}^{-}$ and $\pi_{\mathrm{T}}^{\pm}\mathrm{W}_{\mathrm{L}}^{\mp}$. This is mainly due to different thresholds, which arise for $m_{\pi_{\mathrm{T}}} \neq m_{\mathrm{W}}$.

Where kinematically allowed, $e^+e^- \to \pi_T^+\pi_T^-$ is dominant.

a) b)

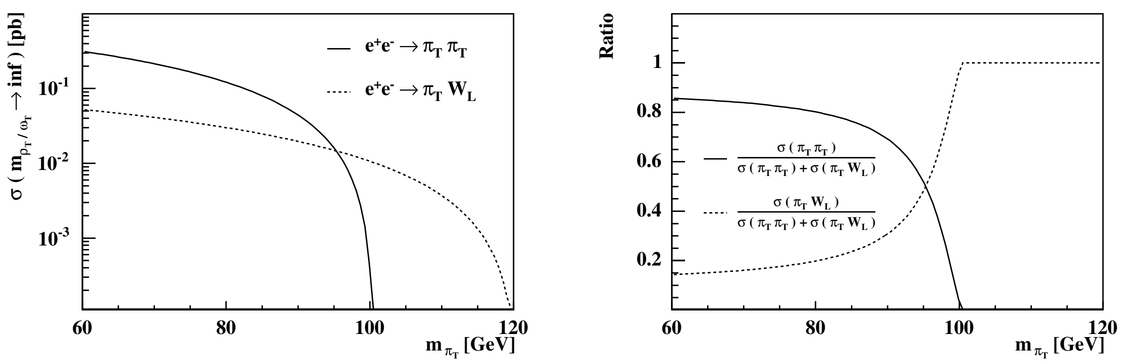

Figure 2.21: *Cross-sections for* $e^+e^- \to \pi_T^+\pi_T^-$ *and* $\pi_T^\pm W_L^\mp$ *in the limit of* $m_{\rho_T/\omega_T} \to \infty$ *a). The two channels have different thresholds at* $m_{\pi_T} = \sqrt{s}/2$ *and* $m_{\pi_T} = \sqrt{s} - m_W$*, respectively. b) shows the relative cross-section ratios. Where kinematically allowed,* $e^+e^- \to \pi_T^+\pi_T^-$ *is dominant.* $\sqrt{s} = 200\,\mathrm{GeV}$ *and* $\sin\chi = 1/3$ *are used for the plots. Other model parameters are assumed as listed in Tab. 2.2.*

Experimental prospects

Searches for Technicolor in e^+e^- collisions with collision energy $\sqrt{s} \approx 200\,\mathrm{GeV}$ are possible by two general approaches:

- Re-interpretation of cross-section measurements of $e^+e^- \to f\bar{f}$ and $e^+e^- \to W^+W^-$. An additional contribution to these channels is expected from decays of ρ_T^0 and ω_T^0 Technicolor vector states, which are produced in the *s*-channel via propagator mixing with the Z-boson. Due to the large cross-section of the SM processes, the method is only sensitive if $m_{\rho_T} \lesssim \sqrt{s}$ or $m_{\omega_T} \lesssim \sqrt{s}$.

- Direct search for final states compatible with technipion production. Three channels are possible: Technipion pair production $e^+e^- \to \pi_T^+\pi_T^-$ and associate production with a W-boson $e^+e^- \to \pi_T^\pm W^\mp$ or neutral gauge bosons $e^+e^- \to \pi_T^0 Z$, $\pi_T^0\gamma$. The latter only is possible through ρ_T^0 or ω_T^0 decays, and is limited to relatively light vector states, thus. In contrast, the channels with charged technipions have non-vanishing cross-sections even in the limit of $m_{\rho_T^0}/m_{\omega_T^0} \to \infty$.

Technicolor searches at Lep so far are performed by the Delphi [45], L3 [46] and Opal [47, 48] collaboration. It should be mentioned, that searches for Technicolor are also performed for $p\bar{p}$ collisions at Tevatron [49]. Technicolor production at hadron colliders however is not discussed here in more detail. A summary of recent mass limits on particles from TC inspired models (not only the TCSM) is given in [11], pp. 1040-1046.

Chapter 3

e^+e^- Experiments

The interplay between hadron and lepton colliders has been very fruitful throughout the last decades. One of the great successes in this field is the discovery of the weak gauge bosons in $p\bar{p}$ collisions at SPPS, which then have been studied in great detail at the e^+e^- machines LEP and SLC. In turn, the clear experimental environment and great precision at e^+e^- machines allowed to restrict the top quark mass, although this particle is much too heavy for direct production. The TEVATRON then discovered the top-quark, again in hadron collisions, with a mass in perfect agreement with the indirect prediction.

The next generation hadron collider LHC is already under construction at CERN and will start operation within the next years. Plans for a complementary e^+e^- collider ILC are in an advanced state. Only recently, the technology for such a machine has been selected from the three international proposals TESLA, NLC and GLC.

In this chapter, LEP and one of its experiments, OPAL, will be introduced, followed by a description of the ILC and a proposed detector. The chapter is concluded with an overview of the most common interactions observed at LEP and expected at ILC.

3.1 Large Electron Positron Collider

The Large Electron Positron Collider LEP was an e^+e^- storage ring at the European Laboratory for Particle Physics (CERN, Geneva, Switzerland). It was in operation from 1989 to 2000 and is shown in Fig. 3.1. The machine parameters such as beam energy, beam-spot size and luminosity are summarized in Tab. 3.1. Particles were brought to collision at four points, equipped with the experiments ALEPH, DELPHI, L3 and OPAL.

Center-of-mass energy	$\sqrt{s}$	$189 - 209\,\mathrm{GeV}$
Beam-spot size	σ_x, σ_y	$200\,\mu\mathrm{m}$, $2.5\,\mu\mathrm{m}$
Collision frequency	f_b	$22\,\mu\mathrm{s}$
Bunch charge	Q	$3 \times 10^{11}\,e$
Luminosity	$\mathcal{L}$	$10^{31}\,\mathrm{cm}^{-2}\,\mathrm{sec}^{-1}$
Acceleration gradient		up to $7\,\mathrm{MV/m}$

Table 3.1: *The LEP parameters in the period from 1998 to 2000.*

During Run I from 1989 to 1995, LEP was operated at center-of-mass energies $\sqrt{s} \sim 91\,\mathrm{GeV}$. At this energy, the Z-boson is produced as s-channel resonance with large cross section. About six million recorded Z-bosons allowed for the precise measurement of this

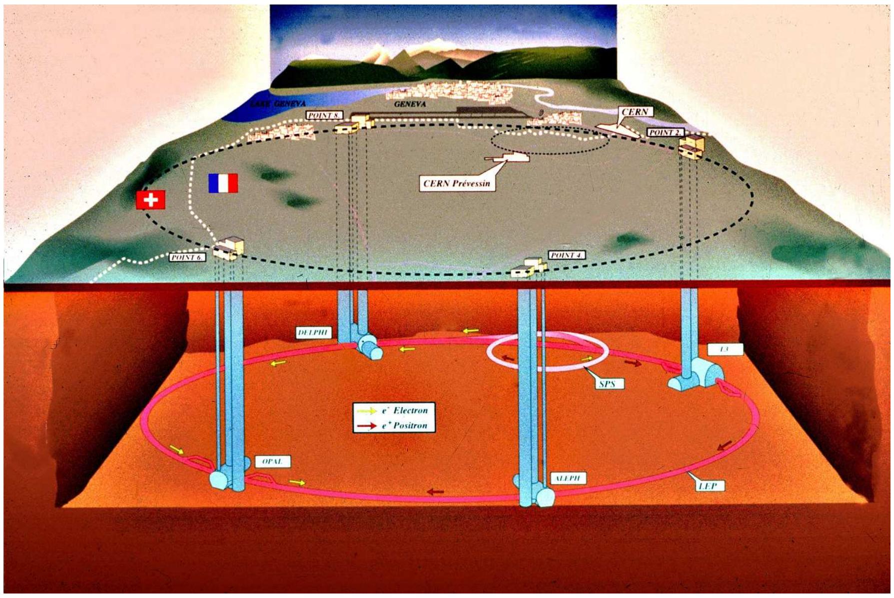

Figure 3.1: *The Large Electron Positron Collider* LEP *at CERN.*

particle's properties and of fundamental parameters of the Standard Model.

In Run II, starting from 1996, the collision energy has been increased to more than $\sqrt{s} \sim 161\,\text{GeV}$, where W- and Z-bosons can be pair-produced. Also at this scale, LEP measurements successfully confirmed the Standard Model, often with precision at the per-cent level or better. A great success was the experimental confirmation of the triple gauge boson coupling in W-boson pair production.

From 1998 to 2000, LEP provided e^+e^- collisions at the highest energies recorded so far, ranging from $\sqrt{s} = 189 - 209\,\text{GeV}$. Main focus of the measurements during this period was the search for new phenomena, especially the SM Higgs boson.

From the experimental point of view, the energy and the luminosity provided by the collider are crucial. Tab. 3.2 shows the beam energy and integrated luminosity recorded during the running of LEP.

Year	Energy $\sqrt{s}$ [GeV]	Luminosity $\int\mathcal{L}$ [pb^{-1}]
1989 – 1995	91.2	46.3
1996	130 – 172	25.6
1997	183	54.1
1998	189	172.1
1999	192 – 202	217.0
2000	199 – 209	207.3

Table 3.2: *Integrated luminosity recorded by* OPAL. *During the* LEPII *phase from 1996 to 2000, additional data has been recorded at* $\sqrt{s} = 91.2\,\text{GeV}$ *for calibration purposes, which is not considered in this listing.*

Beam energy measurements

The beam energy of LEP is measured by two different techniques. During LEPI, with beam energies around 45 GeV, beam electrons aquire transverse polarization via the Sokolov-Ternov mechanism [50]. The polarization can be measured from the angular distribution of Compton back-scattered laser photons. By transverse oscillating magnetic fields, the beam can be depolarized with a resonance frequency depending on the beam electrons' boost [51]. By this, the beam energy can be determined with an uncertainty of about 200 keV or $\Delta E/E \sim 4\times10^{-6}$.

At beam energies above 60 GeV, no transverse polarization is build up at LEP. Therefore, at LEPII the beam is deflected in a magnetic chicane. Inside the chicane, the beam position depends on the beam energy and is measured by beam position monitors. The method yields energy uncertainties of about 15 MeV or $\Delta E/E \sim 2 \times 10^{-4}$ [52] and is cross calibrated with the method of resonant depolarization at lower beam energies.

Luminosity measurements

Luminosity at LEP is measured by the detection of electrons from low angle Bhabha scattering $e^+e^- \to e^+e^-$. This is a pure QED process, and the cross-section is calculated with very high accuracy. The recorded event rate from Bhaba scattering thus allows a precise measurement of the luminosity. At OPAL (see Sec. 3.2), two dedicated detectors are installed in the forward region: The Forward Detector FD and the Silicon Tungsten Luminometer SW. Luminosity is measured with a relative accuracy of about 0.15 % with the SW.

3.2 The OPAL Detector

OPAL [53] is an acronym for Omni Purpose Apparatus at LEP, which is the most simple description of the experiment by itself. It is a complex assembly of different sub-detectors, which are oriented in cylindrical shells around one of the LEP interaction points. The whole detector is about 10 m wide and 12 m long. A schematic view is shown in Fig. 3.2.

From inner to outer, the detector systems serve different purposes:

- **Impact parameter measurement of charged particles**
  The innermost detectors are installed as close to the interaction point as possible. Their aim is to reconstruct the impact parameters from charged particles. This is needed to identify decay vertices of heavy, unstable particles with decay lengths of order $\mathcal{O}(100\,\mu\text{m})$, such as b- and c-hadrons.

- **Momentum measurement and identification of charged particles**
  The main tracking system reconstructs charged particles' trajectories. Located in a magnetic field, the momentum of the particle can be measured from the bending radius of the tracks. The energy loss through ionization, $\mathrm{d}E/\mathrm{d}x$ can be used together with the momentum information for particle identification.

- **Energy measurement of charged and neutral particles**
  In the electromagnetic and hadronic calorimeters just outside the coil for the magnetic field, charged and neutral particles are absorbed allowing for the determination of their energy. While charged particles are already registered by the inner detector components as well, the calorimeters are the only devices to recognize neutral particles like photons, long lived neutral kaons and neutrons.

- **Muon identification**
  Muons will pass the whole detector without being stopped. They are registered outside the calorimeters with muon detectors.

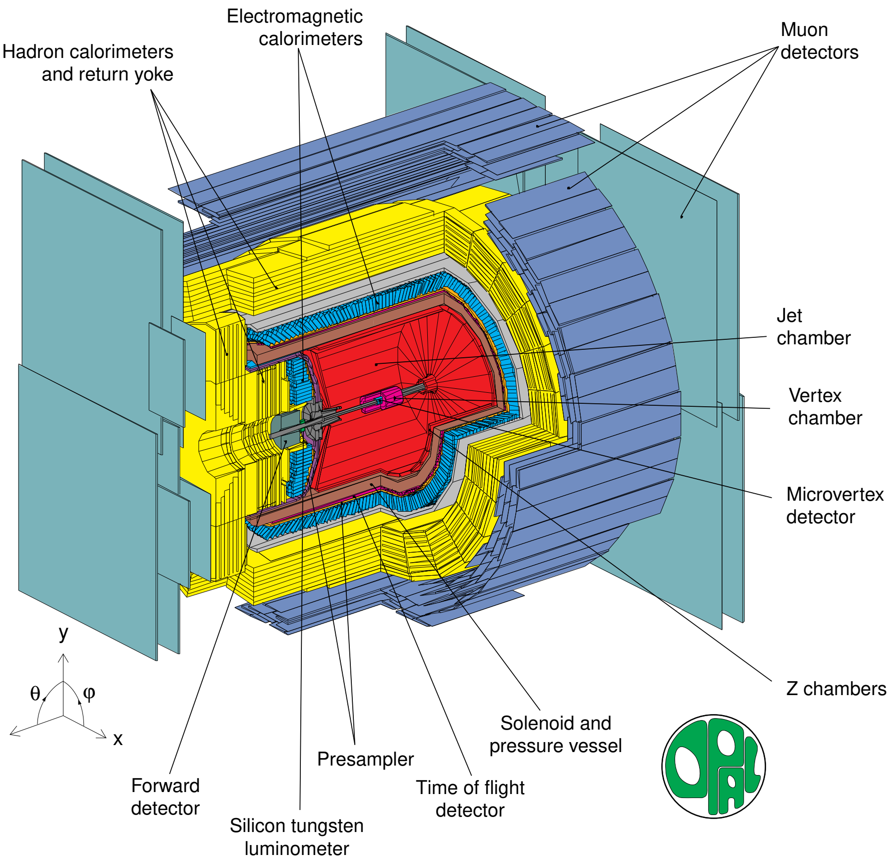

Figure 3.2: The OPAL detector.

OPAL uses a right handed coordinate system with the interaction point as origin. The $+z$-axis is defined as the direction of the electron beam, the $+x$-axis points to the center of the LEP ring. The azimuthal angle φ is measured with respect to the $+x$-axis, the polar angle θ with respect to the $+z$-axis.

In the following, the sub-detectors of OPAL will be introduced in some detail, starting from inner to outer arrangement. A cut view in $r-\varphi$ and $r-z$ is depicted in Fig. 3.3.

Silicon Microvertex Detector (SI)

The interaction point IP is surrounded by a 1.1 mm thick beryllium beampipe with 53.5 mm radius, which preserves the low pressure within the LEP accelerator. The Microvertex Detector is build up from 18.3 cm long and 33 mm wide modules of silicon microstrips. Two layers with 12 and 15 modules are located at radii of 63 mm and 75 mm respectively.

The silicon strips have a pitch of 25 μm and are mounted on both sides of each module. On the front side, where strips are oriented parallel to the z-direction, every second strip is read out yielding point resolutions of 5 μm in $r-\varphi$. On the rear side, only every fourth strip is read out yielding resolutions of 12 μm in z. The twisted arrangement allows true two-dimensional hit reconstruction.

The Silicon Microvertex detector is most important to reconstruct secondary vertices. The impact parameter resolution is $18\,\mu$m in $r-\varphi$ and $85\,\mu$m in z. This is much better than the average decay length of B-mesons, which is about $400\,\mu$m.

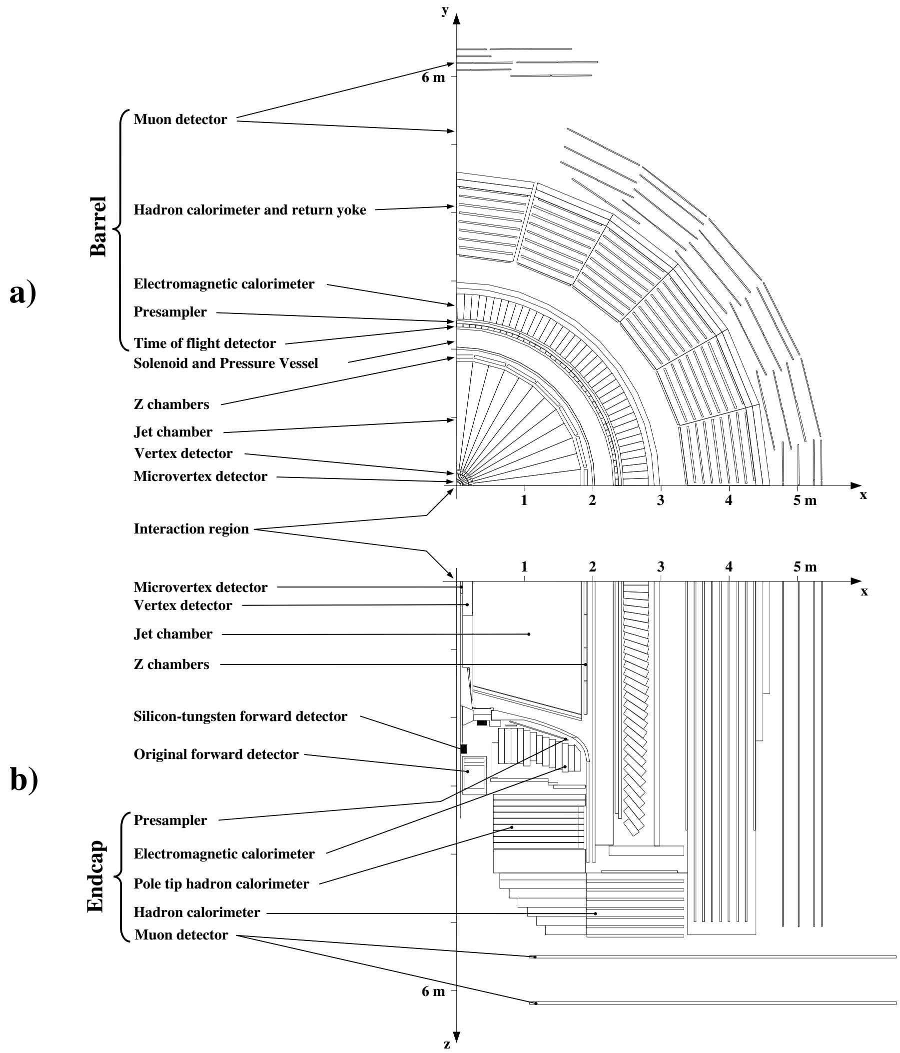

Figure 3.3: Cut-view of the OPAL detector in $r-\varphi$-direction **a)** and in z-direction **b)**.

Vertex Chamber (CV)

The Vertex Chamber is the first detector being located inside a pressure vessel. It is a cylindrical drift chamber of 1.1 m with inner and outer radius of 8.8 cm and 23.5 cm respectively. It is operated with a gas mixture of argon (88.2 %), methane (9.2 %), and isobutane (2.0 %). The gas mixture is common to all detectors inside the pressure vessel.

The Vertex Chamber is divided in two layers of 36 sectors each. In the inner section, 12 signal wires per sector are spanned parallel to the z-axis. The 6 signal wires in each of the sections of the outer layer are mounted at a stereo angle of 4° with respect to the z-axis. This improves the resolution of the z-coordinate of tracks to $300\,\mu$m. The resolution perpendicular to the beam is much better, $50\,\mu$m.

Originally, the Vertex Chamber was the only detector to measure the impact parameters of tracks. After the installation of the Microvertex Detector, it was still useful for the association of hits in the Microvertex Detector with tracks reconstructed in the Central Jet Chamber.

Central Jet Chamber (CJ)

The Central Jet Chamber is 4 m long and has an outer radius of 1.85 m and is the main tracking detector. It is operated with the same gas mixture as the vertex chamber and also located within the pressure vessel. A solenoidal magnetic field of 0.435 T is used to bend charged particles traversing the large volume. From the bending radius, the momentum of the particles is measured.

In azimuthal direction, the Jet Chamber is divided in 24 identical sections with 159 anode wires each, divided by cathode planes. The anode wires are spanned parallel to the z-axis in a radial plane with 1 cm spacing. A small off-set of $\pm 100\,\mu$m in $r - \varphi$ is used for consecutive wires to solve measurement left-right ambiguities.

Along their bended trajectory, charged particles leave ionized argon atoms and free electrons. The amount of ionizations is proportional to the specific energy loss $\mathrm{d}E/\mathrm{d}x$. Together with the momentum, this is used for particle identification. The ionization electrons will start to drift in the electrical field between anode wires and cathode planes. The field strength of 1 kV/cm is constant over most of the drift distance, which might be as long as 25 cm in the outer regions of the chamber. In the vicinity of the anode wires, where the field strength is much higher, drift electrons will initiate an avalanche of electrons, which is detected on the wire.

The gas pressure within the central jet chamber is $p = 4$ bar, as in the whole pressure vessel. Several aspects are considered when fixing this value: Higher pressure leads to more ionization, meaning more primary electrons and a better resolution for the specific energy loss $\mathrm{d}E/\mathrm{d}x$. Also, diffusion of the drifting electrons is smaller resulting in a better point resolution. On the contrary, high pressure slows down the drift velocity and introduces the need of higher drift fields. This in turn requires higher tensions of the spanned wires and thus yields, together with the pressure vessel, additional material for mechanical stabilization of the chamber. More material means more multiple scattering of high energetic particles and dilutes the energy measurement in the calorimeters.

The point of primary ionization is reconstructed using two methods. The distance to the anode wires, this is a measure for the position in $r - \varphi$, is determined by measuring the drift time. The z-component is determined by charge sharing on either side of the wires. While the point resolution for single tracks in $r - \varphi$ is about $130\,\mu$m, it is only 6 mm in z. The double track resolution, which is of primary importance to reconstruct tracks in dense jets of particles, is about 2 mm.

The combination of all points associated with one track allows the measurement of track momentum and energy loss. The resolutions obtained for tracks within the central part of the detector, where all 159 anode wires are hit, are

$$\frac{\sigma_{p_t}}{p_t} = \sqrt{0.02^2 + (0.0015\, p_t)^2} \qquad \text{and} \qquad \frac{\sigma_{\mathrm{d}E/\mathrm{d}x}}{\mathrm{d}E/\mathrm{d}x} = 3.8\,\% \tag{3.1}$$

for momentum p_t transversal to the z-direction and energy loss $\mathrm{d}E/\mathrm{d}x$, respectively.

z-Chambers (CZ)

24 Drift chambers around the outer radius of the CJ, but still within the pressure vessel, are used to improve the measurement of the z-component or jets. These z-chambers are divided

in 8 cells along the z-axis containing 6 anode wires each. The wires are spanned perpendicular to the beam axis and yield impact parameter resolutions of $300\,\mu$m.

The z-Chambers are the last detector components located within the pressure vessel and inside the coil for the magnetic field.

Time-of-Flight detector (TOF)

This sub-detector consists of plastic scintillator strips oriented in parallel to the beam axis. They are read out by photo-multipliers at both ends and yield time resolutions of 300 ps. The time-of-flight information is primarily used for trigger purposes and to reject cosmic events.

Presampler (PB and PE)

The material of pressure vessel and coil corresponds to approximately two radiation lengths. Thus, particles often will start to shower before they reach the calorimeters located further outside. If so, this is detected by the presamplers. They are divided in a cylindrical barrel part (PB) and two endcaps (PE).

The preshowers comprise two layers of streamer tubes in the barrel and multi wire proportional chambers in the endcaps. Both devices measure particle multiplicity and shower size, both being proportional to the energy loss of the initial particle.

Electromagnetic Calorimeter (EB and EE)

The Electromagnetic Calorimeter ECAL is the main device to measure the energy of photons and electrons. These are stopped completely, while hadrons and muons only lose part of their energy. The calorimeter comprises of lead glass blocks, in which the energy is measured via the Čerenkov light emitted by the secondary shower electrons.

In the barrel part (EB), the blocks are $10 \times 10\,\mathrm{cm}^2$ wide and 24.6 radiation lengths deep. The faces of the 9940 blocks do not directly point to the IP to avoid primary photons to escape detection within the block spacings. The light is collected using photo multipliers. The energy resolution for single particles is

$$\frac{\sigma_E}{E}\bigg|_{\mathrm{EB}} = \sqrt{0.015^2 + \frac{0.16^2}{E/\mathrm{GeV}}}. \tag{3.2}$$

In the endcaps (EE), blocks are $9.2 \times 9.2\,\mathrm{cm}^2$ wide and at least 20.5 radiation lengths deep. On each side of the pressure vessel, 566 blocks are mounted parallel to the z-axis. The ECAL endcaps are located within the inhomogeneous part of the magnetic field. Thus, phototriods are used for read-out. Energy resolution obtained is

$$\frac{\sigma_E}{E}\bigg|_{\mathrm{EE}} = \sqrt{0.018^2 + \frac{0.218^2}{E/\mathrm{GeV}}}. \tag{3.3}$$

Hadronic Calorimeter (HB, HE and HP)

The Hadronic Calorimeter HCAL enhances the energy measurement of strongly interacting particles like pions, kaons, protons and neutrons. These will not be stopped completely in the electromagnetic calorimeter due to their large mass. In addition, the hadronic calorimeter assists in muon identification. It comprises three parts: the cylindrical barrel (HB), the endcap regions outside the coil radius (HE) and the so-called pole-tips (HP), which are located inside the coil radius, behind the EE.

Build up as sampling calorimeter with stainless steel absorber, the HCAL also serves as return yoke for the magnetic field. The spacial resolution is limited by the segmentation of the active materials, which are streamer tubes in the barrel (HB) and endcap (HE) and multi wire proportional chambers in the pole-tips (HP). Energy resolution is

$$\left.\frac{\sigma_E}{E}\right|_{\mathrm{HB,\,HE}} = \frac{1.2}{\sqrt{E/\mathrm{GeV}}} \tag{3.4}$$

In total, the hadronic calorimeter is about one meter thick, covers 97 % of the solid angle and corresponds to seven hadronic interaction lengths.

Muon Chambers (MB and ME)

As outermost detectors, the Muon Chambers are installed. The barrel part (MB) is build from 110 flat drift chambers, arranged in four layers, the endcap region (ME) is instrumented with four layers of streamer tubes.

Since more than seven interaction length of material shield the muon chambers from the interaction point, the probability of a pion of 5 GeV to fake a muon is less than 1 %. The identification efficiency within the angular coverage of $|\cos\theta| < 0.98$ is basically 100 % for muons above 3 GeV.

Detectors in the forward region

In the forward region, four detectors are installed. The Forward Detector (FD) and the Silicon Tungsten Luminometer (SW), both used for luminosity determination via detection of electrons from low-angle Bhabha-scattering. The MIP Plug aims at the unambiguous determination of the collision time, and the Gamma Catcher improves hermeticity.

The FD comprises drift chambers, proportional counters and a lead-scintillator sandwich calorimeter. The luminosity is measured with an uncertainty of 0.4 %.

The SW is a sandwich calorimeter with 22 layers of tungsten absorber and 23 silicon layers as active material. It was installed in 1993 and enhanced luminosity measurements to a precision of 0.15 %.

The MIP Plug comprises very fast scintillator detectors with a timing resolution of 3 ns. It is located in front of the pole-tip hadronic calorimeter.

The Gamma Catcher finally is a lead-scintillator calorimeter closing the hole between FD and EB.

3.3 The International Linear Collider

Circular electron accelerators are limited through energy losses from synchrotron radiation, which grows with the fourth power of the beam energy. At highest LEP energies, the electrons and positrons lost approximately 3.5 GeV per circulation. Future e$^+$e$^-$ machines therefore are planned as linear colliders.

Three projects have been proposed for a next generation collider providing collision energies between 500 GeV and 1 TeV with very high luminosity in excess of $10^{34}\,\mathrm{cm^{-2}s^{-1}}$: The European TeV Energy Superconducting Linear Accelerator TESLA [54], the North-American Next Linear Collider NLC [55] and the Asian Global Linear Collider GLC [56]. All projects are based upon a two-arm accelerator with total length of more than 30 km. Electrons and positrons are accelerated in either arm and brought into collision at one or two central interaction points.

The main difference between the proposals is the technology used for acceleration. At NLC and GLC, normal conducting (warm) copper cavities are used with radio frequencies around 11.4 GHz, while at TESLA superconducting (cold) niobium cavities are operated at 1.3 GHz.

The main differences of the two technologies arises from the quality factors[1] Q_0 of the cavities. This has especially influence on the time structure of the beams, which is not made of equally spaced bunches anymore, but structured in bunch trains. Each bunch train is powered by a single klystron pulse. Due to the lower quality factor at the warm technology, the pulse lengths are much shorter, and the machine is operated with shorter bunch trains at a higher repetition rate. The relevant parameters are listed in Tab. 3.3. At the cold machine, it is possible to have as long pulses that the spacing between two successive bunches in a train is longer than the complete bunch train with ≈ 200 bunches at the warm machine.

	TESLA (cold)	NLC/GLC (warm)
Repetition rate [Hz]	5	120 – 150
Bunch train length [μs]	950	0.267
Bunches per train	2 820	192
Bunch separation [ns]	337	1.4

Table 3.3: *Beam parameters for the three linear collider proposals. All values refer to operation at* 500 GeV *and are taken from [57].*

Recently, the projects have been evaluated by the International Technology Recommendation Panel ITRP [58], which proposes to build the so-called International Linear Collider ILC based on the superconducting TESLA technology [59].

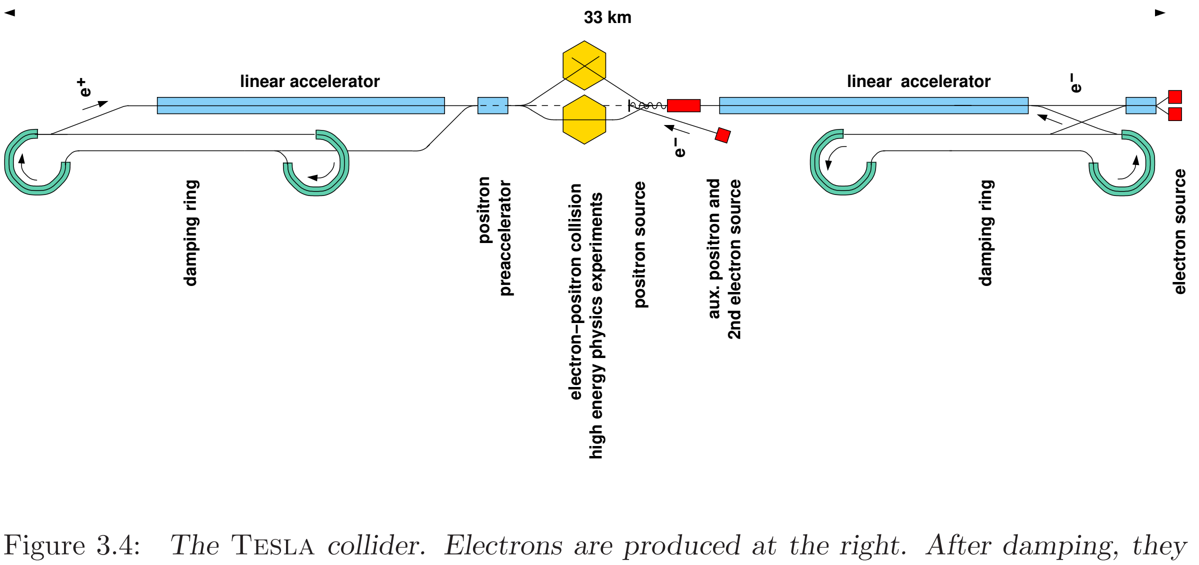

Figure 3.4: *The* TESLA *collider. Electrons are produced at the right. After damping, they are accelerated to full energy and used for positron creation before interacting.*

The general layout of the TESLA design is shown in Fig. 3.4. On the right side, electrons are produced in a laser driven source. It is designed to allow for longitudinal electron polarization of up to 80 % and is currently under study at DESY's Photon Injector Test stand in Zeuthen (PITZ) [60].

[1]The quality factor is proportional to the inverse of the surface resistant of the cavities.

After creation, electron bunches are pre-accelerated to 5 GeV and dampened in a dog-bone shaped storage ‘ring’, shown at the bottom right. The right arm of the main linear accelerator finally pushes the electron to maximum energy.

Before collision, electrons traverse an undulator. The hard gamma-radiation emitted is used to create positrons with longitudinal polarization up to $60 - 65\,\%$. The number of positrons gained is a function of the undulator’s length. On the contrary, the energy spread of the electron beam gets wider with longer undulator, so an optimum has to be found.

The positron are pre-accelerated right after production and transported to the left side of the machine. Damping is achieved with a similar damping ring as used for electrons. Final acceleration is done by a second arm of accelerator.

Two interaction regions are foreseen fore ILC. One can be designed for head-on collisions without crossing angle. Due to the beam time structure, this option is unique to the TESLA proposal and is not applicable at NLC/GLC. A second interaction region at is eventually foreseen with crossing angle and might be used to record high energetic photon collisions. For this running scheme, electron and positron beams are transformed to photon beams by Compton backscattering of laser light [61].

The ILC is designed to have a luminosity in excess of $10^{34}\mathrm{cm}^{-2}\mathrm{s}^{-1}$, which is three orders of magnitude higher than achieved at LEP. The luminosity is approximately given by

$$\mathcal{L} = \frac{n_b\, N_\mathrm{e}^2 f}{4\pi\ (\sigma_x \times \sigma_y)}. \tag{3.5}$$

Here, N_e is the number of particles in the two colliding bunches, f is the repetition rate of collider (i.e. the number of bunch trains per second), n_b is the number of bunches per train and $\sigma_x\,(sigma_y)$ is the beam spot size at the interaction point in $x\,(y)$-direction. To achieve high luminosity, both high N_i, i.e. a high total bunch charge Q_i, and small $\sigma_x/sigma_y$ are needed. This leads to a very high charge density at the interaction point. One of the resulting effects is beamstrahlung, i.e. photon radiation from beam particles in the strong electromagnetic field of the opposite bunch. Beamstrahlung might have significant impact on measurements at the ILC, as will be discussed in more detail in Chpt. 6.

3.4 ILC Detector Concepts

The International Linear Collider will provide very high luminosity, allowing for precision measurements with low statistical uncertainty. But, best measurement results are only achieved if the detector performance keeps up with this high precision. In contrast to LHC, the radiation environment and the amount of background events sets only weak constraints to the detector, and the detector design can be driven by physics requirements.

- **Vertexing**
  In most scenarios, signatures of new physics involve heavy quark final states. The tagging ability of b- and c-quarks therefore is a critical issue in the detector design. Besides the identification of b-quarks, the identification of c-quarks is a great challenge. Charmed hadrons yield much shorter decay lengths, and impact parameter resolutions of few μm are necessary for effective charm tagging.

- **Tracking**
  The recoil spectrum of the Z-boson in processes $e^+e^- \to Z\phi$ is the least model dependent technique to find any new spin 0 state ϕ, if ϕ couples to the Z. The most precise determination of the recoil spectrum is by detecting $Z \to \ell^+\ell^-$ final states. If the

momentum resolution for isolated tracks is of order $\Delta p/p^2 \approx 10^{-4}\,\mathrm{GeV}^{-1}$, the recoil mass resolution is limited by the Z-boson width and beamstrahlung effects only.

- **Calorimetry**
  Hadronic final states are not only the most dominant decay modes, but at ILC they also comprise more jets than at LEP energies. For instance, $t\bar{t}$ production yields six final state jets in about half of all decays. A jet energy resolution of $\Delta E/E \sim 40\,\%/\sqrt{E(GeV)}$ is necessary for precision studies.

- **Hermeticity and forward sensitivity**
  Besides heavy quarks, undetectable particles are expected from physics beyond the Standard Model, especially from SUSY models. The detector therefore should cover as much of the solid angle as possible. On the other hand, the very far forward region is the only part of the detector, where radiation damage to detector components is an issue.

Several detector layouts have been developed for all three proposals for the ILC. For the studies of this thesis, the detector design as proposed in the TESLA technical design report [62] is assumed. A schematic view of one detector octant is shown in Fig. 3.5.

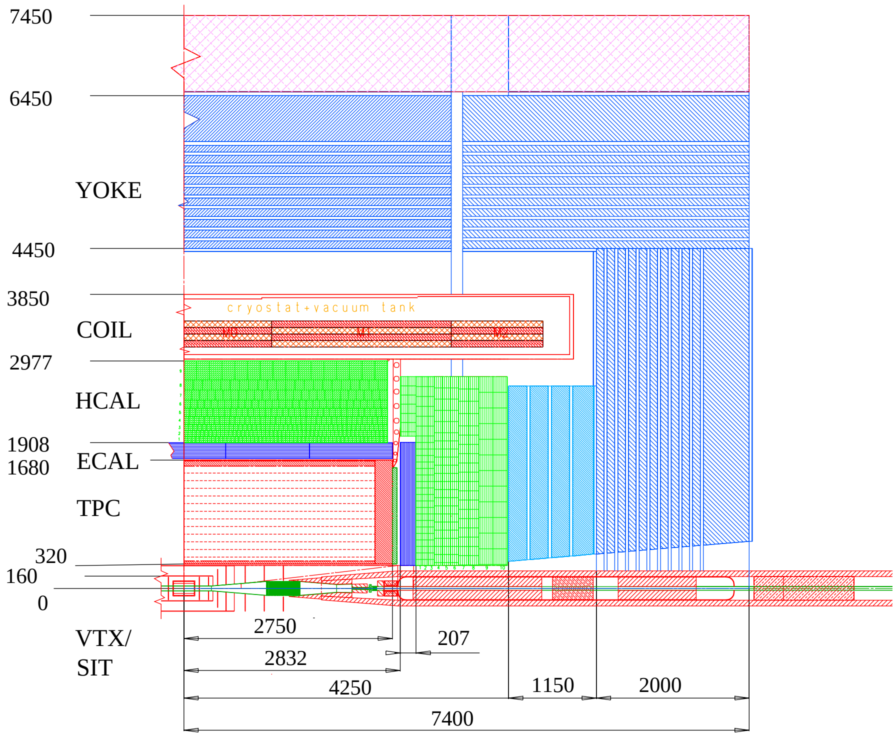

Figure 3.5: *The* TESLA *detector layout. The interaction point is shown at the lower left, surrounded by the vertex detector, the tracking detectors and the calorimeters. Both electromagnetic and hadronic calorimeter are positioned inside the coil for the magnetic field.*

Vertex detector

The vertex detector (VTX) is based on silicon pixels. Several different technologies are under study, e.g CCD [63], CMOS [64], DEPFET [65] and hybrid pixels [66]. Up to 800 million channels are foreseen with pixel sizes of $20 \times 20\mu\mathrm{m}^2$. The detector will be organized in up to five layers, with the innermost only 1.6 cm from the interaction point, and the outermost at $r = 6$ cm. The material budget of the whole device is less than a percent of a radiation length.

Design performances are point resolutions of $1.5\,\mu$m and impact parameter resolutions of $5\,\mu$m.

Tracking system

Besides the vertex detector, four more tracking detectors are considered. The main tracker is foreseen as Time Projection Chamber TPC. Between VTX and TPC, the Silicon Intermediate Tracker SIT is located. In the forward region, the Forward Tracking Discs FTD measure tracks with low polar angles, and the Forward Chambers FCH detect particles which do not pass the whole radius of the TPC.

The TPC is roughly 5.5m long and has inner/outer radius of 32/168 cm respectively. The chamber is a large gas filled volume divided by a cathode plane. Ionizing electrons drift towards the chamber endplates, where they are detected by gas amplification. The $r-\varphi$ information is derived from the position of the detected charge cloud, while information on the z-position of the primary ionization is derived from the drift time. For a particle traversing the whole radius of the chamber, up to 200 space points can be reconstructed with precision in $r-\varphi, z$ of $100\,\mu\text{m}, 1\,\text{mm}$ respectively.

The SIT consists of two layers of silicon strip detectors at radii of 16 cm and 30 cm. The measurement of two very accurate space points with precisions of $10\,\mu$m in $r-\varphi$ and $50\,\mu$m in z enhances the overall momentum resolution and the matching between track segments in the VTX and the TPC.

The FTD consist of seven discs on either side of the interaction point. The three innermost discs on either side are silicon pixel detectors, while the other four are planned with silicon strip technology. The FTD provides seven to four space point measurements for particles with polar angles between 7° and 25° with precision of $25\,\mu$m in $r-\varphi$.

The FCH measure the polar angle of particles which do not traverse the complete TPC radius. Two planes of straw tubes are located behind either TPC endcap and measure three space points per particle with resolutions of $100\,\mu$m in $r-\varphi$.

The momentum resolution of the complete tracking system is designed to reach $\Delta p/p^2 = 1.4 \times 10^{-4}\,\text{GeV}^{-1}$ for central tracks with polar angles $|\cos\theta| < 0.75$ and $3.4 \times 10^{-4}\,\text{GeV}^{-1}$ for forward tracks with $|\cos\theta| \approx 0.9$.

Calorimeters

To yield best jet energy resolution, both the electromagnetic calorimeter ECAL and the hadronic calorimeter HCAL are highly segmented both transversal and longitudinal to the shower evolution. Both devices are located inside the coil for the magnetic field. Besides the most favored devices presented below, additional designs are under study.

The electromagnetic calorimeter (ECAL) proposal is based on tungsten absorber with silicon as active material. It is highly segmented in three dimensions and corresponds to a thickness of 24 radiation lengths. Transversally, the segmentation is determined by the pad sizes of the silicon readout chips, which is of order $1 \times 1\,\text{cm}^2$. Longitudinally, the ECAL is build of 40 layers, of which the first 30 have $1.4\,\text{mm} = 0.4\,X_0$ thick absorber plates, while the last ten plates are thicker by a factor 3 ($4.2\,\text{mm} = 1.2\,X_0$).

The combination of high segmentation and a small Molière radius is needed to yield optimal separation of neutral and charged energy depositions (particle flow), which is essential to achieve the energy resolution needed. For single particles, the resolution is

$11 - 14\,\%/\sqrt{E\ [\mathrm{GeV}]}$. Electrons are reconstructed with almost 100 % efficiency, and are misinterpreted as pions with a probability of few 10^{-3}. Moreover, it has been shown that with the current design it is possible to track photons inside the ECAL and to extrapolate their origin with a resolution on the impact parameter of a few cm [67].

The hadronic calorimeter (HCAL) is foreseen with stainless steel absorber and scintillator as active material. The readout cells are larger than in the ECAL and range from $5 \times 5\,\mathrm{cm}^2$ to $25 \times 25\,\mathrm{cm}^2$. The device comprises 38/53 layers in the barrel/endcap part and has a total thickness of 4.5/6.2 hadronic interaction lengths λ. In addition, a pole tip calorimeter in the forward direction with 4 layers and $6.7\,\lambda$ is foreseen for better containment in the forward direction.

The energy resolution of the hadronic calorimeter is about $35\,\%/\sqrt{E}$ for single hadrons. However, due to the limited thickness in the barrel part, the muon system outside the coil is needed to identify leaking shower tails.

Magnetic field and muon chambers

Outside the calorimeters, a solenoidal coil will provide a magnetic field of 4 T. The coil design is based on the coil currently under construction for the CMS[2] experiment at LHC. The superconducting coil has an inner radius of 3 m and is approximately 9.2 m long. It consists of five modules in z, of which the inner will store a maximum current of 24.5 kA.

The return yoke is made of iron and is about 2 m thick. It is instrumented with either streamer tubes or resistive plate chambers. 12 layers of detectors are foreseen, which is sufficient for identification of muons and shower tails.

Forward detectors and mask

The very forward part of the detector is equipped with a mask shielding the inner detector from beam background radiation. The front of the mask is equipped with two calorimetric detectors, the low angle tagger (LAT) and the luminosity calorimeter (LCAL).

The main purpose of the LAT is to extend the coverage of the endcap calorimeters down to polar angles below 30 mrad. Like the main ECAL, it is based on tungsten absorber with silicon as active material.

The LCAL is used to tag high energetic electrons from low angle Bhabha scattering, which are used for luminosity measurements. Furthermore, the LCAL will be hit by 2×10^4 electron positron pairs per bunch-crossing from beam-beam interactions. Therefore, a radiation hard readout with diamond detectors is foreseen. The amount of beam background indicates the luminosity of each individual bunch crossing. Very fast readout of the LCAL is desired for a bunch-to-bunch final focus adjustment.

[2] CMS is the Compact Muon Solenoid, a omni purpose detector for hadron collisions at the Large Hadron Collider (LHC) at CERN.

Chapter 4

Search for Technicolor in the Four Jet Channel at OPAL

In this chapter, a search for charged technipions in the channels $e^+e^- \to \pi_T^+\pi_T^- \to b\bar{q}\,q\bar{b}$ and $e^+e^- \to \pi_T^\pm W^\mp \to b\bar{q}\,q\bar{q}$ in data recorded by the OPAL detector at LEP in the years 1998 to 2000 is presented. Separate analyses for these channels are already available [48, 47] for OPAL, but are based on the data recorded in 2000 only. Both analyses exhibit a large overlap, i.e. substantial numbers of data events are candidate events in both search channels. Therefore, the new analysis presented here aims at a combined selection of both channels.

Starting with an event selection following closely the analyses from [48], a decision for each event is made, whether it is interpreted as candidate for $e^+e^- \to \pi_T^+\pi_T^-$ or $e^+e^- \to \pi_T^\pm W^\mp$, respectively. The reconstructed technipion mass in the respective channels is taken as separating variable to find evidence for Technicolor production. No excess over background expectation is observed, and limits on the masses for charged technipions $\pi_T^\pm$ and technivector states ρ_T^0/ω_T^0 are obtained using signal cross-section predictions of the Technicolor Straw-man Model, which is presented in more detail in Sec. 2.7.

4.1 Signal and Background Processes

Signal topology

Charged technipions $\pi_T^\pm$ decay to a pair of quarks including one b-quark. In events $e^+e^- \to \pi_T^+\pi_T^-$, this leads to four-quark final states with two b-quarks, as depicted in Fig. 4.1 a).

The SM W-boson decays to quarks (leptons) with approximately 70 (30) % probability. No b-quarks are expected in the decays to quarks. Thus, events from $e^+e^- \to \pi_T^\pm W^\mp$ also yield four-quark final states with a branching ratio of approximately 70 %. These events contain

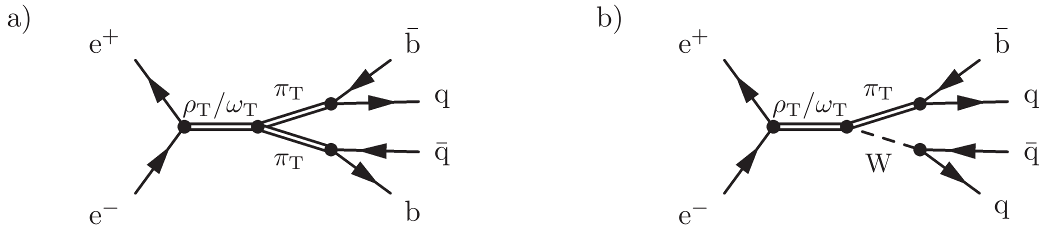

Figure 4.1: *The two signal channels in this analysis: Technipion pair production a) and technipion production in association with a W-boson b) with four-jet final states.*

only one b-quark, see Fig. 4.1 b).

Quarks are not observed directly. Due to confinement in QCD, they form bunches of color-neutral particles, mainly pions. These so-called jets include also heavy long-lived hadrons, if the initial quark is a b-quark. These b-hadrons fly some $100\,\mu$m, before they decay further at a secondary vertex. With high resolution vertex detectors, these secondary vertices can be recognized. Complex algorithms are used for b-tagging, i.e. to derive a probability estimator for a jet to contain a b-hadron. The method is explained in more detail in Sec. 4.3.3.

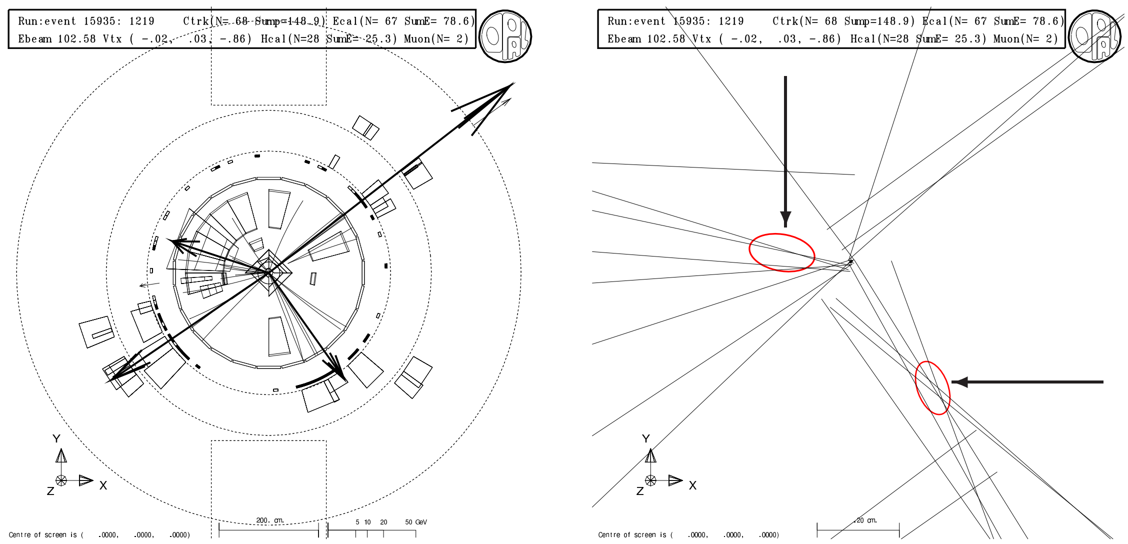

Figure 4.2: *A candidate event for* $\mathrm{e^+e^-} \to \pi_\mathrm{T}^+\pi_\mathrm{T}^- \to \mathrm{b\,q\,q\bar{b}}$, *recorded with the* OPAL *detector at* $\sqrt{\mathrm{s}} \approx 205\,\mathrm{GeV}$. *On the left, the whole detector is shown in the* $r-\varphi$ *projection. Four well separated jets are reconstructed, the jet momenta after a 4C fit implying energy and momentum conservation are superimposed as arrows. On the right, a zoomed view of the vertex region is shown. Two secondary vertices are observed at the indicated track intersections, which are an indication for jets with* b*-hadrons.*

Candidate events for technipion production via $\mathrm{e^+e^-} \to \pi_\mathrm{T}^+\pi_\mathrm{T}^-$ ($\mathrm{e^+e^-} \to \pi_\mathrm{T}^\pm \mathrm{W}^\mp$) are depicted in Fig. 4.2 (4.3). On the respective left plots, a schematic view of the whole OPAL detector is shown. In both events, four well separated jets are reconstructed, which are shown as large arrows superimposed to the reconstructed particles. The respective right plots show a zoomed view of the vertex region. Two (one) secondary vertices are identified in the $\pi_\mathrm{T}^+\pi_\mathrm{T}^-$ ($\pi_\mathrm{T}^\pm \mathrm{W}^\mp$) candidate events at the indicated intersection of particles.

These signatures are not unique to events from the two signal channels, but arise also from other processes. In principle, all processes should be investigated as potential source of background. However, signal events contain four jets and thus many reconstructed particles. Therefore, only events which pass the OPAL multi-hadron selection (MHS) [68] are considered further. The detailed requirements are:

- Events contain at least four tracks and six calorimeter clusters. For tracks and clusters, a minimal number of hits in the tracker and a minimal number of calorimeter cell hits are required.

- The total visible energy must be more than $14\,\%$ of the center-of-mass energy.

- Each hemisphere must contain at least $25\,\%$ of the visible energy.

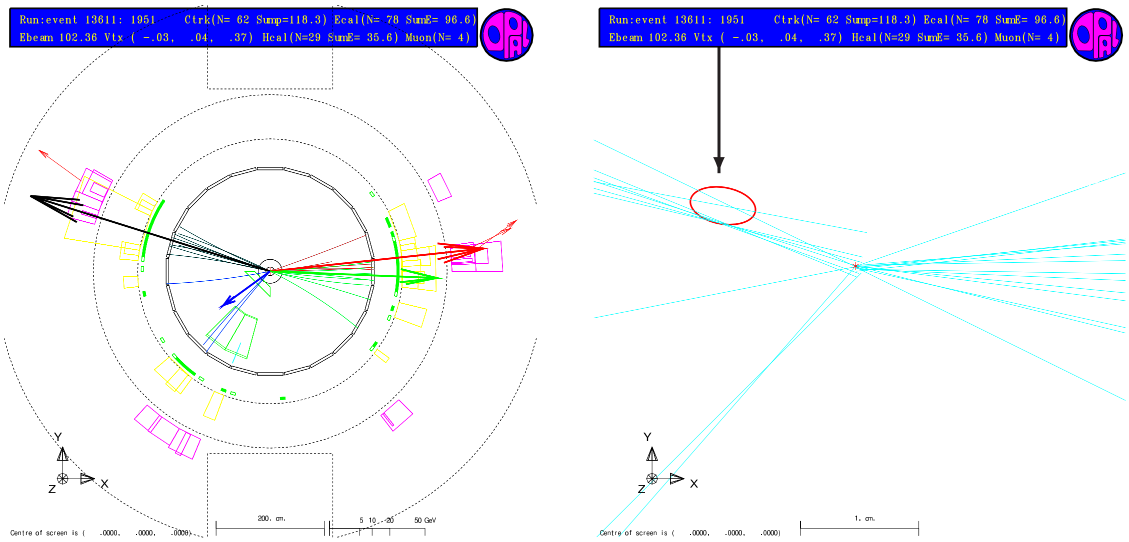

Figure 4.3: *A candidate event for* $e^+e^- \rightarrow \pi_T^\pm W^\mp \rightarrow b\bar{q}\, q\bar{q}$, *recorded with the* OPAL *detector at* $\sqrt{s} \approx 205\,\mathrm{GeV}$. *On the left, the whole detector is shown in the* $r - \varphi$ *projection. Four jets are reconstructed, the jet momenta after a 4C fit implying energy and momentum conservation are superimposed as arrows. Although the jets seem to overlap in this projection, they are well separated along the* z*-direction. On the right, a zoomed view of the vertex region is shown. One secondary vertex is observed at the indicated track intersection, which is an indication for a jet with a* b*-hadron.*

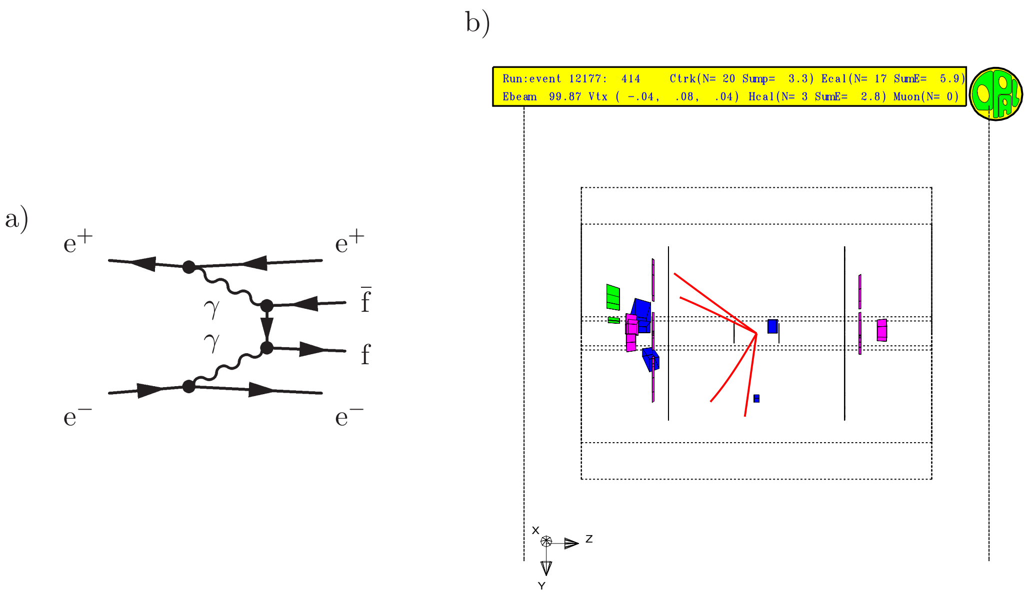

Figure 4.4: *Two-photon process: The beam electrons both radiate quasi-real photons, which then collide to create a fermion-anti-fermion pair. In b) a typical two photon event recorded with the* OPAL *detector at* $\sqrt{s} = 200\,\mathrm{GeV}$ *is shown. The event is characterized by low multiplicity, low energy and large longitudinal momentum imbalance.*

Most events with purely leptonic final states like for example $e^+e^- \to Z^{(*)} \to \mu^+\mu^-$ do not pass these cuts. Also two-photon events are rejected. Here, the beam electrons radiate quasi-real photons, which then collide to form e.g. a pair of fermions, see Fig. 4.4 a). These events are characterized by low multiplicity, momentum imbalance and a reduced total event energy. A typical event recorded with the OPAL detector is shown in Fig. 4.4 b).

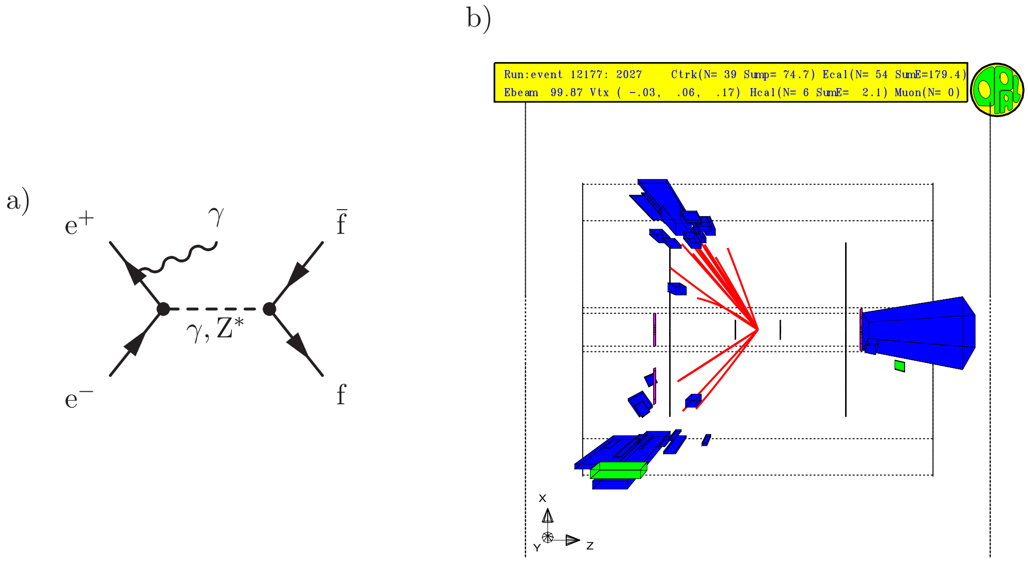

Figure 4.5: *Radiative return events: By initial state photon radiation, the effective center-of-mass energy is lowered to the* Z*-pole. In b) a typical event recorded with the* OPAL *detector at* $\sqrt{s} = 200\,\mathrm{GeV}$ *is shown. The photon is visible as high energetic cluster in the electromagnetic calorimeter on the right side.*

Among the events passing the MHS criteria, two-quark final states are most frequent. The process involves an s-channel photon or Z-boson, $e^+e^- \to \gamma, Z^{(*)} \to q\bar{q}$. The cross-section is resonant at $\sqrt{s} \sim m_Z$. For larger center-of-mass energies, the resonance energy can be realized by radiation of a hard photon by one of the beam electrons (initial state radiation ISR). Events of this type are named 'radiative return events', an example is shown in Fig. 4.5.

Naïvely, only two jets are expected from a two-quark final state. However, the final state quarks might radiate gluons, which also can initiate separate jets or form a second $q\bar{q}$ pair (gluon splitting). Quarks from gluon splitting are mostly light u, d, s-quarks, while c- and b-quarks occur only at the per-mille level. Primary quarks in contrast are b-quarks in approximately 12 % of all two-quark events at $\sqrt{s} \sim 200\,\mathrm{GeV}$.

Although the cross-section of two-quark background is several orders of magnitude larger than that of the signal processes, this kind of background events can be suppressed to a moderate level by the selection presented in Sec. 4.4. Suppression of events with four fermions in the final state is not so simple, because the event topology can be very similar to that of the signal.

Four-fermion background arises dominantly from W- and Z-boson pairs, see Fig. 4.7. The successive decays yield leptonic/semi-leptonic/hadronic final states for approximately 9/42/49 % of the events. Purely leptonic events with four leptons are rejected by the multi-hadron selection already. Semi-leptonic final states with each one pair of leptons and quarks are also distinct in topology from the signal and contribute only very little to the remaining background of this analysis. Events with four quarks in the final state however yield hadronic four-jet topologies similar to those of the signal processes.

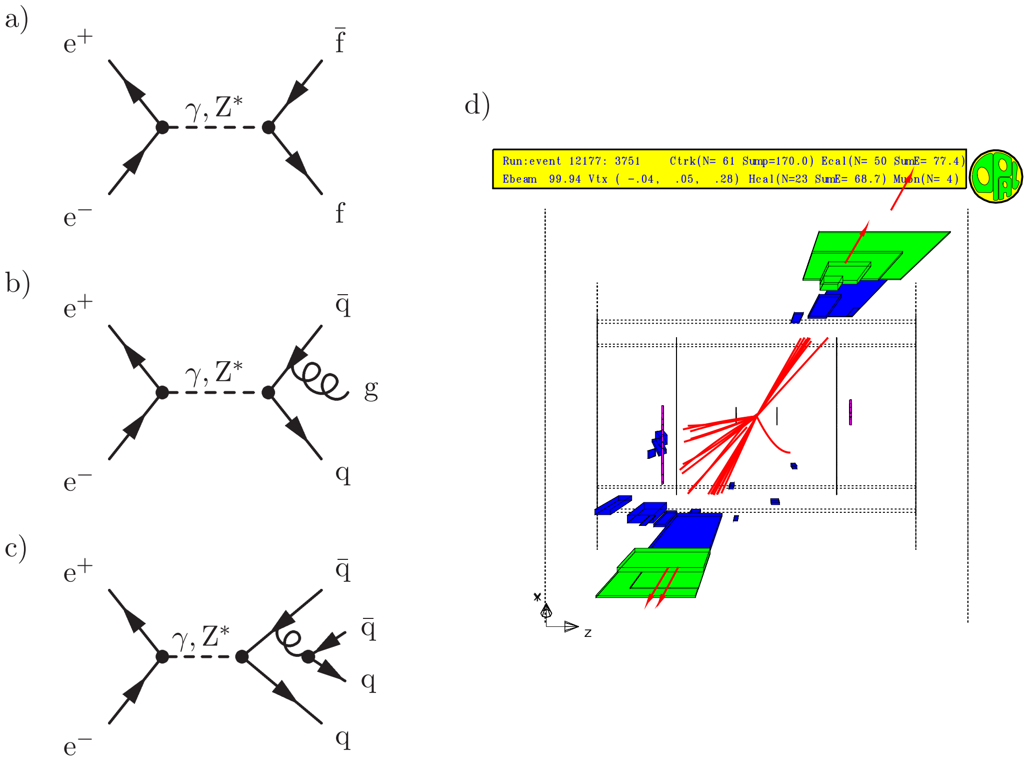

Figure 4.6: *Two-fermion events: Without ISR, the two final state fermions are back-to-back. If the fermions are quarks, gluon radiation in the final state is a common feature (b+c). In d) a two-jet event recorded with the* OPAL *detector at* $\sqrt{s} = 200\,\mathrm{GeV}$ *is shown. One jet is broadened, which might be an indication for soft gluon radiation.*

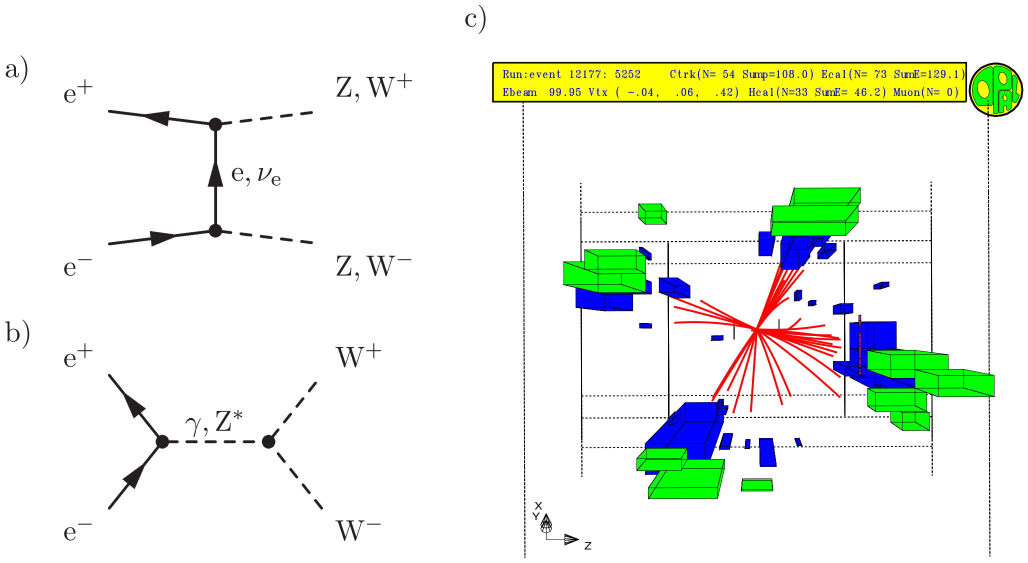

Figure 4.7: *Pairs of* W- *and* Z-*bosons yield four final state fermions. In* $\approx 49\,\%$ *of the events, all fermions are quarks and yield four jets. A sample event recorded with the* OPAL *detector at* $\sqrt{s} = 200\,\mathrm{GeV}$ *is shown in c). Four-jet events are the dominating source of background to this analysis.*

Jets from b-quarks arise in events including $Z \rightarrow b\bar{b}$ decays only, which make up less than 5 % of all hadronic four-quark events. b-tagging thus is the most important tool to reject events from four-quark background.

4.2 Data Set and Monte Carlo Samples

The search for Technicolor presented within this thesis is based on data recorded by the OPAL experiment during the last three years of LEP operation, where the highest energetic e^+e^- collisions ever were recorded. The data correspond to an integrated luminosity $\mathcal{L} = 596.4\text{pb}^{-1}$. The energy weighted luminosity spectrum is depicted in Fig. 4.8. For this analysis, data events are divided to eight bins in $\sqrt{s}$ as defined in Tab. 4.1.

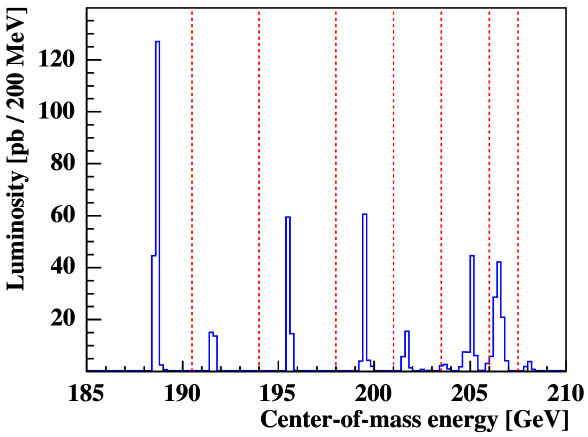

Figure 4.8: *The integrated luminosity recorded by* OPAL *as a function of the center-of-mass energy* $\sqrt{s}$. *Vertical lines indicate the* $\sqrt{s}$*-bins used in this analysis.*

Center-of-mass energy [GeV]			Integrated
Data range	Data mean	MC	luminosity [pb^{-1}]
185.0 – 190.5	188.6	189	175.0
190.5 – 194.0	191.6	192	28.9
194.0 – 198.0	195.5	196	74.6
198.0 – 201.0	199.5	200	71.1
201.0 – 203.5	201.7	202	24.3
203.5 – 206.0	205.0	205	78.2
206.0 – 207.5	206.5	207	102.3
207.5 – 210.0	208.0	208	7.1
		total	596.4

Table 4.1: *The bins in* $\sqrt{s}$ *as used in this analysis. The table lists the range of energies, luminosity weighted mean energy in data,* $\sqrt{s}$ *for MC events and the integrated luminosity.*

Data events are compared to simulated Monte Carlo (MC) events of all relevant Standard Model background processes, which are discussed in more detail in the previous section. Different MC programs are used to simulate the hard interaction, the decays/hadronization to a final states of stable (and thus observable) particles and the measurement of these particles in the detector.

Depending on the process, different MC generators are used for event simulation. Samples are generated with one fixed center-of-mass energy for each of the energy bins. The respective values are listed in the third column of Tab. 4.1.

- **Signal events** from $e^+e^- \to \pi_T^+\pi_T^-$ and $e^+e^- \to \pi_T^\pm W^\mp$ are generated using the TCSM implementation in `PYTHIA 6.2` [69]. Although only $W \to q\bar{q}$ decays are are selected, also decays $W \to \ell\nu$ are simulated. This has to be taken into account when interpreting the selection efficiency for $\pi_T^\pm W^\mp$ signal events. The masses of the intermediate Technicolor vector mesons ρ_T and ω_T are set to be much higher than $\sqrt{s}$ during event generation. With this setting, the event topology becomes independent of the ρ_T/ω_T mass, as long as they are not produced at resonance.

- **2-Fermion events** are simulate with the `KK2F` generator [70]. In this program, photon and gluon radiation is accounted for.

- **4-Fermion events** are obtained from two different generators. Events from the process $e^+e^- \to e^+e^- q\bar{q}$ are generated using `grc4f` [71]. Processes $e^+e^- \to q\bar{q}\,q\bar{q}$ and $e^+e^- \to \ell^+\ell^- q\bar{q}$ with $\ell = \mu$, τ are simulated with `KoralW` [72]. For some center-of-mass energies, both processes are contained in one sample and cannot be studied separately.

Hadronization of final state quarks is simulated using the string fragmentation model of `JETSET` [73]. Hadronization via cluster fragmentation is studied by `Herwig` [74] as a source of systematic uncertainty (see also Sec. 4.6).

Detector response is simulated by the OPAL detector simulation `GOPAL` [75], which is based on `GEANT3` [76]. The output from `GOPAL` for MC events is technically equivalent to data, and events from both sources are treated the same way during all analysis steps.

All MC samples for background processes are taken from the central OPAL database. A complete list of all samples used in this analysis is summarized in App. D. Events for the two signal channels are generated for different masses of the technipions as summarized in Tab. 4.2. In the mass range $m_{\pi_T} = 70...100\,\mathrm{GeV}$, samples are available in steps of 1 GeV.

4.3 Event Reconstruction

Central information of measurements at OPAL are tracks of charged particles, reconstructed by the tracking detectors, and energy depositions of any long-lived or stable particle in the electromagnetic and hadronic calorimeters. While charged leptons yield isolated tracks/clusters, quarks will hadronize and form jets of particles leaving a bunch of tracks and clusters in the detector. Dedicated algorithms are used to cluster reconstructed particles to jets, which in turn can be associated with the primary quarks. The quark flavor can be estimated by identifying signatures of heavy hadrons containing b- or c-quarks.

4.3.1 Reconstruction of Particle Energies and Momenta

In multi-hadronic events, particles are expected to be mainly charged pions or photons from neutral pion decays. Under this hypothesis, momentum measurements from tracks and energy measurements from clusters both yield fully determined four-momenta, so-called energy flow objects.

$\sqrt{s}$ [GeV]	Channel	m_{π_T} [GeV], each sample contains 5000 events
189	$\pi_T^+\pi_T^-$	50, 55, 60, 65, 70-94
189	$\pi_T^\pm W^\mp$	50, 55, 60, 65, 70-100, 105, 108
192	$\pi_T^+\pi_T^-$	50, 55, 60, 65, 70-95
192	$\pi_T^\pm W^\mp$	50, 55, 60, 65, 70-100, 105, 110, 111
196	$\pi_T^+\pi_T^-$	50, 55, 60, 65, 70-97
196	$\pi_T^\pm W^\mp$	50, 55, 60, 65, 70-100, 105, 110, 115
200	$\pi_T^+\pi_T^-$	50, 55, 60, 65, 70-99
200	$\pi_T^\pm W^\mp$	50, 55, 60, 65, 70-100, 105, 110, 115, 119
202	$\pi_T^+\pi_T^-$	50, 55, 60, 65, 70-100
202	$\pi_T^\pm W^\mp$	50, 55, 60, 65, 70-100, 105, 110, 115, 120, 121
205	$\pi_T^+\pi_T^-$	50, 55, 60, 65, 70-100, 102
205	$\pi_T^\pm W^\mp$	50, 55, 60, 65, 70-100, 105, 110, 115, 120, 124
207	$\pi_T^+\pi_T^-$	50, 55, 60, 65, 70-100, 103
207	$\pi_T^\pm W^\mp$	50, 55, 60, 65, 70-100, 105, 110, 115, 120, 125, 126

Table 4.2: *MC samples for the signal processes* $e^+e^- \rightarrow \pi_T^+\pi_T^-$ *and* $e^+e^- \rightarrow \pi_T^\pm W^\mp$ *are generated for different values of the technipion mass. In the range* $m_{\pi_T} = 70...100\,\mathrm{GeV}$, *samples are available in steps of* 1 GeV.

Naïve summation over all objects of an event would overestimate the total energy due to double-counting of the contributions from charged particles. The matching track (MT) algorithm [77] is used for compensation:

- Isolated clusters and tracks are interpreted as photons and pions, respectively. Photon energies and momenta are calculated using the energy measurements of the calorimeter, while for pions the momenta are measured from the track curvatures and the energy is calculated using pion mass hypothesis.
- Clusters with an associated track can originate from a single charged particle, or from a charged and a neutral particle close together. The track information is used to calculate the expected energy under pion mass hypothesis. If significantly more energy is measured from the calorimeter cluster, an additional photon is assumed.
- Electrons are treated separately. Often, electrons do not leave a clear track or a well defined calorimeter cluster due to radiation of bremsstrahlung and multiple scattering inside the tracking detectors. Therefore, electrons are identified by an artificial neural network ANN, which uses measurements from $\mathrm{d}E/\mathrm{d}x$, p/E, time of flight and cluster shape. The energy of electrons is best determined from calorimeter measurements, while its direction is determined from tracking information.

4.3.2 Jet Reconstruction

All reconstructed particles of an event are clustered to four jets using the Durham jetfinder [78]. For more details on jet algorithms, see App. A. From this procedure, four jets with four momenta p_D^i are obtained.

In a second step, the distance parameter of the JADE jetfinder is evaluated for any (Durham-)jet-particle combination. Particles are assigned to the closest jet, and the final jet momenta are calculated as the sum over all particles in that jet. This re-assignment improves the jet energy resolution [79].

From the jets, the effective center-of-mass energy $\sqrt{s'}$ is determined, which is defined as the center-of-mass energy corrected for initial state photon radiation (ISR) and can be determined in two ways:

- Sometimes, the ISR photon is directly visible in the detector. Under this hypothesis, $\sqrt{s'}_a$ is calculated as the square of the four-momentum difference of the double beam energy $(\sqrt{s}, 0, 0, 0)$ and the energy of the highest energetic cluster in the electromagnetic calorimeters.

- More often, the ISR photon(s) stay inside the beam pipe and escape detection. The momentum sum in the z-direction of all jets will be unbalanced in this case. A kinematic fit with three constraints is applied, which implies conservation of transverse momentum $\sum_i p_x^i = \sum_i p_y^i = 0$. The third constraint assumes that the difference of energy and longitudinal momentum originates from one undetected (massless) photon with no transverse momentum, e.g. $(\sum_i E^i - \sqrt{s})^2 - (\sum_i p_z^i)^2 = 0$. Here, $p^i = (E^i, p_x^i, p_y^i, p_z^i)$ is the momentum of the i-th jet after the kinematic fit. The effective center-of-mass energy in this case is defined as the sum over all jet energies, $\sqrt{s'}_b = \sum_i E^i$.

Both possibilities $\sqrt{s'}_a$ and $\sqrt{s'}_b$ are evaluated, and the effective center-of-mass energy is taken to be the minimum of both

$$\sqrt{s'} = \min\left(\sqrt{s'}_a, \sqrt{s'}_b\right). \tag{4.1}$$

4.3.3 Identification of Jets from b-Quarks

Jets originating from b-quarks can be recognized by three means: The existence of rather long-lived particles with decay length of some $100\,\mu$m, the appearance of leptons in the jet and the overall jet shape. Not all jets from b-quarks will show clear signatures of all three effects.

Therefore, each b-property is exploited separately by either likelihood or neural network techniques. All three output values finally are combined to an overall likelihood $\mathcal{B}$, which is close to one for b-jets and close to zero for jets from light quarks u, d and s. Jets from c-quarks yield intermediate values for $\mathcal{B}$. Also c-quarks form long-lived hadrons, but the decay length, i.e. the mean flight distance before decay, is shorter than that of b-hadrons. The secondary vertices of these decays therefore are not reconstructed as efficiently as for b-quarks. The algorithm for b-tagging is documented in [80] and summarized below.

Lifetime likelihood $\mathcal{L}_{lt}$

The time-scale of the weak b-decays is much longer than the QCD-mediated hadronisation process. Primary b-quarks therefore will be confined in color-neutral b-hadrons, mostly B-mesons. These particles are semi-stable and decay after flying some $100\,\mu$m. They do not enter the sensitive volume of the detector, but nevertheless can be recognized by secondary vertices or tracks with large impact parameter with respect to the primary interaction point. Two likelihood estimators $\mathcal{L}_{sv}$ and $\mathcal{L}_{ip}$ are used to evaluate either effect, which are highly correlated. Therefore, $\mathcal{L}_{sv}$ and $\mathcal{L}_{ip}$ are combined using an artificial neural network (ANN), and the combined lifetime likelihood $\mathcal{L}_{lt}$ is formed using the ANN output.

Secondary vertex likelihood $\mathcal{L}_{sv}$: Most sensitive for b-quark identification is the appearance of secondary vertices in a jet. Cascade decays b → c → s might in addition yield tertiary vertices, which however often cannot be resolved. Searches for secondary vertices then will find a point in between both decays.

All particles in a jet are grouped to sub-jets by a cone algorithm (see App. A for details). An ANN is used to calculate an ordering parameter for each track of the sub-jet from the track impact parameters, its polar angle and its angle with respect to the sub-jet axis.

The tracks with the highest ordering parameters (six at most) are used to fit a common vertex. As long as one of the tracks contributes more than a factor of 5 to the total χ^2 of the vertex fit, this track is omitted and the vertex is re-fitted. This procedure is referred to as tear-down algorithm. Of course, a secondary vertex is only found if at least two tracks remain.

All vertices found are now re-evaluated with the so-called build-up algorithm. For all tracks in the initial jet, an ordering parameter is calculated from the geometrical distance to the vertex. Starting with the closest, tracks are added to the vertex tracks, and the vertex is re-fitted. If all tracks contribute less than 5 to the total fit χ^2, the old vertex is replaced by the new one, and the procedure is repeated.

For vertices found, the decay length significance is calculated as the distance of the vertex divided by the distance error. The latter has contributions both from the primary and from the secondary vertex position. The reduced decay length significance is calculated in analog, but with the vertex fitted without the leading particle in the tear-down part of the algorithm.

The vertex likelihood $\mathcal{L}_{sv}$ is calculated from the highest decay length significance and its reduced analog.

Impact parameter likelihood $\mathcal{L}_{ip}$: Even if no secondary vertex is found, hadrons with b-quark content will most likely yield tracks with large impact parameter. The impact parameter significances in $r-\varphi$ and $r-z$ are used as input parameters for the impact parameter likelihood $\mathcal{L}_{ip}$, which gains values close to one for tracks from b-hadron decays, and close to zero for tracks from the hadronisation process.

The impact parameter likelihood improves the overall lifetime likelihood in cases, where no secondary vertex could be found.

Lepton likelihood $\mathcal{L}_{lpt}$

About one out of five b-hadrons decays semi-leptonically. The electrons or muons from these decays usually have a large transverse momentum with respect to the hadron's flight direction due the large mass of the decaying particle.

Electrons/muons are required to have at least momentum of $2/3\,\mathrm{GeV}$ and are identified by the OPAL standard ANN-based selection. The initial flight direction of the b-hadron is unknown, but assumed to coincide with the jet direction when calculating the transverse momentum of the lepton. The likelihood $\mathcal{L}_{lpt}$ uses the transverse momentum and yields values close to one for leptons from b-decays.

Leptons are only found in about 6 % of all b-jets. Therefore, the impact on the overall efficiency to identify b-jets is relatively small. Nonetheless, the efficiency is improved significantly for the cases where a lepton is found.

Jet-shape likelihood $\mathcal{L}_{js}$

Due to cascade decays of b-quarks like $\mathrm{b} \rightarrow \mathrm{f\bar{f}\,c} \rightarrow\rightarrow \mathrm{f\bar{f}\,f\bar{f}\,s}$, the multiplicity of b-jets is higher than of light jets. The large mass of b-hadrons in addition leads to particles with large transverse momentum with respect to the jet axis, thus broadening the jet.

Both effects are used as input for an ANN, which yields values close to one for b-jets and close to zero for jets from u-, d- and s-quarks. From the ANN output, the jet-shape likelihood

$\mathcal{L}_{js}$ is formed. The evaluation of jet-shape parameters is less sensitive than lifetime tag or lepton identification.

Combined b-likelihood $\mathcal{B}$

Lifetime likelihood, lepton likelihood and jet shape likelihood are combined to an overall b-likelihood

$$\mathcal{B} = \frac{w_{\mathrm{b}} \left(\prod_{i=lt,\,lpt,\,js} \mathcal{L}_i^{\mathrm{b}} \right)}{\sum_{j=\mathrm{b,\,c,\,uds}} w_j \left(\prod_{i=lt,\,lpt,\,js} \mathcal{L}_i^{j} \right)}. \tag{4.2}$$

The weight factors w_i can be used to account for the initial flavor composition of an analyzed data set. For events recorded at the Z-pole, it is known that the quark flavors occur approximately at rates $N_{\mathrm{b}} : N_{\mathrm{c}} : N_{\mathrm{uds}} \approx 1 : 1 : 3$, and weights $w_{\mathrm{b}} = w_{\mathrm{c}} = 0.2$, $w_{\mathrm{uds}} = 0.6$ can be used to further enhance the selection efficiency and purity of b-quarks. On the contrary, if the initial ratios are unknown or selected events come from a variety of processes, assuming different weights might bias the selection in an artificial way. The latter is the case for the analysis presented here, and all weights are set to unity consequently.

The b-tag likelihood and ANN selections have been trained and optimized using data taken at calibration runs with $\sqrt{\mathrm{s}} = m_{\mathrm{Z}}$ throughout the whole LepII phase. The energy scale of jets in $\mathrm{e^+e^-} \to \mathrm{q\bar{q}}$ events at $\sqrt{\mathrm{s}} = m_{\mathrm{Z}}$ is similar to that of jets from four-fermion events at LepII energies $\sqrt{\mathrm{s}} \sim 200\,\mathrm{GeV}$. The calibration at the Z-pole therefore can also be used for the analysis of LepII data.

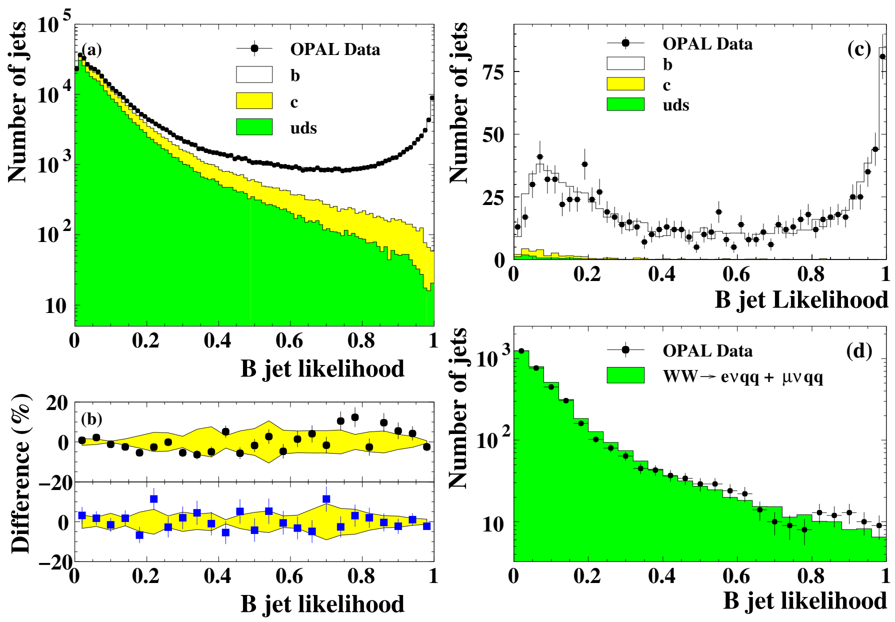

Figure 4.9: *Tests of the detector calibration through the* b*-tagging performance. a)-c) Are based on events recorded in calibration runs at* $\sqrt{\mathrm{s}} = m_{\mathrm{Z}}$*. The* b*-probability of all jets is shown in a). c) Includes only those jets, where the opposite jet is identified as a* b*-jet. Mainly* b*-jets enter the distribution, since* b*-quarks are produced pair-wise. In b), the difference of data and MC expectation is shown for jets opposite to anti-b-tagged jets (upper part) and jets opposite to b-tagged jets (lower part). This calibration is checked at* LEPII *energies, as shown in d), where jets from* W*-decays enter the distribution. Agreement between data and MC is good for all tests.*

Tests of the calibration based on data recorded in 1999 are presented in Fig. 4.9. In hadronic events at $\sqrt{s} = m_Z$, two jets are produced. Fig. 4.9 (a) shows the comparison of data and Standard Model MC for $\mathcal{B}$. If one jet in a two-jet event is tagged as b-jet, the same is expected for the second jet. This is shown in Fig. 4.9 (c), which displays the b-likelihood of jets opposite to b-tagged jets. Fig. 4.9 (b) shows the relative difference of data and MC for jets opposite to anti-b-tagged jets (upper part) and opposite to b-tagged jets (lower part). In both cases, the shaded region indicates the fluctuation expected from data statistics. Finally, few b-tagged jets are expected from W-decays, as is shown in Fig. 4.9 (d). Evaluations of all aspects on b-tagging show good agreement between data and MC [81].

4.4 Pre-Selection

A common pre-selection is used for both search channels. The aim of this part of the analysis is to reject significant amount of background events whilst retaining most of those from signal. The pre-selection is based on the following cuts, which are universal to all center-of-mass energies.

1. **Effective center-of-mass energy $\sqrt{s'}$**
   The effective center-of-mass energy $\sqrt{s'}$ (see Sec 4.3) is required to be larger than 82 % of the collision energy $\sqrt{s}$. This constraint is much tighter than $E_{vis} > 0.14\sqrt{s}$ from the multi hadron criteria and most efficiently rejects radiative return events, where initial state photon radiation lowers the effective center-of-mass energy to the Z-resonance.

2. **Durham jet parameter y_{43}**
   Events should be four jet like. This is tested by the Durham parameter y_{43}, which is evaluated during jet finding and is required to be larger than 0.003. The parameter y_{43} separates three- and four-jet like events and is introduced in App. A. Especially events from qq (γ) background are rejected by this criteria.

3. **Event shape parameter C**
   The event shape parameter C [82] is a measure for the sphericity of an event. It is defined as
   $$C = 3\,(e_1\,e_2 + e_2\,e_3 + e_3\,e_1)\,, \tag{4.3}$$
   where e_i are the eigenvalues of the normalized momentum tensor
   $$\Theta_{ij} = \frac{\sum_{a=1}^{N} p_i^a p_j^a / |\vec{p}^a|}{\sum_{a=1}^{N} |\vec{p}^a|}. \tag{4.4}$$
   Here, N denotes the number of particles in an event, and p_i^a is the i-th three momentum component of the a-th particle. C is required to be greater than 0.45, which further reduces contributions from qq (γ) events, where particles are not as evenly distributed in the detector as in events with four initial quarks.

4. **Number of tracks per jet N_{trk}**
   Each jet should comprise at least two tracks. This criterion aims at reducing four fermion events with leptons in the final state. Further on, it is a quality check for b-identification, since at least two tracks are needed to reconstruct a secondary vertex.

5. **Energy and momentum conservation 4C fit**
   A kinematic fit with four constraints is applied. For details on kinematic fits see App. B.

The constraints assume energy and momentum conservation, e.g. $\sum E_i = \sqrt{s}$ and $\sum \vec{p}_i = 0$. Here, E_i is the energy of the i-th jet, and $\vec{p}_i$ is its momentum. Events are required to yield a converged fit with a χ^2 probability larger than 10^{-5}.

6. **Jet configuration 5C fits**
Two further kinematic fits are applied to test whether the event topology is compatible with the expected signal processes. In $\pi_T^+\pi_T^-$ production, two jet pairs are expected to yield the same invariant masses, while in $\pi_T^\pm W^\mp$ one jet pair is expected to have $m_{jj} = m_W$. Both hypotheses are explored by kinematic fits with five constraints, of which four imply energy and momentum conservation and the fifth forces jets to obey the mass configuration. In $\pi_T^+\pi_T^-$ ($\pi_T^\pm W^\mp$), three (six) jet pair combinations are possible. The best fit χ^2 probabilities are $PROB(\chi^2_{\pi_T\pi_T})$ and $PROB(\chi^2_{\pi_T W})$ respectively. Events should be compatible with at least one of the mass hypotheses, thus requiring $\max(PROB(\chi^2_{\pi_T\pi_T}), PROB(\chi^2_{\pi_T W})) > 10^{-5}$.

The distributions of the respective variables are shown in Fig. 4.10 in consecutive order, i.e. only events passing one cut enter the distribution of the next. The distributions measured in data are displayed as dots with error bars indicating the statistical uncertainty. The contributions from background expectation are divided into three different categories:

- Contributions from two-quark background $e^+e^- \rightarrow q\bar{q}(\gamma)$ are displayed in green (medium shaded).

- Contributions from hadronic four-fermion final states $e^+e^- \rightarrow q\bar{q}\,q\bar{q}$ are displayed in yellow (light shaded). For $\sqrt{s} \geq 205\,\mathrm{GeV}$, no separate MC samples for hadronic final states are available. Thus, also semi-leptonic final states $e^+e^- \rightarrow \ell^+\ell^-\,q\bar{q}$ with $\ell \neq e$ enter this part of the distributions.

- Contributions from semi-leptonic final states $e^+e^- \rightarrow e^+e^-\,q\bar{q}$ and $\ell^+\ell^-\,q\bar{q}$ are displayed in blue (dark shaded). For $\sqrt{s} \geq 205\,\mathrm{GeV}$, the latter are not available as separate MC samples and enter the yellow (light shaded) distributions.

In addition, the contributions from hypothetical technipion signals are shown for $m_{\pi_T} = 80\,\mathrm{GeV}$ and a cross-section of 5 pb in each of the two production channels $e^+e^- \rightarrow \pi_T^+\pi_T^-$ and $e^+e^- \rightarrow \pi_T^\pm W^\mp$. The distributions shown are luminosity-weighted sums over the distributions arising from all eight center-of-mass energy ranges defined in Tab. 4.1.

The evolution of the event rate for data and background through the pre-selection is demonstrated in Tab. 4.3. The agreement of data and MC expectation is good at all selection steps. The contributions from two-quark and four-fermion background are also listed separately. Note, that contributions from all four-fermion final states are taken together, although they are labeled $q\bar{q}\,q\bar{q}$ after the dominant contribution at the end of the selection. Semi-leptonic four-fermion events are rejected to a negligible level, and they are not distinguished from those from hadronic four-fermion final states from here on.

In the last two columns, the effect of the pre-selection on the efficiency of the respective signal processes is listed. Events from $\pi_T^+\pi_T^-$ and $\pi_T^\pm W^\mp$ production pass the pre-selection with probabilities of 80 % and 54 %, respectively. The large difference of the two signal processes follows from leptonic W-decays in $\pi_T^\pm W^\mp$, which are characterized by missing energy through neutrinos. Only events with hadronic W-decays pass the cut on the effective center-of-mass energy $\sqrt{s'}$.

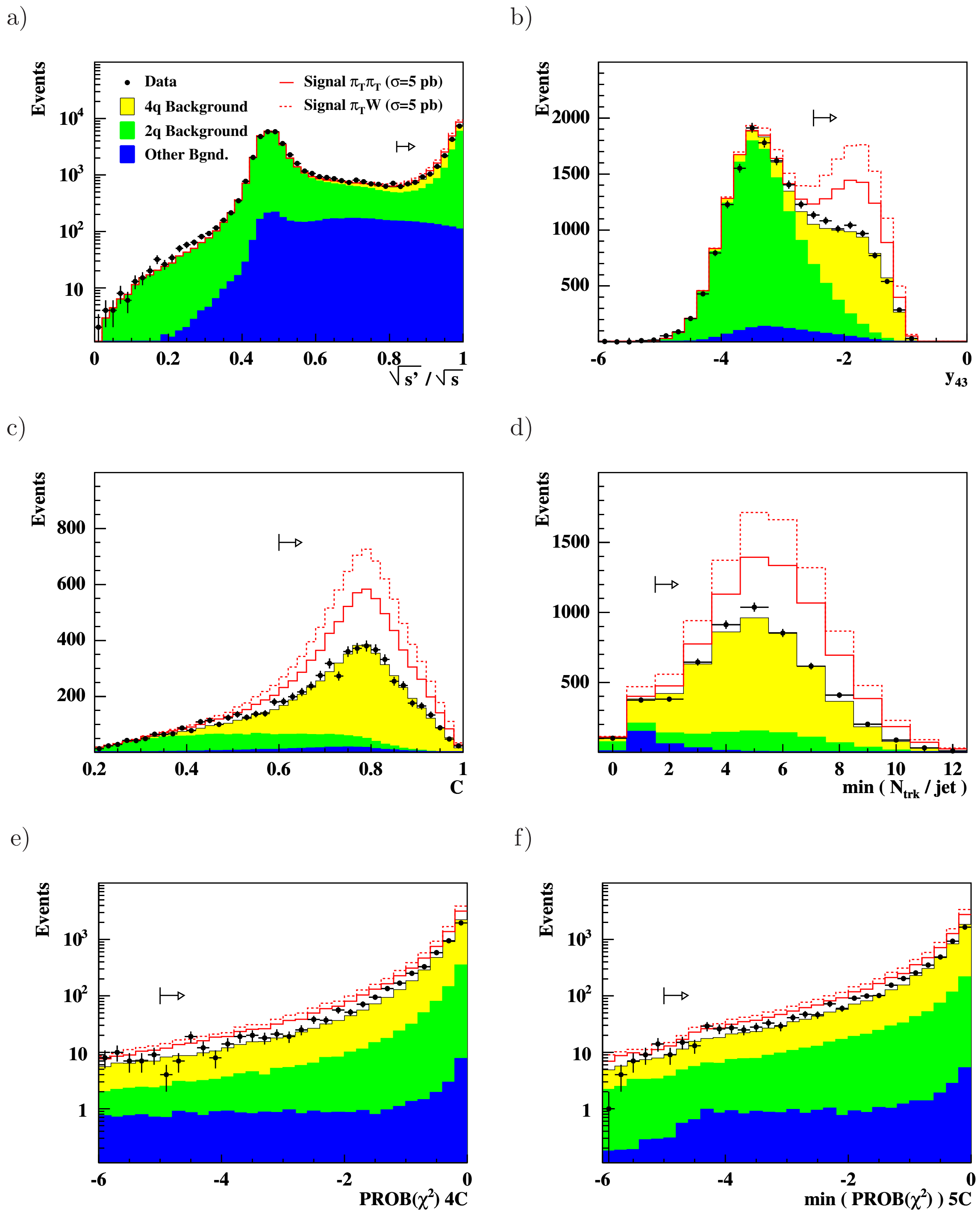

Figure 4.10: *Distributions of the cutflow variables in consecutive order. Cuts indicated by arrows and the different contributions shown are explained in the text.*

	Cut	Data	Background			Signal $m_{\pi_T} = 80\,\mathrm{GeV}$	
			Total	$\mathrm{q\bar{q}\,q\bar{q}}$	$\mathrm{q\bar{q}}\,(\gamma)$	$\pi_T^+\,\pi_T^-$	$\pi_T^\pm\,\mathrm{W}^\mp$
	MHS	19 200	19 064	6 682	12 383	0.977	0.776
1.	$\sqrt{s'}$	6 387	6 2278	4 717	1 511	0.853	0.606
2.	y_{43}	5 646	5 505	4 555	950	0.840	0.594
3.	C_{par}	5 662	5 505	4 555	950	0.840	0.594
4.	N_{trk}	5 187	5 017	4 189	827	0.832	0.572
5.	4C fit	4 909	4 744	3 972	772	0.813	0.550
6.	5C fits	4 813	4 652	3 921	732	0.802	0.542

Table 4.3: *Evolution of the event rate from data and background, starting from events selected by the* OPAL *multi-hadron selection (MHS). Note, that the background contribution from* $\mathrm{q\bar{q}\,q\bar{q}}$ *also includes admixtures from semi-leptonic final states* $\ell^+\ell^-\,\mathrm{q\bar{q}}$, $\ell = \mathrm{e}, \mu, \tau$*, which are negligible at the end of the pre-selection. The last two columns show the effect on the signal selection efficiency for the respective channels. Event samples from* $\pi_T^\pm \mathrm{W}^\mp$ *signal include also* $\mathrm{W} \to \ell\nu$ *decays, which are not selected. Thus, the selection efficiency is lower in this channel w.r.t. the one from* $\pi_T^+\pi_T^-$ *production.*

4.5 Likelihood Selections

After pre-selection, a set of likelihood selections (see App. C) is used for a better separation of signal and background events. Also, a separation between the two signal channels is achieved. Likelihood selections used are:

- **the $\pi_T^+\pi_T^-$ likelihood $\mathcal{L}_{\pi_T\pi_T}$**, which distinguishes $\mathrm{e^+e^-} \to \pi_T^+\pi_T^-$ signal from two and four fermion background;
- **the $\pi_T^\pm \mathrm{W}^\mp$ likelihood $\mathcal{L}_{\pi_T \mathrm{W}}$**, which distinguishes $\mathrm{e^+e^-} \to \pi_T^\pm \mathrm{W}^\mp$ signal from two and four fermion background; and
- **the separating likelihood $\mathcal{L}_{sep}$**, which distinguishes the two signal processes from background by combining the output values of $\mathcal{L}_{\pi_T\pi_T}$ and $\mathcal{L}_{\pi_T \mathrm{W}}$.

The general design, i.e. the event classes and input variables, of the likelihoods $\mathcal{L}_{\pi_T\pi_T}$ and $\mathcal{L}_{\pi_T \mathrm{W}}$ is adopted from a previous analysis at OPAL [48], where the two channels are analyzed separately. The general idea of that analysis is shown in Fig. 4.11 a). After pre-selection (not shown), the likelihood selections $\mathcal{L}_{\pi_T\pi_T}$ and $\mathcal{L}_{\pi_T \mathrm{W}}$ are used to further distinguish background and signal from $\mathrm{e^+e^-} \to \pi_T^+\pi_T^-$ and $\mathrm{e^+e^-} \to \pi_T^\pm \mathrm{W}^\mp$, respectively. Background is rejected by two cuts on the corresponding likelihood output values, and distributions of the reconstructed technipion mass are formed. Since both signal channels are relatively close in their signatures, these distributions have a significant overlap in data and background events, indicated by the circles in Fig. 4.11 a). Therefore, only separate limits for each channel can be calculated (for details on limit calculation and model exclusion see Sec. 4.7).

With this approach, only model points are excluded, where at least one signal channel is excluded from data. More exclusion power is expected, if both channels could be combined coherently. In this case, model points are excluded from the combined limit, which can even be possible if both channels cannot be excluded separately. Of course, a combination is only sensible, if both signal channels are kinematically possible. This is the case for technipion masses $m_{\pi_T} < \sqrt{s}/2$, while for $m_{\pi_T} = \sqrt{s}/2 ... \sqrt{s} - m_\mathrm{W}$ only $\mathrm{e^+e^-} \to \pi_T^\pm \mathrm{W}^\mp$ is possible.

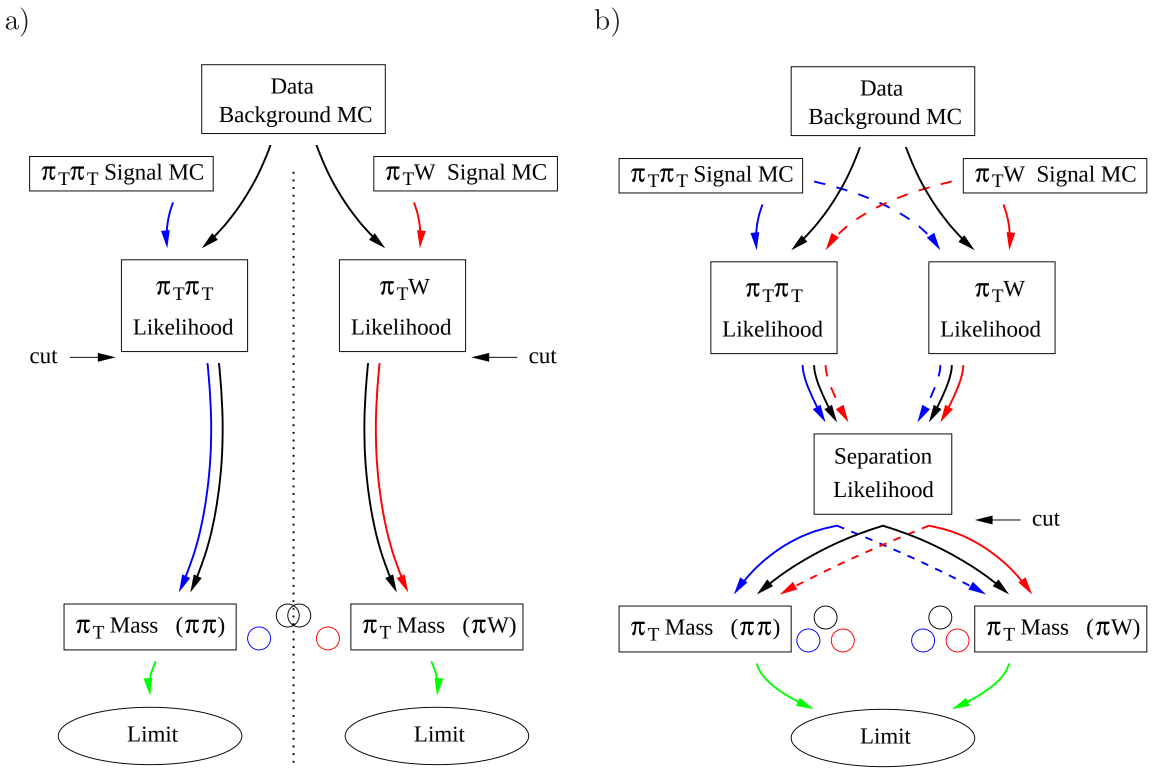

Figure 4.11: *Schematic view on a) separate analyses for the two signal channels and b) the combined approach of this analysis. See the text for more details.*

$\sqrt{s}$ [GeV]	m_{sep} [GeV]	m_{max} [GeV]
189	94.5	108.5
192	96.0	111.5
196	98.0	115.5
200	100.0	119.5
202	101.0	121.5
205	102.5	124.5
207	103.5	126.5
208	104.0	127.5

Table 4.4: *Technipion pair production* $e^+e^- \to \pi_T^+\pi_T^-$ *is only possible for* $m_{\pi_T} < m_{sep} = \sqrt{s}/2$, *while technipion production in* $\pi_T^\pm W^\mp$ *is possible up to* $m_{\pi_T} < m_{max} = \sqrt{s} - m_H$. *The table lists the respective values for the eight bins in* $\sqrt{s}$ *of this analysis.*

Fig. 4.11 b) shows the scheme of the combined analysis. Separation between signal and background events is based on the same likelihood selections as used for the separate analyses. On the basis of the likelihood output values, a decision is made for each event, whether it is interpreted as $e^+e^- \to \pi_T^+\pi_T^-$ or $e^+e^- \to \pi_T^\pm W^\mp$ candidate, respectively. This is accomplished by the separation likelihood $\mathcal{L}_{sep}$, which is also used to reject background events. In addition, cross talk between the signal channels is allowed, indicated by dashed arrows. The resulting technipion mass distributions thus contain contributions from both signal channels. Since every event is present exclusively in one of the distributions, these are independent and can be used to calculate a combined limit.

The threshold mass $m_{sep} = \sqrt{s}/2$, up to which both channel are kinematically allowed, is listed in Tab. 4.4 for all bins in the center-of-mass energy defined in Tab. 4.1. A complete set of independent technipion mass distributions is obtained by analyzing each bin in the center-of-mass energy separately. For technipion masses $m_{\pi_T} < m_{sep}(\sqrt{s})$, two independent distributions are formed after the selection likelihood $\mathcal{L}_{sep}$, as is described in Sec. 4.5.3. For technipion masses $m_{\pi_T} = \sqrt{s}/2...\sqrt{s} - m_W$, the technipion mass distribution is formed directly after the $\pi_T^\pm W^\mp$ likelihood $\mathcal{L}_{\pi_T W}$, as described in Sec. 4.5.2.

In the following, the three likelihood selections $\mathcal{L}_{\pi_T\pi_T}$, $\mathcal{L}_{\pi_T W}$ and $\mathcal{L}_{sep}$ will be introduced.

4.5.1 $\pi_T^+\pi_T^-$ Likelihood $\mathcal{L}_{\pi_T\pi_T}$

The $\pi_T^+\pi_T^-$ likelihood $\mathcal{L}_{\pi_T\pi_T}$ is designed to separate events from $\pi_T^+\pi_T^-$ production from the two classes of background events left after pre-selection. It considers three event classes:

- Four-quark background $e^+e^- \to q\bar{q}\,q\bar{q}$,
- two-quark background $e^+e^- \to q\bar{q}\,(\gamma)$, and
- signal from technipion pair production $e^+e^- \to \pi_T^+\pi_T^- \to b\bar{q}\,q\bar{b}$.

Jets are paired according to a 5C kinematic fit, of which four imply energy and momentum conservation. The fifth constraint requires two jet pairs to have the same invariant mass. Three combinations are possible, and the one with the best χ^2 probability is retained. If the fit fails, i.e. the best χ^2 probability is less than 10^{-5}, an event is assumed to be incompatible with $\pi_T^+\pi_T^-$ production. However, these events are not rejected, since they still can be compatible with the second technipion production process $e^+e^- \to \pi_T^\pm W^\mp$. Therefore, these events are assigned a value $\mathcal{L}_{\pi_T\pi_T} = -1$, but retained.

For all other events, the likelihood $\mathcal{L}_{\pi_T\pi_T}$ is calculated from the following six input variables:

1. The product of di-jet charge and cosine of di-jet production angle, $Q_{\mathrm{di-jet}} \times \cos\theta_{\mathrm{di-jet}}$. The di-jet charge is set to $+1\,(-1)$ for the di-jet with the higher (lower) sum of momentum weighted jet charges, where the momentum weighted jet charge Q_j for jet j is defined as
$$Q_j = \frac{\sum_{i=1}^{N} q^i \sqrt{p_L^i}}{\sum_{i=1}^{N} \sqrt{p_L^i}}. \tag{4.5}$$
$i = 1...N$ is an index over the particles in the jet, which have electric charge q^i and longitudinal momentum p_L^i with respect to the jet axis. $Q_{\mathrm{di-jet}} \times \cos\theta_{\mathrm{di-jet}}$ is strongly correlated with the decay axis of the two technipions in signal events.

2. The cosine of the polar angle of the thrust axis, $\cos\theta_{\mathrm{thrust}}$. If the sum over longitudinal momentum over all particles with respect to a direction $\vec{n}$ is calculated, the thrust axis is defined as the direction which maximizes this sum. For small technipion masses, where the technipions have a large boost, the thrust axis is correlated with the direction of the intermediate technipions and thus with $Q_{\mathrm{di-jet}} \times \cos\theta_{\mathrm{di-jet}}$. This correlation vanishes for technipions close to the kinematic limit, which have only small boost (see also Fig. 4.12).

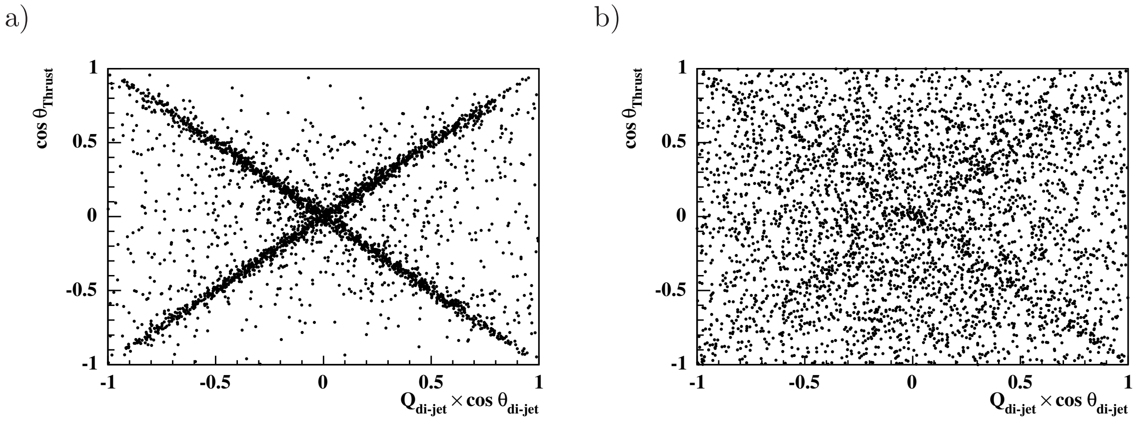

Figure 4.12: *Correlation between $Q_{\mathrm{di-jet}} \times \cos\theta_{\mathrm{di-jet}}$ and $\cos\theta_{\mathrm{thrust}}$ is large for small technipion masses, while it vanishes for masses close to the kinematic limit. Shown are the correlation for a) $m_{\pi_{\mathrm{T}}} = 50\,\mathrm{GeV}$ and b) $m_{\pi_{\mathrm{T}}} = 100\,\mathrm{GeV}$ at $\sqrt{\mathrm{s}} = 200\,\mathrm{GeV}$.*

3. The cosine of the smallest angle between any two jets, $\cos\alpha_{min}$. When two-quark events are forced to four jets, at at least two jets are expected to be very close together. Jets in signal events and in events from four-quark background are well separated.

4. The largest energy difference of any two jets, $E_{max} - E_{min}$. This cut also aims at separating two-quark background, where the difference in jet energies is expected to be much larger than for signal or four-quark background.

5. The b-likelihood of the more energetic of the two jets with the highest b-likelihood, $\mathcal{B}_1$. Two jets with high b-probability are expected in signal events, while events from background mainly comprise light quarks only. Energy ordering of $\mathcal{B}_1$ and $\mathcal{B}_2$ minimizes the correlation among the two values.

6. The b-likelihood of the less energetic of the two jets with the highest b-likelihood, $\mathcal{B}_2$.

The distributions of the likelihood input parameters from data events and background expectation are shown in Fig. 4.13. Also shown are the distributions from a hypothetical signal with $m_{\pi_{\mathrm{T}}} = 80\,\mathrm{GeV}$ and a cross-section of 5 pb. Distributions shown are luminosity-weighted sums over all bins in the center-of-mass energy as listed in Tab. 4.1. However, the likelihood is evaluated with independent reference distributions for each center-of-mass energy separately. To avoid a dependence on the unknown technipion mass, reference distributions for the $\pi_{\mathrm{T}}^{+}\pi_{\mathrm{T}}^{-}$ event class are averaged over all generated MC samples for each center-of-mass energies. The respective technipion masses are listed in Tab. 4.2.

As can be seen, data is well described by the expectation from background. Small deviations, which are observed for instance for $\cos\alpha = 0.4...0.7$ are treated as systematic uncertainty. Details on the method are given in Sec. 4.6.

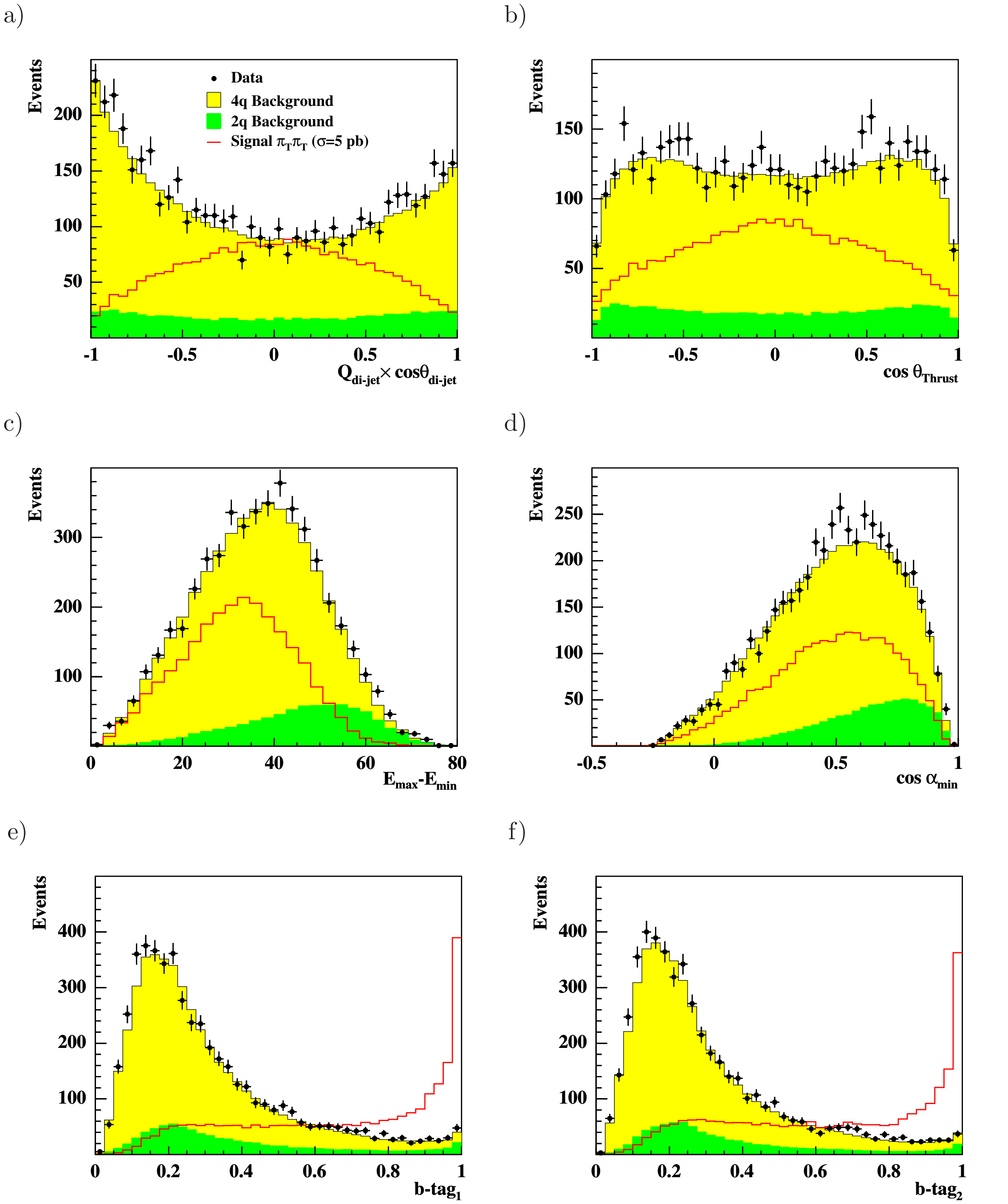

Figure 4.13: *Distributions of the input variables for the $\pi_T^+\pi_T^-$ likelihood $\mathcal{L}_{\pi_T\pi_T}$. Details are given in the text.*

The power of the likelihood to separate the three event classes depends on the difference in shape of the input variable distributions from the respective processes. The main sensitivity of the signal likelihood arises from the two b-tagging variables $\mathcal{B}_1$ and $\mathcal{B}_2$.

The distribution of the likelihood $\mathcal{L}_{\pi_T\pi_T}$ is shown in Fig. 4.14. The plot shows again a luminosity-weighted sum over distributions from all center-of-mass energies and includes a hypothetical $\pi_T^+\pi_T^-$ signal with $m_{\pi_T} = 80\,\mathrm{GeV}$ and $\sigma = 1\,\mathrm{pb}$. Events in the underflow bin with $\mathcal{L}_{\pi_T\pi_T} < 0$ are those which were found to be incompatible with $\pi_T^+\pi_T^-$ production during jet pairing. However, these events can be good candidates for $\pi_T^\pm W^\mp$ production and thus are not rejected completely.

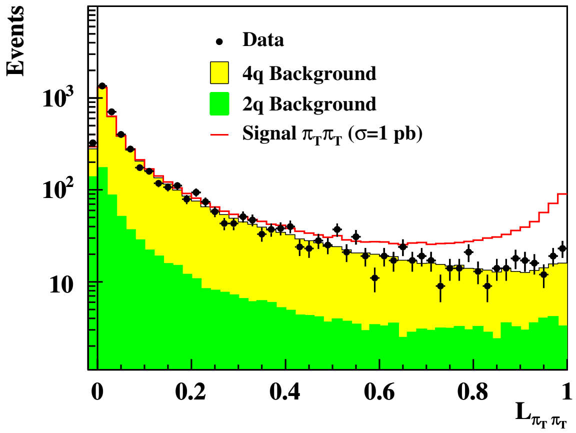

Figure 4.14: *Distribution of the $\pi_T^+\pi_T^-$ likelihood $\mathcal{L}_{\pi_T\pi_T}$. Events in the underflow-bin are not compatible with $\pi_T^+\pi_T^-$ production, but may be good candidates for $\pi_T^\pm W^\mp$.*

4.5.2 $\pi_T^\pm W^\mp$ Likelihood $\mathcal{L}_{\pi_T W}$

The likelihood $\mathcal{L}_{\pi_T W}$ aims at separation between $\pi_T^\pm W^\mp$ signal and the two classes of background events left after pre-selection. Like the $\pi_T^+\pi_T^-$ likelihood, three classes of events are defined:

- Four-quark background $e^+e^- \to q\bar{q}\,q\bar{q}$,
- two-quark background $e^+e^- \to q\bar{q}\,(\gamma)$, and
- signal from technipion production in $e^+e^- \to \pi_T^\pm W^\mp \to b\bar{q}\,q\bar{q}$.

Jet pairing is accomplished by the jet-combination likelihood $\mathcal{L}_{comb}$, which takes two input parameters:

1. The best χ^2 probability of a kinematic fit with five constraints, $PROB(\chi^2)$. Four of the constraints imply energy and momentum conservation and the fifth requires one jet-pair to be compatible with a W-boson, i.e. to have invariant mass of m_W. Six combinations are possible.

2. The flavor content, described by the parameter $\mathcal{F}$. The two jets assigned to the W-boson are expected to have a low b-probability. From the other two jets, interpreted as π_T, one

high and one medium or low b-probability is assumed. This is reflected in the definitions

$$\mathcal{F} = \max(\mathcal{B}_{j_3}, \mathcal{B}_{j_4})\ \overline{\min(\mathcal{B}_{j_3}, \mathcal{B}_{j_4})}\ \overline{\mathcal{B}_{j_1}}\ \overline{\mathcal{B}_{j_2}} \tag{4.6}$$

$$= \max(\mathcal{B}_{j_3}, \mathcal{B}_{j_4})\ (1 - \min(\mathcal{B}_{j_3}, \mathcal{B}_{j_4}))\ (1 - \mathcal{B}_{j_1})\ (1 - \mathcal{B}_{j_1}), \tag{4.7}$$

where j_1 and j_2 are the two jets assigned to the W-boson.

The probability density functions (p.d.f.) of both variables are shown in Fig. 4.15 for the right and wrong jet pair combinations, respectively. As can be seen, also the wrong combination tend to have a high χ^2 probability. Since five wrong combinations arise from the pairing logic, the efficiency to choose the right combination by $PROB(\chi^2)$ only is small. Therefore, the jet-pairing is decided according to the highest value of the combination likelihood $\mathcal{L}_{comb}$ instead.

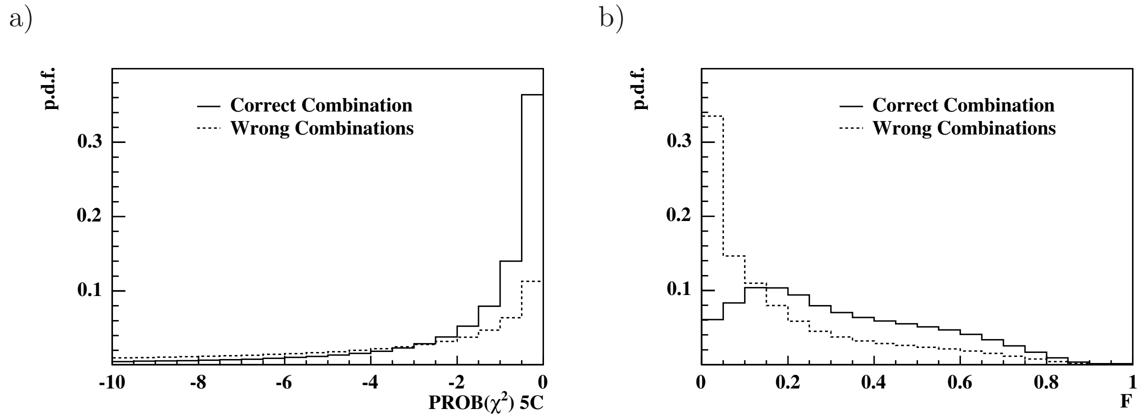

Figure 4.15: *The probability density functions (p.d.f.) of the input variables to the jet-combination likelihood $\mathcal{L}_{comb}$. The definition of $\mathcal{F}$ is given in the text.*

Although the highest $PROB(\chi^2)$ value does not necessarily arise from the correct jet-pair combination, the correct combination is expected to have a not too small χ^2 probability. Events with $PROB(\chi^2) < 10^{-5}$ for the pairing with the highest value for the combination likelihood $\mathcal{L}_{comb}$ are assumed to be incompatible with $\pi_T^{\pm}W^{\mp}$ production. Since these events can still be compatible with $\pi_T^{+}\pi_T^{-}$-production, they are not rejected, but the $\pi_T^{\pm}W^{\mp}$ likelihood $\mathcal{L}_{\pi_T W}$ is set to -1.

For all events with $PROB(\chi^2) > 10^{-5}$ for the combination with the highest value of $\mathcal{L}_{comb}$, the $\pi_T^{\pm}W^{\mp}$ likelihood is evaluated based on the following four input variables:

1. The product of di-jet charge and cosine of di-jet production angle, $Q_{\mathrm{di-jet}} \times \cos\theta_{\mathrm{di-jet}}$. The variable is defined as for $\mathcal{L}_{\pi_T\pi_T}$, but evaluated for the di-jet combination obtained from $\mathcal{L}_{Comb}$.

2. The cosine of the polar angle of the thrust axis, $\cos\theta_{\mathrm{thrust}}$.

3. The matrix element for WW pair production, calculated from the measured jet-momenta. The difference between $\pi_T^{\pm}W^{\mp}$ and WW is small, especially if $m_{\pi_T} \approx m_W$. However, some separation from two-quark background is achieved.

4. The highest b-probability from the two jets assigned to the technipion.

The distribution for the likelihood input variables for data and background expectation are shown in Fig. 4.16 together with a hypothetical signal from $\pi_{\mathrm{T}}^{\pm}\mathrm{W}^{\mp}$ production with $m_{\pi_{\mathrm{T}}} = 80\,\mathrm{GeV}$ and a cross-section of 5 pb. The plots show the luminosity-weighted sum over all bins of the center-of-mass energies. The likelihood however is evaluated for each of the eight energy bins of Tab. 4.1 separately. The reference distributions for the $\pi_{\mathrm{T}}^{\pm}\mathrm{W}^{\mp}$ signal class are averaged over all technipion masses available.

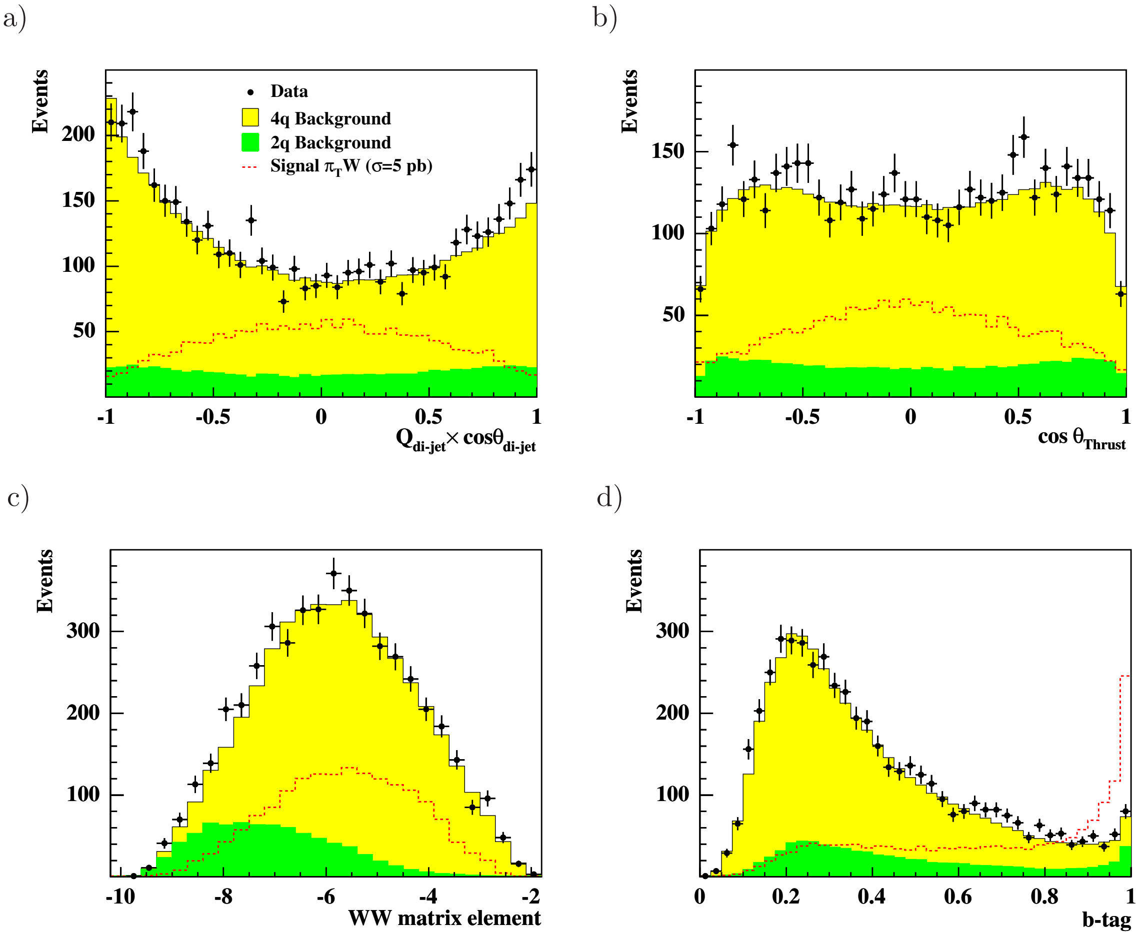

Figure 4.16: *Distributions of the input variables of the $\pi_{\mathrm{T}}^{\pm}\mathrm{W}^{\mp}$ likelihood $\mathcal{L}_{\pi_{\mathrm{T}}\mathrm{W}}$. Details are given in the text.*

The distributions of the likelihood output $\mathcal{L}_{\pi_{\mathrm{T}}\mathrm{W}}$ are shown in Fig. 4.17 a) for data and background MC, respectively. Also shown is a hypothetical signal from $\pi_{\mathrm{T}}^{\pm}\mathrm{W}^{\mp}$ production with $m_{\pi_{\mathrm{T}}} = 80\,\mathrm{GeV}$ and a cross-section of 1 pb. The plot shows the luminosity-weighted sum over the distributions obtained separately for all bins in the center-of-mass energy.

The separation between the three likelihood classes is not as good as for the $\pi_{\mathrm{T}}^{+}\pi_{\mathrm{T}}^{-}$ likelihood described in the previous section. The main sensitivity arises again from the b-tagging variable. However, only one b-jet is expected in events from $\pi_{\mathrm{T}}^{\pm}\mathrm{W}^{\mp}$ signal and the probability that of one jet from a light quark in background events yields a high value for $\mathcal{B}$ is not negligible.

For technipions with masses between the beam energy $m_{\pi_{\mathrm{T}}} = \sqrt{\mathrm{s}}/2$ and the kinematic threshold $m_{\pi_{\mathrm{T}}} = \sqrt{\mathrm{s}} - m_{\mathrm{W}}$, technipion pair production $\mathrm{e}^{+}\mathrm{e}^{-} \rightarrow \pi_{\mathrm{T}}^{+}\pi_{\mathrm{T}}^{-}$ is forbidden, while $\pi_{\mathrm{T}}^{\pm}\mathrm{W}^{\mp}$ production is still possible. A combination of both channels for limit calculation in this case is senseless and a mass distribution for limit calculation is formed directly.

a) b)

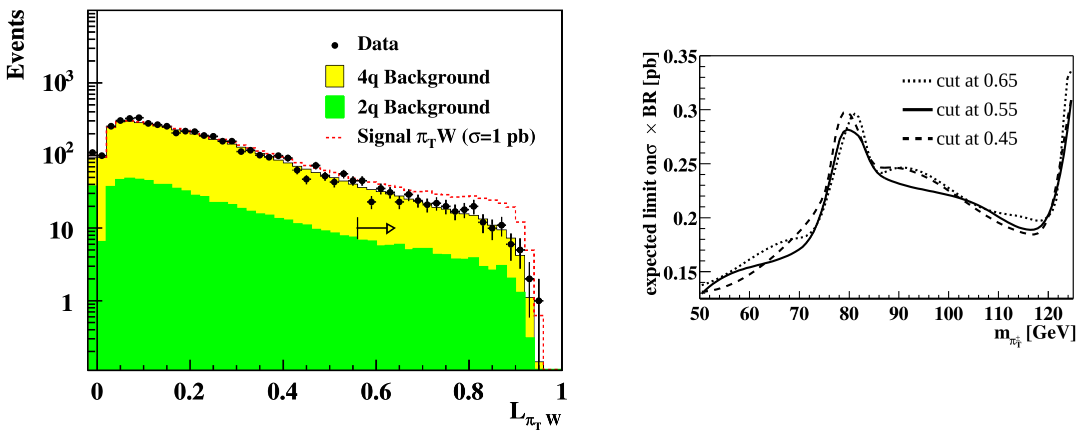

Figure 4.17: *Distribution of the $\pi_T^\pm W^\mp$ likelihood $\mathcal{L}_{\pi_T\pi_T}$. Events in the underflow-bin are not compatible with $\pi_T^\pm W^\mp$ production, but may be good candidates for $\pi_T^+\pi_T^-$. Events for $\mathcal{L}_{\pi_T\pi_T} > 0.55$ (indicated by the arrow) are selected. The cut on the likelihood has been optimized w.r.t. the expected cross-section exclusion, which is shown in b). (Fig. b) From [48])*

The technipion mass is calculated according to the jet-pairing described at the beginning of this section from the jet momenta after the 4C kinematic fit. Forcing the jets to obey known boundary conditions improves the mass resolution with respect to mass calculation from the measured jet momenta.

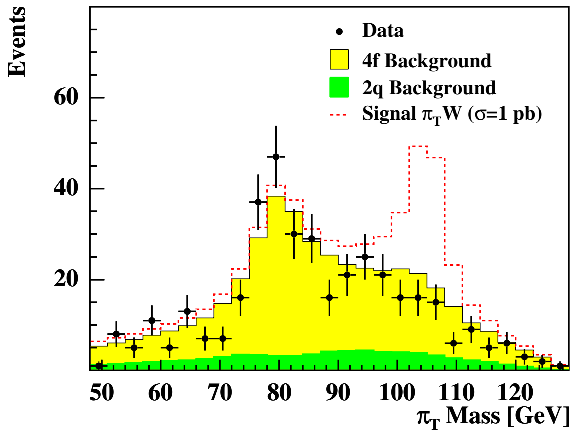

Figure 4.18: *Reconstructed technipion mass distribution after the $\pi_T^\pm W^\mp$ likelihood from events with $\mathcal{L}_{\pi_T W} > 0.55$. This distribution is used for calculation of confidence levels and exclusion limits at model points with $m_{\pi_T} = \sqrt{s}/2 ... \sqrt{s} - m_W$.*

Only events with $\mathcal{L}_{\pi_T W}$ above a certain likelihood cut are considered, as indicated by the arrow in Fig. 4.17 a). The value of this cut has been optimized in to yield best cross-section exclusion potential. Details on the calculation of confidence levels and exclusion limits are discussed in Sec. 4.7.1. The expected limit on the product of cross-section $e^+e^- \to \pi_T^\pm W^\mp \to q\bar{q}q\bar{q}$ is shown in Fig. 4.17 b) for different values of the likelihood cut (from [48]). Best exclusion potential is achieved with a likelihood cut $\mathcal{L}_{\pi_T W} > 0.55$.

The technipion mass distribution after the likelihood cut is shown in Fig. 4.18. Besides data and expectations from background, a hypothetical signal from $\pi_T^{\pm}W^{\mp}$ production with $m_{\pi_T} = 105\,\mathrm{GeV}$ and $\sigma = 1\mathrm{pb}$ is included. The plot shows a luminosity weighted sum over all energy bins. The number of events observed in data and expected from background is listed in Tab. 4.5 for each bin in the center-of-mass energy separately. In no case, a significant excess in data over the expected background is observed.

$\sqrt{s}$ [GeV]	Data	Background Total	$q\bar{q}\,q\bar{q}$	$q\bar{q}(\gamma)$
189	123	106.4	80.5	25.9
192	23	17.8	14.2	3.6
196	46	47.9	38.2	9.7
200	37	47.1	37.9	9.2
202	26	24.4	19.8	4.6
205	59	49.7	40.6	9.1
207	68	73.0	59.2	13.8
208	6	4.8	3.9	0.9
Total	388	371.1	294.3	76.8

Table 4.5: *The number of events selected after a cut $\mathcal{L}_{\pi_T W} > 0.55$, broken up by the center-of-mass energy. No significant excess in data over the expectation from SM background is observed at any energy.*

The selection efficiency for events from $\pi_T^{\pm}W^{\mp}$ signal depends on the mass hypothesis of the technipions, as shown in Fig. 4.19 as luminosity-weighted sum over all center-of-mass energies. For the calculation of confidence levels, the contributions from different energies are studied separately, however. The distribution is interpolated with a spline. This allows the determination of the selection efficiency for mass hypothesis, where no MC is available, and the influence of statistical fluctuations is minimized for mass hypotheses, where MC samples have been generated.

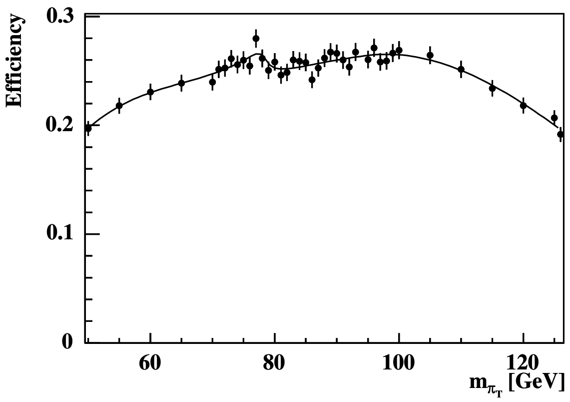

Figure 4.19: *The selection efficiency for signal events with $\mathcal{L}_{\pi_T W} > 0.55$ as a function of the technipion mass m_{π_T}. The distribution is interpolated with a spline.*

4.5.3 Event Classification Likelihood $\mathcal{L}_{sep}$

The separation likelihood $\mathcal{L}_{sep}$ aims at distinguishing $\pi_T^+\pi_T^-$-like and $\pi_T^\pm W^\mp$-like events from background and from each other. Therefore, it is designed with the following three event classes:

- technipion pair production $e^+e^- \to \pi_T^+\pi_T^-$,
- technipion production in $e^+e^- \to \pi_T^\pm W^\mp$, and
- any background contribution.

It combines the output values of the two likelihoods $\mathcal{L}_{\pi_T\pi_T}$ and $\mathcal{L}_{\pi_T W}$. The corresponding probability densities, shown in Fig. 4.20, serve as reference distributions. As for the previous likelihood selections, distributions for TC signal are averaged over all technipion masses, where MC samples are available. The plots show the luminosity-weighted sum of the distributions from all center-of-mass energies listed in Tab. 4.1. For the limit calculation, all center-of-mass energies are analyzed separately, however.

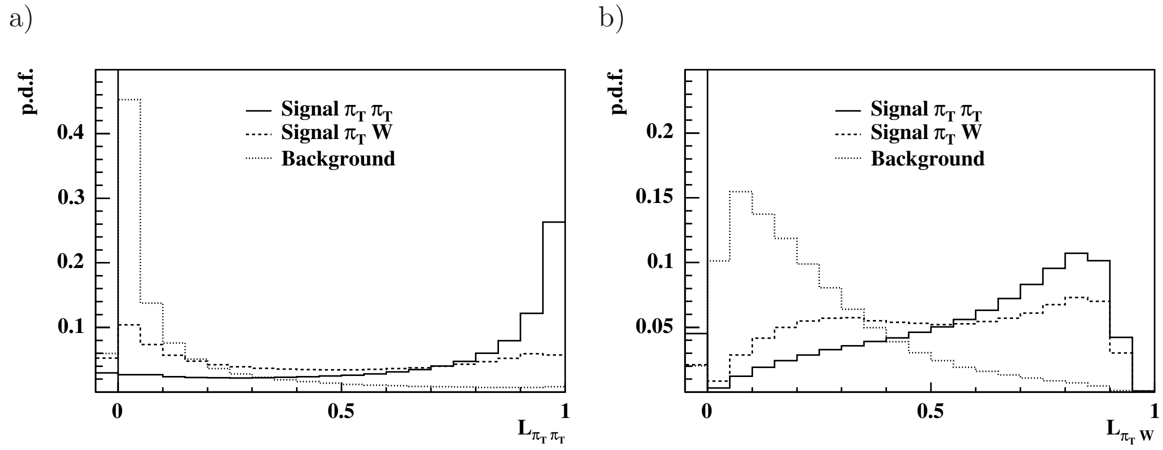

Figure 4.20: *The probability density functions (p.d.f.) of a) the $\pi_T^+\pi_T^-$ likelihood $\mathcal{L}_{\pi_T\pi_T}$ and b) the $\pi_T^\pm W^\mp$ likelihood $\mathcal{L}_{\pi_T W}$ for events from background and the two signal channels, respectively. Both variables serve as input to the event classification likelihood $\mathcal{L}_{sep}$.*

The likelihood is evaluated with respect to the two signal hypotheses, and the output values are denoted as $\mathcal{L}_{sep}^{\pi_T\pi_T}$ and $\mathcal{L}_{sep}^{\pi_T W}$ respectively. Both values are strongly correlated, as shown in Fig. 4.21, which is another indication for the fact, that the two signal channels are similar to a large extent. Events of all classes accumulate along a banana shape, where $\mathcal{L}_{sep}^{\pi_T\pi_T}$ ranges from zero to one, while $\mathcal{L}_{sep}^{\pi_T W}$ has a maximum of about 0.6. This shows that identification of $\pi_T^+\pi_T^-$ events is much better than that of $\pi_T^\pm W^\mp$. Background events cluster at $\left[\mathcal{L}_{sep}^{\pi_T\pi_T}, \mathcal{L}_{sep}^{\pi_T W}\right] = [0, 0]$, while signal events align along $\mathcal{L}_{sep}^{\pi_T\pi_T} + \mathcal{L}_{sep}^{\pi_T W} \approx 1$. Two variables are defined from the output, which are the projections to diagonal lines with positive and negative gradient in the $\mathcal{L}_{\pi_T\pi_T} - \mathcal{L}_{\pi_T W}$ plain, respectively:

$$\mathcal{S}^\Sigma = \mathcal{L}_{sep}^{\pi_T\pi_T} + \mathcal{L}_{sep}^{\pi_T W} = 1 - \mathcal{L}_{sep}^{B} \qquad \text{and} \qquad \mathcal{S}^\Delta = \mathcal{L}_{sep}^{\pi_T\pi_T} - \mathcal{L}_{sep}^{\pi_T W}. \tag{4.8}$$

The distributions of both variables for data and background are depicted in Fig. 4.22 together with hypothetical signals from both technipion production channels with $m_{\pi_T} = 80\,\text{GeV}$ and

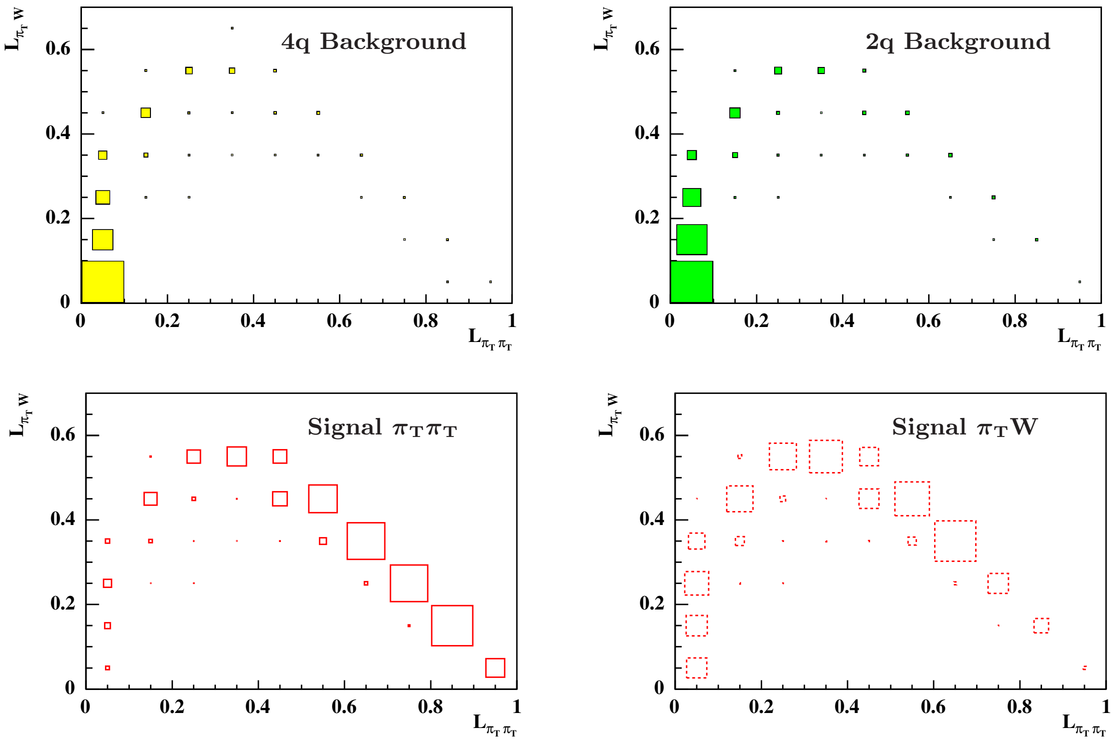

Figure 4.21: *The event classification likelihood $\mathcal{L}_{sep}$ is evaluated with respect to the both signal event classes separately. Both values are correlated.*

$\sigma = 1\,\mathrm{pb}$ each. The figure shows the luminosity-weighted sum over distributions from all center-of-mass energies, while for the analysis separate distributions are used.

The variable $\mathcal{S}^{\Sigma}$ describes the likelihood not to belong to the background event class, which is low for events from all background sources and high for events from both signal channels. Separation of signal and background is accomplished by a cut $\mathcal{S}^{\Sigma} > 0.9$.

a) b)

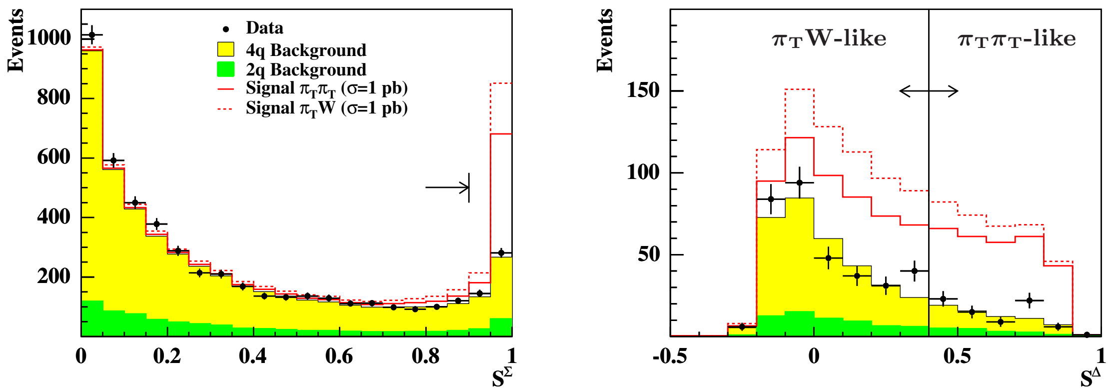

Figure 4.22: *Distributions for a) the sum $\mathcal{S}^{\Sigma}$ and b) the difference $\mathcal{S}^{\Delta}$ of the likelihood $\mathcal{L}_{sep}$ w.r.t. the two signal classes. A cut on $\mathcal{S}^{\Sigma} > 0.9$ is used for separation of signal and background. Events passing this cut are interpreted as $\pi_T^{+}\pi_T^{-}$ ($\pi_T^{\pm}W^{\mp}$) candidate, if they have $\mathcal{S}^{\Delta} > 0.4\,(< 0.4)$. The respective cuts are indicated by arrows.*

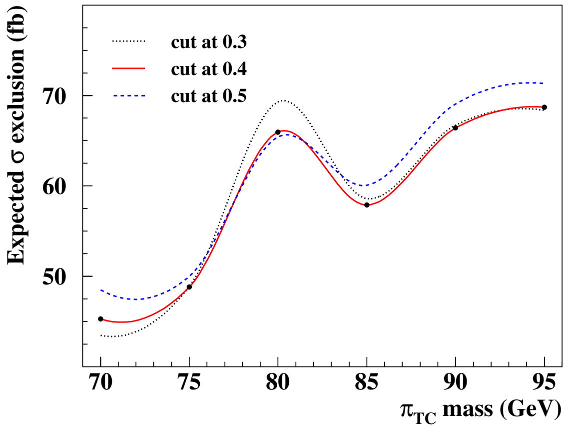

Figure 4.23: *The value of the separation parameter $\mathcal{S}^{\Delta}$ is fixed to optimize the expected cross-section exclusion for technipion pair production* $e^+e^- \rightarrow \pi_T^+\pi_T^-$*, which is the more sensitive of the two signal channels.*

The variable $\mathcal{S}^{\Delta}$ is used to classify the events as $\pi_T^+\pi_T^-$ or $\pi_T^{\pm}W^{\mp}$ candidate, respectively. The value of the transition threshold is optimized by the expected cross-section exclusion for $e^+e^- \rightarrow \pi_T^+\pi_T^-$ (on details about the procedure of cross-section limit calculation see Sec. 4.7.1). As discussed above, this is the more sensitive signal process. The expected cross-section limit at 95 % confidence level is shown in Fig. 4.23. If the hypothetical mass of the technipion is in the range of m_W or m_Z, the background contribution is higher and the cross-section exclusion worse. A soft separation cut of $\mathcal{S}^{\Delta} = 0.3$ yields good sensitivity for mass regions with low background expectation, while a hard cut $\mathcal{S}^{\Delta} = 0.5$ yields a better limit if the background contribution is relatively high. An intermediate value $\mathcal{S}^{\Delta} = 0.4$ combines both characteristics and yields optimal cross-section exclusion over a wide range of technipion masses.

a)

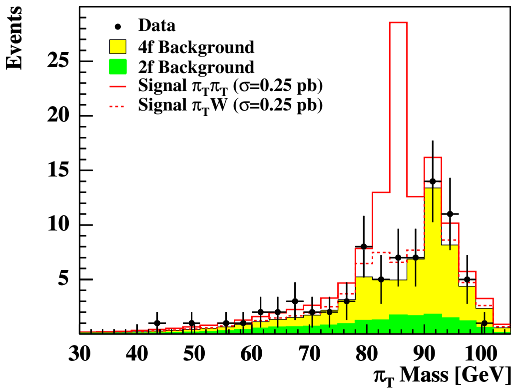

b)

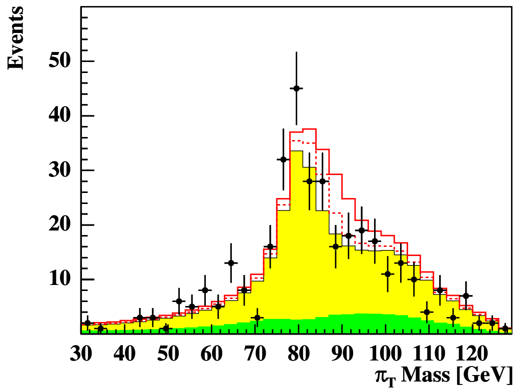

Figure 4.24: *Reconstructed technipion mass distribution after the classification likelihood from events with* $\mathcal{L}_{sep}^{\Sigma} > 0.9$*. These distributions are used to derive the confidence levels and exclusion limits at model points with* $m_{\pi_T} < \sqrt{s}/2$.

Two distributions of technipion masses are formed. The first contains all events classified as $e^+e^- \rightarrow \pi_T^+\pi_T^-$ candidate, i.e. with $\mathcal{S}^{\Delta} > 0.4$. In this case, m_{π_T} is taken from that

$\sqrt{s}$ [GeV]	Data	Interpreted as $\pi_T^+\pi_T^-$ Background Total	$q\bar{q}\,q\bar{q}$	$q\bar{q}\,(\gamma)$	Data	Interpreted as $\pi_T^\pm W^\mp$ Background Total	$q\bar{q}\,q\bar{q}$	$q\bar{q}\,(\gamma)$
189	27	17.4	11.8	5.6	96	93.0	72.3	20.7
192	3	3.0	2.1	0.9	21	15.8	13.0	2.8
196	11	7.9	6.0	1.9	41	40.8	33.2	7.6
200	10	8.6	6.5	2.1	25	40.4	33.2	7.2
202	3	4.4	3.3	1.1	22	20.5	17.0	3.5
205	9	9.6	7.6	2.0	55	42.4	35.1	7.3
207	10	13.7	10.7	3.0	75	63.1	51.8	11.3
208	3	0.8	0.6	0.2	3	4.2	3.4	0.8
Total	76	65.4	48.6	16.8	338	320.2	259.0	61.2

Table 4.6: *The number of events selected after a cut $\mathcal{L}^{\Sigma}_{sep} > 0.9$, broken up by the center-of-mass energy. No significant excess in data over the expectation from SM background is observed at any energy.*

one 5C kinematic fit, which forces two jet pairs to the same invariant mass. The second mass distribution contains all $e^+e^- \to \pi_T^\pm W^\mp$ candidates, i.e. events with $\mathcal{S}^\Delta < 0.4$. The technipion mass is calculated from the 4C fit jet momenta of the jet pair assigned to the technipion. Both distributions are shown in Fig. 4.24. Again, a luminosity-weighted sum over the distributions from all eight center-of-mass energy ranges is presented. Contributions from hypothetical signal production is also shown for $m_{\pi_T} = 80\,\text{GeV}$ and $\sigma = 0.25\,\text{pb}$ for each of the two channels. The number of events observed in data and expected from background are listed in Tab. 4.6, broken up into the separate center-of-mass energy bins.
In total, four distributions from technipion signal arise:

Events from	$e^+e^- \to \pi_T^+\pi_T^-$		$e^+e^- \to \pi_T^\pm W^\mp$	
interpreted as	$\pi_T^+\pi_T^- \to b\bar{q}\,q\bar{b}$	$\pi_T^\pm W^\mp \to b\bar{q}\,q\bar{q}$	$\pi_T^+\pi_T^- \to b\bar{q}\,q\bar{b}$	$\pi_T^\pm W^\mp \to b\bar{q}\,q\bar{q}$.

The respective selection efficiencies are shown in Fig. 4.25 as a function of the technipion mass. As usual, the distributions shown are luminosity-weighted sums over all center-of-mass energies, while the search for technipion production is based on separate analyses at each energy. The selection efficiencies of the MC samples are interpolated with splines. This method is already introduced and applied in Sec. 4.5.2.

No obvious excess of data events over background expectation is observed. The results will be interpreted using the predictions of the TCSM. To do so, the robustness of the MC prediction for background events and signal selection efficiencies has to be quantified. This is accomplished by the evaluation of systematic uncertainties, as explained in the next section.

4.6 Systematic Uncertainties

The expectations for signal and background Monte Carlo are not determined completely correct. Uncertainties arise from the imperfect knowledge and simulation of the detector as well as from model uncertainties during event generation. These systematic uncertainties can affect the number of background events expected from Monte Carlo and the selection efficiency for signal events.

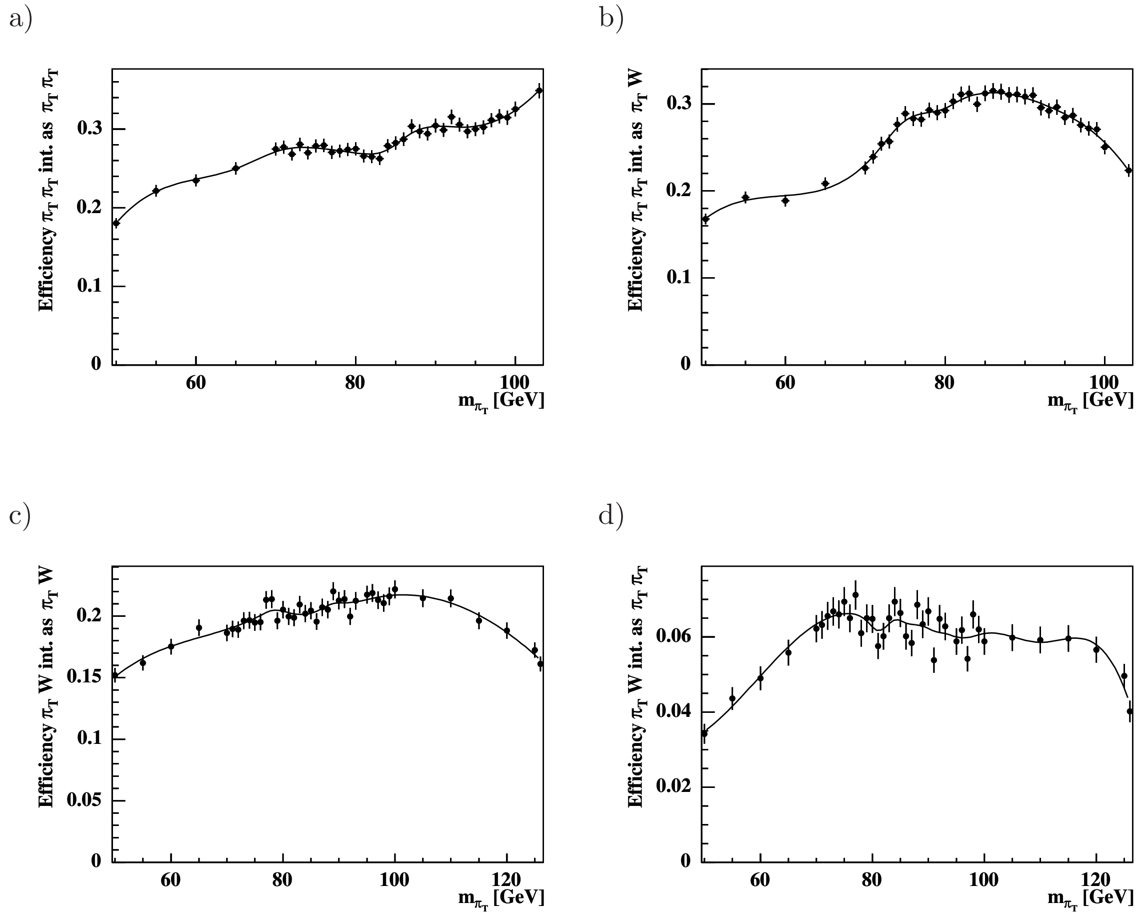

Figure 4.25: *The selection efficiency for signal events with* $\mathcal{L}^{\Sigma}_{sep} > 0.9$ *as a function of the technipion mass* m_{π_T}. *Four different distributions arise for the two technipion production modes and two interpretations. The distributions are interpolated with splines.*

Systematic uncertainties cannot be determined from first principles. Therefore, for each uncertainty the analysis is repeated separately with varied assumptions of the corresponding source. The relative difference for the number of selected background events and signal efficiency is taken as systematic uncertainty.

Systematic uncertainties can be correlated, if they have a common source. For instance, incorrect detector modeling affects all processes in the same manner, although the size of the effect might be different. In the following, the sources of systematic uncertainties relevant for this analysis are discussed.

Monte Carlo statistics

Signal and background expectations are derived from MC samples with finite size. Therefore, results have statistical uncertainties depending on the number of selected MC events. This source of uncertainty is uncorrelated between all processes and center-of-mass energies.

Modeling of pre-selection and likelihood variables

From pre-selection variables, uncertainties on the selection efficiency arise from shifts of the distributions. This effect is accounted for by shifting the Monte Carlo distributions to have the same mean as the distributions from data.

For variables used in the likelihood selections $\mathcal{L}_{\pi_T\pi_T}$ and $\mathcal{L}_{\pi_T W}$, uncertainties arise from miss-modeling in the shape of the distributions. Therefore, events are re-weighted to reproduce the shape of the distributions from data. However, the total number of events expected from background is kept fixed.

Re-weighting and shifting of distributions is a rather crude way to evaluate systematic effects. Therefore, the systematic effects on the b-tagging variables are studied in more detail, since these are the most sensitive input observables for the likelihood selection. All other variables are studied separately as described above. The total systematic uncertainty on variable modeling is derived via summing in quadrature. It is assumed uncorrelated between different processes, but correlated between all center-of-mass energies for each process.

Track reconstruction

Differences in quality and efficiency, with which tracks are reconstructed might have a significant input to the reconstruction of secondary vertices and thus on the b-tagging efficiency.

To evaluate track reconstruction effects in the $r-\varphi$ plane, an additional smearing of 5 % is applied to the impact parameter in $r-\varphi$, the azimuthal angle φ and the track curvature. Smearing by 5 % covers the uncertainties observed from calibration data shown in Fig. 4.9.

Separately, the impact parameter in z-direction and the track parameter $\tan\lambda = \cot\theta$ are varied also within 5 %. The total systematic uncertainty due to track reconstruction is obtained by the quadratic sum and treated correlated among all processes and center-of-mass energies.

Hit matching efficiency in the silicon microvertex detector

The most important device for identification of secondary vertices is the silicon microvertex detector. It provides only very few measured space points (hits) per track. Thus, the matching between hits in the silicon microvertex detector and reconstructed tracks is very sensitive to missing hits.

This effect is studied by separately dropping 1 % (3 %) of all hits in $r-\varphi$ (z). The deviations obtained from both methods are summed in quadrature. The resulting uncertainty is treated correlated among all processes and center-of-mass energies.

Modeling of B- and C-hadron decay parameters

b-Quark identification is also sensitive to the average number of charged particles (multiplicity) in decays of b-hadrons and in the energy spectrum of hadrons containing *bq*- and *cq*-quarks. All these parameters influence the efficiency to identify secondary vertices, leptons from heavy quark decays or the jet-shape parameters. Uncertainties arising are studied using event re-weighting.

To estimate the influence of *b*-decay multiplicities, events are re-weighted to vary the charged multiplicity in the range measured by the LEP Electroweak Heavy Flavor Working Group [83], $n_\mathrm{b} = 4.955 \pm 0.062$.

The average fraction $\langle x_E \rangle$ of beam energy carried by hadrons with b- or c-quarks is described by fragmentation functions in Monte Carlo generators. Events are re-weighted, so that these fragmentation functions yield mean energy fractions within $\langle x_E(\mathrm{b}) \rangle = 0.702 \pm 0.008$ for hadrons with *bq*-quarks and $\langle x_E(\mathrm{c}) \rangle = 0.484 \pm 0.008$ for hadrons with c-quarks respectively [83].

Deviations from all three sources are added in quadrature and treated as correlated among all processes and center-of-mass energies.

Uncertainties on four-fermion background

The most important source of background arises from hadronic four-fermion processes, especially from W- and Z-boson pairs. An uncertainty of 2 % arises from the measured cross-sections [44] and is assumed as systematic uncertainty here.

The fragmentation of quarks to form color-neutral hadrons is described by empirical models. The string fragmentation used in `JETSET` is compared with the cluster fragmentation approach of `Herwig` [74].

The deviations observed for four-fermion background are combined to one uncertainty by summing in quadrature and treated as correlated among all center-of-mass energies.

Total systematic uncertainty

The systematic uncertainties from the above sources are evaluated for each of the three technipion mass distributions separately. The relative effect on the number of events in these distributions is studied for background, while for signal the effect on the selection efficiencies, i.e. the fraction of events from each signal channel selected for the respective distribution, will be evaluated.

The same sources of systematic uncertainties on the first mass distribution built after the $\pi_{\mathrm{T}}^{\pm}\mathrm{W}^{\mp}$ likelihood $\mathcal{L}_{\pi_{\mathrm{T}}\mathrm{W}}$ are already studied in [48] for MC at $\sqrt{\mathrm{s}} = 206\,\mathrm{GeV}$. The systematic uncertainties are assumed to be independent on the center-of-mass energy, and so the old results are re-used here. Values are listed in Tab. 4.7.

[%]	Signal $\pi_{\mathrm{T}}^{\pm}\mathrm{W}^{\mp}$	Background
MC stat.	2.8	1.5
Var. mod.	4.7	5.3
B/D mod.	1.4	0.5
Si eff.	1.5	1.1
Trk. res.	1.8	5.4
MC gen.		2.9
Total	6.1	8.3

Table 4.7: *Systematic uncertainties on signal efficiency and background event rate for the one technipion mass distribution build after the $\pi_{\mathrm{T}}^{\pm}\mathrm{W}^{\mp}$ likelihood $\mathcal{L}_{\pi_{\mathrm{T}}\mathrm{W}}$. (From [48])*

In Tab. 4.8, the sources of systematic uncertainties considered are summarized. Values given are luminosity-weighted sums over all center-of-mass energies. However, for calculation of the exclusion limit all center-of-mass energies are treated separately.

4.7 Interpretation of Results

4.7.1 Calculation of Confidence Levels

In a simple counting experiment, the probability to observe d events, when n events are expected is give by the Poisson distribution

$$P\,(d\,|\,n) = \frac{e^{-n}\,n^{d}}{d!}. \tag{4.9}$$

[%]	Signal $\pi_T^+\pi_T^-$		Signal $\pi_T^\pm W^\mp$		Background	
Interpretation:	$\pi_T\pi_T$	π_TW	$\pi_T\pi_T$	π_TW	$\pi_T\pi_T$	π_TW
MC stat.	2.0	2.0	2.0	2.0	5.4	2.6
Var. mod.	5.3	6.5	6.9	6.0	5.5	7.5
B/D mod.	2.4	2.8	5.2	3.0	3.2	1.6
Si eff.	1.3	1.0	2.7	0.8	1.4	0.2
Trk. res.	1.9	1.8	4.0	2.4	6.0	6.7
MC gen.					5.4	5.4
Total	6.6	7.6	10.1	7.5	11.7	11.8

Table 4.8: *Systematic uncertainties on signal efficiencies and on background event rate for the two technipion mass distributions build after the classification likelihood $\mathcal{L}_{sep}$.*

In the background only hypothesis, no events from signal are expected. If b background events are expected, the background only confidence level CL_b is defined as

$$\mathrm{CL}_b = \sum_{i=0}^{d} P\left(i \,|\, n = b\right) = \sum_{i=0}^{d} \frac{e^{-b}\, b^i}{i!}. \tag{4.10}$$

If in addition s signal events are expected, the corresponding confidence level CL_{s+b} is calculated in analogy as

$$\mathrm{CL}_{s+b} = \sum_{i=0}^{d} P\left(i \,|\, n = s+b\right) = \sum_{i=0}^{d} \frac{e^{-(s+b)}\ (s+b)^i}{i!}. \tag{4.11}$$

Very small values of $1 - \mathrm{CL}_b$ are an indication for signal events in data. The observed number of events in this case is most likely not explained by a statistical upward fluctuation of background. On the contrary, if CL_{s+b} is small, it is unlikely to miss a true signal by a downward fluctuation of data.

The ratio of expected signal and background events s/b is critical for the sensitivity of an experiment. Two examples are shown in Fig. 4.26 with $s/b = 6/3$ and $s/b = 3/6$ respectively. The red areas indicate the CL_b in case $n = s+b$ events are observed. For $s/b = 2$, this upward fluctuation of background is tiny, while the probability is still around 10 % for $s/b = 1/2$. However, a $5\,\sigma$ discovery is not possible at both experiments. The blue areas show the CL_{s+b} in the case where $n = b$ events are observed. The probability to miss a signal by downward fluctuation is less than 3 % for $s/b = 2$, which means exclusion of the signal plus background hypothesis under common definitions. For $s/b = 1/2$ the probability of downward fluctuation is still 15 %, and no signal exclusion is possible.

In insensitive cases, e.g. low signal expectation, the confidence level CL_{s+b} has odd behavior. For $s \to 0$, $\mathrm{CL}_{s+b} \to \mathrm{CL}_b$. This means, that in about 5 % of all experiments, the background only hypothesis is excluded at 95 % confidence level, if the exclusion limit is derived from CL_{s+b}. In the modified frequentist's approach, the limit is calculated from

$$\mathrm{CL}_s = \frac{\mathrm{CL}_{s+b}}{\mathrm{CL}_b} = \frac{e^{-(s+b)}\ (s+b)^d\,/d!}{e^{-b}\, b^d/d!}. \tag{4.12}$$

If an experiment is sensitive, e.g. s/b is large, CL_s and CL_{s+b} are almost equal. In the above example, a significant difference between CL_s and CL_{s+b} is only observed for $s/b = 1/2$.

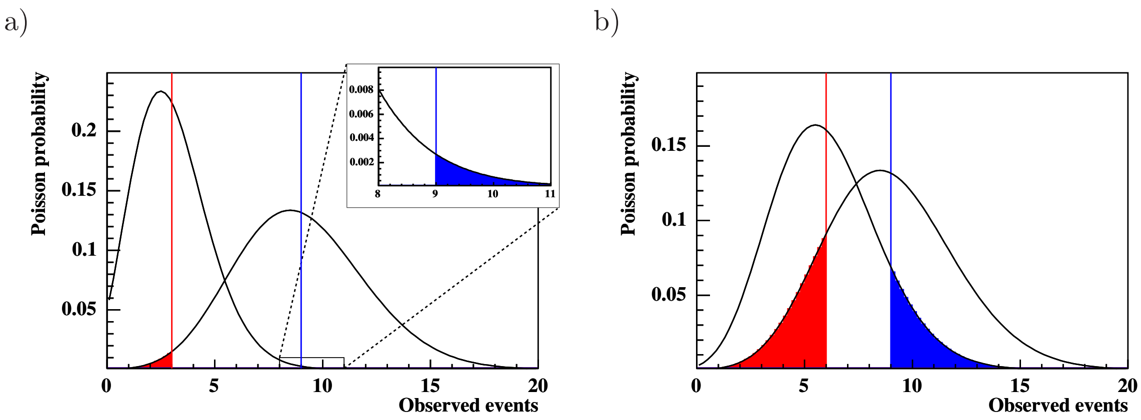

Scenario	s	b	$1-\mathrm{CL}_b$ $d=s+b$	CL_{s+b} $d=b$	CL_s $d=b$
left	6	3	2.24×10^{-3}	0.987	0.976
right	3	6	1.16×10^{-1}	0.841	0.699

Figure 4.26: *Example of two simple counting experiments with a) six (three) and with b) three (six) expected signal (background) events. For each experiment, the probability functions from Poisson statistics to observe $d=b$ and $d=s+b$ data events are shown.*

Multiple independent experiments, e.g. the bins of a histogram, can be combined by the likelihood ratio method. A test statistic Q is defined as

$$Q=\prod_i \mathrm{CL}_s^i=\prod_i \frac{e^{-(s_i+b_i)}\;(s_i+b_i)_i^d/d_i!}{e^{-b_i}\,b_i^{d_i}/d_i!}, \tag{4.13}$$

where the index i runs over all experiments or channels with s_i, b_i expected and d_i observed events. The expression re-reads as

$$-2\ln Q=2\sum_i s_i-2\sum_i d_i\ln\left(1+\frac{s_i}{b_i}\right), \tag{4.14}$$

where the factor -2 is introduced to scale $1\,\sigma$ deviation to a difference of one in $-2\ln Q$. Each channel with d_i observed events acquires a weight $w_i=\ln(1+s_i/b_i)$, which is zero for $s_i=0$, e.g. if the channel is completely insensitive. Fig. 4.27 shows two probability density functions (p.d.f.) of Q. The right curves are obtained under background only hypothesis, i.e. varying d_i according to a Poisson probability $P\,(d_i\,|\,b_i)$ with expectation b_i. In analog, the left curves are obtained from $P\,(d_i\,|\,s_i+b_i)$, e.g. signal plus background expectation.

The confidence levels CL_b and CL_{sb} are derived from the test statistic $-2\ln Q$ in the same way as for the simple counting experiment:

$$\mathrm{CL}_b=\mathcal{P}\,(Q>Q_{obs}|\text{background only}) \qquad \text{and} \qquad \mathrm{CL}_{s+b}=\mathcal{P}\,(Q>Q_{obs}|\text{signal}+\text{background})\,. \tag{4.15}$$

$\mathcal{P}$ denotes the integrated probability density function (p.d.f.) of $-2\ln Q$. The signal confidence level is again calculated from the modified frequentist's approach $\mathrm{CL}_s=\mathrm{CL}_{s+b}/\mathrm{CL}_b$. This definition of the confidence levels is equivalent to the definitions used for simple counting experiment, since $-2\ln Q$ is a monotone function of the observed number of events.

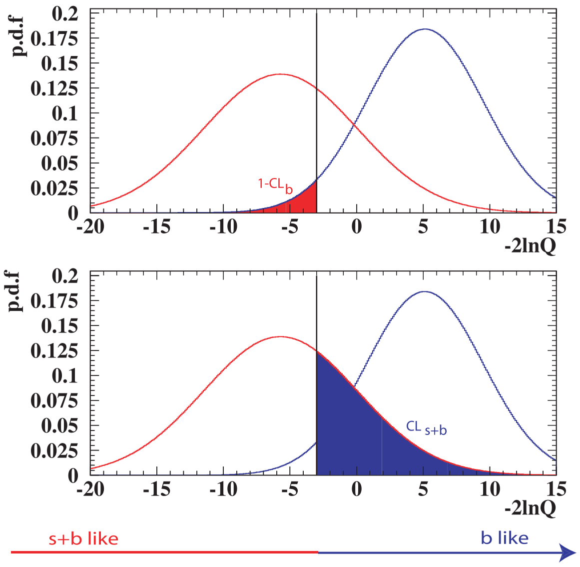

Figure 4.27: *Example distributions for the test statistic $-2\ln Q$, which is used to derive confidence levels as indicated. Details are explained in the text. (From [84]).*

The test statistic $-2\ln Q$ is derived from a large number of Monte Carlo experiments, where the 'observed' number of events in each channel is varied according to Poisson statistics plus an additional Gaussian smearing, which accounts for systematic uncertainties in signal and background expectation. The numerical precision of the confidence levels increases with the number of MC experiments N_{MC}, where $N_{MC} = \mathcal{O}(10\,000)$ is sufficient.

4.7.2 Exclusion Limits

The mass distributions from Fig. 4.18 and Fig. 4.24 are interpreted in the framework of the TCSM as described in Sec. 2.7. Model exclusion is presented in terms of mass limits on charged technipion and technirho/techniomega at the 95 % confidence level.

Confidence levels are calculated using the reconstructed technipion mass as separating variable. Independent distributions will be used for each bin of the center-of-mass energy. For technipions with $m_{\pi_\mathrm{T}} < \sqrt{\mathrm{s}}/2$, the independent mass distributions in the $\pi^+_\mathrm{T}\pi^-_\mathrm{T}$ and $\pi^\pm_\mathrm{T}\mathrm{W}^\mp$ interpretation derived from $\mathcal{L}_{sep}$ as described in Sec. 4.5.3 are used. For model points with $m_{\pi_\mathrm{T}} > \sqrt{\mathrm{s}}/2$ and $m_{\pi_\mathrm{T}} < \sqrt{\mathrm{s}} - m_\mathrm{W}$, the mass distributions obtained from $\mathcal{L}_{\pi_\mathrm{T}\mathrm{W}}$ as discussed in Sec. 4.5.2 are used.

Distributions for signal expectation are assumed to be independent of the technirho/techniomega mass. Different mass hypotheses ('test masses') for technipions are accounted for by using signal mass distribution from MC with the respective technipion mass. For masses with no MC available, the distributions are interpolated bin-wise between the distributions derived at the closest MC mass points. The signal selection efficiency for all test masses (also those, where MC is available) is taken from the spline interpolation of the selection efficiency in the respective channel and interpretation. Signal distributions are scaled to correspond to the cross-sections predicted by the TCSM. The parameters of the model are chosen as proposed in [41, 43]. All MC distributions are smoothed before calculation of the confidence level calculation to achieve continuous and numerically stable results.

All mass distributions are separated in bins of 1 GeV width, and every bin is considered as independent measurement. All measurements are combined to calculate the test statistic $-2\ln Q$ as described in Sec. 4.7.1, which in turn determines the confidence levels CL_b and CL_s.

Fig. 4.28 shows the measured values of the signal significance $1 - \mathrm{CL}_b$ as a function of the technipion mass. For all technipion masses, recorded date is compatible with the background-only hypothesis within two standard deviations, as indicated by the yellow (light shaded) region in the plot.

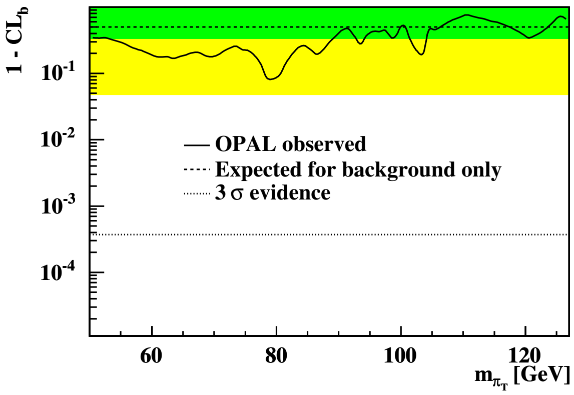

Figure 4.28: *The observed signal significance $1 - \mathrm{CL}_b$ as a function of the technipion mass. If no signal is present, $1 - \mathrm{CL}_b = 0.5$ is expected. The green (medium shaded) and yellow (light shaded) regions indicate variations of one and two standard deviations, respectively. No significant deviation from background expectation is observed at any technipion mass.*

Mass limits for charged technipions $\pi_\mathrm{T}^\pm$ and neutral TC vector states $\rho_\mathrm{T}^0/\omega_\mathrm{T}^0$ are derived from a scan in the $m_{\pi_\mathrm{T}} - m_{\rho_\mathrm{T}/\omega_\mathrm{T}}$ plane. The vector states are assumed to be degenerate in mass, i.e. $m_{\rho_\mathrm{T}^0} = m_{\omega_\mathrm{T}^0} = m_{\rho_\mathrm{T}/\omega_\mathrm{T}}$. At each point, the predicted TCSM cross-sections for $\mathrm{e}^+\mathrm{e}^- \rightarrow \pi_\mathrm{T}^+\pi_\mathrm{T}^-$ and $\mathrm{e}^+\mathrm{e}^- \rightarrow \pi_\mathrm{T}^\pm \mathrm{W}^\mp$ are taken to calculate the confidence level CL_s. The TCSM is excluded at the 95 % confidence level at any $m_{\pi_\mathrm{T}} - m_{\rho_\mathrm{T}/\omega_\mathrm{T}}$ combinations, where $\mathrm{CL}_s < 5\,\%$ is found.

The technipion decay rate for $\pi_\mathrm{T}^- \rightarrow \mathrm{b}\bar{\mathrm{q}}$ is assumed to be 100 % with no restriction on the second quark flavor. With this assumption, the results are independent on the ratio of the decay rates $\pi_\mathrm{T}^- \rightarrow \mathrm{b}\bar{\mathrm{c}}$ and $\pi_\mathrm{T}^- \rightarrow \mathrm{b}\bar{\mathrm{u}}$, which are anyhow not distinguished during the analysis. Branching ratios of the W-boson are already considered during simulation of events from $\mathrm{e}^+\mathrm{e}^- \rightarrow \pi_\mathrm{T}^\pm \mathrm{W}^\mp$ and enter the respective selection efficiencies. Therefore, no special assumption is necessary at this point.

The observed exclusion region depending in the $m_{\pi_\mathrm{T}} - m_{\rho_\mathrm{T}/\omega_\mathrm{T}}$ is shown in Fig. 4.29. Apart from m_{π_T} and $m_{\rho_\mathrm{T}/\omega_\mathrm{T}}$, all parameters of the TCSM are set to the values proposed in [41] and listed in Fig. 4.29. A strong dependence on the cross-section ratio of the two technipion production channels $\mathrm{e}^+\mathrm{e}^- \rightarrow \pi_\mathrm{T}^+\pi_\mathrm{T}^-$ and $\mathrm{e}^+\mathrm{e}^- \rightarrow \pi_\mathrm{T}^\pm \mathrm{W}^\mp$ is expected from the value of $\sin\chi$, however. Therefore, the region of excluded combinations of m_{π_T} and $m_{\rho_\mathrm{T}/\omega_\mathrm{T}}$ is also evaluated for $\sin\chi = 1/\sqrt{2}\,(N_D = 2)$, where the cross-section of the more sensitive channel $\mathrm{e}^+\mathrm{e}^- \rightarrow \pi_\mathrm{T}^+\pi_\mathrm{T}^-$ is suppressed. Small values for $\sin\chi$ however are preferred, as discussed in Sec. 2.7, where also details on the other TCSM parameters are given.

$\sin\chi$ (N_D)	N_{TC}	m_{A}	m_{V}	Q
1/3 (9)	4	200 GeV	200 GeV	5/3

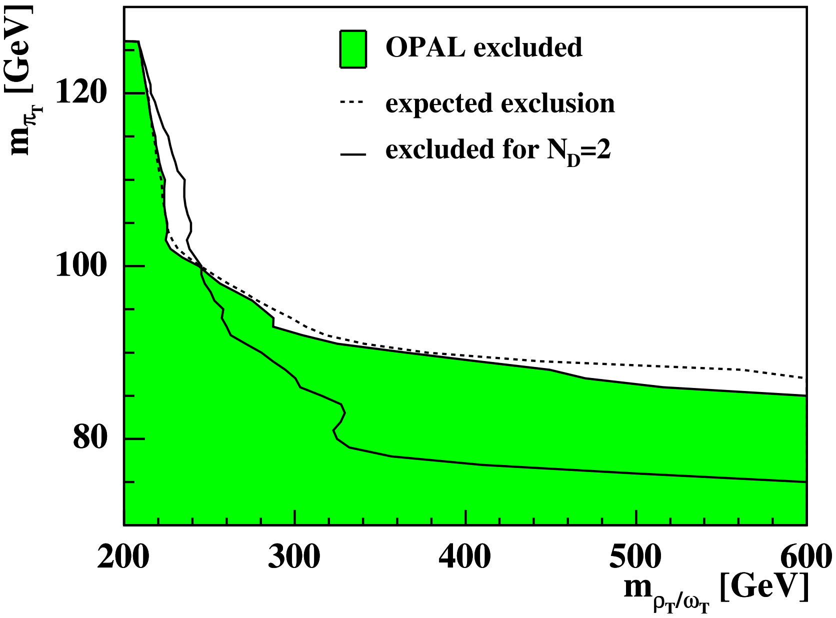

Figure 4.29: *Final mass limits for particles of the TCSM. The shaded area shows the measured exclusion for the parameter set listed on the top. It agrees reasonably well with the dashed line, which indicates the expected exclusion. The solid line corresponds to the measured exclusion for $N_D = 2 \Rightarrow \sin\chi = 1/\sqrt{2}$ with all other parameters unchanged. This scenario is disfavored by theoretical considerations, however.*

4.8 Summary

Four-jet events recorded with the OPAL detector between 1998 and 2000 are analyzed for contributions from technipion production in the channels $\mathrm{e^+e^-} \rightarrow \pi_{\mathrm{T}}^{+}\pi_{\mathrm{T}}^{-} \rightarrow \mathrm{b\bar{q}\,q\bar{b}}$ and $\mathrm{e^+e^-} \rightarrow \pi_{\mathrm{T}}^{\pm}\mathrm{W}^{\mp} \rightarrow \mathrm{b\bar{q}\,q\bar{q}}$. In contrast to a previous analysis of these channels at OPAL for the data of the year 2000 only, a combined selection of both channels is performed. No significant excess of data events over expectation from SM background is observed, and exclusion limits are given in the plane $m_{\pi_{\mathrm{T}}}$ vs. $m_{\rho_{\mathrm{T}}/\omega_{\mathrm{T}}}$ assuming signal cross-sections predicted by the Technicolor Straw-man Model.

An absolute limit $m_{\pi_{\mathrm{T}}} > 87\,\mathrm{GeV}$ is obtained at the 95 % confidence level independent of the mass of the vector states $\rho_{\mathrm{T}}^{0}/\omega_{\mathrm{T}}^{0}$ for $N_D = 9\,(\sin\chi = 1/3)$. For the disfavored case of $N_D = 2\,(\sin\chi = 1/\sqrt{2})$, a lower technipion mass limit of $\approx 75\,\mathrm{GeV}$ is observed at the 95 % CL. The absolute technipion mass limit is approximately 10 GeV higher than that obtained from the previous OPAL analysis [48, 47]. The improvement arises from the combination of both channels into one analysis and from a larger data set with about equal contribution.

The observed exclusion in the $m_{\pi_{\mathrm{T}}} - m_{\rho_{\mathrm{T}}/\omega_{\mathrm{T}}}$ plane is shown in Fig. 4.29. Results are comparable with those published by the DELPHI collaboration [45], which are only based on data recorded in 1999 and 2000, but consider also other search topologies. Limits from the TEVATRON cannot be easily compared due to different model assumptions and production modes.

Chapter 5

Higgs Resonance Reconstruction at ILC

At recent colliders, no direct signal of Higgs bosons is observed. However, evidence of a light Higgs boson with $m_{\mathrm{H}} \approx 120\,\mathrm{GeV}$ has been found indirectly, as discussed in more detail in Sec. 2.3. The future International Linear Collider ILC is ideal for precision Higgs analyses, as has been demonstrated by numerous simulations [85, 86]. Most of these studies concentrate on Higgs masses $m_{\mathrm{H}} \lesssim 200\,\mathrm{GeV}$.

The study presented in this chapter aims at the analysis of Higgs bosons in the mass range $m_{\mathrm{H}} = 200...320\,\mathrm{GeV}$, which is at the edge of being consistent with electroweak precision measurements. In this mass range, the total Higgs decay width in the Standard Model is predicted to be of the order of 1 GeV, which would allow the direct measurement from the reconstructed Higgs mass distribution. For lighter Higgs bosons, the width is predicted to much smaller, and a model independent measurement is only possible indirectly via the Higgs couplings to photons [87] and W-bosons [88].

Higgs masses between $200 - 320\,\mathrm{GeV}$ at $\sqrt{\mathrm{s}} = 500\,\mathrm{GeV}$ are studied. An integrated luminosity of $\int\mathcal{L} = 500\,\mathrm{fb}^{-1}$ is assumed, which corresponds to $1 - 2$ years of ILC operation. The Higgs mass distribution is reconstructed from Higgs bosons produced in Higgsstrahlung $\mathrm{e^+e^-} \rightarrow \mathrm{HZ}$ with the final state $\mathrm{e^+e^-} \rightarrow \mathrm{HZ} \rightarrow 2\ell\,4\mathrm{q}$. From the lineshape, the Higgs width Γ_{tot}, mass m_{H} and event rate N_{H} are determined in a model independent fit. Therefore, the results can be used to compare measurements with SM expectations and with predictions from alternative scenarios as well. Also, the branching fractions[1] $\mathrm{BR}^{\mathrm{H}}_{\mathrm{WW}}$ and $\mathrm{BR}^{\mathrm{H}}_{\mathrm{ZZ}}$ can be determined assuming these are the only sizeable Higgs decay modes.

5.1 Signal and Background Processes

Choice of signal topology

Standard Model Higgs bosons in the mass range $m_{\mathrm{H}} = 200 - 320\,\mathrm{GeV}$ are studied. Production cross-sections of $\sigma_{\mathrm{HZ}} = 15 - 45\,\mathrm{fb}$ and $\sigma_{\mathrm{H}\nu_e\bar{\nu}_e} = 5 - 30\,\mathrm{fb}$ at $\sqrt{\mathrm{s}} = 500\,\mathrm{GeV}$ are predicted for Higgsstrahlung and WW-fusion, respectively (see also Fig. 2.7). The dominant decays are $\mathrm{H} \rightarrow \mathrm{WW}$ and $\mathrm{H} \rightarrow \mathrm{ZZ}$, making up more than 99.5 % of all Higgs decays throughout the whole mass range. A complete list of final states including successive W- and Z-decays is given in Tab. 5.1.

[1] Throughout this thesis, for branching ratios the notation $\mathrm{BR}^{\mathrm{i}}_{\mathrm{f}} = \Gamma(\mathrm{i} \rightarrow \mathrm{f})/\Gamma(\mathrm{i} \rightarrow \mathrm{any})$ is used, where $\Gamma(a \rightarrow b)$ is the partial width of the transition or decay $a \rightarrow b$.

	e^+e^- $\to$	Final state	H $\to$ WW	H $\to$ ZZ	Ratio	Events per $500\,\mathrm{fb}^{-1}$
1.	$\mathrm{H}\nu_e\bar{\nu}_e$	$2\nu + X$	$\times$	$\times$	100 %	15 000
2.	HZ	$2\nu + X$	$\times$	$\times$	33.7 %	7 580
3.	HZ	qq qq qq	$\times$	$\times$	34.3 %	7 720
4.	HZ	qq qq $\ell\nu$	$\times$		20.6 %	4 630
5.	HZ	$\ell\ell$ qq qq	$\times$	$\times$	7.84 %	1 765
6.	HZ	$\ell\ell$ qq $\ell\nu$	$\times$		2.94 %	660
7.	HZ	$\ell\ell\,\ell\ell$ qq		$\times$	0.63 %	140
8.	HZ	$\ell\ell\,\ell\ell\,\ell\ell$		$\times$	0.03 %	5

Table 5.1: *Successive decays of Higgs production modes. Numbers given are estimates with cross-sections* $\sigma_{\mathrm{HZ}} = 45\,\mathrm{fb}$ *(Higgsstrahlung),* $\sigma_{\mathrm{H}\nu_e\bar{\nu}_e} = 30\,\mathrm{fb}$ *(WW-fusion) and branching ratios* $\mathrm{BR}^{\mathrm{H}}_{\mathrm{WW}} = 0.7$, $\mathrm{BR}^{\mathrm{H}}_{\mathrm{ZZ}} = 0.3$, *which are typical values for* $m_{\mathrm{H}} \approx 200\,\mathrm{GeV}$. *Here,* ℓ *is any charged lepton flavor and* q *any quark flavor kinematically allowed. Crosses indicate the Higgs decay channel, in which the respective final state arises. Channel 5 is the signal process of this analysis.*

As can be seen, all events from WW-fusion and about 55 % of events from Higgsstrahlung are expected to yield high energetic neutrinos (channels 1, 2, 4 and 6). These events are characterized by missing energy and momentum imbalance, and the application of kinematic fits for improved mass resolution is difficult.

Among the other channels, fully hadronic events HZ $\to$ 6q (channel 3) are the most frequent. Unfortunately, this also applies to the expected background $e^+e^- \to$ hadrons. Even though processes like $e^+e^- \to \mathrm{WW} \to 4\mathrm{q}$ or $e^+e^- \to t\bar{t} \to 6\mathrm{q}$ have a different event topology than the Higgs signal, their cross-sections are larger by several orders of magnitude. Reconstruction of the Higgs mass spectrum is possible, but background rejection requires a relatively complicated event selection. Additional combinatoric challenges are expected for identifying the jets from the Higgs decay.

On the contrary, the six-lepton final state (channel 8) provides easy signal identification in a clear environment, but the event rate is much too low for precision studies on the Higgs mass distribution.

Considering all this, events from $e^+e^- \to \mathrm{HZ} \to 2\ell\,4\mathrm{q}$ with $\ell = e, \mu$ are taken into account as signal in this study. The advantages of this signal choice are:

- Although corresponding to only 5 % of all events from Higgsstrahlung[2], about 1 200 events are expected in this channel for $\int\mathcal{L} = 500\,\mathrm{fb}^{-1}$ and $m_{\mathrm{H}} = 200\,\mathrm{GeV}$.
- Two leptons from Z-decays are easy to reconstruct and give a good handle on background suppression. The selection can be kept simple, especially since $\ell = \tau$ is omitted.
- The application of kinematic fits is not difficult due to the absence of high energetic neutrinos.

Background processes

All relevant Standard Model background processes are considered. They can be classified as follows:

[2]Note, that numbers in Tab. 5.1 take into account all lepton flavors, while only events with $\ell = e, \mu$ are considered as signal

6f Six-fermion processes with the same signature as the signal process, $e^+e^- \to 2\ell\,4q$. A complete set of all possible processes is used, which is explained in more detail in Sec. 5.2.

$t\bar{t}$ Top-quark pair production $e^+e^- \to t\bar{t} \to b\bar{b}W^+W^-$, Fig. 5.2. This process also yields six fermions in the final states, but with different parton composition as the signal. Since high energetic leptons might appear in decays of b-hadrons as well as of W-bosons, all successive decay modes of the t-quarks are considered.

4f Four-fermion processes including Z-pair production $e^+e^- \to 2\ell\,2q$. Event topology differs from signal events. However, due to much larger cross-section, this background class was considered.

Further processes (e.g. $e^+e^- \to WW \to qq\,\ell\nu$) are expected to be negligible due to missing isolated leptons, large missing energy, less than four jets or low mass of the hadronic system.

Six-fermion final states have contributions from a large variety of processes. Almost irreducible is triple gauge boson production (Fig. 5.1 a), since also the signal is based on three intermediate gauge bosons. Other large contributions arise from four-fermion processes with an additional fermion pair from radiation of a photon or weak boson from one of the initial or final state fermions (Fig. 5.1 b).

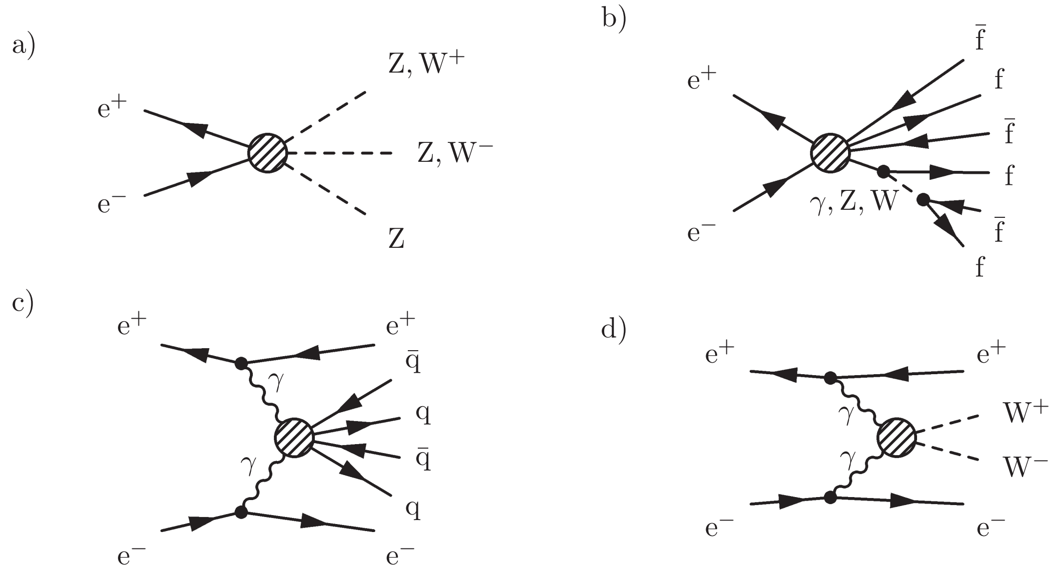

Figure 5.1: *Dominant contributions to $2\ell\,4q$ final states: a) triple boson production, b) four-fermion processes with gauge boson radiation, c) radiative processes with the major contribution of d) $\gamma\gamma \to WW$.*

Six-fermion final states with electrons, i.e. $e^+e^-\,4q$ also have contributions from processes like (Fig. 5.1c). Here, both beam electrons radiate quasi-real photons, which then collide to form a four-quark final state. The most important contribution arises from $\gamma\gamma \to W^+W^-$ (Fig. 5.1 d).

Four-fermion backgrounds are dominated by gauge boson pair production. Only Z-boson pairs (Fig. 5.3 a) can contain two isolated leptons and hadrons, as expected from the signal. Final states with electrons $e^+e^-\,qq$ have additional contribution from single-Z production (Fig. 5.3 b).

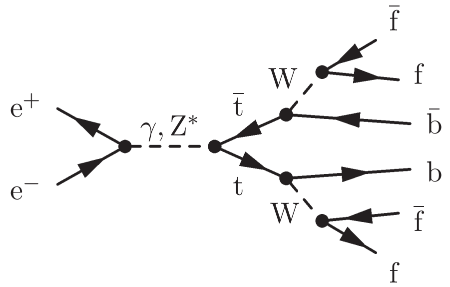

Figure 5.2: *Top-quark pair production. All decays* $\mathrm{W} \to \mathrm{q\bar{q}}$ *and* $\mathrm{W} \to \ell\nu$ *are considered.*

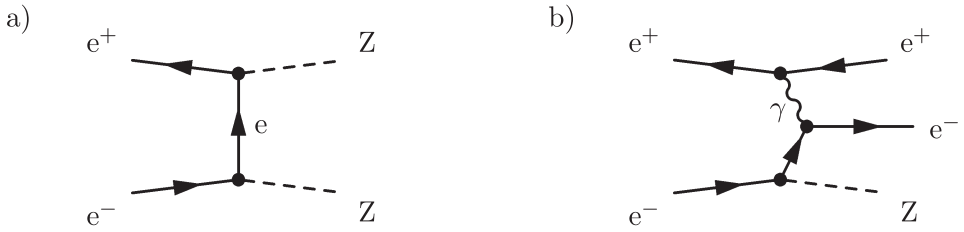

Figure 5.3: *Dominant contributions to* $2\ell\,2\mathrm{q}$ *final states: a)* Z*-pair and b) single-*Z *production.*

5.2 Simulation of Events and Detector Response

Signal events are generated in two steps: `WHiZard` [89] is used to generate final state leptons and quarks. Hadronization of the latter is simulated using `PYTHIA` [69].

`WHiZard` is best suited to generate complex final states with complicated interference pattern. The program integrates the phase space of sets of Feynman diagrams obtained from external sources. For this analysis, diagrams are provided using `MADGraph` [90]. Higher order corrections are not taken into account except of initial state photon radiation (ISR) and final state parton showers.

Some simplifications are necessary to derive reasonably accurate results with acceptable consumption of computing resources. Quarks (apart from top) are assumed to be massless, and the CKM matrix is set to unity. This leads to equivalence of u- and c-quark as well as of d-, s- and b-quark, respectively. Electrons and muons are assumed massless as well. Tree level cuts of $> 10\,\mathrm{GeV}$ are applied to all fermion pair invariant masses. This does not affect signal processes (where the mass of fermion pairs is expected to be of order m_{Z}), but improves both precision and integration time for background in phase space regions overlapping with signal.

Assuming quark universality as described above, the signal process is described by three independent final states:

- $\boldsymbol{\ell^+\ell^-\,\mathrm{u\bar{u}\,s\bar{s}}}$ only arises from $\mathrm{H} \to \mathrm{ZZ}$ decays;
- $\boldsymbol{\ell^+\ell^-\,\mathrm{u\bar{d}\,s\bar{c}}}$ only arises from $\mathrm{H} \to \mathrm{WW}$ decays;
- $\boldsymbol{\ell^+\ell^-\,\mathrm{u\bar{d}\,d\bar{u}}}$ arises from both Higgs decays and includes interference between the two channels.

Interference between the two channels is small, as can be estimated by comparison of the total cross-sections. It is found, that

$$\sigma\left(\mathrm{e^+e^-} \to \mathrm{HZ} \to \mathrm{e^+e^-\,u\bar{u}\,s\bar{s}}\right) + \sigma\left(\mathrm{e^+e^-} \to \mathrm{HZ} \to \mathrm{e^+e^-\,u\bar{d}\,s\bar{c}}\right) \approx \sigma\left(\mathrm{e^+e^-} \to \mathrm{HZ} \to \mathrm{e^+e^-\,u\bar{d}\,d\bar{u}}\right). \tag{5.1}$$

For each Higgs mass, $m_{\mathrm{H}} = 200, 240, 280, 320\,\mathrm{GeV}$, two MC samples with the final states listed in Tab. 5.2 are generated. Since the leptons in signal events originate from Z-boson decays, events with electrons and muons are equivalent. Thus, only MC events with $\ell = \mathrm{e}$ are produced. Considering the more difficult electron reconstruction w.r.t. muons, this is conservative. The event rate used in the analysis however also considers $\ell = \mu$. For estimation of detector effects (see Sec. 5.5), additional samples with $\Gamma_{\mathrm{tot}} = 0$ and 100 000 events each are generated.

Final state	Higgs decay	Events / $500\,\mathrm{fb}^{-1}$	Events generated
$\mathrm{e^+e^-\,u\bar{u}\,s\bar{s}}$	$\mathrm{H \to ZZ}$	$245 - 600$	10 000
$\mathrm{e^+e^-\,u\bar{d}\,s\bar{c}}$	$\mathrm{H \to WW}$	$165 - 520$	10 000

Table 5.2: *Signal MC samples are generated for* $m_{\mathrm{H}} = 200, 240, 280, 320\,\mathrm{GeV}$ *separately. Event rates also include* $\ell = \mu$.

The same final states are generated to simulate background contributions. To account for radiative processes discussed above, the final states are generated also with $\ell = \mu$ separately. All tree level diagrams are taken into account, which amounts to $241 - 1158$ diagrams depending on the channel. cross-section assumptions are taken from the phase space integral by `WHiZard`. In order to account for all final states with arbitrary flavor composition, the cross-sections are scaled by factors of 12.5 and 4 respectively. Also for background, the interference between processes with same-flavored quark-pairs (e.g. $\mathrm{u\bar{u}\,d\bar{d}}$) and opposite-flavored quark-pairs (e.g. $\mathrm{u\bar{d}\,d\bar{u}}$) is neglected. All MC samples generated are listed in Tab. 5.3.

Four-fermion background is simulated by the final states $\mathrm{e^+e^-u\bar{u}}$ and $\mu^+\mu^-\,\mathrm{u\bar{u}}$. The other quark flavors are accounted for by multiplying the cross-section with a factor 5. Only a reduced sample corresponding to $\int\mathcal{L} \sim 120\,\mathrm{fb}^{-1}$ is generated. This is sufficient to show that this type of background can be suppressed to a negligible level by the selection described in Sec. 5.3.

Events from $\mathrm{t\bar{t}}$-production are generated directly by `PYTHIA`. No multiplication factor arises, since all possible final states with all flavor compositions are included already. Also for this background, the sample details are listed in Tab. 5.3.

Detector response for all signal and background processes is simulated with the parametric Monte Carlo `SIMDET` [91]. The detector is not modeled in detail, but smearing of observables like particle energy and momenta is parameterized. This approach is independent of the detailed detector architecture, and the algorithm is much faster than a full simulation. However, full simulations [92] are used to tune the parameters of the detector simulation.

Final state	Cross-section multiplier	Events / $500\,\mathrm{fb}^{-1}$	Events generated
$\mathrm{e^+e^-\,u\bar{u}\,s\bar{s}}$	12.5	60	1 000
$\mu^+\mu^-\,\mathrm{u\bar{u}\,s\bar{s}}$	12.5	50	1 000
$\mathrm{e^+e^-\,u\bar{d}\,s\bar{c}}$	4	2 640	50 000
$\mu^+\mu^-\,\mathrm{u\bar{d}\,s\bar{c}}$	4	1 620	5 000
$\mathrm{e^+e^-\,u\bar{u}}$	5	375 000	100 000
$\mu^+\mu^-\,\mathrm{u\bar{u}}$	5	17 500	100 000
$\mathrm{t\bar{t}} \to X$	–	240 000	240 000

Table 5.3: *Background MC samples. Expected event rates already include the cross-section multipliers, which account for other quark flavors than simulated.*

5.3 Event Selection

Event selection is done in three steps. First, a pair of leptons is searched for. For signal events, this pair originates from the leptonic decay of a Z-boson. The rest of each event is assumed to be of hadronic origin. Within this system, jets (assumed to correspond to final state quarks) and jet-pairs (assumed to be intermediate gauge bosons) are formed. In case of signal events, the intermediate states are expected to be a pair of hadronically decaying W- or Z-bosons. To suppress events from background processes, a cut-based event selection is performed as the last step.

Identification of leptons, jets and jet pairs

Lepton candidates are all particles identified as electrons or muons by the detector simulation, which are isolated within a cone with half opening angle of 5°. Among these, the highest energetic object is considered the first lepton. If more than two lepton candidates are found, the invariant mass of the first lepton combined with any other candidate is calculated. The pairing with $m_{\ell\ell}$ closest to m_{Z} is chosen.

All particles excluding the two leptons from the Z-decay are treated as hadronic part of the event and are clustered to four jets by the Durham jet finder (see App. A).

Jet pairing is performed by applying a kinematic fit with four constraints. For an introduction to kinematic fits, see App. B. The energy and momentum of charged leptons is measured from single tracks and thus is determined with small uncertainty. Quarks in contrast are measured as many particles, which arise from the hadronization process. The particles come along in jets, which are related to the initial quarks. However, energy and momentum of jets and quarks are usually not exactly the same. Due to this additional uncertainty, the energy and momentum of quarks is determined less accurate that those from electrons or muons. Therefore, the lepton momenta are kept fixed during the kinematic fit and only the jet momenta are varied.

The constraints impose that energy and momentum of the hadronic system and the recoil system of the two leptons are equal, allow for one hard ISR or beamstrahlung photon and demand two jet pairs with equal mass. In detail, the constraints are

1. conservation of momentum in x-direction, $\sum p_i^x = p_{exp}^x$;
2. conservation of momentum in y-direction, $\sum p_i^y = p_{exp}^y$;
3. conservation of energy and momentum in z-direction with allowance for one undetected photon in $\pm z$-direction, $\left(\sum E_i - E_{exp}\right)^2 - \left(\sum p_i^z - p_{exp}^z\right)^2 = 0$; and
4. four jets form two pairs with same mass, $(p_1 + p_2)^2 = (p_3 + p_4)^2$.

Here, p_i^x, p_i^y, p_i^z denote the spatial components of the momentum vector, whereas p_i is the complete four momentum of the i-th jet. The expected momentum p_{exp} of the lepton recoil system is calculated as $p_{exp} = (\sqrt{\mathrm{s}}, 0, 0, 0) - p_{\ell\ell}$. For the fourth constraint, three jet-pairings are possible. The fit is calculated for any of them, and the combination with the best χ^2-probability $PROB(\chi^2)$ is retained.

Selection cuts

Background events are rejected by following selection cuts:

- **Lepton and jet polar angle**
  Events are required to yield at least two leptons as described before. These leptons should lie within $|\cos\theta_\ell| < 0.99$ with the lepton's polar angle θ_ℓ. All four jets should have $|\cos\theta_{\mathrm{jet}}| < 0.95$ to be well contained within the detector volume.

  Jets and leptons in signal events are distributed almost isotropic. The probability of one of the six leptons/jets to lie in the restricted forward region is about 20 %. Signal efficiency loss due to unidentified leptons is only few percent, dominated by the detector track reconstruction efficiency, which is conservatively taken to be 99 % independent on the track energy.

  Background processes are partly expected to yield forward peaked leptons, which leave the detector undetected through the beam-pipe. The drastic suppression of four-fermion background results from the rejection of single Z-production $\mathrm{e^+e^-} \to \mathrm{Z\,e^+e^-}$ due to this effect.

  The reduction of events from $\mathrm{t\bar{t}}$-production follows from the fact that not every possible decay chain contains two or more leptons. Decays to six jets are almost completely rejected at this stage, and remaining events most likely contain one leptonic $\mathrm{W} \to \ell\nu_\ell$ decay.

- **Lepton pair energy**
  In signal events, the energy of the Z-lepton pair $E_{\ell\ell}$, Fig. 5.4 (a), is expected to be less than half of the center-of-mass energy due to the large mass of the Higgs compared to the Z. A cut $E_{\ell\ell} < 0.45\sqrt{\mathrm{s}} = 225\,\mathrm{GeV}$ reduces background especially from ZZ-pair production. The effect on six-fermion and $\mathrm{t\bar{t}}$ background is small.

- **Lepton-pair mass**
  The two leptons are required to be compatible with the hypothesis of Z-decay. This is tested by a cut $|m_{\ell\ell} - m_{\mathrm{Z}}| < 5\,\mathrm{GeV}$, as shown in Fig. 5.4 (b). Events from background processes with non-resonant lepton pairs or lepton pairs from intermediate photons are rejected by this cut. This applies to $\mathrm{t\bar{t}}$ events, but also to a substantial amount of four- and six-fermion background.

- **4-Jet topology**
  The hadronic system of the events should be four-jet like, $y_{43} > 10^{-3}$, see Fig. 5.4 (c). y_{43} is the Durham distance parameter as described in App. A. Almost all remaining events from four-fermion background are rejected with this cut. Events from $\mathrm{t\bar{t}}$-production left after this cut are of the type $\mathrm{b\bar{b}\,W^+W^-} \to \mathrm{b\bar{b}\,q\bar{q}'}\,\ell\nu$, with the second lepton coming from one semi-leptonic decay of a b-hadron. Events remaining from six-fermion background at this stage contain intermediate gauge bosons and are very similar to signal events.

- **Kinematic fit χ^2**
  The kinematic fit is not only used to define jet pairs, but also to further suppress background contributions, see Fig. 5.4 (d). A final cut on $PROB(\chi^2) > 10^{-6}$ rejects events which do not satisfy the behavior implied by the fit constraints. Especially for $\mathrm{t\bar{t}}$ events, the convergence of the fit is poor due to the neutrino in the remaining events from this background.

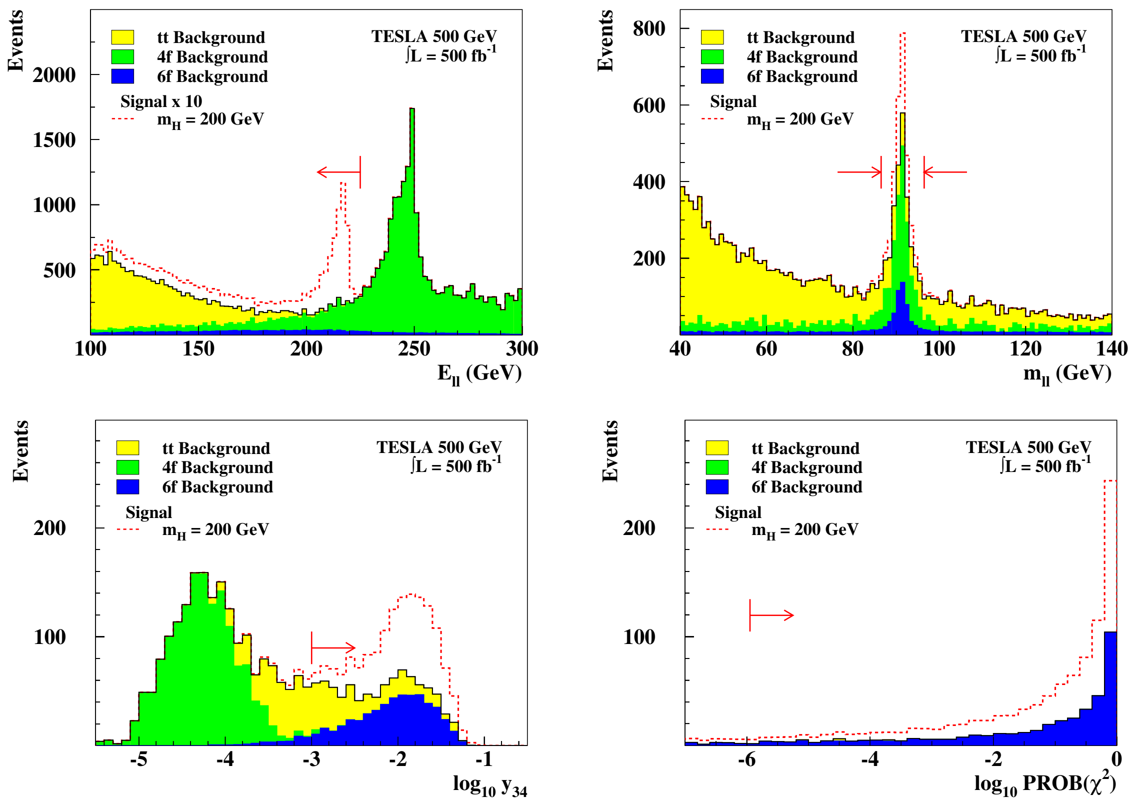

Figure 5.4: *Distributions of the selection variables. Cuts on lepton pair energy a) and mass b) mainly suppress events with non-resonant leptons and Z-pair production. Events with less than four jets are rejected by a cut on y_{34}, and a kinematic fit d) does not converge for $t\bar{t}$-pairs. These events are not shown in d), since no sensible value of $PROB(\chi^2)$ can be calculated. Arrows indicate cuts as explained in the text.*

	Variable (range)		Signal m_{H} [GeV] 200	240	280	320	Background 6f	4f	$\mathrm{t\bar{t}}$
	Events / $500\,\mathrm{fb}^{-1}$		1120	880	630	410	4340	392 000	240 000
1.-3.	$\geq 2\ell$, $\cos\theta_\ell$, $\cos\theta_{\mathrm{jet}}$		904	706	498	322	1803	38 000	90 000
4.	$E_{\ell\ell}$	$(< 225\,\mathrm{GeV})$	897	705	497	321	1512	5764	90 000
5.	$m_{\ell\ell}$	$(m_{\mathrm{Z}} \pm 5\,\mathrm{GeV})$	770	600	425	275	369	1506	750
6.	y_{34}	$(> 10^{-3})$	745	581	413	268	343	5	357
7.	$\mathrm{PROB}(\chi^2)$	$(> 10^{-6})$	585	463	333	216	271	0	4
	Efficiency		52 %	53 %	53 %	53 %			

Table 5.4: *Influence of the cuts on the different event classes. Only events from six-fermion processes remain as substantial background. Event rates assume $\sqrt{\mathrm{s}} = 500\,\mathrm{GeV}$ and $\int\mathcal{L} = 500\,\mathrm{fb}^{-1}$.*

The performance of the complete selection is summarized in Tab. 5.4. The signal efficiency is stable with respect to the Higgs mass and lies at $\epsilon_{Signal} \approx 50\,\%$. Background suppression is possible to a level $S/B \approx 1$ or better, depending on the Higgs mass. As will be shown later, the background is flat in the reconstructed Higgs mass, while the signal peaks. In a small mass window around the peak, the signal over background ratio is much better.

5.4 Separation of ZWW- and ZZZ-Events

The quark and lepton pairs formed during event selection are regarded as intermediate vector boson states. The Higgs boson is reconstructed from a pair of these bosons (di-boson), where three combinations are possible. The correct combinations exhibit a peak in the invariant mass, while the two wrong combinations yield flat distributions.

Depending on the Higgs decay, the spread of the peak, i.e. the mass smearing due to detector effects, is different. In $\mathrm{H} \rightarrow \mathrm{WW}$ decays, the correct di-boson combination always arises from four jets, while also correct combinations with two isolated leptons plus two jets arise in $\mathrm{H} \rightarrow \mathrm{ZZ}$ decays. The latter yield a better mass resolution, i.e. a smaller peak spread, as is shown in Fig. 5.6. Best results for the measurement of the Higgs width are obtained, if the detector smearing effects are evaluated for each channel separately, as explained in Sec. 5.5. To describe the smearing effects in a data sample with mixed contributions, the separate smearing functions are weighted with the number ratios R_{WW} and R_{ZZ} respectively and added. The number ratios are defined as

$$R_{\mathrm{WW}} = \frac{N_{\mathrm{WW}}}{N_{\mathrm{WW}} + N_{\mathrm{ZZ}}} \qquad \text{and} \qquad R_{\mathrm{ZZ}} = \frac{N_{\mathrm{ZZ}}}{N_{\mathrm{WW}} + N_{\mathrm{ZZ}}}, \tag{5.2}$$

where N_{WW} and N_{ZZ} are the number of events from $\mathrm{H} \rightarrow \mathrm{WW}$ and $\mathrm{H} \rightarrow \mathrm{ZZ}$ contained in the data sample. Best separation between the two Higgs decay channels is achieved using the jet-pair mass obtained from the kinematic fit. The distribution is shown in Fig. 5.5 for $m_{\mathrm{H}} = 200\,\mathrm{GeV}$. Two peaks at m_{W} and m_{Z} are clearly separated. However, an event-by-event separation is not possible due to overlapping tails. Also, contributions from background processes remain. The number ratios R_{WW} and R_{ZZ} thus cannot be derived from simple counting and a statistical approach is used.

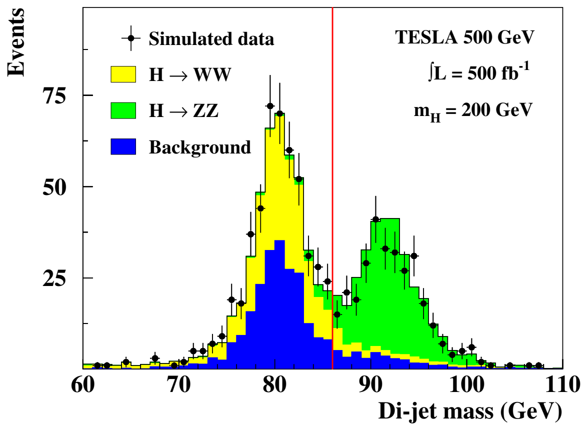

Figure 5.5: *Di-jet mass spectrum as obtained from the kinematic fit. Two peaks at* m_{W} *and* m_{Z} *are clearly distinguished, however with overlapping tails. Background dominantly incorporates* W *bosons.*

The distribution of the jet pair masses is divided by an arbitrary cut, chosen to be $m_{cut} = 85.8\,\mathrm{GeV} \approx (m_\mathrm{W} + m_\mathrm{Z})/2$. In a data sample, the numbers N^+ and N^- of events above and below this value are counted. Subtraction of the background expectation $N_B^\pm$ yields the number of signal events $N_S^\pm$ and their probability $P_S^\pm$ to lie above or below the cut

$$N_S^\pm = N^\pm - N_B^\pm \qquad \text{and} \qquad P_S^\pm = \frac{N_S^\pm}{N_S^+ + N_S^-}. \tag{5.3}$$

The corresponding probabilities $P_\mathrm{WW}^\pm$ and $P_\mathrm{ZZ}^\pm$ for $\mathrm{H} \to \mathrm{WW}$ and $\mathrm{H} \to \mathrm{ZZ}$ events separately can be used to express $P_S^\pm$ as a weighted sum, where R_WW and R_ZZ are the respective weights

$$P_S^\pm = R_\mathrm{WW}\, P_\mathrm{WW}^\pm + R_\mathrm{ZZ}\, P_\mathrm{ZZ}^\pm. \tag{5.4}$$

By definition, $R_\mathrm{WW} + R_\mathrm{ZZ} = 1$ is valid, and the number ratios can be determined by

$$R_\mathrm{WW} = \frac{P_S^- - P_\mathrm{ZZ}^-}{P_\mathrm{WW}^- - P_\mathrm{ZZ}^-} \qquad \text{and} \qquad R_\mathrm{ZZ} = \frac{P_S^+ - P_\mathrm{WW}^+}{P_\mathrm{ZZ}^+ - P_\mathrm{WW}^+}. \tag{5.5}$$

$P_S^\pm$ are derived from event counting in the data sample and all other $P_i^\pm$ can be obtained from Monte Carlo without assumptions on $\mathrm{BR}_\mathrm{WW}^\mathrm{H}$ and $\mathrm{BR}_\mathrm{ZZ}^\mathrm{H}$.

This method for determination of the number ratios is model independent, i.e. no assumptions on the Higgs branching ratios are necessary. However, the observed number ratios R_WW and R_ZZ depend on the (absolute) Higgs branching ratios

$$\mathrm{BR}_\mathrm{WW}^\mathrm{H} = \frac{\Gamma(\mathrm{H} \to \mathrm{WW})}{\Gamma(\mathrm{H} \to X)} \qquad \text{and} \qquad \mathrm{BR}_\mathrm{ZZ}^\mathrm{H} = \frac{\Gamma(\mathrm{H} \to \mathrm{ZZ})}{\Gamma(\mathrm{H} \to X)}. \tag{5.6}$$

The selection of Sec. 5.3 only accepts events from $\mathrm{H} \to \mathrm{WW}$ and $\mathrm{H} \to \mathrm{ZZ}$ decays, however, and the number ratios R_WW and R_ZZ are only sensitive to the respective BR-ratios

$$B_\mathrm{WW} = \frac{\mathrm{BR}_\mathrm{WW}^\mathrm{H}}{\mathrm{BR}_\mathrm{WW}^\mathrm{H} + \mathrm{BR}_\mathrm{ZZ}^\mathrm{H}} \qquad \text{and} \qquad B_\mathrm{ZZ} = \frac{\mathrm{BR}_\mathrm{ZZ}^\mathrm{H}}{\mathrm{BR}_\mathrm{WW}^\mathrm{H} + \mathrm{BR}_\mathrm{ZZ}^\mathrm{H}}. \tag{5.7}$$

With reversed argumentation, B_WW and $bfzz$ can be derived from the number ratios R_WW and R_ZZ with additional knowledge of the selection efficiencies $\varepsilon_\mathrm{WW}\,(\varepsilon_\mathrm{ZZ})$ for events from $\mathrm{H} \to \mathrm{WW}\,(\mathrm{H} \to \mathrm{ZZ})$ and the SM branching ratios $\mathrm{BR}_X^{\mathrm{W},\mathrm{Z}}$ of the W- and Z-boson. With the abbreviations

$$C_\mathrm{WW} = \varepsilon_\mathrm{WW}\,\mathrm{BR}_{\ell\ell}^\mathrm{Z}\,\left(\mathrm{BR}_\mathrm{qq}^\mathrm{W}\right)^2 \qquad \text{and} \qquad C_\mathrm{ZZ} = 3\,\varepsilon_\mathrm{ZZ}\,\mathrm{BR}_{\ell\ell}^\mathrm{Z}\,\left(\mathrm{BR}_\mathrm{qq}^\mathrm{Z}\right)^2, \tag{5.8}$$

the BR-ratios B_WW and B_ZZ are

$$B_\mathrm{WW} = \frac{C_\mathrm{ZZ}\,R_\mathrm{WW}}{C_\mathrm{ZZ}\,R_\mathrm{WW} + C_\mathrm{WW}\,R_\mathrm{ZZ}} \qquad \text{and} \qquad B_\mathrm{ZZ} = \frac{C_\mathrm{WW}\,R_\mathrm{ZZ}}{C_\mathrm{ZZ}\,R_\mathrm{WW} + C_\mathrm{WW}\,R_\mathrm{ZZ}}. \tag{5.9}$$

It should be pointed out, that this method is independent on the absolute branching ratios $\mathrm{BR}_\mathrm{WW}^\mathrm{H}$ and $brzz$. In the Standard Model, $\mathrm{BR}_\mathrm{WW}^\mathrm{H} + \mathrm{BR}_\mathrm{ZZ}^\mathrm{H} \approx 1$ is predicted, from which follows

$$\mathrm{BR}_\mathrm{WW}^\mathrm{H}(\mathrm{SM}) \approx B_\mathrm{WW} \qquad \text{and} \qquad \mathrm{BR}_\mathrm{ZZ}^\mathrm{H}(\mathrm{SM}) \approx B_\mathrm{ZZ}. \tag{5.10}$$

The statistical uncertainties ΔB_WW and ΔB_ZZ on the BR-ratios B_WW and B_ZZ are determined by the statistical spread of the number of selected signal events N_S. All parameters derived from MC are assumed to be known exactly, which is justified, if the total uncertainty is dominated by statistical effects. Values obtained are listed in Tab. 5.5.

$m_{\rm H}$ [GeV]	$\frac{\Delta B_{\rm WW}}{B_{\rm WW}}$	$\frac{\Delta B_{\rm ZZ}}{B_{\rm ZZ}}$
200	3.5 %	9.9 %
240	5.0 %	10.8 %
280	7.7 %	16.2 %
320	8.6 %	17.3 %

Table 5.5: *Statistical uncertainty for the model independent determination of the ratios $B_{\rm WW}$ and $B_{\rm ZZ}$ as defined in Eq. 5.6. In the Standard Model, it is $B_{\rm WW} \approx {\rm BR}^{\rm H}_{\rm WW}$ and $B_{\rm ZZ} \approx {\rm BR}^{\rm H}_{\rm ZZ}$.*

5.5 Detector Smearing and Combinatoric Background

The Higgs boson is reconstructed by pairing two of the three boson candidates obtained during event selection. The invariant Higgs mass distribution of the correct di-bosons is expected to exhibit a peak, which can be described as the convolution of a Breit-Wigner function with the mass smearing from detector effects, while the two wrong boson pairs will yield a flat combinatoric background.

From Monte Carlo events with zero Higgs width, the detector smearing is estimated for each Higgs mass under study and for H → WW and H → ZZ decays separately by parameterizing the resulting mass distribution of the correct di-boson combination. The combinatoric background is estimated by parameterization of the mass distribution from the wrong combinations of the same MC samples.

Detector smearing

As can be seen from Fig. 5.6, the smearing is not of simple Gaussian shape. Non-linear detector effects (e.g. varying precision of track momentum measurements with $\cos\theta$) yield longer tails to either end of the distribution. Asymmetry in the distribution originates from the kinematic fit.

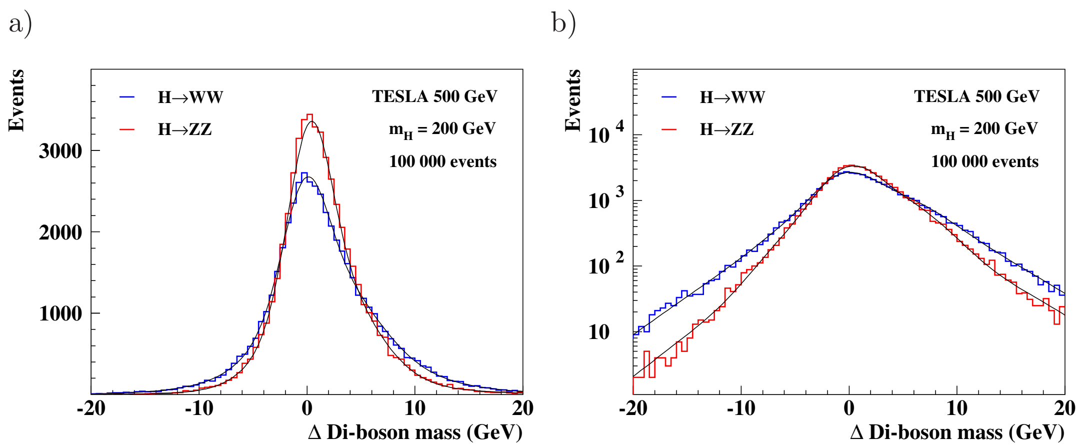

Figure 5.6: *Di-boson mass spectrum for the right combination. The spectrum is obtained from MC width $\Gamma_{\rm tot} = 0$ and shifted by the nominal Higgs mass. b) is the same plot as a) but with logarithmic y-axis. The parameterization used as smearing function (see text) describes the core of the distributions as well as the tails.*

The detector smearing is parameterized by the sum of three gaussian functions. The function has nine free parameters,which are determined for each Higgs mass and for H → WW and H → ZZ events separately. There is no deep physical justification for this choice apart from the good agreement between Monte Carlo distribution and parameterization, as is shown in Fig. 5.6. Especially, the tails are described correctly. The normalized parameterizations for all four Higgs masses and for the two Higgs decay channels are shown in Fig. 5.7. They can be regarded as probability density (p.d.f.) of the difference of true and reconstructed Higgs mass for events of the respective channel and central Higgs mass. The statistical smearing of events from a mixed sample is described by the weighted sum of the separate smearing probabilities of the two Higgs decay channels. The number ratios R_{WW} and R_{ZZ} as introduced above serve as weights.

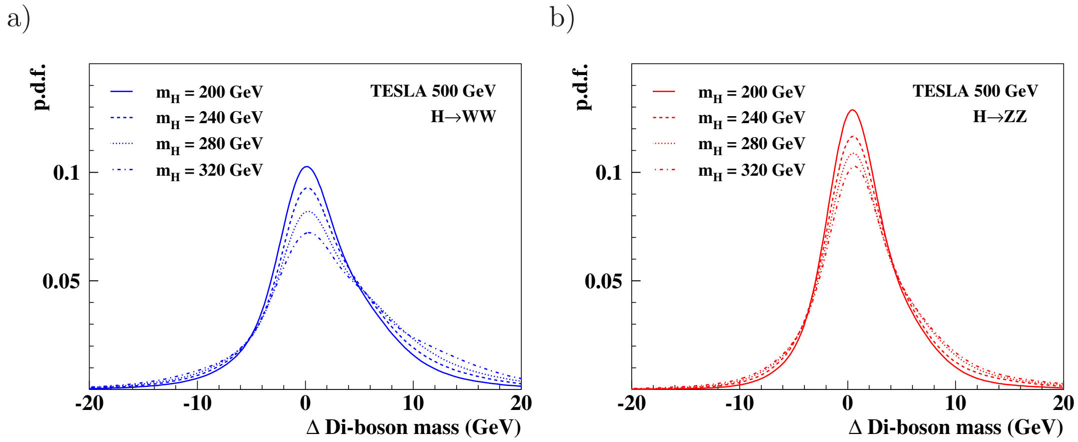

Figure 5.7: *Detector smearing for different Higgs mass hypotheses; a) shows the smearing for* H → WW *events, b) for* H → ZZ *respectively.*

At a later experiment, the parameterization of detector smearing as described here can be obtained from MC simulations as well. However, the detector MC has to be tuned very carefully and cross-calibrated with data. This is possible with dedicated calibration runs at lower energies (as has been done at LEP) or through the study of well known physical processes (e.g. W- and Z-pair production).

Combinatoric background

The combinatoric background is flat over large mass ranges and has soft tails at either end. It does not depend on the Higgs width, but scales with the number of signal events and thus depends on the signal cross-section. For each Higgs mass m_{H} under study, the distribution is parameterized by a function

$$\mathcal{C}\,(m) = \frac{(a_2 + a_3\,(m - a_1))}{[1 + \exp\,(-a_4\,(m - a_1))]\,[1 + \exp\,(-a_5\,(m - a_1))]} \tag{5.11}$$

with five free parameters a_i. The function is the product of two step functions and a straight line. Two step functions are needed to allow for two different curvature radii at the step, and the straight line is necessary to describe non-constant behavior far away from the step position. As can be seen from Fig. 5.8, agreement between MC and parameterization is not as good as for the peak of the correct di-boson combinations. However, the parameterization is sufficient since the contributions of the combinatoric background to the total event rate is small, as will be shown in Sec. 5.6.

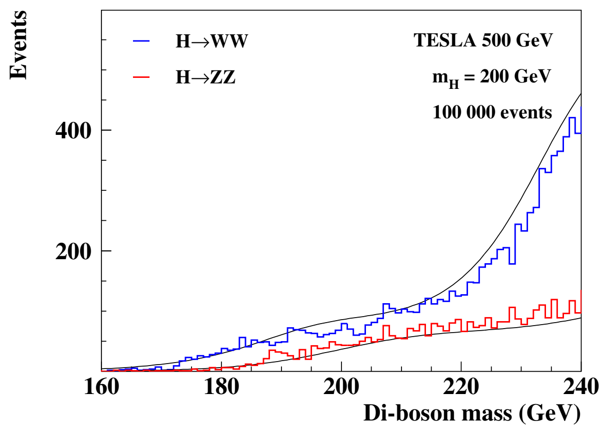

Figure 5.8: *Di-boson mass spectrum for the wrong combinations. The distributions are obtained from the same MC samples as Fig. 5.6. Also shown are the parameterizations used to describe combinatoric background.*

5.6 Fit of Higgs Resonance Parameters

Finally, the spectrum of the reconstructed di-boson masses is built. The lepton and jet pairs formed during event selection are regarded as originating from intermediate W- or Z-bosons. No distinction is made and a threefold ambiguity for the two bosons coming from the Higgs decay arises. Each event yields three entries for the different combination to the distributions of the reconstructed Higgs mass, which are displayed in Fig. 5.9 for the four Higgs mass hypotheses studied.

The mass spectrum is fitted with a function that reflects three contributions to the distribution:

1. The correct combinations of di-bosons in signal events form a clear peak. This contribution can be described as a Breit-Wigner function convoluted with the detector smearing parameterization as described in Sec. 5.5. The Breit-Wigner parameters Γ (FWHM), μ (mean value) and N (normalization) are free parameters of the fit, while the parameters of the detector smearing are fixed from MC as determined in Sec. 5.5.

2. The wrong combinations of signal di-boson masses form a flat combinatoric background, which is parameterized as discussed in Sec. 5.5. The parameters describing the shape of the distributions are fixed, while the number of entries is determined in the fit by the free parameter N of the Higgs peak Breit-Wigner function.

3. This physical background is parameterized by a similar step function as the combinatoric background. In this case besides the parameters for the shape also the number of entries is fixed by MC expectation[3].

In total, 100 MC experiments corresponding to $\int\mathcal{L} = 500\,\mathrm{fb}^{-1}$ each are simulated. In each experiment, signal and background events are chosen randomly from the complete MC sets, which correspond to at least twentyfold luminosity. The different experiments therefore are almost statistically independent.

[3] In later experiments, the background parameters can be determined off-peak from data.

From each MC experiment, the Higgs resonance parameters $\Gamma = \Gamma_{\rm H}$, $\mu = m_{\rm H}$ and $N = \sigma \times {\rm BR} \times \varepsilon$ are fitted to the corresponding mass distributions, as also shown in the examples of Fig. 5.9. The mean uncertainties on the fit values are shown in Tab. 5.6 together with the mean uncertainties for the BR-ratios $B_{\rm WW}$ and $B_{\rm ZZ}$ as defined in Eq. 5.7.

The Higgs width can be determined with accuracies of order 25 %. The dependence on the Higgs mass reflects the two limiting aspects from detector resolution (which dominates at $m_{\rm H} = 200\,{\rm GeV}$) and small statistics (dominating at $m_{\rm H} = 320\,{\rm GeV}$). Best width resolution is obtained for intermediate masses $m_{\rm H} = 240 - 280\,{\rm GeV}$.

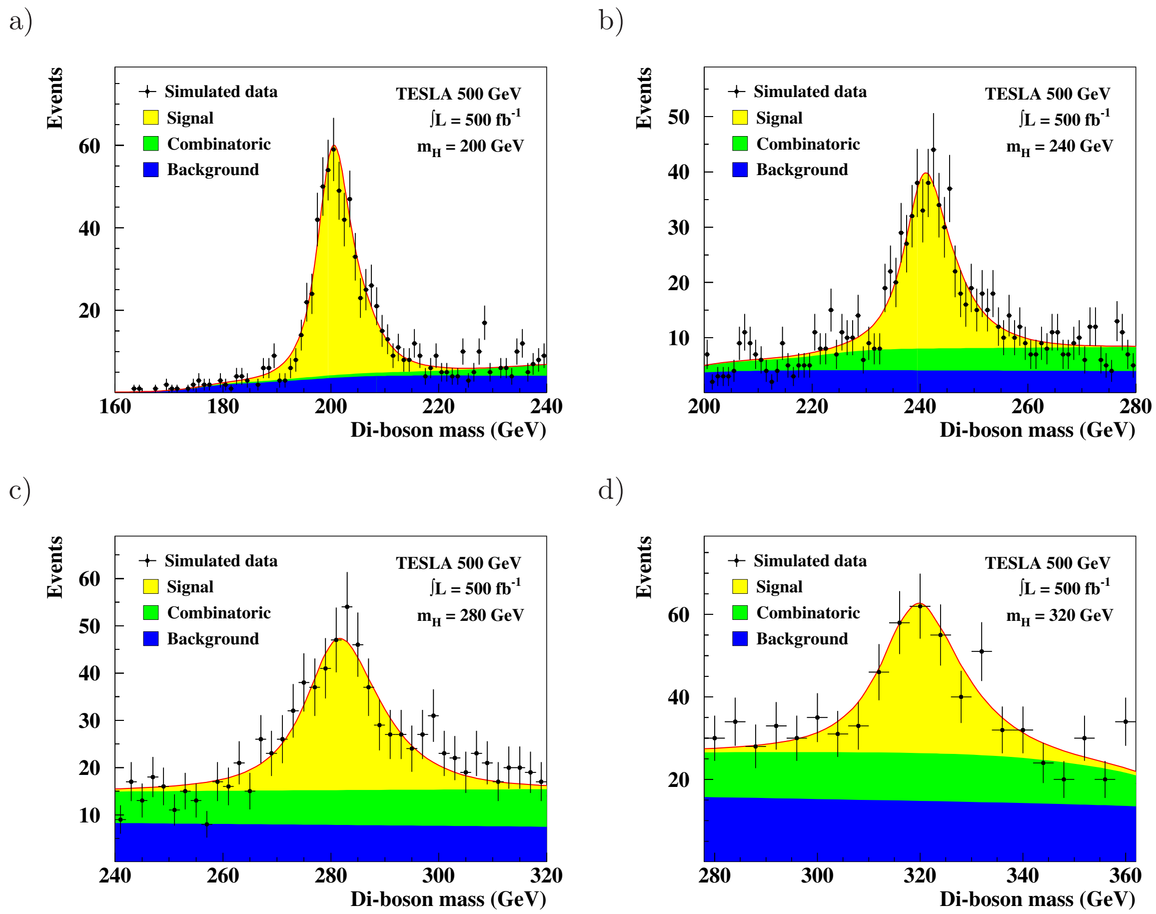

Figure 5.9: *Reconstructed Higgs mass distributions for the different Higgs masses. Data points are examples of one MC experiment corresponding to $\mathcal{L} = 500\,{\rm fb}^{-1}$. Also shown are the results of a fit to the distribution with contributions from correct signal di-boson combinations (light shaded), wrong signal di-boson combinations (medium shaded) and all di-boson combinations from background processes (dark shaded). Note the different bin widths.*

The Higgs mass can be determined with a precision of $0.11 - 0.36\,\%$, which corresponds to a resolution of some $220 - 1\,150\,{\rm MeV}$. The accuracy depends on the Higgs mass and roughly scales with $1/\sqrt{N}$, where N is the expected number of reconstructed events (see Tab. 5.4). This implies, that the mass uncertainty on the Higgs mass is dominated by statistical effects.

The same is true for the determination of the event rate N and the branching fractions $B_{\rm WW}$ and $B_{\rm ZZ}$. The former can be determined with an uncertainty of $3.6 - 6.3\,\%$, while the errors on the latter range from $3.5 - 8.6\,\%$ and $9.9 - 17.3\,\%$ respectively.

The pull distributions of all observables at all Higgs masses are evaluated to test the statistical stability of the method. The pull is defined as the difference of measured and true value divided by the measurement error. Ideally, the pull follows a normal distribution. Shifted mean $\mu \neq 0$ or standard deviation $\sigma \neq 1$ indicate systematic biases of measurement and error respectively. As long as the shape of the pull is still a Gaussian, these biases can be corrected for.

m_{H}	$\Delta\Gamma_{\mathrm{H}}$ [GeV]	$\frac{\Delta\Gamma_{\mathrm{H}}}{\Gamma_{\mathrm{H}}}$	Δm_{H} [MeV]	$\frac{\Delta m_{\mathrm{H}}}{m_{\mathrm{H}}}$	$\frac{\Delta N}{N}$	$\frac{\Delta B_{\mathrm{WW}}}{B_{\mathrm{WW}}}$	$\frac{\Delta B_{\mathrm{ZZ}}}{B_{\mathrm{ZZ}}}$
200 GeV	0.48	34.0 %	220	0.11 %	3.6 %	3.5 %	9.9 %
240 GeV	0.91	26.8 %	408	0.17 %	3.8 %	5.0 %	10.8 %
280 GeV	1.48	22.7 %	672	0.24 %	4.4 %	7.7 %	16.2 %
320 GeV	3.25	26.4 %	1 152	0.36 %	6.3 %	8.6 %	17.3 %

Table 5.6: *Uncertainties for Higgs width Γ_{H}, Higgs mass m_{H}, and event rate N from a fit to the di-boson mass spectrum. Also listed are measurement uncertainties for the BR-ratios B_{WW} and B_{ZZ} (see Sec. 5.4). All numbers are mean values obtained from 100 independent MC experiments corresponding to $\int\mathcal{L} = 500\,\mathrm{fb}^{-1}$ at $\sqrt{s} = 500\,\mathrm{GeV}$ each.*

Mean and standard deviation for the pull distributions on the measurements of Higgs width, mass, event rate and branching fractions are shown in Tab. 5.7 for all Higgs masses. Additionally, in Fig. 5.10 the distributions for m_{H} are shown. All distributions are of Gaussian shape. The corrections for measurements and their errors are moderate. Only for mass determination and for width measurements at $m_{\mathrm{H}} = 200\,\mathrm{GeV}$, the measurement have to be corrected by more than one standard deviation. This follows from the imperfect parameterization of the detector smearing, which does not describe a small region in the core of the distribution correctly, see also Fig. 5.6.

The errors are generally determined to be somewhat too large, i.e. the pull distributions have $\sigma < 1$. The results of Tab. 5.6 thus can be considered as conservative.

Pull	$m_{\mathrm{H}} = 200\,\mathrm{GeV}$		$m_{\mathrm{H}} = 240\,\mathrm{GeV}$		$m_{\mathrm{H}} = 280\,\mathrm{GeV}$		$m_{\mathrm{H}} = 320\,\mathrm{GeV}$	
on	μ	σ	μ	σ	μ	σ	μ	σ
Γ_{H}	1.01	0.99	0.34	0.75	-0.09	0.85	-0.57	0.70
m_{H}	0.66	0.81	-0.11	1.43	0.92	1.33	1.26	1.05
N	0.15	1.11	0.91	0.82	0.76	0.88	-0.73	0.73
B_{WW}	0.26	0.89	-0.94	0.62	0.20	0.68	0.29	0.70
B_{ZZ}	-0.24	0.91	0.93	0.62	-0.17	0.68	-0.28	0.70

Table 5.7: *Mean and spread of pull distributions for all measured Higgs parameters at $m_{\mathrm{H}} = 200 - 320\,\mathrm{GeV}$. Only the determination of the Higgs mass exhibits a systematic bias of order one standard deviation.*

5.7 Summary and Conclusions

It is shown, that the total decay width of SM Higgs bosons can be derived from a fit to the reconstructed Higgs lineshape. The method uses minimal model assumptions, but is restricted to Higgs bosons with width of at least some GeV and substantial decay rates to W- and Z-bosons. The SM predicts these properties for Higgs bosons with masses in excess of $m_{\mathrm{H}} \approx 200\,\mathrm{GeV}$.

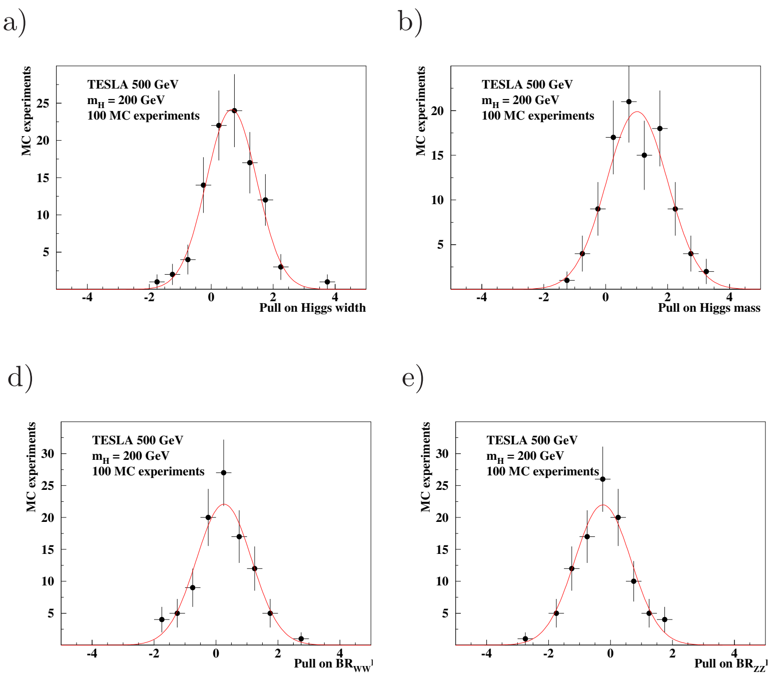

Figure 5.10: *Pull distributions from 100 MC experiments for the measurement of a) Higgs width, b) Higgs mass, c) Higgs event rate, d) relative branching to* W-bosons*, and e) relative branching to* Z-bosons *for* $m_{\mathrm{H}} = 200\,\mathrm{GeV}$*. All distributions are of Gaussian shape, so that biases on mean and spread can be corrected for.*

In addition, the Higgs mass and event rate can be determined from the same fit. For parameterization of detector effects, the relative fractions of events from $\mathrm{H} \to \mathrm{WW}$ and $\mathrm{H} \to \mathrm{ZZ}$ in a data sample have to be determined. These values can be used to determine the relative branching fractions B_{WW} and B_{ZZ} as defined in Eq. 5.7. If there are no other substantial decay modes (as for the SM Higgs), the relative branching fractions equal the total branching ratios $\mathrm{BR}^{\mathrm{H}}_{\mathrm{WW}}$ and $\mathrm{BR}^{\mathrm{H}}_{\mathrm{ZZ}}$ respectively.

Higgs masses $m_{\mathrm{H}} = 200 - 320\,\mathrm{GeV}$ are studied at $\sqrt{\mathrm{s}} = 500\,\mathrm{GeV}$. Events from Higgs-strahlung with successive decays $\mathrm{ZH} \to \mathrm{ZWW/ZZZ} \to 2\ell\,4\mathrm{q}$, $\ell = \mathrm{e}, \mu$ are selected. This final state allows for good background suppression in a simple cut-based selection and application of a kinematic fit for optimized mass resolution. However, the channel corresponds to only 5 % of all Higgsstrahlung final states. In total, $410 - 1120$ signal events are expected depending on the Higgs mass, which are selected with $\approx 50\,\%$ efficiency.

After selection, background contamination is reduced to $S/B = 1 - 2$ again depending on the Higgs mass. However, the reconstructed Higgs mass forms a clear peak for signal, while the corresponding distribution in background is flat. Within $\pm 40\,\mathrm{GeV}$ around the central Higgs mass, signal to background ratios are much better, as can be seen from the reconstructed mass distributions in Fig. 5.9.

It is shown, that the Higgs width can be determined from a fit to the mass distribution with precisions $\Delta\Gamma/\Gamma = 22 - 34\,\%$ depending on the Higgs mass. For small masses/narrow widths, the uncertainty is dominated by detector resolution, while at large masses/wide widths statistical effects dominate. Results are shown in Fig. 5.11 a) together with the uncertainties on Higgs width measurements from two previous studies. The indirect determination via the Higgs coupling to W-bosons (measured in the cross-section of WW-fusion [88]) is the most precise method. However, so far only decays $H \to b\bar{b}$ have been investigated, which restricts the method to $m_H \lesssim 150\,\mathrm{GeV}$. Extending the method to $H \to WW$ decays would explore the complete Higgs mass range.

At LHC, the Higgs width can be measured from the lineshape in $gg \to H \to ZZ \to 4\mu$ events [93]. Statistical precision is slightly better for an integrated luminosity of $\int\mathcal{L} = 300\,\mathrm{fb}^{-1}$. However, the results of [93] exhibit systematic shifts of the measurements, which arise from the naive assumption of simple Gaussian detector smearing. These shifts have not been studied in detail, and it is not shown, that the measurements can be corrected.

a) b)

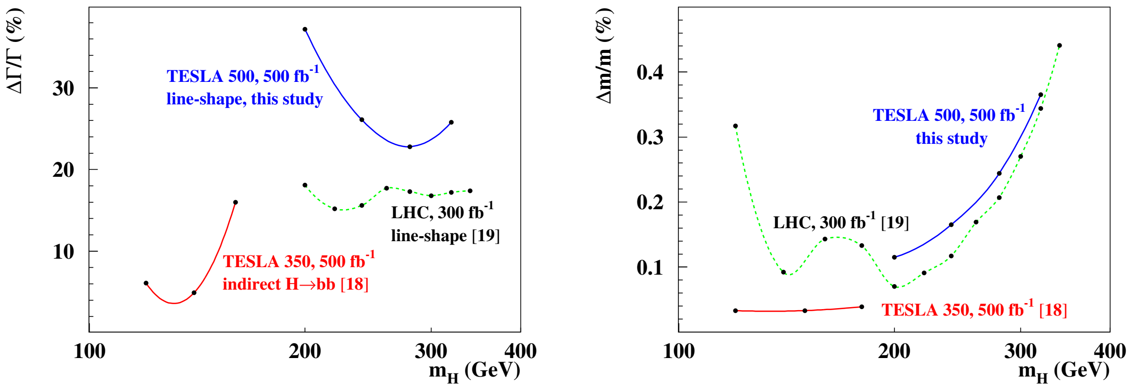

Figure 5.11: *Precisions of Higgs width (left) and mass (right) measurements at* ILC*. Results from former studies are shown in red, those of this simulation in blue.*

From the lineshape reconstruction at ILC, the Higgs mass can be determined with precision of $0.11 - 0.36\,\%$ or $265 - 1\,150\,\mathrm{MeV}$. The uncertainties scale with $1/\sqrt{N}$ and are of statistical origin. Evaluations of the pull distributions exhibit a systematic shift of the same order at all Higgs masses. The spread of 100 MC experiments is of Gaussian shape and the bias can be corrected for.

Previous simulations for ILC [94] at $\sqrt{s} = 350\,\mathrm{GeV}$ revealed better precision due to higher statistics, to which higher cross-section and the selection of more common decay channels contribute. Also mass measurements from the lineshape reconstruction at LHC are slightly better in statistical accuracy. A comparison of all three mass measurement is shown in Fig. 5.11 b).

The determination of the Higgs branching ratios from this study is the first simulation for heavy Higgs bosons. The accuracy of $4 - 9\,\%$ and $10 - 17\,\%$ for BR^{H}_{WW} and BR^{H}_{ZZ} respectively are dominated by statistic uncertainties.

The signal channel chosen corresponds to only $5\,\%$ of all Higgsstrahlung events, so poor statistics can be overcome by analyzing more common final states. Results of this study, which are all limited by statistical effects, thus could be improved most probably. However, further studies on more complicated event reconstruction and background suppression are needed for quantitative statements.

Chapter 6

Overlaid Two-Photon Background at the ILC

At a future linear e^+e^- collider with high luminosity, the interaction of colliding bunches cannot be treated as collision of a single electron-positron pair. Unlike at previous electron-positron colliders like Lep, effects from beam-beam interaction become sizable. The dominant effect is beamstrahlung, i.e. radiation of photons from beam particles in the strong field of the opposite bunch.

One of the secondary effects of beamstrahlung are hadronic reactions $\gamma\gamma \rightarrow$ hadrons from colliding beamstrahlung photons. Significant overlap of these reactions with other events from e^+e^- collisions is expected due to the high photon density from beamstrahlung and the large cross-section of the reaction. Additionally, pile-up of beamstrahlung background in recorded events can occur, if the detector is not able to tag (time-stamp) single bunch crossings at a very short bunch separation.

Two general acceleration technologies are proposed for the Ilc. The time structure of the beams is very different due to technical constraints, see Sec. 3.3. With the superconducting Tesla technology, consecutive bunches are separated by $\approx 150 - 300\,$ns, while the bunch spacing for the normal-conducting Nlc/Glc technology is less than 2 ns. Pile-up of hadrons from collisions of beamstrahlung photons is studied in four scenarios assuming different time-stamping capabilities of the detector.

In particular, the overlap of events from WW-fusion with hadrons from colliding beamstrahlung photons is simulated, assuming the same scenarios for the detector's time-stamping capabilities. It is found, that the separation from background critically depends on the amount of accumulated beam background. In case of the Nlc/Glc technology, detector time-stamping better than 10 ns is necessary.

6.1 Beamstrahlung and Hadronic Two-Photon Reactions

Beamstrahlung photons are produced at very low polar angles and leave the interaction region through the beam-pipe. The dominant effects from beamstrahlung with impact on the experiment are the following:

1. Energy loss of the incoming particles leading to a broad energy distribution of the incoming beams. The size of the effect is similar to that of initial state radiation (ISR) of the colliding particles.

2. The beamstrahlung photons convert to create e^+e^- pairs inside the bunches. These

pairs typically have low transverse momentum. With a high magnetic field (more than 3 T), the largest fraction is constrained to the beam-pipe. However, a sizeable number of particles might hit the most forward part of the detector and elements of the accelerator. This leads to a) hits in the most forward calorimeters used for luminosity measurements and b) secondary particles from nuclear interactions. Especially neutrons from these reactions might re-enter the detector and produce hits in the central part.

3. Creation of hadrons in collisions of beamstrahlung photons, $\gamma\gamma \to$ hadrons. Although much lower in production rate than e^+e^- pairs, this process has a tail to higher transverse momenta. Therefore, particles created in these collisions can lead to additional reconstructed particle flow objects. In case of neutral particles (mainly photons from π^0 decays), they are not collimated to the forward region by the magnetic field.

The effect of beamstrahlung-induced background in terms of additional occupancy of detector components [95] and the resulting difficulties in pattern recognition and event reconstruction have been studied in detail [96] already. In this analysis, the impact of two-photon reactions $\gamma\gamma \to$ hadrons from colliding beamstrahlung photons on the reconstruction of events from Higgs production in WW-fusion is studied.

One particular aspect of the analysis is the possibility of accumulating two-photon events from more than one bunch-crossing, if the detector is not capable to tag the reconstructed particle flow objects (i.e. reconstructed charged and neutral particles) with their associated bunch-crossing. This time-stamping depends on timing informations of associated hits in all contributing detector components (vertex detector, central tracker, calorimeter), but does not require readout of the respective detector signals. Since a large part of the additional background particles is neutral, the time-stamping capability of the calorimeter alone is of particular importance.

The bunch schemes for the superconducting Tesla technology and for the normal-conducting Nlc/Glc technology are very different. At Tesla, the bunch separation is 337 (176) ns at $\sqrt{s} = 500\,(800)$ GeV. At Nlc/Glc, consecutive bunches are separated by only 1.4 ns. Therefore, the effort needed to achieve efficient bunch tagging is more challenging at the warm machine.

	Tesla		Nlc/Glc	
	500 GeV	800 GeV†	500 GeV	1 000 GeV
Number of bunches per train	2 820	4 886	192	
Bunch separation Δt [ns]	337	176	1.4	
Bunch train length [μs]	950	860	0.267	
Average number of $\gamma\gamma \to$ hadrons / BX‡	0.248	0.399	0.103	0.270

Table 6.1: *Machine parameters relevant for the different time structures of* Tesla *and* Nlc/Glc. *Values from [57].*
† Tesla *parameters are available for* 800 GeV *only*
‡ *The number of background interactions corresponds to photon collisions with center-of-mass energy* $W > 5$ GeV.

The average number of two-photon reactions $\langle N_{\gamma\gamma}\rangle$ recorded as one event is given by

$$\langle N_{\gamma\gamma}\rangle = n_{\gamma\gamma}^{BX}\,\frac{\sigma_t}{\Delta t}, \tag{6.1}$$

with the average number $n_{\gamma\gamma}^{BX}$ of $\gamma\gamma \to$ hadrons reactions per bunch crossing, the detector time-stamping capability σ_t and the bunch spacing Δt. Numbers of the relevant machine parameters for the Tesla and Nlc/Glc proposals [54, 55, 56] are summarized in Tab. 6.1. The expected average $n_{\gamma\gamma}^{BX}$ is estimated using the luminosity per bunch crossing, simulations on the luminosity spectrum of colliding beamstrahlung photons and a lower cut-off on the $\gamma\gamma$ invariant mass of 5 GeV at the calculation of the $\gamma\gamma \rightarrow$ hadrons cross-section.

Four scenarios are studied, which are summarized in Tab. 6.2:

1. The Tesla case. Due to the large bunch spacing, single bunch-tagging is feasible.

2. The Nlc/Glc with very fast time-stamping capability of 5.6 ns. This scenario corresponds to background pile-up from 4 bunch-crossings.

3. The Nlc/Glc with time-stamping capability as foreseen for the Lhc detectors, which is approximately 25 ns. This scenario assumes background pile-up from 18 bunch-crossings.

4. The Nlc/Glc with time-stamping capabilities of recent detectors at Hera or Tevatron, which is of the order of 90 ns. This scenario assumes background pile-up from 64 bunch-crossings.

Scenario	Machine	# BX	Tagging resolution [ns]	$\langle N_{\gamma\gamma} \rangle$ 500 GeV	1 000 GeV
1	Tesla	1	337/176	0.24	0.4
2	Nlc/Glc	4	5.6	0.4	1.1
3	Nlc/Glc	18	25	1.8	4.9
4	Nlc/Glc	64	89	6.4	17.3

Table 6.2: *Four scenarios are defined for different collider technology and detector time-stamping ability. The table summarizes the average number of hadronic two-photon interactions overlaid to one measured event.*

6.2 Event Simulation and General Properties

Hadronic two-photon reactions are simulated in two steps. With `GUINEA-PIG` [97], the energy of two beamstrahlung photons is simulated according to the different accelerator parameters [57], which are summarized in Tab. 6.3. In the case of Tesla, machine parameters given for $\sqrt{s} = 800$ GeV are assumed to be valid at $\sqrt{s} = 1\,000$ GeV as well.

	Tesla†	Nlc/Glc
Center-of-mass energy $\sqrt{s}$ [GeV]	1 000	1 000
Bunch charge Q $\left[10^{10}\,e\right]$	1.4	0.75
Beam cross section σ_x/σ_y [nm]	392.0/2.8	219.0/2.1
Bunch length σ_z [μm]	300	110
Emittances ϵ_x/ϵ_y [μrad]	8.0/0.015	3.6/0.04
Beta functions β_x/β_y [mm]	15.0/0.4	13.0/0.11

Table 6.3: *Machine parameters used to generate the beamstrahlung spectrum with* `GUINEA-PIG`*. Values taken from [57].*
† *Parameters for* Tesla *at* 800 GeV.

The hadronic interaction of the two photons is simulated with PYTHIA [69]. Only photon pairs with center-of-mass energy $W > 5\,\text{GeV}$ are accepted. The PYTHIA default setting MSEL=2 is used, which includes hard QCD scattering, semi-hard QCD processes and diffractive scattering. Events with $W < 5\,\text{GeV}$ are not considered, although they yield further charged and neutral particles, which enter the sensitive detector volume [98].

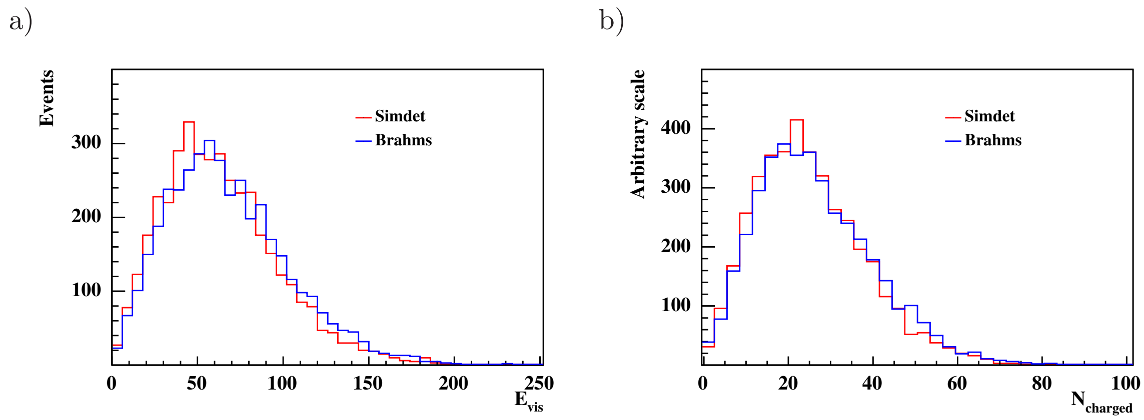

Figure 6.1: *Comparison of a) visible energy and b) number of reconstructed charged objects for the full simulation* BRAHMS *and the fast Monte Carlo* SIMDET.

The HADES library [99] finally is used to overlay the simulated two-photon interactions to physical events from an arbitrary source. The number of events overlaid is varied according to Poisson statistics with the mean of $\langle N_{\gamma\gamma} \rangle$.

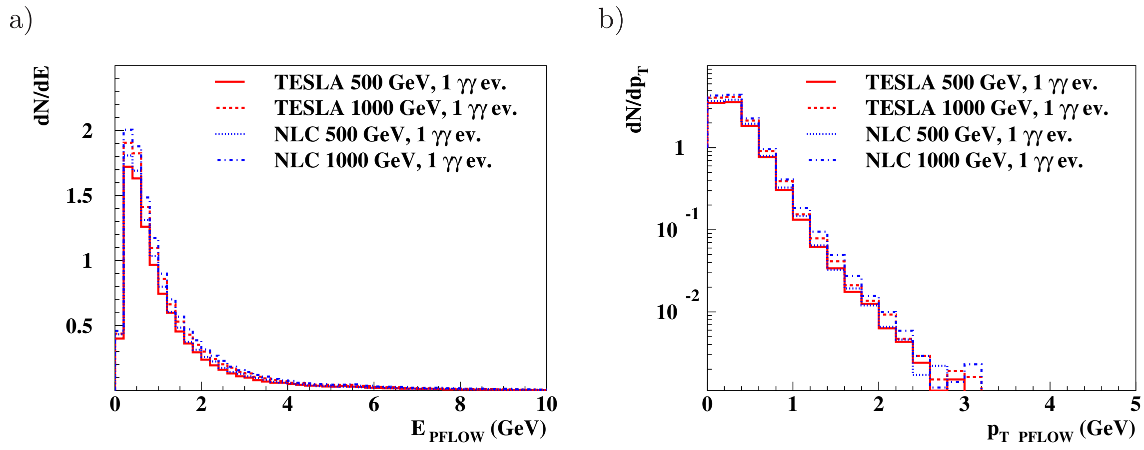

Figure 6.2: *Distributions of a) energy and b) transverse momentum for particles from one hadronic two-photon event at* TESLA *and* NLC/GLC *at* $\sqrt{s} = 500$ *and* $1\,000\,\text{GeV}$.

The detector response is simulated using the fast parametric Monte Carlo SIMDET [91]. Cross checks with the full GEANT 3-based [76] simulation BRAHMS [92] are performed in a scenario, where hadronic two-photon events are integrated over 64 bunch crossings at $\sqrt{s} = 500\,\text{GeV}$. The total visible energy as well as the number of reconstructed charged particles are in reasonable agreement for both methods, justifying the use of the fast simulation (see Fig. 6.1).

Properties of hadronic two-photon events

Particles from hadronic two-photon events tend to have low energy and small transverse momentum, see Fig. 6.2. Only 5 % of all interactions contain particles with energy $E_{pflow} >$ 5 GeV.

For single two-photon reactions, only small differences are expected between different accelerator proposals and center-of-mass energies. However, the picture changes dramatically if pile-up effect due to limited detector timing resolution are taken into account. Fig. 6.3 shows the energy spectrum and polar angle distribution of the energy deposition for recorded pile-up according to the four scenarios defined in Tab. 6.2. The main fraction of energy is deposited under small polar angles θ, and the particles have low energy on average. Particles entering the central detector are mainly photons from π^0 decays. Low energy charged particles are deflected towards the forward detectors by the magnetic field. However, some 10 GeV of energy

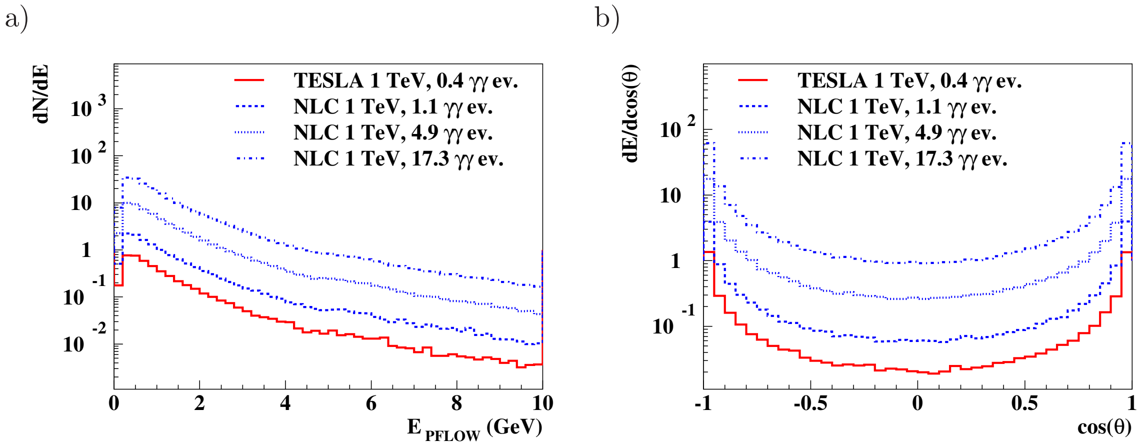

Figure 6.3: *Cumulated spectra from hadronic two-photon events for the four scenarios of Tab. 6.2. Shown are a) the number density as a function of the particle energy and b) the cumulated energy deposition as a function of the polar angle θ.*

are deposited in the central part of the detector with $|\cos\theta| < 0.8$, if one third of a NLC/GLC bunch train is integrated. Already with time-stamping capabilities of 25 ns, more than one high energetic particle with $E_{pflow} > 5$ GeV per recorded event is expected on average.

6.3 Overlaid Events in WW-Fusion

A precise measurement of the cross section of WW-Fusion $\mathrm{e^+e^-} \rightarrow \mathrm{H}\,\nu\bar{\nu}$ (Fig. 6.4) is important to deduce the total Higgs decay width, yield an improved measurement of the Higgs branching fractions [100] and an improved global fit of Higgs couplings [101]. WW-fusion is the dominant Higgs production process at high center-of-mass energies, as already outlined in Sec. 2.2.1. The cross-section for $m_{\mathrm{H}} = 120$ GeV at $\sqrt{\mathrm{s}} = 1\,000$ GeV is approximately 210 fb, while Higgsstrahlung only has a cross-section of approximately 17 fb.

For Higgs bosons with $m_{\mathrm{H}} = 120$ GeV, the dominant decay mode is $\mathrm{H} \rightarrow \mathrm{b\bar{b}}$. The excellent b-tagging abilities at planned ILC detectors provide good suppression of hadronic background without b-quarks, as is shown in a previous study of the cross-section measurement of WW-fusion [88]. The most important background remaining arises from $\mathrm{e^+e^-} \rightarrow \mathrm{b\bar{b}}\,\nu\bar{\nu}$, which has major contributions from WW-fusion to Z-bosons (Fig. 6.4 b). This background processes includes the decay $\mathrm{Z} \to \mathrm{b\bar{b}}$ and can be separated from the Higgs signal by a cut on the visible mass, i.e. the invariant mass of all detected particles.

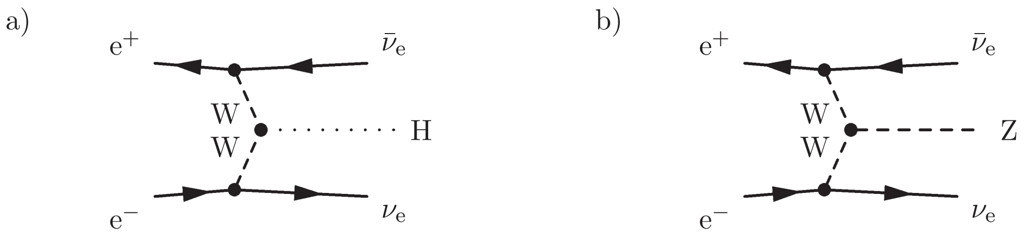

Figure 6.4: *Production in* WW*-fusion a) is the dominant Higgs process at high center-of-mass energies. The main contribution for SM background from* $\mathrm{e^+e^-} \to \mathrm{b\bar{b}}\,\nu\bar{\nu}$ *arises from the equivalent process with* Z*-bosons b).*

Assuming $\int\mathcal{L} = 500\,\mathrm{fb}^{-1}$ of data, about 11 500 signal events from Higgs production through WW-fusion and 7 000 events from $\mathrm{b\bar{b}}\,\nu\bar{\nu}$ background are expected for $\sqrt{s} = 1\,000\,\mathrm{GeV}$ and $m_{\mathrm{H}} = 120\,\mathrm{GeV}$. Events are generated using `WHiZard` [89] with `MADGraph` [90] matrix elements. All tree-level diagrams contributing to $\mathrm{e^+e^-} \to \mathrm{b\bar{b}}\,\nu\bar{\nu}$ are considered for background.

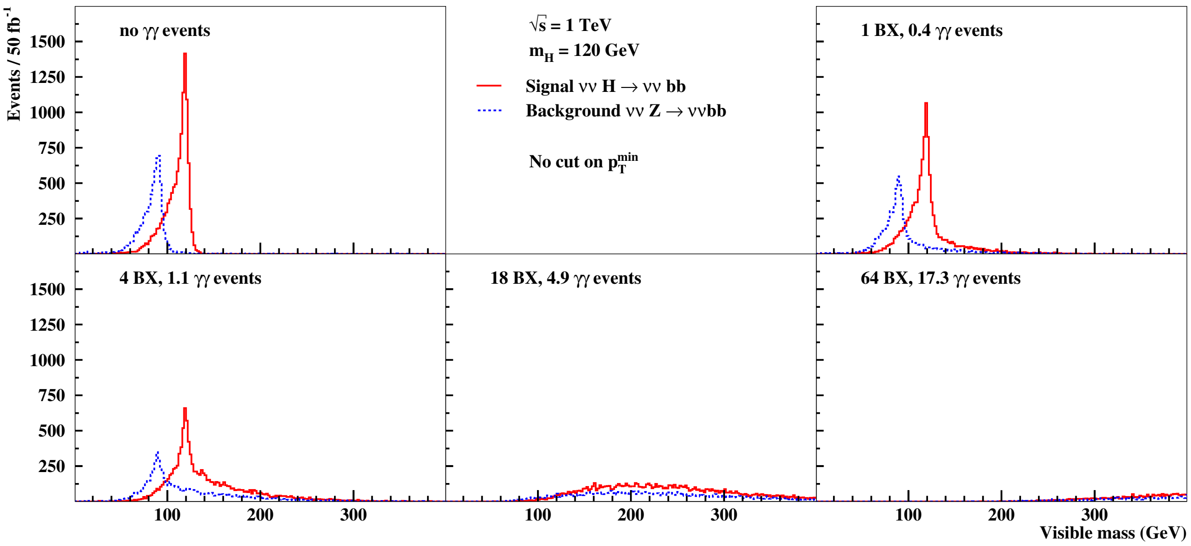

Figure 6.5: *Distributions of the visible mass for* $\mathrm{H}\nu\bar{\nu}$ *signal and* $\mathrm{b\bar{b}}\,\nu\bar{\nu}$ *background with varying amount* $\langle N_{\gamma\gamma}\rangle$ *of overlaid two-photon interactions. The respective mass peaks are washed out completely for* $\langle N_{\gamma\gamma}\rangle = 4.9$ *and* $\langle N_{\gamma\gamma}\rangle = 17.3$.

The distribution of the visible mass for events from signal and background is shown in Fig. 6.5. The top-left plot shows the reference case without overlaid two-photon interactions. The peaks have tails to lower masses due to undetected neutrinos in decays of b-hadrons. For the other plots, two-photon interactions are overlaid according to the pile-up scenarios defined in Tab. 6.2. If few two-photon interactions are overlaid, significant amounts of events from signal and $\mathrm{b\bar{b}}\,\nu\bar{\nu}$ background remain unaffected. These events still exhibit the original mass peak, while events with additional particles from two-photon interactions yield a much broader distribution. Already for the best NLC/GLC scenario with an average of 1.1 overlaid interactions, the mass spectrum is significantly deteriorated. For the other two scenarios with pile-up of 4.9 and 17.3 two-photon interactions, no clear mass peak for H $\nu\bar{\nu}$ signal or b$\bar{\text{b}}$ $\nu\bar{\nu}$ background is observed at all.

In a previous study for TESLA, an attempt was made to recover the undeteriorated mass distributions by rejection of events with overlaid interactions. Since the collision of beamstrahlung photons usually happens at another point within the colliding bunches, this can be accomplished by rejecting events with a secondary vertex, which is displaced only along the z-direction. Displacements in x- and y-direction within the bunches cannot be resolved, see also the bunch parameters in Tab. 6.3. A loss in effective luminosity of 20 % is obtained already for $\langle N_{\gamma\gamma}\rangle = 0.1$ at $\sqrt{s} = 350$ GeV [102]. This method thus is not applicable here due to the much higher pile-up expected in some of the scenarios. Also, the method is not suited for NLC/GLC, where the bunches are too short for effective identification of the vertices from two-photon interactions.

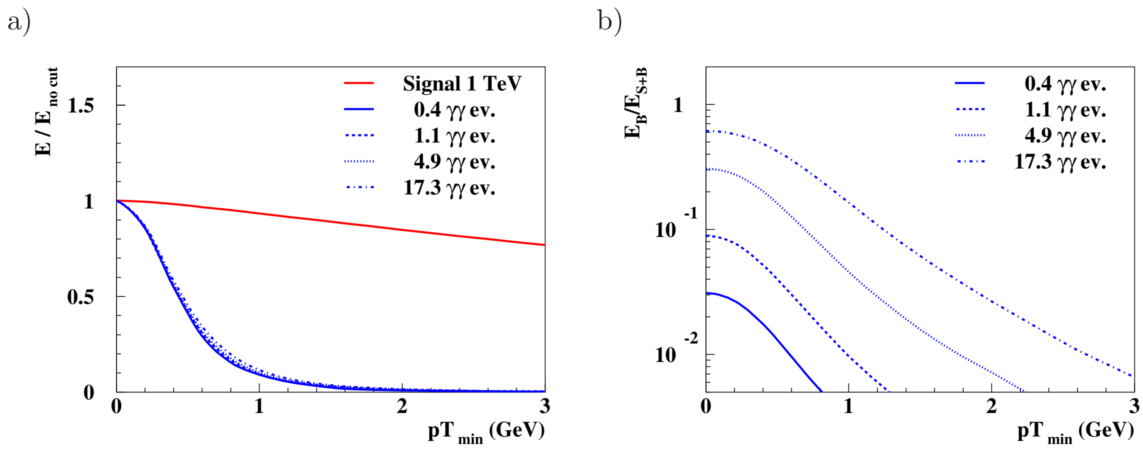

Figure 6.6: *Dependence of the reconstructed energy on a cut on p_T: a) Shows the ratio with respect to no cut for signal and the four background scenarios separately. In b), the background contamination is shown when signal and background are overlaid.*

Therefore, a simple criterion is used to reject single particles if they originate from two-photon interactions. These particles are expected to have low transverse momentum, as discussed above. A cut p_T^{min} on the transverse momentum p_T is introduced, and the visible mass is calculated only from particles with $p_T > p_T^{min}$.

	TESLA	NLC/GLC		
	1 BX	4 BX	18 BX	64 BX
$\langle N_{\gamma\gamma}\rangle$	0.4	1.1	4.9	17.3
p_T^{min} [GeV]	0.0	0.6	1.0	1.6

Table 6.4: *Values for the cut parameter p_T^{min} as optimized for each scenario. Events are counted within a mass window of* 30 GeV *width. The respective windows are shifted to cover the signal peak.*

Fig. 6.6 a) shows the fraction of energy from two-photon interactions and H$\nu\bar{\nu}$ signal still accepted as a function of p_T^{min}. Already values $p_T^{min} \sim 1$ GeV significantly suppress particles from two-photon interactions, while the effect on the signal from H $\nu\bar{\nu}$ remains moderate. In Fig. 6.6 b), the energy E_B from two-photon interactions relative to the total event energy E_{S+B} is shown. Large differences between the four scenarios of Tab. 6.2 are observed.

The value of p_T^{min} is fixed for each scenario such, that less than 5 % of the energy of the accepted particles comes from two-photon interactions. This leads to the values of p_T^{min} listed in Tab. 6.4.

The distributions of the visible mass from $\mathrm{H}\,\nu\bar{\nu}$ signal and $\mathrm{b\bar{b}}\,\nu\bar{\nu}$ background after the p_T^{min} cut are shown in Fig. 6.7. Also in the scenario with $\langle N_{\gamma\gamma}\rangle = 17.3$, it is possible to recover the original mass distributions to some extent. However, the mass peaks broaden significantly, which dilutes the separation of signal and background.

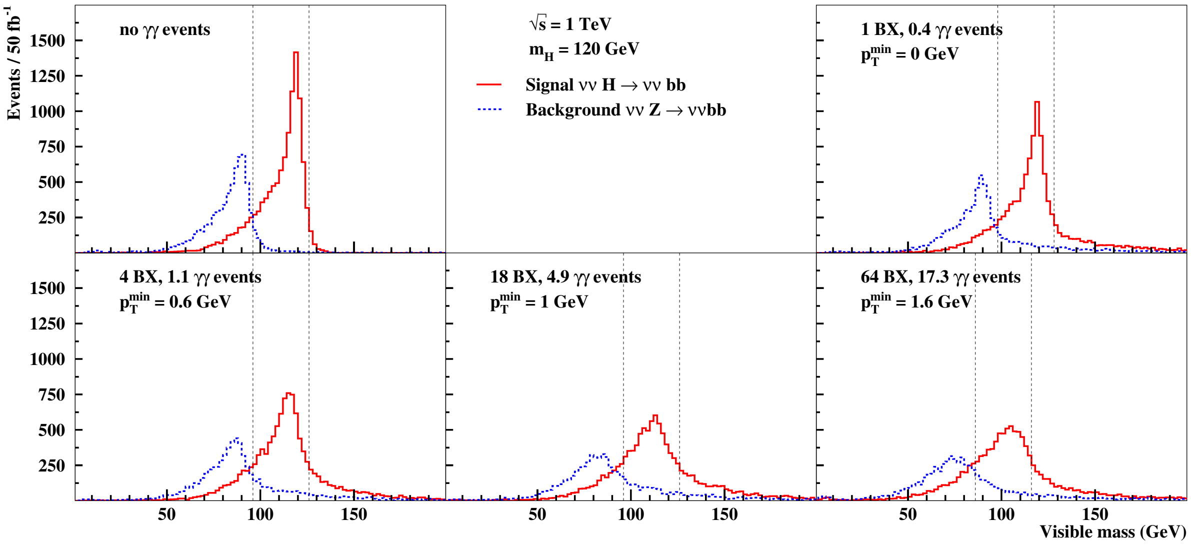

Figure 6.7: *Distributions of the visible mass for Higgsstrahlung and background. The top-left plot shows the reference with no overlaid two-photon interactions.*

To quantify the effect, events are counted within a mass window of 30 GeV width around the signal mass peak. Since the mass distributions are not only widened but are also shifted to lower masses with increasing number of overlaid interactions, the position of the window is adjusted for each scenario separately to optimize the signal to background ratios. The number of $\mathrm{H}\,\nu\bar{\nu}$ signal and $\mathrm{b\bar{b}}\,\nu\bar{\nu}$ background events within the mass window are listed in Tab. 6.5. A significant degradation is observed with increasing pile-up of two-photon interactions.

Fig. 6.8 shows the number of signal events and the signal over background ratio as a function of the number of integrated bunch crossings and normalized to the values obtained for 1 BX at Tesla, which offers the best experimental conditions among all studied scenarios. However, already in this scenario a loss in signal events of 25 % is observed, which is of the same order than explored in [102] as discussed above.

All Nlc/Glc scenarios yield reduced signal reconstruction efficiency. For scenario 2, a loss in signal events of few % is observed when compared to the Tesla scenario. However, the signal to background ratio drops by 18 %. More severe are the effects in scenarios 3 and 4 with more than 15 % loss in signal events and a signal to background ratio smaller by more than 30 %.

6.4 Conclusions

It is shown, that beam-beam background can have significant impact on high precision measurements at Ilc. Hadronic interactions of colliding beamstrahlung photons have a significant probability to overlap with hard scattering processes. If detector time-stamping does not allow tagging of individual bunches, this effect is further amplified through pile-up of two-photon interactions.

	Number of events		
Scenario	Signal	Background	S/B ratio
no $\gamma\gamma$	9 666	790	12.24
1 BX	7 657	1 206	6.35
4 BX	7 425	1 387	5.35
18 BX	6 626	1 450	4.57
64 BX	6 433	1 586	4.06

Table 6.5: *The numbers of events from* WW*-fusion signal and* $\mathrm{b\bar{b}}\,\nu\bar{\nu}$ *background within an optimized mass window of* 30 GeV *width. A clear degradation is observed, when hadronic two-photon events are overlaid.*

Four different scenarios are studied motivated by the different accelerator technologies proposed for ILC. For the superconducting TESLA technology, bunches are separated by some 100 ns and single bunch tagging is possible with today's detector technology. At the normal-conducting NLC/GLC technology in contrast, bunches are separated by less than 2 ns, and scenarios with pile-up from 64, 18, 4 bunch-crossings are studied to account for different detector time-stamping capabilities. A cut on the transverse momentum of reconstructed particles is used to reject particles from two-photon interactions.

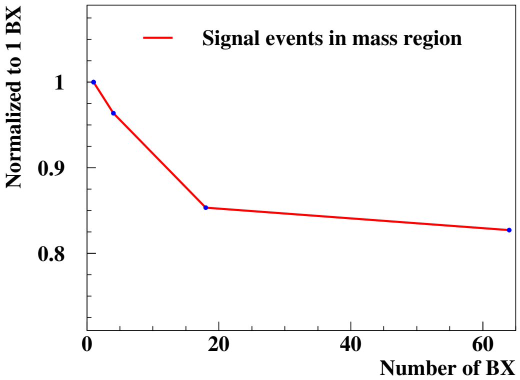

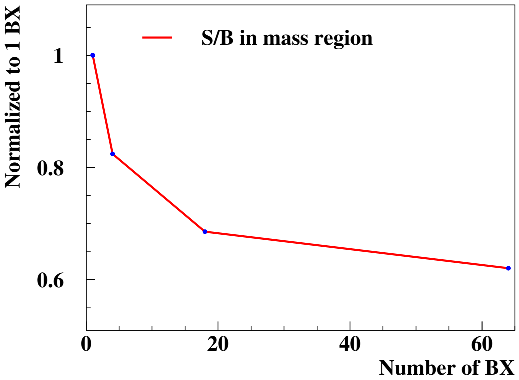

Figure 6.8: *Degradation of the ratio of signal to background events as a function of the integration time. Values are normalized with respect to integration over one bunch-crossing.*

In a simplified selection of WW-fusion events $\mathrm{e^+e^-} \rightarrow \mathrm{H}\,\nu\bar{\nu} \rightarrow \mathrm{b\bar{b}}\,\nu\bar{\nu}$ the separation from signal and $\mathrm{e^+e^-} \rightarrow \mathrm{b\bar{b}}\,\nu\bar{\nu}$ background is studied. When two-photon interactions are overlaid, a decrease of accepted signal events of 25 % is observed for the TESLA scenario. Compared to this best experimental conditions, results for NLC/GLC are worse by 3 – 16 % for integration over 4 – 64 bunch-crossings. The signal to background ratio even is worse by 15 – 36 %. For the NLC/GLC technology very fast detectors with time-stamping capability of better than 10 ns are necessary.

The study presented here was initiated together with other benchmark Higgs analyses [103] as input to the International Technology Recommendation Panel. The task of this panel was to decide for the ILC accelerator technology. Recently, the final decision in favor of the TESLA technology was announced [59].

Chapter 7

Summary

The Standard Model is a well tested theory of elementary particles and their interaction. It provides a coherent description of electromagnetic, weak and strong interactions based on the principle of local gauge invariance. However, the invariance of the gauge group describing the electroweak interactions is broken, which is most obvious from the fact that the respective gauge bosons $\mathrm{W}^{\pm}$ and Z^0 are massive. In the Standard Model, electroweak symmetry breaking is explained by the Higgs mechanism, which predicts one scalar Higgs boson. This particle has not yet been observed. The current limits are $m_{\mathrm{H}} > 114.4\,\mathrm{GeV}$ from direct searches and $m_{\mathrm{H}} < 252\,\mathrm{GeV}$ from indirect fits to SM precision measurements, both at the 95 % confidence level. The mechanism of electroweak symmetry breaking is the only part of the Standard Model, which has not yet been resolved experimentally, and also alternative explanations for the breaking of electroweak symmetry are studied.

In $\mathrm{e}^+\mathrm{e}^-$ collisions at $\sqrt{\mathrm{s}} = 189-209\,\mathrm{GeV}$ recorded with the Opal detector in the years 1998 to 2000, a search is performed for signatures with technipions. These particles are expected from Technicolor theories, which describe dynamical breaking of electroweak symmetry by new strong interactions. No excess of data over SM background expectations is observed, and exclusion limits are derived in the framework of the Technicolor Straw-man Model (TCSM), an effective low-energy description of Technicolor phenomena. Mass limits are placed in the plane of $m_{\pi_{\mathrm{T}}}$ vs. $m_{\rho_{\mathrm{T}}/\omega_{\mathrm{T}}}$. An absolute lower limit $m_{\pi_{\mathrm{T}}} > 87\,\mathrm{GeV}$ is obtained for a well motivated set of TCSM parameters proposed in [41].

If the SM Higgs boson exists, it can be discovered at the Lhc. This machine is also sensitive to most alternative theories predicting other new particles beyond the spectrum of the Standard Model. Some of these models include Higgs bosons, which might have similar properties as those predicted for the SM Higgs boson. Best suited for precision measurements needed to distinguish between particles of different models is the Ilc.

A simulation is performed to investigate the prospects to measure the SM Higgs decay width from the reconstructed Higgs lineshape at Ilc. In order to disentangle the physical Higgs width from the detector mass smearing, the width must be at least of order 1 GeV, which is the case for $m_{\mathrm{H}} \gtrsim 200\,\mathrm{GeV}$ in the Standard Model. A model independent fit is applied to the reconstructed Higgs mass distribution, from which the Higgs width, Higgs mass and event rate are obtained. In addition, the branching ratios of the Higgs boson to pairs of W- and Z-bosons can be derived from the analysis, assuming these are the only sizeable Higgs decay modes. For $\int\mathcal{L} = 500\,\mathrm{fb}^{-1}$ of integrated luminosity, the total width is measured with an uncertainty of $23-34\,\%$ for Higgs bosons with $m_{\mathrm{H}} = 200-320\,\mathrm{GeV}$.

Proposals for the Ilc are based on two general acceleration concepts, the superconducting Tesla technology and the normal-conducting Nlc/Glc technology. Due to different time-structures of the beams, the impact of overlaid background from colliding beamstrahlung photons can be very different at both technologies. Particularly, beam-induced two-photon background can be accumulated over several bunch-crossings, if the detector is not capable to tag single bunch-crossings at the NLC/GLC technology. The effect of hadrons from colliding beamstrahlung photons overlaid to events from Higgs production in WW-fusion is investigated. It is found, that the separation from $e^+e^- \rightarrow b\bar{b}\,\nu\bar{\nu}$ background events critically depends on the pile-up of beam-induced background, and that a very fast detector with time-stamping capabilities better than 10 ns is needed for the NLC/GLC technology.

Appendix A

Jet Algorithms

Quarks produced in particle collisions never appear as isolated particles. Due to confinement, they hadronize and form a bunch of color neutral mesons and baryons. These so-called jets are somewhat collimated, depending on the initial quark energy and the quark flavor. Algorithms are used to group the reconstructed tracks and clusters of an event to jets. Thereby, two general approaches are used:

- **Cluster jet algorithms** group particles according to a distance factor $y(p_i, p_j)$, which is a function of two four-momenta p_i and p_j. Different algorithms are distinguished by the varying definition of y. Cluster algorithms cluster all particles of an event to jets and therefore are generic jetfinders for e^+e^- colliders.

- **Cone algorithms** use geometrical information only. The algorithm needs two parameters: a minimum energy E_{min} and a cone radius R. Most important feature of the cone algorithms is, that not every particle of an event is necessarily assigned to a jet. Cone algorithms have been developed for hadron colliders, where beam remnants from spectator quarks are detected which do not originate from the hard process.

Throughout this thesis, cluster algorithms are used to group events to jets. Additionally, a cone algorithm is used for b-tagging at Opal (Sec. 4.3.3).

A.1 Cluster Algorithms

Cluster jetfinder are characterized by the definition of the distance parameter $y(p_i, p_j)$. In this thesis, the Durham parameter y_D and the JADE parameter y_J are used, defined according to

$$y_D\left(p_i, p_j\right) = \frac{2\,\min\left(E_i^2, E_j^2\right)}{E_{vis}^2}\left(1 - \cos\theta_{ij}\right) \qquad y_J\left(p_i, p_j\right) = \frac{E_i\,E_j}{E_{vis}^2}\left(1 - \cos\theta_{ij}\right) \tag{A.1}$$

with the particles' energies E_i and E_j, the angle θ_{ij} between the two particles and the total visible energy of the event E_{vis}.

Jets are found starting with considering all particles of an event as pseudo-jets. For all possible pairs, the distance parameters are calculated, and the pair with the smallest distance is combined thus decreasing the number of pseudo-jets N by one. The minimum distance is also denoted as $Y_{N,N-1}$. The number of pseudo-jets is reduced iteratively, until either N reaches a fixed number, or $Y_{N,N-1}$ lays above a certain value. At any step, $Y_{N,N-1}$ can be interpreted as a measure of how N-jet like an event is.

A.2 Cone Algorithms

Cone algorithms start with a set of seed particles. Usually, these are the most energetic particles found in an event, but the definition in principle is arbitrary. A fixed cone with opening radius R (which might be a function of the seed particle energy) is formed around each seed particle. The total four momentum sum of all particles within the cone is calculated, and from this a new cone axis and radius is determined. The procedure is repeated, until a stable cone axis is found. At this stage, the cone four momentum is considered a pseudo-jet.

All pseudo-jets of an event are not necessarily independent, e.g. some particles might be double assigned. One is free to chose the criteria for solving these double assignments. In the end, all pseudo-jets with an energy in excess of a fixed minimum energy E_{min} are finally taken as reconstructed jets.

Appendix B

Kinematic Fits

Often, boundary conditions can be assumed in measurements. They can be formulated as

$$f\left(\vec{x}\right) = 0, \tag{B.1}$$

where $\vec{x}$ is a set of measured quantities. Generally, this formula will not be satisfied due to measurement uncertainties, which are described by the covariance matric V. The measured values now can be varied within their uncertainties in order to fulfill the boundary conditions. This is done by minimizing

$$\chi^2\left(\vec{x}', \lambda\right) = \left(\vec{x} - \vec{x}'\right)^t V^{-1} \left(\vec{x} - \vec{x}'\right) + 2\lambda \sum_i f_i\left(\vec{x}'\right) \tag{B.2}$$

with the varied observables $\vec{x}'$ and boundary conditions f_i. The factor λ is called Lagrange multiplier. It is set to arbitrary high values during the fit to ensure the boundary conditions to be satisfied.

The best fit result $\chi^2 = \min\left(\chi^2\left(\vec{x}', \lambda \to \infty\right)\right)$ follows a χ^2 distribution $\xi(\chi^2, N)$, where N is the number of constraints.

A measure of the goodness of the fit is the χ^2 probability

$$PROB\left(\chi^2\right) = \int_{\chi^2}^{\infty} \xi(x, N)\, \mathrm{d}x \tag{B.3}$$

This is expected to be a flat distribution, if the measurement uncertainties are gaussian, their values are estimated correctly and the assumptions of the boundary conditions are justified. Otherwise, $PROB\left(\chi^2\right)$ will tend to lower values, that is a general higher χ^2 than expected. Especially if the boundary conditions are not satisfied, $PROB\left(\chi^2\right)$ will be very small.

Kinematic fits are used for two purposes. If the boundary conditions are known to be correct, the measurement precision often increases when the measured values are fitted to obey the conditions. On the other hand, kinematic fits can be used to test whether measurements are compatible with assumed boundary conditions. Both applications are used within this thesis.

If jet momenta are used as input parameters for a kinematic fit, they are usually not defined in Cartesian coordinates. A common way is to fix the jet mass and use $\log|p|$, θ and φ to describe the jet momenta. This choice provides uncorrelated values with approximately gaussian distributions.

Appendix C

Likelihood Method

Likelihood estimators are used to compare a set of observables with a given hypothesis for the distribution of this observables. Output values lie within zero (poor agreement) and one (good agreement). It is possible to define several classes of hypotheses, and the likelihood is evaluated according to one among these.

As input to the likelihood estimator, a set of probability density functions f_i^j is needed, which describe the expectation of the i-th observable in the j-th event class. For a likelihood from n observables and m classes, $n \times m$ input functions are needed.

The probability of measuring the value x_i in the i-th observable in an event of the j-th class is

$$p_i^j(x_i) = \frac{f_i^j(x_i)}{\sum_{k=1}^{m} f_i^k(x_i)}. \tag{C.1}$$

For an event with the measured set of observables $x_1 ... x_n$, these probabilities can be combined to the likelihood of the event to belong to the j-th event class as

$$\mathcal{L}^j = \frac{w^j \prod_{l=1}^{n} p_l^j(x_l)}{\sum_{k=1}^{m} w^k \prod_{l=1}^{n} p_l^k(x_l)}, \tag{C.2}$$

where w^j is a weight factor for the j-th class. The weights can be used to account e.g. for the relative occurrence of the different classes. Since these usually are not known, the unweighted likelihood estimator

$$\mathcal{L}^j = \frac{\prod_{l=1}^{n} p_l^j(x_l)}{\sum_{k=1}^{m} \prod_{l=1}^{n} p_l^k(x_l)} \tag{C.3}$$

is used much more often.

Obviously, the likelihood values of all classes sum up to one. However, the likelihood cannot generally be regarded as probability. Only in the special case, where all observables combined in the likelihood are uncorrelated and all weights are equal, the likelihood $\mathcal{L}^j$ is the probability of an event belonging to class j.

Appendix D

OPAL Monte Carlo Files

$\sqrt{s}$ [GeV]	Process $e^+e^- \to$	Number of events	Cross section [pb]	Integrated luminosity $\left[\mathrm{pb}^{-1}\right]$	MC run No.
189	$q\bar{q}(\gamma)$	500 000	99.78	5	5188, 5189
189	$q\bar{q}\,q\bar{q}$	171 478	8.58	20	8636
189	$\ell^+\ell^-\,q\bar{q},\ \ell \neq e$	176 007	8.80	20	8637
189	$e^+e^-\,q\bar{q}$	127 583	25.52	5	7849
192	$q\bar{q}(\gamma)$	250 000	94.84	2.64	5195
192	$q\bar{q}\,q\bar{q}$	43 704	8.74	5	9204
192	$\ell^+\ell^-\,q\bar{q},\ \ell \neq e$	44 986	9.00	5	9205
192	$e^+e^-\,q\bar{q}$	207 129	41.423	5	9277
196	$q\bar{q}(\gamma)$	250 000	90.09	2.78	5196
196	$q\bar{q}\,q\bar{q}$	89 210	8.92	10	9201
196	$\ell^+\ell^-\,q\bar{q},\ \ell \neq e$	91 802	9.18	10	9202
196	$e^+e^-\,q\bar{q}$	202 483	40.50	5	9280
200	$q\bar{q}(\gamma)$	300 000	85.56	3.51	5119
200	$q\bar{q}\,q\bar{q}$	180 395	9.02	20	9207
200	$\ell^+\ell^-\,q\bar{q},\ \ell \neq e$	186 489	9.32	20	9208
200	$e^+e^-\,q\bar{q}$	197 391	39.48	5	9318
202	$q\bar{q}(\gamma)$	250 000	83.36	3	5199
202	$q\bar{q}\,q\bar{q}$	90 342	9.03	10	9701
202	$\ell^+\ell^-\,q\bar{q},\ \ell \neq e$	93 969	9.40	10	9702
202	$e^+e^-\,q\bar{q}$	195 239	39.05	5	9713
205	$q\bar{q}(\gamma)$	250 000	81.31	3.07	5183
205	$e^+e^-\,q\bar{q}$	191 676	38.33	5	11202
205	$f\bar{f}\,f\bar{f},\ \neq e^+e^-\,q\bar{q}$	218 776	21.88	10	11218
207	$q\bar{q}(\gamma)$	500 000	79.38	6.30	5190
207	$e^+e^-\,q\bar{q}$	190 557	38.11	5	10788
207	$f\bar{f}\,f\bar{f},\ \neq e^+e^-\,q\bar{q}$	218 652	21.87	10	11212
208	$q\bar{q}(\gamma)$	250 000	78.44	3.19	5191
208	$e^+e^-\,q\bar{q}$	188 939	37.79	5	10452
208	$f\bar{f}\,f\bar{f},\ \neq e^+e^-\,q\bar{q}$	109 591	21.91	5	10713

Table D.1: *Monte Carlo samples from the* Opal *MC database, which are used to describe the background estimation for the search for Technicolor in Chpt. 4.*

List of Figures

List of Tables

Bibliography

[1] P. W. Higgs, *Broken symmetries, massless particles and gauge fields*, Phys. Lett. **12**(1964) 132.

P. W. Higgs, *Broken symmetries and the masses of gauge bosons*, Phys. Rev. Lett. **13**(1964) 508.

F. Englert and R. Brout, *Broken symmetry and the mass of gauge vector mesons*, Phys. Rev. Lett. **13**(1964) 321.

G. S. Guralnik, C. R. Hagen, and T. W. B. Kibble, *Global conservation laws and massless particles*, Phys. Rev. Lett. **13**(1964) 585.

[2] S. L. Glashow, *Partial symmetries of weak interactions*, Nucl. Phys. **22**(1961) 579.

S. Weinberg, *A model of leptons*, Phys. Rev. Lett. **19**(1967) 1264.

A. Salam, *Weak and electromagnetic interactions*, Proceedings of the Nobel Symposium held 1968 at Lerum, Sweden (1968) 367.

[3] C. S. Wu, E. Ambler, R. W. Hayward, D. D. Hoppes, and R. P. Hudson, *Experimental test of parity conservation in beta decay*, Phys. Rev. **105**(1957) 1413.

[4] Super-Kamiokande Collaboration, M. B. Smy *et al.*, *Precise measurement of the solar neutrino day/night and seasonal variation in Super-Kamiokande-I*, Phys. Rev. **D69**(2004) 011104, `hep-ex/0309011`.

[5] K2K Collaboration, M. H. Ahn *et al.*, *Indications of neutrino oscillation in a 250-km long-baseline experiment*, Phys. Rev. Lett. **90**(2003) 041801, `hep-ex/0212007`.

[6] SNO Collaboration, Q. R. Ahmad *et al.*, *Measurement of day and night neutrino energy spectra at SNO and constraints on neutrino mixing parameters*, Phys. Rev. Lett. **89**(2002) 011302, `nucl-ex/0204009`.

[7] KamLAND Collaboration, K. Eguchi *et al.*, *First results from KamLAND: Evidence for reactor anti-neutrino disappearance*, Phys. Rev. Lett. **90**(2003) 021802, `hep-ex/0212021`.

[8] G. 't Hooft and M. J. G. Veltman, *Regularization and renormalization of gauge fields*, Nucl. Phys. **B44**(1972) 189.

[9] J. Goldstone, A. Salam, and S. Weinberg, *Broken symmetries*, Phys. Rev. **127**(1962) 965.

[10] P. D. B. Collins, A. D. Martin, and E. J. Squires, *Particle physics and cosmology* NEW YORK, USA: WILEY (1989) 496p.

[11] Particle Data Group Collaboration, S. Eidelman *et al.*, *Review of particle physics*, Phys. Lett. **B592**(2004) 1.

[12] M. L. Mangano *et al.*, *Event generators for discovery physics* (1996), `hep-ph/9602203`.

[13] A. Djouadi, J. Kalinowski, and M. Spira, *HDECAY: A program for Higgs boson decays in the Standard Model and its supersymmetric extension*, Comput. Phys. Commun. **108**(1998) 56, `hep-ph/9704448`.

[14] J. F. Gunion, L. Poggioli, R. Van Kooten, C. Kao, and P. Rowson, *Higgs boson discovery and properties*, ECONF **C960625**(1996) LTH092, `hep-ph/9703330`.

[15] B. W. Lee, C. Quigg, and H. B. Thacker, *Weak interactions at very high-energies: The role of the HIGGS boson mass*, Phys. Rev. **D16**(1977) 1519.

[16] T. Hambye and K. Riesselmann, *Matching conditions and Higgs mass upper bounds revisited*, Phys. Rev. **D55**(1997) 7255, `hep-ph/9610272`.

[17] ALEPH Collaboration, R. Barate *et al.*, *Search for the Standard Model Higgs boson at LEP*, Phys. Lett. **B565**(2003) 61, `hep-ex/0306033`.

[18] *LEP and SLD electroweak working group* (2004), from `http://lepewwg.web.cern.ch/LEPEWWG/`.

[19] CDF and D0 Collaboration, P. Azzi *et al.*, *Combination of CDF and D0 results on the top-quark mass* (2004), `hep-ex/0404010`.

[20] S. Asai *et al.*, *Prospects for the search for a Standard Model Higgs boson in ATLAS using vector boson fusion*, Eur. Phys. J. **C32S2**(2004) 19, `hep-ph/0402254`.

[21] G. L. Kane, *Perspectives on searching for Higgs physics* Lectures at the XXI GIFT International Seminar on Theoretical Physics and the XVIII International Meeting on Fundamental Physics, Santander, Spain, Jun 4-9, 1990.

D. A. Ross and M. J. G. Veltman, *Neutral currents in neutrino experiments*, Nucl. Phys. **B95**(1975) 135.

[22] B. W. Lee, *Perspectives on theory of weak interactions* Report to a plenary session of 16th ICHEP, Chicago (Batavia), Sep 1972.

[23] H.-S. Tsao, *Higgs boson quantum numbers and the Pell equation* To be publ. in Proc. of Guangzhou Conf. on Theoretical Particle Physics, Guangzhou, PRC, Jan 5-12, 1980.

[24] S. L. Glashow and S. Weinberg, *Natural conservation laws for neutral currents*, Phys. Rev. **D15**(1977) 1958.

[25] J. F. Gunion, H. E. Haber, G. L. Kane, and S. Dawson, *The Higgs hunter's guide* SCIPP-89/13.

J. F. Gunion, H. E. Haber, G. L. Kane, and S. Dawson, *Errata for the Higgs hunter's guide* (1992), `hep-ph/9302272`.

[26] P. Fayet and S. Ferrara, *Supersymmetry*, Phys. Rept. **32**(1977) 249.

H. P. Nilles, *Supersymmetry, supergravity and particle physics*, Phys. Rept. **110**(1984) 1.

H. E. Haber and G. L. Kane, *The search for supersymmetry: Probing physics beyond the Standard Model*, Phys. Rept. **117**(1985) 75.

[27] J. F. Gunion, H. E. Haber, and J. Wudka, *Sum rules for Higgs bosons*, Phys. Rev. **D43**(1991) 904.

[28] R. S. Chivukula and M. Golden, *Hiding the electroweak symmetry breaking sector*, Phys. Lett. **B267**(1991) 233.

J. D. Bjorken, *A full acceptance detector for SSC physics at low and intermediate mass scales: An expression of interest to the SSC*, Int. J. Mod. Phys. **A7**(1992) 4189.

T. Binoth and J. J. van der Bij, *The stealthy Higgs model at future linear colliders* (1999), `hep-ph/9908256`.

[29] G. B. Gelmini and M. Roncadelli, *Left-handed neutrino mass scale and spontaneously broken lepton number*, Phys. Lett. **B99**(1981) 411.

[30] J. C. Pati and A. Salam, *Lepton number as the fourth color*, Phys. Rev. **D10**(1974) 275.

R. N. Mohapatra, J. C. Pati, and L. Wolfenstein, *The superweak model of CP - violation in unified gauge theories*, Phys. Rev. **D11**(1975) 3319.

G. Senjanovic and R. N. Mohapatra, *Exact left-right symmetry and spontaneous violation of parity*, Phys. Rev. **D12**(1975) 1502.

R. E. Marshak and R. N. Mohapatra, *Quark - lepton symmetry and b-l as the U(1) generator of the electroweak symmetry group*, Phys. Lett. **B91**(1980) 222.

R. N. Mohapatra and D. P. Sidhu, *Implications for gauge theories if search for parity violation in atomic physics fails*, Phys. Rev. Lett. **38**(1977) 667.

[31] L. Randall and R. Sundrum, *A large mass hierarchy from a small extra dimension*, Phys. Rev. Lett. **83**(1999) 3370, `hep-ph/9905221`.

L. Randall and R. Sundrum, *An alternative to compactification*, Phys. Rev. Lett. **83**(1999) 4690, `hep-th/9906064`.

[32] OPAL Collaboration, G. Abbiendi *et al.*, *Flavour independent h0 A0 search and two Higgs doublet model interpretation of neutral Higgs boson searches at LEP* (2004), `hep-ex/0408097`.

L3 Collaboration, P. Achard *et al.*, *Flavour independent search for neutral Higgs bosons at LEP*, Phys. Lett. **B583**(2004) 14, `hep-ex/0402003`.

ALEPH Collaboration, A. Heister *et al.*, *A flavor independent Higgs boson search in* $\mathrm{e}^+\mathrm{e}^-$ *collisions at* $\sqrt{\mathrm{s}}$ *up to 209 GeV*, Phys. Lett. **B544**(2002) 25, `hep-ex/0205055`.

[33] S. Weinberg, *Implications of dynamical symmetry breaking*, Phys. Rev. **D13**(1976) 974.

S. Weinberg, *Implications of dynamical symmetry breaking: An addendum*, Phys. Rev. **D19**(1979) 1277.

[34] L. Susskind, *Dynamics of spontaneous symmetry breaking in the Weinberg- Salam theory*, Phys. Rev. **D20**(1979) 2619.

[35] B. Holdom, *Raising the sideways scale*, Phys. Rev. **D24**(1981) 1441.

[36] K. Yamawaki, M. Bando, and K.-i. Matumoto, *Scale invariant Technicolor model and a technidilaton*, Phys. Rev. Lett. **56**(1986) 1335.

[37] T. W. Appelquist, D. Karabali, and L. C. R. Wijewardhana, *Chiral hierarchies and the flavor changing neutral current problem in Technicolor*, Phys. Rev. Lett. **57**(1986) 957.

[38] T. Appelquist and L. C. R. Wijewardhana, *Chiral hierarchies and chiral perturbations in Technicolor*, Phys. Rev. **D35**(1987) 774.

[39] T. Appelquist and L. C. R. Wijewardhana, *Chiral hierarchies from slowly running couplings in Technicolor theories*, Phys. Rev. **D36**(1987) 568.

[40] K. D. Lane, *Technicolor 2000* (2000), `hep-ph/0007304`.

[41] K. D. Lane, *Technihadron production and decay in low-scale Technicolor*, Phys. Rev. **D60**(1999) 075007, `hep-ph/9903369`.

[42] S. Mrenna, *Technihadron production and decay at LEP2*, Phys. Lett. **B461**(1999) 352, `hep-ph/9907201`.

[43] K. D. Lane, *Technihadron production and decay rates in the Technicolor Straw man Model* (1999), `hep-ph/9903372`.

[44] M. W. Gruenewald, G. Passarino, *et al.*, *Four-fermion production in electron-positron collisions* (2000), `hep-ph/0005309`.

[45] DELPHI Collaboration, J. Abdallah *et al.*, *Search for technicolor with DELPHI*, Eur. Phys. J. **C22**(2001) 17, `hep-ex/0110056`.

[46] L3, *Search for technicolor production at LEP* L3 Note 2428, June 1999, submitted to the International Europhysics Conference on High Energy Physics (Tampere, Finland, July 1999).

[47] The OPAL Collaboration, *Searches for Technicolor with the OPAL detector in* e^+e^- *collisions at the highest LEP energies* OPAL PN-485.

[48] N. Gollub, *Search for Technicolor with the OPAL detector in* e^+e^- *collisions at the highest LEP energies* DESY-THESIS-2001-063.

[49] CDF Collaboration, T. Handa, *Technicolor limits at the Tevatron* To be published in the proceedings of 13th Topical Conference on Hadron Collider Physics, Mumbai, India, 14-20 Jan 1999.

CDF Collaboration, T. Affolder *et al.*, *Search for color singlet technicolor particles in* $p\bar{p}$ *collisions at* $\sqrt{s} = 1.8\ TeV$, Phys. Rev. Lett. **84**(2000) 1110.

[50] A. A. Sokolov and I. M. Ternov, *On polarization and spin effects in the theory of synchrotron radiation*, Phys. Dokl. **8**(1964) 1203.

[51] L. Arnaudon *et al.*, *Accurate determination of the LEP beam energy by resonant depolarization*, Z. Phys. **C66**(1995) 45.

[52] LEP Energy Working Group Collaboration, A. Blondel *et al.*, *Evaluation of the LEP centre-of-mass energy above the W pair production threshold*, Eur. Phys. J. **C11**(1999) 573, `hep-ex/9901002`.

C. Menot *et al.*, *The LEP spectrometer* (1999), Prepared for 9th LEP Performance Workshop, Chamonix, France, Januar 26th-29th.

[53] OPAL Collaboration, K. Ahmet *et al.*, *The OPAL detector at LEP*, Nucl. Instrum. Meth. **A305**(1991) 275.

[54] R. Brinkmann *et al.*, *TESLA technical design report partII: The accelerator* DESY-01-011.

[55] *2001 report on the Next Linear Collider: A report submitted to Snowmass '01* Prepared for APS / DPF / DPB Summer Study on the Future of Particle Physics (Snowmass 2001), Snowmass, Colorado, 30 Jun - 21 Jul 2001.

[56] *GLC project: Linear collider for TeV physics* KEK-REPORT-2003-7.

[57] G. A. Loew *et al.*, *International Linear Collider Technical Review Committee, ILC-TRC report 2003* document available from `http://www.slac.stanford.edu/xorg/ilc-trc/2002/2002/report/03rep.htm`.

[58] Document available from `http://www.fnal.gov/directorate/icfa/ITRP_Charge.pdf`.

[59] Document available from `http://www.interactions.org/pdf/ITRPexec.pdf`.

[60] R. Bakker *et al.*, *First beam measurements at the Photo Injector test facility at DESY Zeuthen*, Nucl. Instrum. Meth. **A507**(2003) 210.

[61] ECFA/DESY Photon Collider Working Group Collaboration, B. Badelek *et al.*, *TESLA technical design report, part VI, chapter 1: Photon collider at TESLA* (2001), `hep-ex/0108012`.

[62] T. Behnke, S. Bertolucci, R. D. Heuer, and e. Settles, R., *TESLA technical design report partIV: A detector for TESLA* DESY-01-011.

[63] C. J. S. Damerell, *A CCD based vertex detector for TESLA* (2001), LC-DET-2001-023.

[64] M. Winter *et al.*, *A CMOS based VTX detector* (2001), LC-DET-2001-017.

[65] P. Fischer *et al.*, *A DEPFET based pixel vertex detector for the detector at TESLA* (2002), LC-DET-2002-004.

[66] M. Battaigla *et al.*, *A pixel vertex tracker for the detector at TESLA* (2001), LC-DET-2001-042.

[67] S. Ambrosanio and G. A. Blair, *Extracting GMSB parameters at a linear collider* (1998), `hep-ph/9911360`.

[68] OPAL Collaboration, K. Ackerstaff *et al.*, *Tests of the Standard Model and constraints on new physics from measurements of fermion pair production at 130-GeV to 172-GeV at LEP*, Eur. Phys. J. **C2**(1998) 441, `hep-ex/9708024`.

[69] T. Sjostrand, L. Lonnblad, and S. Mrenna, *PYTHIA 6.2: Physics and manual* (2001), `hep-ph/0108264`.

[70] S. Jadach, B. F. L. Ward, and Z. Was, *The precision Monte Carlo event generator KK for two- fermion final states in* $\mathrm{e^+e^-}$ *collisions*, Comput. Phys. Commun. **130**(2000) 260, `hep-ph/9912214`.

S. Jadach, B. F. L. Ward, and Z. Was, *Coherent exclusive exponentiation CEEX: The case of the resonant* $\mathrm{e^+e^-}$ *collision*, Phys. Lett. **B449**(1999) 97, `hep-ph/9905453`.

[71] J. Fujimoto *et al.*, *grc4f v1.1: a four-fermion event generator for* e^+e^- *collisions*, Comput. Phys. Commun. **100**(1997) 128, `hep-ph/9605312`.

[72] S. Jadach, W. Placzek, M. Skrzypek, B. F. L. Ward, and Z. Was, *Monte Carlo program KoralW 1.42 for all four-fermion final states in* e^+e^- *collisions*, Comput. Phys. Commun. **119**(1999) 272, `hep-ph/9906277`.

[73] T. Sjostrand, *The PYTHIA and JETSET programs* Prepared for Particles & Fields 92: 7th Meeting of the Division of Particles Fields of the APS (DPF 92), Batavia, Illinois, 10-14 Nov 1992.

[74] G. Marchesini *et al.*, *HERWIG: A Monte Carlo event generator for simulating hadron emission reactions with interfering gluons. Version 5.1 - April 1991*, Comput. Phys. Commun. **67**(1992) 465.

[75] D. R. Ward, *The OPAL Monte Carlo program: GOPAL* In *Amsterdam 1991, Proceedings, MC 91: Detector and event simulation in high energy physics* 204-226. (see HIGH ENERGY PHYSICS INDEX 30 (1992) No. 3237).

[76] R. Brun *et al.*, *GEANT: Simulation program for particle physics experiments. User guide and reference manual*, CERN-DD-78-2-REV 1978.

[77] S. Makahara and S. Yamashita, *MT 3.00 a new algorithm to calculate energy flow based on MT package* OPAL Technical Note TN575 (1998).

[78] N. Brown and W. J. Stirling, *Jet cross-sections at leading double logarithm in* e^+e^- *annihilation*, Phys. Lett. **B252**(1990) 657.

S. Bethke, Z. Kunszt, D. E. Soper, and W. J. Stirling, *New jet cluster algorithms: Next-to-leading order QCD and hadronization corrections*, Nucl. Phys. **B370**(1992) 310.

S. Catani, Y. L. Dokshitzer, M. Olsson, G. Turnock, and B. R. Webber, *New clustering algorithm for multi - jet cross-sections in* e^+e^- *annihilation*, Phys. Lett. **B269**(1991) 432.

N. Brown and W. J. Stirling, *Finding jets and summing soft gluons: A new algorithm*, Z. Phys. **C53**(1992) 629.

[79] S. Yamashita, *Attempt to develop new jet-particle association methods for four-jet topology with OPAL detector* OPAL Technical Note TN579 (1998).

[80] I. Nakamura and S. Yamashita, *A new b-tagging tool for LEP2* OPAL Technical Note TN576 (1998).

[81] OPAL Collaboration, G. Abbiendi *et al.*, *Search for the Standard Model Higgs boson with the OPAL detector at LEP*, Eur. Phys. J. **C26**(2003) 479, `hep-ex/0209078`.

[82] G. Parisi, *Super inclusive cross-sections*, Phys. Lett. **B74**(1978) 65.

J. F. Donoghue, F. E. Low, and S.-Y. Pi, *Tensor analysis of hadronic jets in quantum chromodynamics*, Phys. Rev. **D20**(1979) 2759.

[83] SLD and LEP Collaboration, R. Barate *et al.*, *Parameters for the LEP/SLD electroweak heavy flavour results for summer 1998 conferences* (1998), LEPHF/98-01.

[84] E. Gross and A. Klier, *Higgs statistics for pedestrians* (2002), `hep-ex/0211058`.

[85] ECFA/DESY LC Physics Working Group Collaboration, J. A. Aguilar-Saavedra *et al.*, *TESLA technical design report part III: Physics at an* e^+e^- *linear collider* (2001), hep-ph/0106315.

[86] American Linear Collider Working Group Collaboration, T. Abe *et al.*, *Linear collider physics resource book for Snowmass 2001* Resource book for Snowmass 2001, 30 Jun - 21 Jul 2001, Snowmass, Colorado.

[87] S. Soldner-Rembold and G. Jikia, *Light Higgs production at a photon collider*, Nucl. Instrum. Meth. **A472**(2001) 133, hep-ex/0101056.

M. Melles, W. J. Stirling, and V. A. Khoze, *Higgs boson production at the Compton collider*, Phys. Rev. **D61**(2000) 054015, hep-ph/9907238.

[88] K. Desch and N. Meyer, *Study of Higgs boson production through WW-fusion at TESLA* LC-PHSM-2001-025.

[89] W. Kilian, *WHIZARD: Complete simulations for electroweak multi-particle processes* Prepared for 31st International Conference on High Energy Physics (ICHEP 2002), Amsterdam, The Netherlands, 24-31 Jul 2002.

[90] F. Maltoni and T. Stelzer, *MadEvent: Automatic event generation with MadGraph*, JHEP **02**(2003) 027, hep-ph/0208156.

[91] M. Pohl and H. J. Schreiber, *SIMDET - a parametric Monte Carlo for a TESLA detector* Prepared for 5th International Linear Collider Workshop (LCWS 2000), Fermilab, Batavia, Illinois, 24-28 Oct 2000.

[92] T. Behnke and G. A. Blair, *BRAHMS - version 1.02: A Monte Carlo for a detector at a 500-GeV to 800-GeV linear collider* LC-PHSM-2001-005.

[93] V. Drollinger and A. Sopczak, *Comparison of Higgs boson mass and width determination of the LHC and a linear collider*, Eur. Phys. J. direct **C3**(2001) N1, hep-ph/0102342.

[94] P. Garcia-Abia, W. Lohmann, and A. Raspereza, *Measuring the Higgs mass at TESLA* Prepared for 5th International Linear Collider Workshop (LCWS 2000), Fermilab, Batavia, Illinois, 24-28 Oct 2000.

[95] C. Hensel, *Beam induced background at a TESLA detector* LC-DET-2000-001.

G. Wagner, *Neutron background studies at the TESLA collider* LC-DET-2001-048.

K. Busser and O. Napoly, *Improved TESLA optics and beam induced backgrounds update* LC-M-2003-045.

[96] T. Behnke *et al.*, *Performance study of the proposed TESLA detector using a realistic track reconstruction package* LC-DET-2001-029.

[97] D. Schulte, *Beam-beam simulations with GUINEA-PIG*, eConf **C980914**(1998) 127.

[98] T. Barklow, *Update on gamma-gamma to hadrons calculation* Talk given at the ALCPG meeting, SLAC, Jan. 2004.

[99] D. Schulte, *HADES library* code available from http://dschulte.home.cern.ch/dschulte/physics/hades/hades.html.

[100] T. L. Barklow, *Higgs coupling measurements at a 1-TeV linear collider* (2003), hep-ph/0312268.

[101] K. Desch and M. Battaglia, *Determination of the Higgs profile: HFITTER* Prepared for 5th International Linear Collider Workshop (LCWS 2000), Fermilab, Batavia, Illinois, 24-28 Oct 2000.

[102] M. Battaglia and D. Schulte, *Study of $\gamma\gamma$ background in* $\mathrm{e}^+\mathrm{e}^- \to \mathrm{W}^+\mathrm{W}^-\nu\bar{\nu} \to \mathrm{H}^0\,\nu\bar{\nu}$ *events at the TESLA* $\mathrm{e}^+\mathrm{e}^-$ *linear collider* (1999), hep-ex/0011085.

[103] K. Desch, A. Imhof, N. Meyer, and A. Raspereza, *Impact of hadronic backgrounds on selected Higgs physics analyses at a linear collider* LC-PHSM-2004-009.

Danksagung

Diese Doktorarbeit ist auch nicht anders als andere: Es gibt eine ganze Reihe von Personen, ohne die sie nicht möglich gewesen wäre.

Mein besonderer Dank gilt der Gruppe FLC am DESY, allen voran Ties Behnke, Ramona Matthes und meinem Doktorvater Rolf-Dieter Heuer. Sie haben mir meine Arbeit erst ermöglicht und mich immer nach Kräften unterstützt. Desweiteren bedanke ich mich bei meinen Zweitgutachtern Beate Naroska und Peter Schleper für die faire Beurteilung meiner Promotion.

Großen Anteil am Gelingen der Arbeit hat Klaus Desch, der fachlich wie privat immer ein offenes Ohr für mich hatte. Außerdem konnte ich mich immer auf Philip Bechtle, Nils Gollub, Thorsten Kuhl und Markus Schumacher verlassen, wenn ich mal wieder nicht weiter kam.

Neben den bereits genannnten haben auch die anderen Mitglieder der Gruppe sehr dazu beigetragen, dass ich mich wohlgefühlt habe. Danke an alle, besonders Blanka, Erika und Marius für die gemeinsame Zeit in einem Büro!

Natürlich definiert sich ein Mensch nicht nur über seine Arbeit. Meine Eltern haben den größten Anteil daran, dass ich das bin was ich bin. Trotzdem gebührt der größte Dank am Ende nicht ihnen.

Dany, ich danke Dir dass ich Dich habe und dass Du mich erträgst und mich stützt. Niemand wäscht mir den Kopf so wohltuend wie Du. Ich liebe Dich!